Investigation of P3HT/PCBM Particle-Based Solar Cells

Al

MoO₃

active layer

ZnO

ITO

glass

Dissertation

Birger Freisinger

Investigation of P3HT/PCBM Particle-Based Solar Cells

Dissertation

zur Erlangung des Grades

„Doktor der Naturwissenschaften"

im Promotionsfach Chemie

am Fachbereich Chemie, Pharmazie und Geowissenschaften

der Johannes Gutenberg-Universität in Mainz

vorgelegt von

Birger Freisinger

geboren in Schwäbisch Hall

Mainz 2013

Die vorliegende Dissertation wurde im Zeitraum von Februar 2009 bis Mai 2013 am Max-Planck-Institut für Polymerforschung, Mainz und an der Seoul National University, Seoul, Republik Korea erstellt.

Hiermit erkläre ich, dass ich diese Arbeit selbständig und nur mit den angegebenen Hilfsmitteln angefertigt habe. Alle Stellen, die dem Wortlaut oder dem Sinn gemäß anderen Arbeiten entnommen wurden, sind durch Angabe der Quellen kenntlich gemacht.

Mainz, 10.05.2013   _____

Birger Freisinger

Amtierender Dekan:

Erster Gutachter:

Zweiter Gutachter:

Tag der mündlichen Prüfung: 07.06.2013

Abstract

Aqueous processing of polymer solar cells presents an attractive alternative to the conventional solvent based fabrication of photovoltaics. The benefits of these cells are particularly the environmentally friendly fabrication process and the realization of printable devices. The processability of hydrophobic semiconductors in the aqueous phase is achieved by dispersing the materials as nanoparticles. The emulsification solvent evaporation method is used to transfer the semiconductors into an aqueous dispersion.

The concept of particle-based organic solar cells has been already implemented, however, a detailed characterization of the particles and a fundamental understanding of the entire fabrication process is absent. For that reason, the aim of this thesis is to gain a detailed insight into the preparation process of particle-based solar cells in order to reveal and eradicate potential problems, improving future applications. The donor/acceptor system poly(3-hexylthiophene-2,5-diyl)/[6,6]-phenyl-C61-butyric acid methyl ester (P3HT/PCBM) is used for this approach.

This study focuses on an investigation of particle morphology and the formation of suitable particle layers. Both parameters have a great impact on the device efficiency. The morphology was characterized and investigated both spectroscopically, via photoluminescence measurements, and visually, by electron microscopy. In this manner, the particle morphology was fully clarified and parallels to the structure of solution-processed photovoltaics could be found. Further, the influence of preparation temperature on the morphology was observed, allowing an easy control of the particle structure. In the course of particle layer formation, direct assembly and liquid interface-mediated processes were applied. However, only the spin coating technique has to prove practical for converting particles from a dispersion into a suitable homogeneous film. Moreover, reprocessing of the particle layer by ethanol washing and thermal treatment was also an important aspect of this work. These steps had a positive effect on the efficiency of the devices, contributing decisively to the improvement of particle-based solar cells. The obtained cognitions provided a detailed overview of the challenges arising in the use of aqueous dispersions instead of traditional solvent processing. The requirements of particle-based solar cells could therefore be revealed, in the process allowing successful fabrication of solar cells with an efficiency of 0.53%. However, this result is not the optimum, and room for improvements is still present.

Zusammenfassung

Die Herstellung von Polymer-Solarzellen aus wässriger Phase stellt eine attraktive Alternative zu der konventionellen lösemittelbasierten Formulierung dar. Die Vorteile der aus wässriger Lösung hergestellten Solarzellen liegen besonders in dem umweltschonenden Herstellungsprozess und in der Möglichkeit, druckbare optoelektronische Bauteile zu generieren. Die Prozessierbarkeit von hydrophoben Halbleitern im wässrigen Milieu wird durch die Dispergierung der Materialien, in Form von Nanopartikeln, erreicht. Der Transfer der Halbleiter in eine Dispersion erfolgt über die Lösemittelverdampfungsmethode.

Die Idee der Verwendung von partikelbasierte Solarzellen wurde bereits umgesetzt, allerdings blieben eine genaue Charakterisierung der Partikel sowie ein umfassendes Verständnis des gesamten Fabrikationsvorgangs aus. Deshalb besteht das Ziel dieser Arbeit darin, einen detaillierten Einblick in den Herstellungsprozess von partikelbasierten Solarzellen zu erlangen, mögliche Schwächen aufzudecken, diese zu beseitigen, um so zukünftige Anwendungen zu verbessern. Zur Herstellung von Solarzellen aus wässrigen Dispersionen wurde Poly(3-hexylthiophen-2,5-diyl)/[6,6]-Phenyl-C61-Buttersäure-Methylester (P3HT/PCBM) als Donor/Akzeptor-System verwendet.

Die Kernpunkte der Untersuchungen richteten sich zum einen die auf Partikelmorphologie und zum anderen auf die Generierung einer geeigneten Partikelschicht. Beide Parameter haben Auswirkungen auf die Solarzelleneffizienz. Die Morphologie wurde sowohl spektroskopisch über Photolumineszenz-Messungen, als auch visuell mittels Elektronenmikroskopie ermittelt. Auf diese Weise konnte die Partikelmorphologie vollständig aufgeklärt werden, wobei Parallelen zu der Struktur von lösemittelbasierten Solarzellen gefunden wurden. Zudem wurde eine Abhängigkeit der Morphologie von der Präparationstemperatur beobachtet, was eine einfache Steuerung der Partikelstruktur ermöglicht. Im Zuge der Partikelschichtausbildung wurden direkte sowie grenzflächenvermittelnde Beschichtungsmethoden herangezogen. Von diesen Techniken hatte sich aber nur die Rotationsbeschichtung als brauchbare Methode erwiesen, Partikel aus der Dispersion in einen homogenen Film zu überführen. Des Weiteren stand die Aufarbeitung der Partikelschicht durch Ethanol-Waschung und thermische Behandlung im Fokus dieser Arbeit. Beide Maßnahmen wirkten sich positiv auf die Effizienz der Solarzellen aus und trugen entscheidend zu einer Verbesserung der Zellen bei. Insgesamt liefern die gewonnen Erkenntnisse einen detaillierten Überblick über die Herausforderungen, welche bei dem Einsatz von wasserbasierten Dispersionen

auftreten. Die Anforderungen partikelbasierter Solarzellen konnten offengelegt werden, dadurch gelang die Herstellung einer Solarzelle mit einer Effizienz von 0.53%. Dieses Ergebnis stellt jedoch noch nicht das Optimum dar und lässt noch Möglichkeiten für Verbesserungen offen.

초록

Aqueous process 를 이용한 폴리머 솔라셀은 기존의 솔벤트를 이용하여 제작되는 광전지의 대안을 제시한다. 이러한 디바이스의 잇점으로는 환경친화적 제작 프로세스와 프린팅이 가능한 디바이스의 사용을 들 수 있다. 수상에서의 소수성 반도체의 가공법은 나노파티클을 분산시킴으로서 가능해진다. 유화 솔벤트 증발 방법은 반도체를 수중 분산하여 전송하기 위해 사용된다.

파티클 기반의 유기 솔라셀 컨셉은 이미 기존에 연구되어 왔으나 파티클의 구체적인 특성과 총 제작 프로세스에 대한 근본적인 이해는 아직 부족한 편이다. 이러한 이유로, 현 논문은 잠재적인 문제들, 예를 들면, 추후 어플리케이션을 향상시키는 것과 같은 문제를 밝히고자 파티클 기반 솔라셀의 준비 프로세스에 대해 통찰하고자 함이다. 도너와 억셉터 물질로는 poly(3-hexylthiophene-2,5-diyl)/[6,6]-phenyl-C61-butyric acid methyl ester (P3HT/PCBM)이 사용되었다.

현 연구는 파티클의 형상(morphology) 조사와 적합한 파티클의 레이어의 형성에 촛점을 맞추었다. 두 가지 파라미터는 모두 디바이스의 효율에 지대한 영향을 미친다. Morphology 는 photoluminescence measurement 와 electron microscopy 를 이용하여 조사하였다. 위와 같은 방법으로 파티클 morphology 를 이해하여 이를 솔루션 프로세싱 광전지의 구조와 비교하여 서술하였다. 또한 morphology 에 미치는 온도의 영향에 대해서도 관찰하였으며 이는 파티클 morphology 의 용이한 컨트롤을 허용하였다. 파티클 레이어의 형성과정에서는 직접 조립과 액체계면성 프로세스가 이용되었다. 그러나 dispersion 에서 적합한 homogeneous 한 필름으로의 파티클의 전환은 오로지 스핀코팅 방법을 통해서만 확인되었다. 게다가 에탄올 워싱과 열적 처리방법을 이용한 파티클 레이어의 재가공은 현 논문에서 중요한 요소로 간주된다. 이러한 작업들은 모두 디바이스의 효율에 긍정적인 영향을 미쳤으며 결과적으로는 파티클 기반 솔라셀의 향상에 기여한다. 또한 현 논문에서 전통적인 솔벤트 프로세스 대신에 수상분산을 이용한 방법을 사용하였을 때에 떠오르는 문제점을 전반적으로 살펴보았다. 파티클 기반 솔라셀의 필요조건이 기술되었으며 이를 이용한 솔라셀 제작의 효율은 0.53 %를 보였다. 그러나 이는 최적화된 결과가 아니며 개선의 여지는 여전히 남아있다.

Table of contents

1 Introduction

The modern world relies heavily on the supply of electricity. As world population increases, and emerging nations develop advanced industrial economies, world energy consumption is steadily increasing. Today, the annual requirement is $1.48 \cdot 10^5$ TWh and in the year 2035, a total consumption of $2.26 \cdot 10^5$ TWh is predicted.[1] With a limited world supply of fossil fuels and societal controversy of nuclear power, providing mankind with sustainable energy is one of the major challenges of the 21st century. In the long term, only renewable energy sources, *e.g.* hydro, wind, biomass, tidal, geothermal and solar energy will be in a position to supply humanity with maintainable and non-polluting energy. Except for geothermal and tidal energy, all other forms of renewable energies are outcomes of the sun's energy. The annual solar energy, striking the earth's surface is approximately 10^9 TWh.[2] This is 6757 times the global annual energy consumption. It is estimated that $1.39 \cdot 10^7$ TWh are realistically exploitable, still 94 times of the current energy requirement.[3] Therefore, a direct utilization of solar radiation to produce electricity seems to be a highly promising candidate for meeting the energy demand.

1.1 Why organic solar cells?

Since 1954, when the first modern p-n junction photovoltaic (PV) cell was invented, crystalline silicon devices have dominated the solar cell market.[4] However, these inorganic PVs suffer from the problem of a massive energy input for their production, resulting in high manufacturing costs and a long energy payback time.[5] Thus, many attempts have been made to look for high-efficiency, low-cost solar cells. A promising approach is the use of organic semiconductors, *e.g.* from polymers. Organic solar cell devices consist of a multi-layer structure, featuring an active layer blend of electron donor (D) and electron acceptor (A) material.[6] The use of organic solar cells has several advantages over their inorganic counterparts. Organic PVs (OPVs) do not require high deposition temperatures or complex processing, required by inorganic PVs. Polymers can be dissolved in solvents and deposited on substrates using wet-processing techniques such as spin coating or roll-to-roll printing.[7] This solution processing renders large-scale and low-cost production possible. As a result of the simple and quick manufacturing process, the energy payback time of polymer solar cells may be confined to only a few weeks.[2] Moreover, the flexibility of organic semiconductors enables

application of OPVs in wide ranges, *e.g.* on curved or collapsible surfaces.[8] Additionally, the material and electronic properties can be tailored by modifying the chemical structure, resulting in greater customization than is possible for traditional solar cells.[9, 10] However, fundamental challenges must be resolved before a successful mass production is possible, including improvements in efficiency, device lifetime, encapsulation, and the understanding of basic physical mechanisms. Nevertheless, today, organic semiconducting materials are attractive candidates for applications in electronic devices.[11, 12, 13]

1.2 Why particle-based organic solar cells?

Colloidal systems are heterogeneous mixtures of two (or more) immiscible components. These systems are comprised of a dispersed phase and a dispersion medium, also called the continuous phase. The dispersed phase exists in a well distributed state in the continuous medium. The dimension of the dispersed phase is in a range between approximately a few nanometers to several micrometers. Except systems consisting of gases, both phases can be present in solid, liquid and gaseous physical conditions.[14, 15]

A system consisting of water as the continuous phase and a solid as the dispersed phase is called a dispersion. By using the so called secondary dispersion or solvent evaporation technique,[16, 17] nearly every common semiconducting polymer can be transferred into a dispersion. Here, a polymer is dissolved in a suitable solvent; the polymer solution is emulsified in water. In order to obtain a dispersion, the solvent is evaporated by heating. In general, secondary dispersions can be seen as a polymer "dissolved" in water, as system does not contain any organic solvent any more, but is still wet-processable. Concomitantly, the polymers still exist as a solid material within the colloids, undergoing no change in chemical or physical properties. Besides, the control of nanoparticle size is possible,[18] presetting the dimension of the semiconductor phase. These fantastic characteristics offer new and interesting opportunities that can be used to promote OPVs. Admittedly, it is well known from experiments that the PV performance degrades faster if the OPV devices are exposed to oxygen and/or water, *i.e.* at ambient air.[19] However, water-processed polymer solar cells have been shown to exhibit the same operational stability as solar cells processed by organic solvents.[20]

Today, the active layer of organic polymer solar cells is processed exclusively from organic solvents; most often these are chlorinated and/or aromatic. The use of such solvents will pose

health, safety, and environmental problems. From a laboratory or preindustrial point of view, this is a relatively minor problem. However, in order to scale up to production to industrial levels, it is clear that a viable alternative must be found. In particular, water employed in a dispersion is an ideal choice of solvent, since it is cheap, ecological, and there are no ill effects associated with its use.[21, 22]

Due to the change in polarity of the system from hydrophobic to hydrophilic, aqueous dispersions can be also used to facilitate the construction of multi-layer systems. In multi-layer systems, the materials are often soluble in the same solvents, leading to interdiffusion and undefined interfaces between the layers. Thus, it is difficult to find a selective or rather orthogonal solvent, which dissolves only one material. As water is the best orthogonal solvent for hydrophobic materials, a colloid film can be deposited on an organic film without influencing the bottom layer.[23]

In OPVs, the morphology of the D/A phase is of paramount importance for increase the device efficiency.[24] The dimension of each phase must be in the range of the exciton diffusion length that is the distance traveled by the electron-hole pair before recombination, commonly, a few tens of nanometers. The phase separation that occurs during the active layer formation depends on various parameters such as: the individual solubility of the polymers in the solvent used, their interaction with substrate surface, the layer thickness, the method of deposition, the drying, and annealing conditions.[24-34] Using particles, the phase separation dimension is given by the size of the nanoparticles, which can be adjusted down to a few tens of nanometers.[18] As phase separation is part of the particle preparation process, the morphology formation can be split from the film formation when particles are used. This should allow a better control of morphology and film formation.[35]

1.3 Motivation and aim

Originally, the semiconducting nanoparticle dispersion concept was introduced by Landfester *et al*.[23] Applying this knowledge, Kietzke *et al.* developed the first particle-based organic photovoltaic (PBOPV) device.[35] The resulting device exhibits an external quantum efficiency (EQE) of 1.7%, using polyfluorenes as active layer materials. By changing the polymer ratio, the EQE could be enhanced to 4.2%.[36] Only a few reports on water processed polymer solar cells have been published so far. In a recent report, Andersen *et al.* used the aqueous dispersion concept to pursue the goal of environmentally friendly, commercially viable OPVs by a roll-to-roll technique.[22] However, these

publications have to date only demonstrated a proof of principle for PBOPVs; a detailed study with respect to particle morphology, layer formation, and device preparation conditions is absent. For that reason, the initial approach of Kietzke will be expanded in this thesis to a basic study of PBOPVs, regarding to the above mentioned parameters. The main goal of this thesis is to establish an accurate overview of the whole fabrication process of PBOPVs. Challenges occurring in the individual preparation steps of applying colloids shall be revealed and potential alternative solutions suggested. Finally, starting from these fundamental insights, a particle-based device offering similar characteristics to solution-processed OPVs (SPOPVs) shall be developed. Since the work of Kietzke *et al.* dates back almost 10 years, big changes in organic solar cell materials have led to considerable improvements in the quality and availability of organic semiconductors. Thus, nowadays, much better and more effective materials in the form of polythiophene (D) and fullerene (A) derivatives are available.[37] Consequently, an additional goal of this thesis is the development of devices featuring a higher efficiency than the original Kietzke cells.

1.4 Outline

This thesis is structured as follows: in **chapter 2**, theoretical basics that are vital for a fundamental understanding of the present work will be described. This includes information of particle stability and preparation, phase separation, right up to the morphology formation inside particles. Then, a closer view of OPVs will be provided, including organic semiconducting materials, principles of operation, measurements of solar cell properties, and concepts in organic solar cells. **Chapter 3** introduces relevant characterization methods, supplying an understanding of several fields. The focus will be on particle morphology investigation, appropriate material and spectroscopic characteristics, and the behavior of particle films under certain annealing conditions. Details of wetting or rather dispersion-substrate interaction, the resultant structuring and arrangement of particle films using different coating methods, and finally the performance of the fabricated solar cell devices will also be discussed. As imaging techniques are important for the described investigations, electron microscopy takes a particularly significant role in this thesis. The results are summarized in **chapter 4**, which is subdivided into 4 parts: the investigation on composite particle morphology, the study of active layer formation, the investigation of conditions for the fabrication of PBOPVs, and the development of advanced particle-based solar devices. **Chapter 5** will summarize the results that have been discussed in the previous chapter. In **chapter 6**, all

experimental details will be shown. Additionally, all materials used in this work and their specifications will be listed. The work ends with an appendix (**chapter 7**), here, mainly further results and information going beyond the scope of **chapter 4** will be given.

2 Theoretical framework

2.1 Colloidal systems

2.1.1 Emulsions

The general structure of (direct) emulsions is composed of an aqueous continuous phase and a dispersed oil phase. Depending upon the size of the droplets, the thermodynamic stability of the droplets, and the particular synthesis method, emulsions can also be subdivided into three classes, illustrated in **Figure 1**. The first class of these are macroemulsions, containing droplets on the order of micrometers or larger. In miniemulsions, the droplet size is in the range of tens to hundreds of nanometers, while microemulsions feature droplets a few tens of nanometers in size.
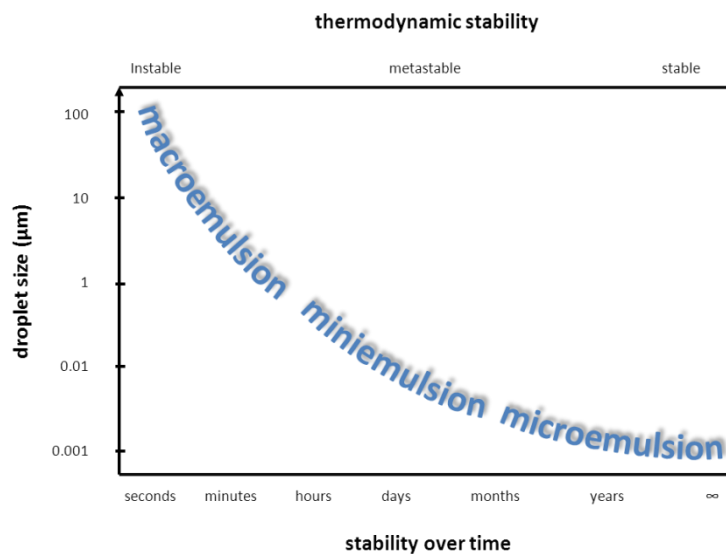
Figure 1: *Overview of droplet size, thermodynamic stability, and stability over time of macroemulsions, miniemulsions, and microemulsions. The emulsions are thermodynamically instable, metastable, or stable, accompanied by a continuous reduction of droplet size.*[38]

In order to understand the process of droplet formation, first note that the water/oil interface increases drastically by preparing an emulsion from two separated phases. The generation of new interfaces needs energy that has to be carried into the system. Usually, this energy is supplied by stirring. After completion of the stirring process, the emulsion is merely stable for a short period. Subsequently, the system turns into the thermodynamically stable state, which is the two layered

initial state. This phenomenon is known as emulsion breaking, and its onset is defined by the smallest possible amount of Gibbs free energy (ΔG):

$$\Delta G = \sum \gamma_{ij} A_{ij} \tag{1}$$

The interfacial energy (γ) is constant, therefore, the only possibility to minimize ΔG is to reduce the interfacial area (*A)*, resulting into two entirely separate phases.[39] Regarding droplets, the breaking of an emulsion into two separate phases is a result of coalescence and molecular diffusion degradation. Coalescence is a process in which two droplets form one larger droplet. For this mechanism, two droplets must get close enough to allow contact of the droplet phases. In the case of the molecular diffusion process, which is also known as Ostwald ripening,[40] two droplets also form a single droplet. One droplet is growing, while the other dissolves. During this process, the droplets are not required to come into contact, because it involves molecular diffusion between the oil phases.[41]

2.1.2 Preventing of breaking

Stabilization of an emulsion against coalescence can be realized by the use of surfactants, preventing droplets from encountering one another. Surfactants are divided into two types: ionic and nonionic surfactants. The most common type of ionic surfactants is anionic surfactants, which have a negatively charged functional head group and a nonpolar alkyl chain. Nonionic surfactants, generally, contain a polar polyhydroxyl or polyether as head group and also feature a hydrophobic alkyl chain. Depending on the nature of the surfactant, the stabilization of droplets occurs as a result of electrostatic repulsion or steric hindrance. Additionally, surfactants lower the interfacial energy, hence, they support the emulsification process in general. Typical examples of ionic surfactants are the anionic sodium dodecyl sulfate (SDS) and the cationic alternative cetyltrimethylammonium chloride (CTAC). Non-ionic agents are often amphiphilic, *e.g.* polymeric alkyl poly(ethylene glycol ethers).

The addition of a sufficient number of molecules, which are not soluble in the continuous phase, provides stabilization against Ostwald ripening. Generally, long chain alkanes such as hexadecane are used as so called ultra-hydrophobic agents.[18] The ultra-hydrophobics are trapped in the organic phase and feature an osmotic pressure that counteracts the Laplace pressure (p_{La}). This pressure is a consequence of the interfacial energy between the dispersed and the continuous phase,

representing the pressure difference between the inside and the outside of a droplet, given by the radius *r*:

$$p_{La} = \frac{2\gamma}{r} \tag{2}$$

Smaller droplets are more unstable and susceptible to being dissolved by diffusion to bigger droplets.[42] The diffusion process from small to large droplets is prevented by ultra-hydrophobic agents, due to the fact that the osmotic pressure is approximately equal for all droplets. If diffusion of the droplets phases (but not the ultra-hydrophobic agents) were to occur, smaller droplets would lose mass, leading to a higher molar concentration of the agents, accompanied by a higher osmotic pressure. In fact, this state is not stable, hence, the droplets will not disappear by this mechanism when ultra-hydrophobic agents are present.

2.1.3 Macro- and microemulsions

By definition, macroemulsions are not stable or only stabilized by surfactants, hence, they are susceptible to Ostwald ripening. Thus, these emulsions become instable over time. In contrast, microemulsions are spontaneously formed, thermodynamically completely stable systems. In order to obtain such small and stable droplets, they require a huge amount of surfactant (50 to 200% relative to the dispersed phase) and usually the addition of a cosurfactant. Cosurfactants are surface-active reagents, reducing the interfacial energy in the presence of surfactants additionally. This leads to a nearly zero interfacial energy. Suitable cosurfactants are alcohols of medium chain length such as butanol and pentanol. Owing to the small droplet size, microemulsions are transparent, and they have the ability to solubilize otherwise immiscible liquids.[43] Due to these special features, especially, the small droplet size, microemulsions should have an enormous potential. However, in practical and synthetic terms, they are not widely used. The removal of surfactant and cosurfactant from the resulting emulsion, without affecting the stability is extremely difficult, if not impossible.[44]

2.1.4 Miniemulsions

The term miniemulsion was proposed by Chou *et al.* for historical reasons.[45] In comparison to microemulsions, miniemulsions are thermodynamically metastable, since the amount of surfactant is much lower. The surfactant concentration is 0.1 to 20% with respect to the dispersed phase, indicating a partially covered droplet surface. Nevertheless, miniemulsions are stabilized against degradation by molecular diffusion, hence, there are kinetically stabilized. For this reason, microemulsions are often labeled as fully stable.[46]

The formation of a miniemulsion utilizes another dispersion technique in addition to stirring. Basically, the formation is divided into two steps, as shown in **Figure 2**. First, the water and oil phases are pre-mixed by stirring, resulting in a kind of macroemulsion or also called a pre-emulsion. The provided energy of stirring is not enough to obtain small and narrowly distributed droplets.[47] As a result, in a second step, the pre-emulsion is transferred to a miniemulsion by high shear forces. Due to the viscous resistance, the system requires much more energy to create new boundary surface, as given by the difference in interfacial energies in **Equation 1**. Most of the energy is absorbed by the system and converted to heat.[48] Different methods can be used to supply the required amount of energy. A common technique is ultrasonication, but rotor stator dispersion like colloid milling and high pressure homogenization are also suitable.[49]
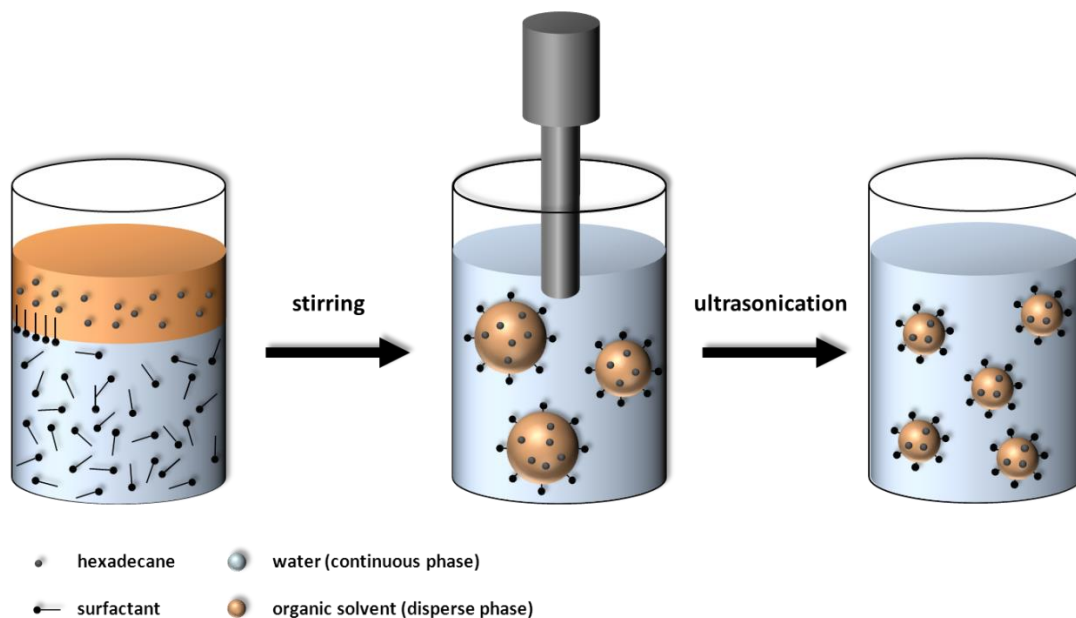
Figure 2: Scheme of miniemulsion formation by using ultrasound.

The mechanism of small droplet formation via ultrasound can be understood as a process of fission and fusion by cavitation. Imploding cavitation bubbles at an ultrasonication tip cause shock waves and the formation of liquid jets of high velocity. This destroys the droplets, followed by droplet consolidation.[50] At the beginning of homogenization, the size and size distribution of the droplets are quite high and broad, but after repeated fission and fusion processes, the droplet size and the polydispersity become smaller. As soon as a state of equilibrium is reached, the droplets do not change their size and size distribution any more.

The eventual droplet size is influenced by the amount of oil and water, and the thermodynamic conditions of both phases, but initially, it is a function of the amount of mechanical agitation. In order to change the droplet size, the variation of the amount and type of surfactant is a convenient and easy to handle method.[51] The use of a liquid monomer as oil can be supplemented by polymerization, leading to a colloidal dispersion. Since there is no diffusion between the droplets, each droplet keeps its identity and can be regarded as a nano-batch-reactor. This gives the opportunity for a controlled design of the particles, and offers a whole variety of applications of the miniemulsion approach.[18, 52]

It should be noted that the polymerization process is not limited to miniemulsions; macro-and microemulsion polymerization is also a suitable method to achieve polymer particles. However, both systems are not stabilized against molecular diffusion, thus, the "nano-batch-reactor feature" is not given anymore.

2.2 Polymeric dispersions

As mentioned, dispersions can be obtained via emulsion, microemulsion, and miniemulsion polymerization processes. Dispersions produced by these techniques are defined as primary dispersions. In these cases, the polymer formation is effected by radical polymerization. Thus, common primary dispersions consist of polymers based on vinyl chloride, styrene, acrylic, and methacrylic acid. Some polymers, *e.g.* semiconducting polymers, are products of other polymerization methods than radical, *e.g.* transition metal catalyzed coupling reactions.[53, 54] Due to the water sensitivity of these reactions, it is difficult to conduct polymerization in an emulsion. Therefore, such a dispersion requires another preparation route.[55]

The manner of transferring existing polymers into a dispersed state is known as secondary dispersion or rather (emulsification) solvent evaporation.[16, 17] In this case, the polymerization process is separated from the entire emulsification step. The polymers are simply synthesized prior to the emulsification step. The procedure of secondary dispersion preparation is shown **Figure 3**. Briefly, a polymer is dissolved in a hydrophobic and water-immiscible solvent, the continuous and dispersed phase are premixed, followed by emulsification. Depending on the kind of emulsion, there is also the possibility of using several stabilization concepts and emulsification techniques. Secondary dispersions, also known as artificial latexes, are obtained by the removal of the solvent during heating.

stirring
+
ultrasonication

evaporation of
solvent

polymer
surfactant
water (continuous phase)
organic solvent (disperse phase)
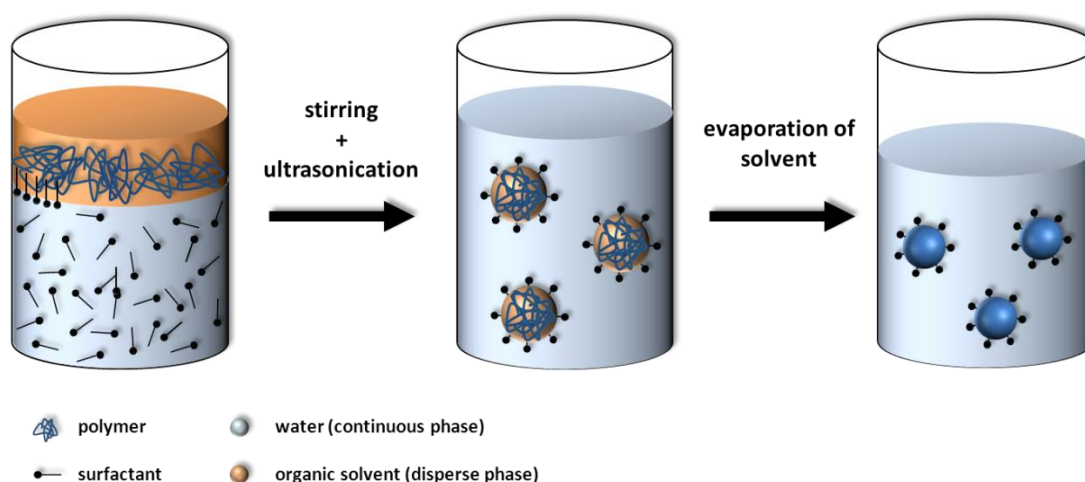
Figure 3: *Basic principle of particle preparation by solvent evaporation method.*

Using ultrasound for emulsification, the heterogeneous system with stable and narrow sized droplets can be considered as a miniemulsion. The polymers are water insoluble, consequently, they act as ultra-hydrophobic agents.[23] During the evaporation process the droplets shrink and solvent molecules are transported from the initial droplet through the aqueous phase to the water/air interface, where the evaporation takes place. Since the amount of solvent decreases during the evaporation process, a phase separation happens within the droplets. Due to the good stabilization of the droplets and the fact that the polymers are not able to diffuse through the water phase, the droplet number does not change upon evaporation. Hence, the polydispersities of the initial droplet sizes and the final colloid sizes are identical.[56]

The applications of artificial latexes are wide-ranging. Moreover, this technique is not limited to polymers. In principle, any organic water resistant molecules and inorganic non-water-soluble

components (provided that they are soluble in the dispersed phase) can be transformed in a dispersion. The big potential advantage of the solvent evaporation method becomes obvious for a particle formation involving more than one component, known as composite particles (see **section 2.4**) and organic-inorganic hybrid particles.[57]

2.3 Phase separation

A relevant process in artificial latex formation is the phase separation, especially, by applying more than one component. A complete description of the demixing process at the molecular level is difficult, for this reason, several models have been developed.[58] The most significant model is the model independently developed by Flory[59] and Huggins[60] in 1941, commonly known as Flory-Huggins theory.

2.3.1 Flory-Huggins theory

The Flory-Huggins theory is a mathematical model and describes the thermodynamics and entropy of a polymer solution. The crux of this theory is the delineation of the components, in terms of their occupation of segments, in a two-dimensional lattice. Starting from a mixture of two different small molecules of the same size, the model can be extended to a polymer solution by simple linking of the segments of one component. Each polymer segment still has the same size as the solvent molecules, pictured in **Figure 4**.
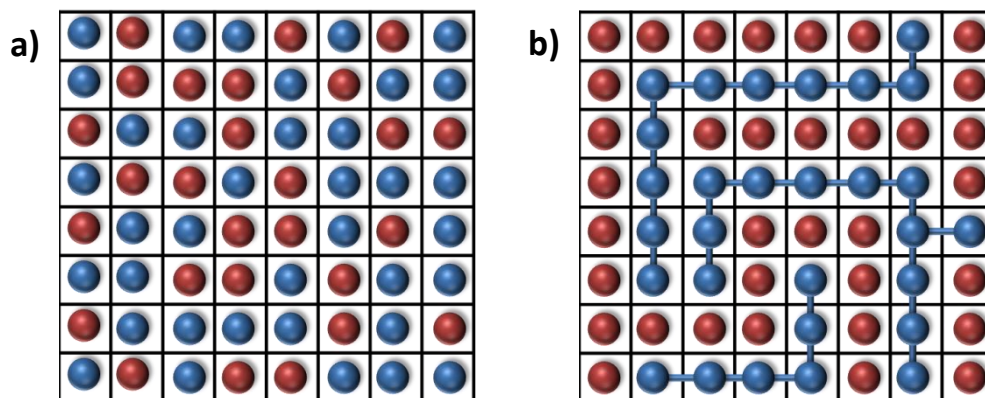
Figure 4: *Illustration of segments in a two-dimensional occupied lattice. (a) System of two small molecules and (b) system of a polymer solution, red is assigned to the solvent and blue to the polymer. The polymer is indicated by the connections between the units.*

The miscibility in such a system depends on the Gibbs free energy of mixing (ΔG_{mix}). The Gibbs free energy of mixing is composed of the enthalpy of mixing (ΔH_{mix}) and the entropy of mixing (ΔS_{mix}). A negative value of ΔG_{mix} indicates that the system is miscible, whereas positive values indicate that the components do not mix:

$$\Delta G_{mix} = \Delta H_{mix} - T\Delta S_{mix} \tag{3}$$

$$\Delta H_{mix} = RT\chi n_1 \varphi_2 \tag{4}$$

$$\Delta S_{mix} = -R\left(n_1 \ln\varphi_1 + n_2 \ln\varphi_2\right) \tag{5}$$

R: gas constant, *T*: temperature, *n*: number of moles, φ: volume ratio, and *χ*: Flory-Huggins parameter

Consequently, the mixing of a two component system is influenced by the interplay of enthalpy and entropy. ΔH_{mix} is mainly the combination of specific and dispersed interaction forces between all components and can be expressed in the Flory-Huggins parameter. For the case, the attractions between component 1 and component 2 are stronger than the 1-1 and 2-2 attractions, *χ* is negative and the mixing process is exothermic. Note that strong interaction forces result in highly negative values of ΔH_{mix}. If the 1-1 and 2-2 attractions are stronger than 1-2 attractions, *χ* is positive and the mixing is endothermic. The intermediate case, where *χ* is zero, is called athermic mixing. Here, all attractive forces are on the same level.[61] ΔS_{mix} represents the number of assembly possibilities of segments in the two-dimensional lattice. Using polymers, the segments are connected and the degree of polymerization must be taken into account.

Assuming an athermic system, upon mixing two kinds of small molecules, the change in ΔH_{mix} is very small or even zero. But there is a large increase in ΔS_{mix}. In a mixture, there are more possible arrangements for the components than in the individual phase. In this case, ΔG_{mix} is smaller than zero and mixing takes place. Even in the case of an endothermic mixture, the increase in entropy compensates the positive enthalpy term; the components are miscible, at least for some range of concentrations. For a typical polymer solution, ΔS_{mix} is much lower than in a comparable small molecule mixture. The segments of polymers are linked, therefore, the number of possible configurations in the lattice is restricted. Due to the lower entropy change, the enthalpic factor comes more to the fore. Principally, ΔH_{mix} determines whether the polymer is soluble or not. For an endothermic mixture at room temperature, full miscibility does not exist anymore and can be expected only for a small concentration of polymer in a solvent, as shown in **Figure 5** in **section 2.3.2**.

For the sake of completeness, it should be noted that by appraising the interactions and the resulting solubility, Hildebrand implemented the solubility parameter δ:[62, 63]

$$\chi = \frac{V_R}{RT}\left(\delta_1 - \delta_2\right)^2 \tag{6}$$

V_R: reference volume (size of lattice)

The solubility parameter is a good indication of miscibility by allowing simple comparison of the values. Materials with similar values of δ are likely to be miscible. However, this definition is valid only for a positive χ, therefore, it is used primarily for non-polar polymers.

2.3.2 Course of phase separation

The principle of phase separation of a polymer solution can be demonstrated well by observing the temperature dependency of solubility upon undercooling, depicted in **Figure 5**. As mentioned earlier, solubility is a function of ΔG_{mix}, hence, the minima and maxima of the ΔG_{mix} isotherms describe the manner of miscibility and phase separation, as shown in **Figure 5** (**a**).
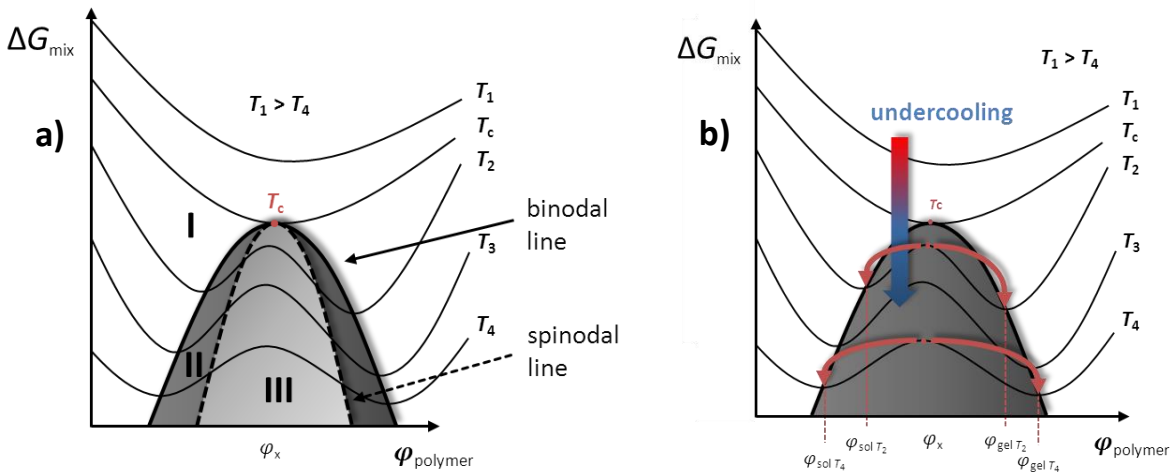
Figure 5: (a) Change in ΔG_{mix} by temperature variation as a function of the composition of the polymer solution with respect to phase separation. (b) More detailed illustration of the dependence of the phase separation process on temperature variation. Upon undercooling, the polymer solution with the composition φ_x separates into a gel and a sol phase. The composition of the sol and the gel phase is given by ΔG_{mix} or rather by the binodal line.

The binodal line $\left(\dfrac{d\Delta G_{mix}}{d\varphi} = 0\right)$ represents the limit of miscibility. The thermodynamically stable

boundary of homogeneous phases is defined by the spinodal line $\left(\dfrac{d^2\Delta G_{mix}}{d^2\varphi} = 0\right)$. This means that a

homogeneous mixture between the inflection points (area III) is not stable, and phase separation occurs. Area II, between the binodal and spinodal lines, represents a metastable region. In this area a phase separation is possible, but the system has to overcome an energetic barrier. Beyond the binodal line (area I), the isotherm features a minimum, thus, the polymer and the solvent are completely miscible.

As shown in **Figure 5** (**b**), lowering the temperature of a polymer solution below a critical temperature (T_c) leads to immiscibility; the polymer is not soluble anymore. A polymer solution with the composition φ_x separates at T_2, given by the binodal line, into a polymer rich phase (gel) and a solvent rich phase (sol). The more the temperature is lowered, the more the phases are enriched (see T_4). Depending on the area, phase separation occurs in two different ways. As a consequence of the energetic barrier in the metastable area II, the phase separation is controlled by a nucleation and growth mechanism.[64] Since there is no miscibility in area III, the phase separation is effected by spontaneous spinodal decomposition. Due to the absence of a thermodynamic barrier, the decomposition is solely described by diffusion.[65]

In the course of particle preparation by using the solvent evaporation technique, the phase separation occurs in a similar fashion to the temperature lowering, described above. By the time the phase separation begins, the polymer has become insoluble and the gel phase and the sol phase are formed. After complete solvent removal, both phases amalgamate and finally only one dispersed polymer phase remains.

2.3.3 Polymer-polymer mixtures

The Flory-Huggins theory was originally developed for polymer solutions, but Scott[66] and Tompa[67] applied it to polymer-polymer mixtures. This system can be considered as one polymer acting as a solvent for the other one. As demonstrated by the lattice model in **Figure 6**, the segments of both compounds are connected to a chain backbone, limiting the number of possible assembly options dramatically. Now, ΔS_{mix} cannot outweigh the unfavorable positive ΔH_{mix}. As a result of this

constraint, only 10% or fewer of all polymers are miscible with each other.[68] According to the Flory-Huggins theory, the key to polymer-polymer miscibility is the use of polymers featuring a negative χ, causing ΔH_{mix} to be negative. In principal, these are polymers having dipole-dipole interactions or hydrogen bonding. Another possibility is increasing ΔS_{mix} by using lower molecular weight polymers.[69]
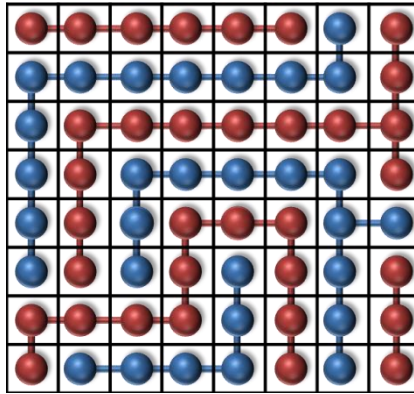
Figure 6: *Scheme of the segments of a polymer-polymer mixture in a two-dimensional occupied lattice.*

2.4 Composite particles

Composite polymer particles are composites consisting of two (or more) different immiscible polymers of various morphologies. For this reason, the phase separation diagram has to be extended to a second polymer. This is illustrated in **Figure 7**, using the example of (natural) rubber, poly(methyl methacrylate) (PMMA), and benzene.
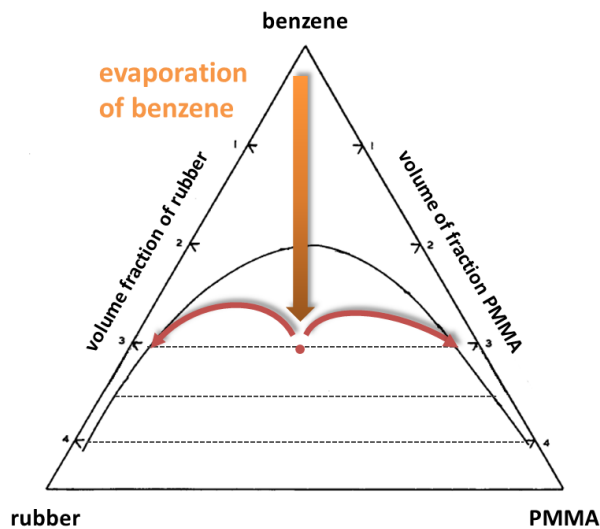
Figure 7: *Phase separation in a ternary rubber-PMMA-benzene system, taken from the work of Bristow[70]. By evaporation of benzene, the system forms a rubber rich and PMMA rich phase, given by the binodal line.*

In the ternary system, the molar fraction of benzene decreases upon solvent evaporation, analogous to **section 2.3.2**, a phase separation happens. Due to the fact that the polymers are immiscible, two phases are formed, a rubber rich phase and a PMMA rich phase. Note that both phases contain the other polymer and the solvent. By continuous solvent evaporation, the solvent is entirely removed. Depending on the nature of the polymers, two (almost pure) polymer phases (of a certain morphology) are generated.[71]

The resulting morphology of the composite particles is of crucial relevance. In the literature, there are many morphological investigations in the field of polymeric composite particles. However, these investigations have been made on the system of seeded polymerization. This technique can be also used in order to prepare composite particles of polymers that are difficult to obtain via miniemulsion polymerization. In seeded polymerization, a given polymer 1 is dissolved in a suitable monomer. After emulsification in water, an emulsion is formed. In a second step, the system is transferred into a dispersion by using radical polymerization. The unpolymerized monomer acts as a solvent for polymer 1 as well as for the newly formed polymer 2. In the course of the reaction, the amount of monomer decreases and a phase separation between polymer 1 and polymer 2 takes place. The thermodynamic and kinetic aspects of this process are similar to those of the solvent evaporation method. Therefore, the understanding of morphology formation, obtained by the study of seeded polymerization systems (see **section 2.4.1**), can be transferred directly to solvent evaporation systems.

2.4.1 Particle morphology

The control and prediction of particle morphology is an essential part of the preparation of composite particles. Over 40 years ago, Torza and Mason[72] approached this problem of morphology prediction with the assistance of the spreading coefficient (*S*). Similar to the contact angle (see **section 3.5**), *S* describes the wetting or rather the interactions of two liquids and can be calculated from the interfacial energies:[73]

$$S_i = \gamma_{jk} - \left(\gamma_{ij} + \gamma_{ik} \right) \tag{7}$$

Torza and Mason studied the phase behavior based on a binary droplet system. They used low-viscous, immiscible organic liquids dispersed in an aqueous phase. The droplet morphology of over 20 different systems was investigated. They found that each morphology can be described by three

sets of *S*. The sets and corresponding droplet morphologies are illustrated in **Figure 8**. The subscripts were assigned as follows: 1 for the first organic liquid, 2 for the water phase, and 3 for the second organic liquid. Consequently, γ_{12} represents the interfacial energy between the organic liquid 1 and water, γ_{23} that between liquid 2 and water, and γ_{13} the interfacial energy between both liquids. This convention will be maintained for the further description of composite morphology formation.

With the condition $S_1 < 0$, different sets of *S* correspond to specific morphologies. Torza and Mason show that for $S_2 < 0$ and $S_3 > 0$, 1 is engulfed by 3, leading to a core-shell morphology. For $S_2 < 0$ and $S_3 < 0$, the oils are partially engulfed and generate a hemispherical morphology. Finally, $S_2 > 0$ and $S_3 < 0$ indicates that both liquids are separated.
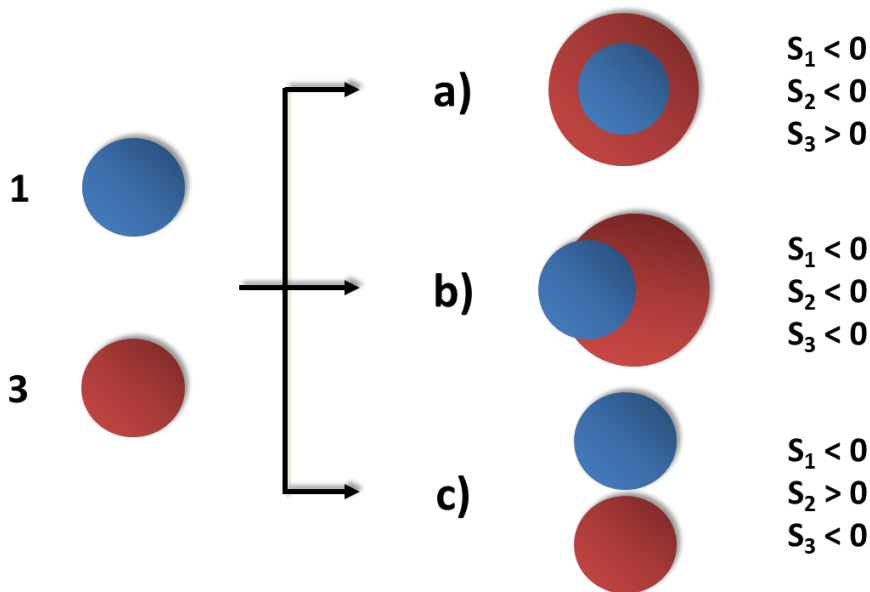
Figure 8: *Possible droplet morphologies corresponding to the three sets of the spreading coefficients; (a) complete engulfing (core-shell), (b) partial engulfing, and (c) non-engulfing.*

This theory describes the morphology formation of low-viscous fluids well, but it cannot be applied to polymeric systems, based on the simple fact that spreading coefficients can be determined only for liquids. Therefore, a new model is required, allowing the prediction of morphology without ascertaining the spreading coefficients. Berg,[74] Winzor,[75] and particularly Sundberg[76] developed a more general approach in order to predict the composite particle morphology formation by using the concept of Gibbs free energy. Studies on seeded polymerization systems demonstrated that the key parameter in morphology formation is the creation of new interfaces, given by the change of Δ*G* (see **Equation 1**). According to this, each particle morphology

can be described as a combination of different $\gamma_{ij}A_{ij}$. Due to the fact that interfacial energy and area are the only important factors, the preferred morphology will be the one offering the smallest value of ΔG. Later, Winzor[77] and Chen[78] demonstrated that this model also applies to solvent evaporation systems. Furthermore, this principle can be extended to more than two polymers.[79]

Regarding the general concept of using ΔG, the idea of simply comparing interfacial energies can even be applied to the studies of Torza and Mason, as shown in **Figure 9**.

a)   **b)**   **c)**   **d)**

$\gamma_{12} > \gamma_{23} , \gamma_{13}$ $\gamma_{12} \geq \gamma_{23}, \gamma_{13}$ $\gamma_{13} > \gamma_{12}$ and γ_{23} $\gamma_{12} = \gamma_{23}, \gamma_{13}$
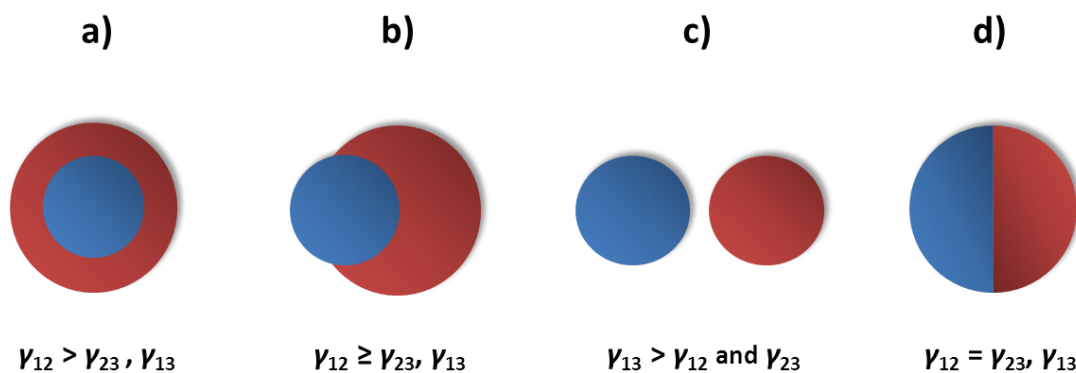
Figure 9: Transferring the investigation of Torza and Mason to the general concept of ΔG, demonstrating the conditions for (a) core-shell, (b) hemispherical, (c) separated, and (d) Janus droplets.

In the case of the core-shell morphology, γ_{12} exhibits the largest interfacial energy in the system. The morphology with the lowest ΔG is the one without any interface between the phases 1 and 2. This is the engulfed configuration, consisting of 1 as the core and 3 as the shell. All the other possible morphologies contain the Interface between the phases 1 and 2, consequently, they are thermodynamically unfavorable and are not formed. Separated droplets have a high γ_{13}, therefore, in order to minimize or eliminate the interfacial energy between the phases 1 und 3, the system forms two separated droplets. The requirement for partially engulfed droplets is that γ_{12} and γ_{13} must be on the same scale. In order to achieve a low ΔG, component 3 (having a lower interfacial energy to water phase) takes more space at the water interface, whereas 1 is partially embedded in 3. In the case where γ_{12} and γ_{13} are commensurate, both liquids occupy the same space at the water interface. This special hemispherical morphology is known as Janus, named after the double-faced Roman god.[80] This system will be discussed in more detail in section **2.4.3**.

2.4.2 Thermodynamic and kinetic aspects

In comparison to liquids, the diffusivity of polymers is very low, this has wide-ranging implications to the particle morphology. During seeded polymerization or solvent evaporation, the chain mobility of the polymers decreases or the viscosity increases because of the decreasing amount of monomer/solvent. In addition to the thermodynamic aspects of interfacial energies, there are also kinetic considerations. In the case of good polymer chain mobility by high diffusion, a thermodynamically favorable morphology is obtained. Otherwise, the system is solidified into a metastable kinetically morphology.[81, 82] In **Figure 10** an overview of some typical thermodynamically and kinetically controlled morphologies achieved with seeded polymerization is shown.[83, 84]
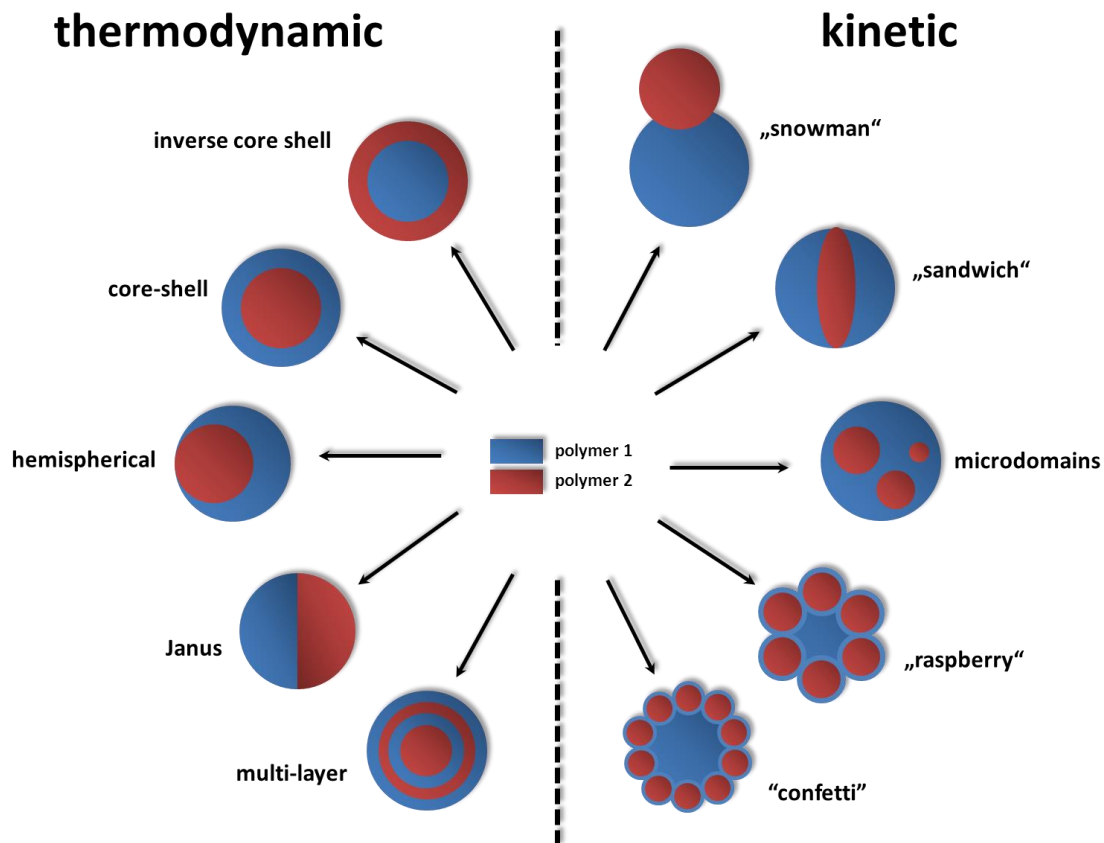
Figure 10: *Overview of thermodynamically and kinetically controlled composite particle morphologies.*[85]

It should be noted that as a consequence of the high viscosity, associated with a reduced diffusivity of polymer chains, the coexistence of multiple kinetic morphologies at the same thermodynamic conditions within one sample is possible.[86] Depending on whether a factor affects

directly the interfacial energy or the chain mobility, the morphology can be assigned to thermodynamic or kinetic parameters.

According to Fowkes,[87] the interfacial energy is defined as a combination of dispersed and polar interactions. For that reason, polymer polarities are a very important factor in morphology prediction and calculation. Using two polymers of different polarities results in core-shell particles, composed in such a way that the hydrophilic polymer acts as the shell, whereas the hydrophobic polymer forms the core.[88] As mentioned in **section 2.1.2,** surfactants reduce the interfacial energy, here, between polymer and water. Consequently, it is possible to obtain different morphologies from the same polymers by choosing the right surfactant[89, 75] and concentration.[90, 91] Compatibility is also of crucial importance for the resulting particle structure. With increasing incompatibility, a phase separation is favored.[92]

The chain mobility of the polymers is affected by interdiffusion[93] and glass transition temperature (T_g),[94] which is an interplay between chain backbone flexibility, type of side chains, molecular weight, and degree of crosslinking. The chain mobility is also generally influenced by the temperature.[84] In particular, with respect to solvent evaporation systems, the evaporation temperature and the concomitant phase separation velocity has a great effect on the resultant morphology.[77]

2.4.3 Janus particles

Janus particles (JPs) are compartmentalized anisotropic colloidal particles, showing segregation into two hemispheres. Parts of their surface may differ in chemical composition, polarity, color, or any other properties. The name Janus goes back to Casagrande and Veyssie,[95] and was popularized by de Gennes[96] in his Nobel Prize lecture in 1991. Their special feature, the combination of two different characteristics in one colloid, makes JPs suitable for a wide range of applications.

If JPs consist of hydrophobic and hydrophilic parts, they are surface active and can be used as emulsion stabilizing agents. This kind of application is very interesting, because these particles uniquely present the so-called Pickering effect,[97] known from particles, with the amphiphilic character of surfactants.[98, 99, 100] Calculations show that JPs with a proper surface improve the adsorption energy up to three times.[101] Other applications deal with the improvement of particle transportation in various systems. JPs offer anisotropic transport under certain conditions: it was found that one-side Au-coated polymeric particles diffuse perpendicularly to an external electric

field. The reason for this phenomenon is induced-charge electrophoresis, causing a flow discrepancy at the particle hemispheres.[102] Another way of movement is by self-propulsion, induced by a catalytically active surface. As a result of the asymmetric reaction, a gradient in osmotic potential is generated, this pushes the particles in a specific direction.[103]

One of the big potential applications, which have been neglected in literature so far, is the use of JPs in solar cells and optoelectronic devices in general. As described in **chapter 1**, OPVs require a biphasic structure of a donor and an acceptor. Besides this desired structure characteristic, the dimension of phases with respect to the exciton diffusion length plays also a significant role. Due to their separated double layered structure and the possibility of size control, JPs can theoretically fulfill both demands.

2.5 Organic Photovoltaics

2.5.1 Photovoltaic history

PV devices generate electrical power by direct conversion of solar radiation into electricity. The absorption of light leading to the generation of electrical current, known as the photovoltaic effect, was discovered 1839 by Becquerel.[104] He observed that an electrode in a conductive solution emitted electrons, when exposed to visible light. By knowing the spectral sensitivity of selenium, studied by Adams and Day in 1877,[105] 6 years later, Fritts[106] built the first functioning solar cell made of selenium and gold. More than 70 years later, in 1954, Chapin, Fuller, and Pearson developed a monocrystalline silicon PV device. With a power conversion efficiency (PCE) of 6%, this was the first solar cell able to convert enough energy to run common electrical equipments. Since that time, a series of developments to silicon based PVs have been implemented, the efficiencies now stand at around 25%.[107, 108] Today, these cells dominate the solar cell market. However, the requirement for high quality silicon crystals and the associated manufacturing cost drives up the prices. Hence, it may take several years to reach a point where purchasing and installation costs are paid back. Thus, alternative materials, requiring a lower energy input during manufacturing, are needed. Amorphous silicon, cadmium-telluride, and copper indium gallium selenide are candidates for such solar cell devices, since only a thin film of the photoactive material is required. With the highest reported

efficiencies of 10.1%, 16.7%, and 19.4%, respectively, these cells still exhibit lower efficiencies than monocrystalline silicon cells.[108]

In 1986, Tang turned over a new leaf in PVs, making an organic device with a PCE of about 1% by using phthalocyanine and perylene derivatives.[109] The idea behind the use of organic materials is the replacement of silicon by a less expensive, easily processable, and better tunable material.[110] After less than two decades of intensive research, OPVs have reached efficiencies of approximately 11% for hybrid[111] and 12% for all-organic solar cells.[112] In **section 2.5.2**, a deeper insight into the organic solar cell types will be given. A detailed overview of all developments in PVs and the resulting efficiencies over the last 35 years is illustrated in **Figure 11**.
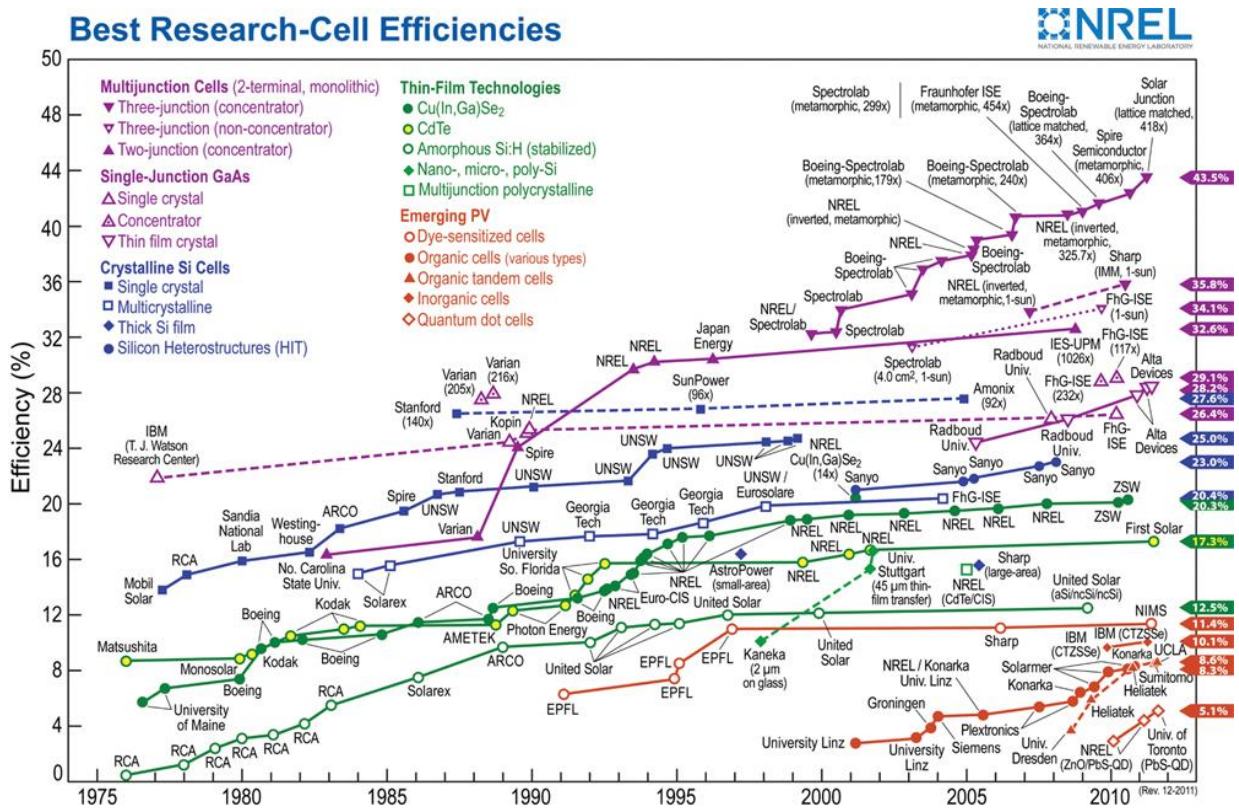
Figure 11: *Overview of research-cell efficiencies of various PV technologies. This graph was created and prepared by the National Renewable Energy Laboratory (NREL) in 12/2011.[113]*

As a supplement to **Figure 11**, it should be noted that the maximum achievable efficiency for a single junction cell is limited to 34%, the so-called Shockley-Queisser limit.[114] This limitation led to the development of cells consisting of more than one active layer. The theoretical limit for such devices, featuring an infinite number of layers, stands at 86% (under highly concentrated

sunlight).[115] Nowadays, the world best PV device is a triple junction device, based on indium gallium arsenide with an efficiency of 43.5% (under 418 suns).

2.5.2 Types of organic photovoltaic devices

OPVs have become a highly popular research topic during the last 10 years. They are still in the development phase, but appear as likely candidates for a large scale PV production. The term "organic solar cell" is not a precise definition; it summarizes various PVs technologies, containing at least one organic semiconductor in the active layer.[116] The most popular technologies are:

- liquid[111] and solid[117] dye-sensitized solar cells, pioneered by Grätzel.[118] These devices consist of an organic dye based electrochemical redox system, an electrolyte, and a mesoporous metal oxide semiconductor.
- hybrid solar cells; here, an organic semiconductor acts as the donor, whereas an inorganic material acts as acceptor. Such devices consist either of inorganic nanoparticles[119] or nanorods,[120] dispersed in a semiconducting polymer matrix, or of inorganic nanostructured semiconducting templates such as ZnO[121] or TiO_2,[122, 123] filled with organic semiconductors.
- all-organic (solid-state) devices; as the name implies, they are made up only of organic compounds. They can be distinguished further into several subtypes:
  - gas phase deposited PVs; the active layer consists of small semiconducting molecules, *e.g.* phthalocyanines and perylenes, deposited by evaporation.[124]
  - solution-processed cells, including:
    - ⇨ all-polymer cells; represented either by blends[125, 126, 127] of a donor and a acceptor or block copolymers,[128] bearing both materials.
    - ⇨ polymer/small molecule devices; the largest and most important type of these are polymer/fullerene based solar cells.[129, 130]

In the further course of this section, device setup, physics, and characteristics of OPVs will be discussed, regarding polymer/fullerene based devices.

2.6 Solar spectrum

Usually, a sun simulator is used as a light source for repeatable and accurate indoor solar cell testing. In order to compare different cells, the AM1.5G solar spectrum is defined as the standard spectrum, shown in **Figure 12**. When light passes through the atmosphere, light is scattered by dust particles and parts of the ultraviolet (UV), visible (Vis), and infrared light are absorbed by O_3, H_2O, O_2, and CO_2. This causes an energy loss and a change in the solar spectrum by the appearance of gaps. AM describes a number of "air masses". In space, outside the atmosphere, where there is no absorption, the original sun spectrum is called AM0. The absorption loss at the equator (0°) corresponds to AM1. At latitudes of northern Europe and northern America (48°), the absorption loss is higher, resulting in the AM1.5G spectrum. The "G" stands for global and includes both, direct and diffuse radiation. Most of the light intensity is concentrated between 280 nm and 2500 nm.
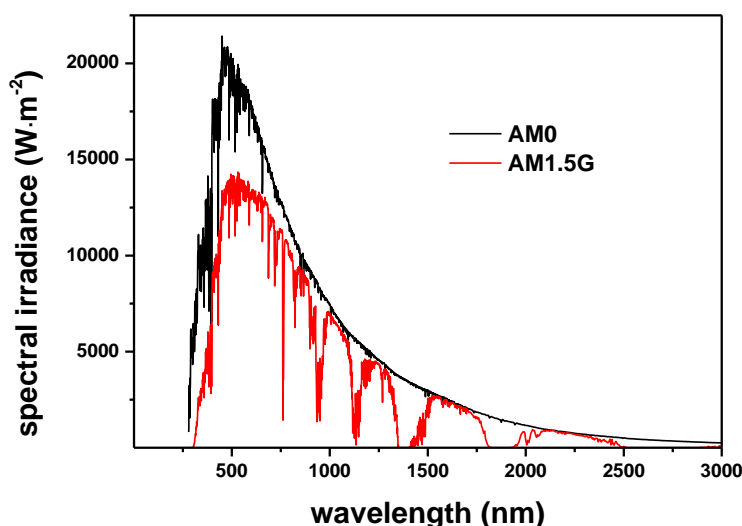
Figure 12: *Illustration of the extraterrestrial sun spectrum AM0 (black line) and the energy loss by dust scattering and absorption of O_3, H_2O, O_2, and CO_2, giving the AM1.5G spectrum (red line). This graphic is created, using data from NREL.*[131]

2.7 Organic semiconducting materials

The discovery of polyacetylene in 1977 by Heeger, MacDiarmid, and Shirakawa[132] opened the door towards plastic electronics. Since then, extensive efforts have been devoted to realizing the application of organic semiconductors in field-effect transistors,[11] light-emitting diodes (LEDs),[12] and PVs.[13] Most polymers are insulators, because of sp^3 hybridization of the carbon atom in the

backbone. In contrast, polymeric semiconductors feature sp^2 hybridized atoms, thus, an extensive π electron system is formed. As a result of Peierls instability, the structure of a π–conjugated polymer is distorted into alternating longer single bonds and shorter double bonds.[133] The more atomic p$_z$ orbitals are involved into conjugation, the denser are the resulting π electronic levels. With a sufficient number of atoms in the chain, a quasi-continuous energy band is formed,[134, 135] as shown in **Figure 13**. The energy difference between π, the highest occupied orbital (HOMO), and π*, the lowest unoccupied orbital (LUMO), is E_g. Since each band can hold two electrons per atom (spin up and spin down), the bonding π band is filled and the antibonding π* band is empty. Consequently, there are no partially filled bands. Insulators also exhibit a fully filled HOMO and empty LUMO, however, E_g is rather large. Semiconductors are distinguished by a small gap, allowing to promote electrons from HOMO to LUMO, resulting in conductivity.[136]
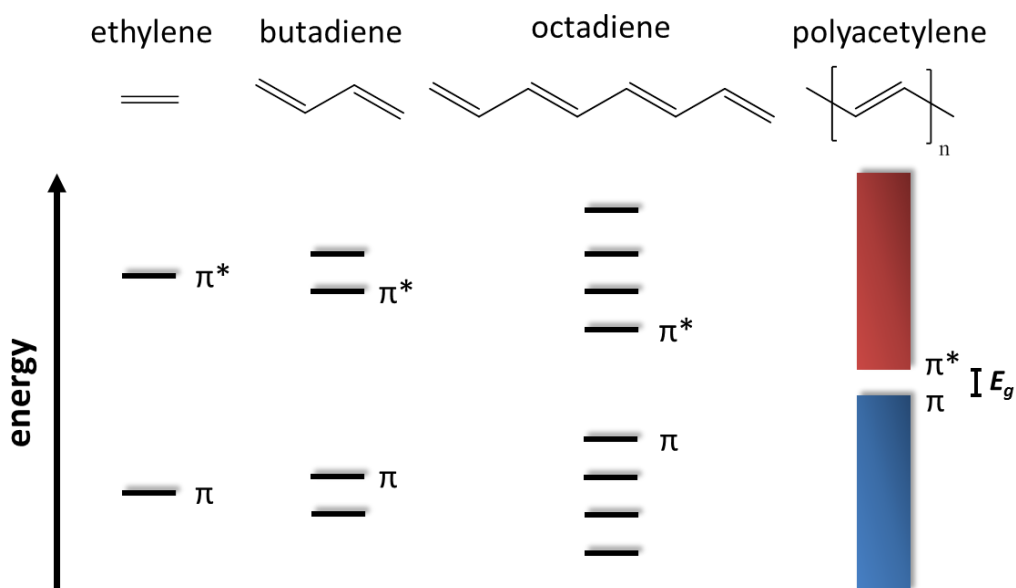
Figure 13: Transition of π and π levels in small molecules to a widespread band structure in polymers by increasing the conjugation.[135]*

The band gap of organic semiconductors can be engineered by changes in the molecular structure[9] and the length of the conjugation.[10] The tunable range is between 3.0 and 0.5 eV (400 to 2500 nm), usually, it is around 2 eV (620 nm).[136] This is considerably higher than the 1.1 eV (1130 nm) band gap of crystalline silicon.[137] Only wavelengths higher than E_g are absorbed (compare **section 3.3**), thus, crystalline silicon exhibits an absorption of around 77%. Organic semiconductors absorb only a relatively small amount of the incident sunlight (30%), diminishing the efficiency of OPVs to a great extent.[138] Therefore, highly efficient organic solar cells need a new class of semiconducting

materials, the so called low band gap polymers, having a band gap below 2 eV. These polymers feature a stronger light absorption in the red and near infrared regions, showing a better overlap with the solar spectrum.[139, 140] In comparison to inorganic semiconductors, organic semiconductors, especially polymers, are photosensitive and may degrade in a poor environment, *e.g.* under illumination and at oxygen atmosphere.[141] Nevertheless, the chemical modification on the molecular structure and the prospect of a low cost and a large-scale production motivates research in this field. As already mentioned, the active layer of organic solar cells requires a two compound system of an donor and an acceptor. A selection of common materials, used in OPVs is shown in **Figure 14**.

MDMO-PPV   P3HT   PFB

CN-MEH-PPV   PCBM   F8BT
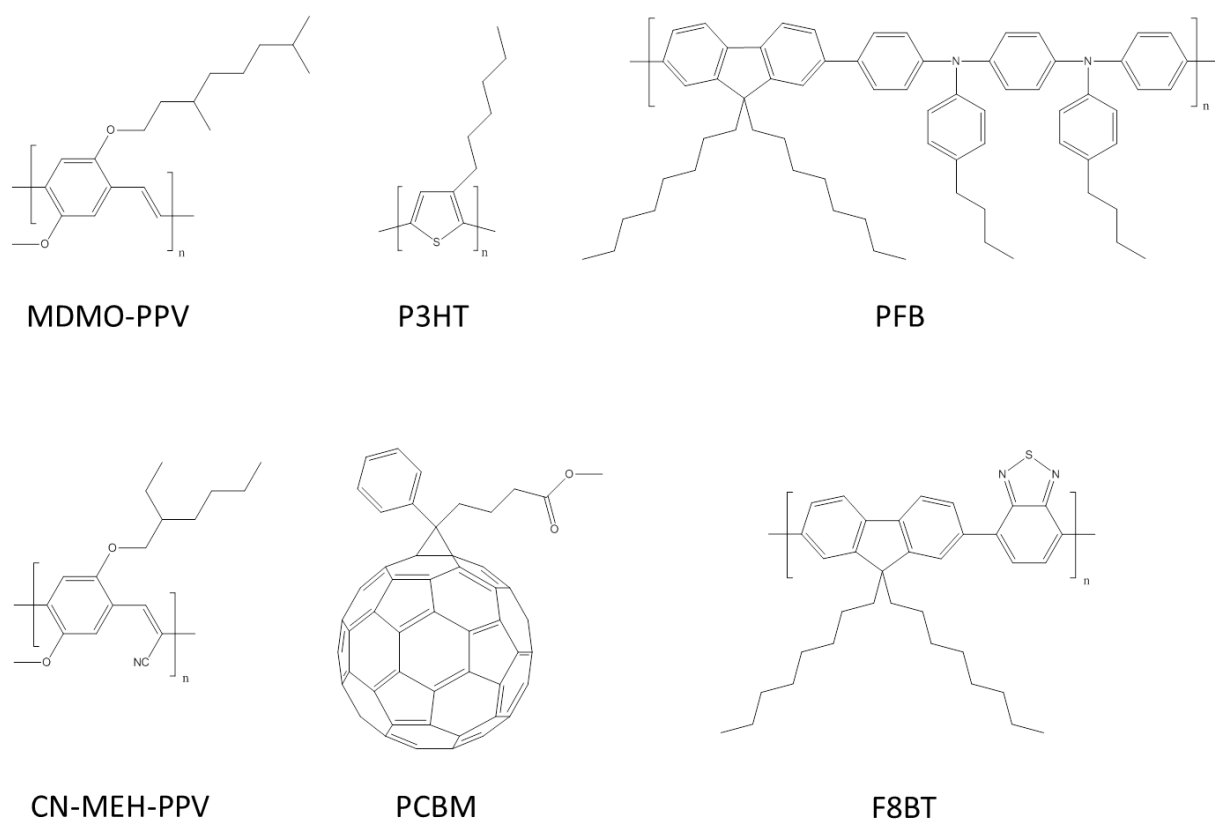
Figure 14: *Overview of (solution processable) organic semiconductors used in OPVs. (Upper row) hole conducting donor polymers: poly[2-methoxy-5-(3',7'-dimethyloctyloxy)]-1,4-phenylenevinylene (MDMO-PPV), poly(3-hexylthiophene-2,5-diyl) (P3HT), and poly(9,9'-dioctylfluorene-co-bis-N,N'-(4-butylphenyl)-bis-N,N'-phenyl-1,4-phenylenediamine) (PFB). (Lower row) electron conducting acceptor materials: poly-[2-methoxy-5-(2'-ethylhexyloxy)-1,4-(1-cyanovinylene)phenylene] (CN-MEH-PPV), [6,6]-phenyl-C61-butyric acid methyl ester (PCBM), and poly(9,9'-dioctylfluorene-co-benzothiadiazole) (F8TB).[142]*

2.8 Operating principles

2.8.1 Device architecture

Organic solar cells have a planar-layered structure. The active layer is sandwiched between two electrodes. One of the electrodes must be (semi) transparent, often indium tin oxide (ITO) is used, but very thin metal layers are also suitable. Aluminum is frequently chosen as counter electrode, calcium and magnesium are also good candidates.

Often a hole conducting buffer interlayer, *e.g.* poly(3,4-ethylenedioxythiophene)-poly(styrene-sulfonate) (PEDOT:PSS) is added between the active layer and ITO. The structure of PEDOT:PSS is shown in **section 7.1.1**. This buffer material helps to avoid local shunts, smoothing the ITO surface, enhancing adhesion to the upper light absorbing layer, providing better energy level matching, and improving device stability by hindering oxygen and indium diffusion into the active layer.[143, 144, 145] Usually, the construction of solar cells starts with ITO-glass substrates, followed by coating of the buffer layer and the active layer. Finally, the counter electrode is vacuum deposited on top of the active layer, as shown in **Figure 15**.

Single layer devices, or so called Schottky-type cells, are the oldest OPVs. In this case, the active consists only of a donor. These cells are intrinsically inefficient.[146, 147] More efficient solar cells are made up of the already introduced two compound system of donor (D) and acceptor (A). The D/A interface is called heterojunction or p-n junction. As will be introduced in **section 2.8.2**, charge separation requires that $LUMO_{donor}$ be above $LUMO_{acceptor}$. For an efficient charge carrier extraction, the same applies to the electrodes. The Fermi level or work function (W_F) of aluminum (cathode) must be lower than or equal to $LUMO_{acceptor}$, whereas the Fermi level of ITO (anode) should be above $HOMO_{donor}$. The work functions of ITO and Al electrodes are -4.7 and -4.24 eV, respectively.[148, 149]

Employing the basic heterojunction concept, there are different configurations of the donor and acceptor phases, the simplest one is the bilayer device. The cell structure and energy levels of this setup are shown in **Figure 15**; another arrangement will be introduced in **section 2.9**.
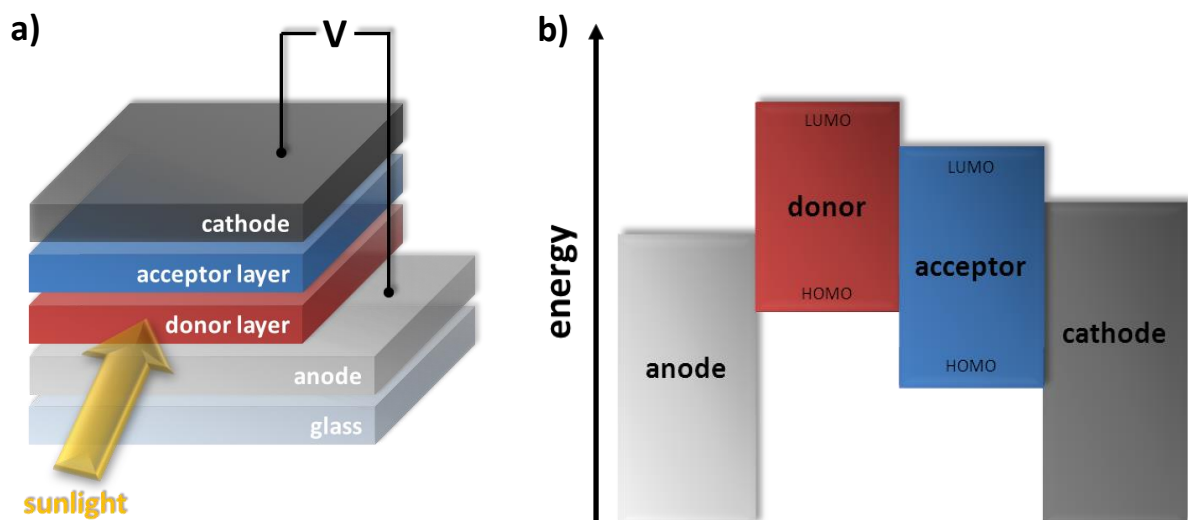
Figure 15: *(a) Bilayer device configuration without buffer layer. (b) Schematic energy level in a bilayer solar cell. Note that electrons move to levels of lower energy; holes require increasing energy levels for transportation.*

2.8.2 Light conversion

The conversion of photons to electrons is described on the basis of a kinetic and energetic perspective, shown in **Figure 16**. In short, the entire transformation mechanism can be classified as:[6, 150]

- excited electron-hole pair (exciton) generation (i);
- exciton diffusion (ii);
- exciton dissociation (iii);
- charge separation (iv);
- charge carrier transport though donor and acceptor phases to electrodes (v);
- charge collection at electrodes (vi).

Usually, light is absorbed in the donor material. In the course of absorption (compare **section 3.3.1**), electrons are promoted from the HOMO to the LUMO, creating excitons. The next step is charge dissociation. However, in comparison to silicon, organic semiconductors feature high exciton binding energies. Therefore, the thermal energy at room temperature is not sufficient for a direct dissociation.[151] Thus, a driving force is needed, which is provided by the electron poor acceptor, as electrons can move from $LUMO_{donor}$ to the lower $LUMO_{acceptor}$. Consequently, in order to dissociate charges, the diffusion of the excitons to a D/A interface is essential. Since excitons are neutral species, their motion is not affected by any electric field. They diffuse via random hops, driven by a

concentration gradient.[152, 153] The lifetime of excitons is limited, meaning that their diffusion length is also restricted (see **section 2.9**). Excitons that do not reach the D/A interface recombine and make no contribution to the photocurrent. Upon reaching the D/A interface, the excitons dissociate, but the charges are still coulombically bound.[154, 155] For separation, a further force in terms of the internal electric field between electrodes or concentration gradients of the respective charge carrier species, is required. This charge separation is often described by the Braun–Onsager model.[156, 157] The charges are then transported to the respective electrodes; the transport is driven by the internal electric field. The donor material is mostly hole conducting, whereas the acceptor is responsible for electron transport. Due to the lack of long-range order, charge transport in organic semiconductors usually occurs by hopping, instead of the band transport found in crystalline semiconductors (compare **section 2.10**).[158, 159] The hopping transport can be imagined as a thermally activated redox process between equal redox partners from one localized state to the next. During the charge transport to the contacts, the free charges can recombine again at a D/A interface. However, the charges do not directly recombine upon meeting each another, first forming a bound pair that has a finite chance of dissociating again.[160] Finally, the charge carriers are collected at the electrodes as photocurrent.
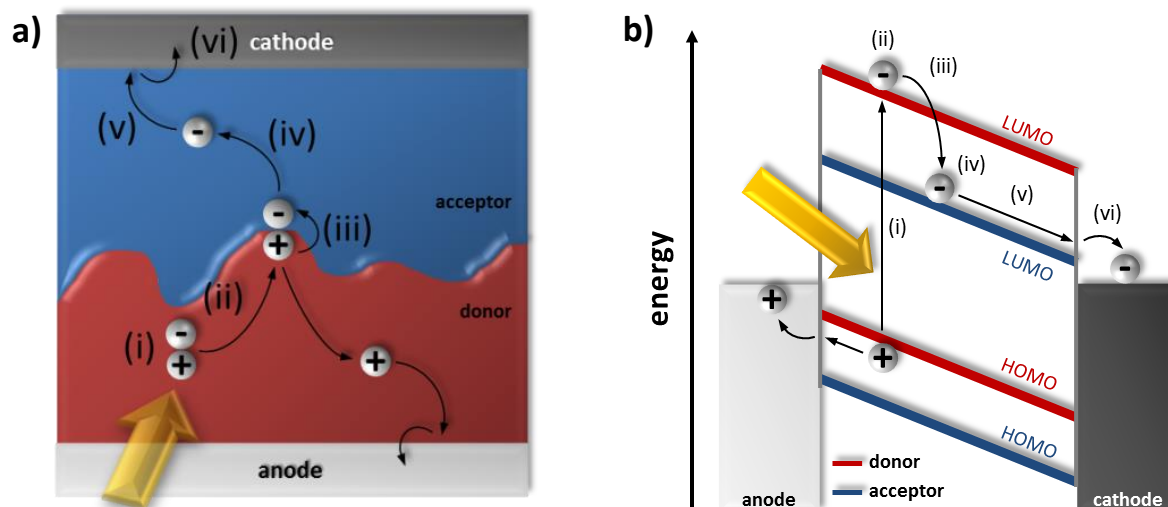
Figure 16: Light conversion in an organic solar cell; (a) schematic point of view and (b) energetic point of view. (i) Exciton creation by absorbing of a photon in the donor material. (ii) Exciton diffusion to D/A interface. (iii) Exciton dissociation by electron transfer to the electron poor acceptor. (iv) Separation of the still coulombically bound electron–hole pair due to electric field and material disorder. (v) Charge transport of electrons and holes by hopping. (vi) Extraction of charges as photocurrent.

Generally speaking, this description of the conversion of light into current is precisely the opposite of what happens inside LEDs. Thus, most factors and effects that are undesirable in solar cells are desirable in LEDs and necessary for a good conversion of electrons into light.

2.8.3 Characterization

The performance of organic solar cells is determined by a current-voltage (*IV*) measurement under illumination. The *IV* characterization is carried out by applying a varying bias to the OPV device. The involved processes can be explained by using the metal-insulator-metal (MIM) model.[161] In this model, a semiconductor is sandwiched between two electrodes with different Fermi levels, as shown in **Figure 17**. The ITO and aluminum electrodes are represented by their W_F. HOMO$_{donor}$ and LUMO$_{acceptor}$ act as the valence and conduction bands of this virtual insulator.
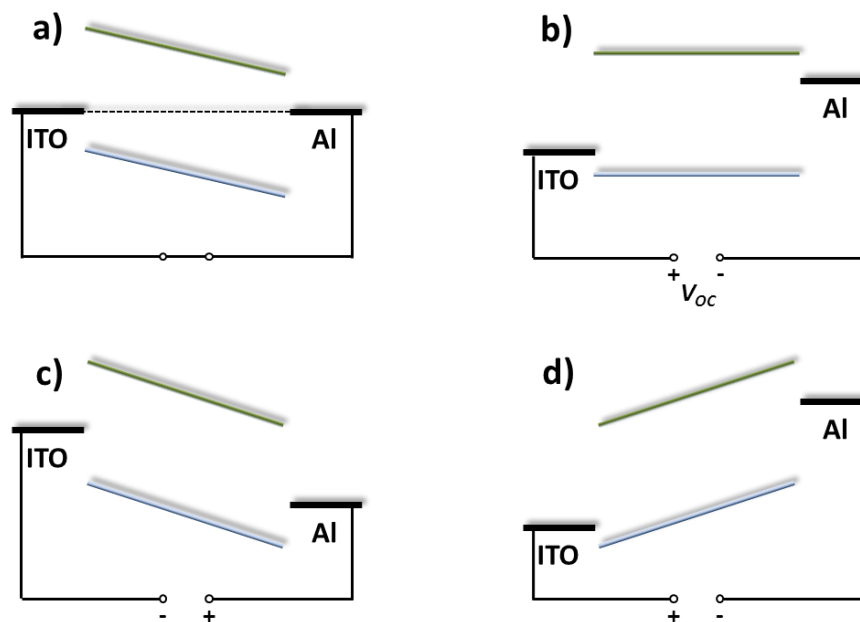
Figure 17: *MIM illustrations under several conditions upon device measurement. (a) Short circuit, (b) open circuit, (c) reverse bias, and (d) forward bias conditions.*

According to the figure, the processes which occur in the introduced MIM device during the *IV* measurements can be described as follows: (**a**) no voltage is applied; there is no current flowing in the dark. The built-in electric field resulting from the difference in W_F is evenly distributed throughout the device. Under illumination, photogenerated charge carriers drift to the contacts

under the influence of the built-in field. The electrons move to the lower work function metal and the holes to the opposite electrode. The device works as a solar cell. The current delivered by the cell under zero bias is called the short circuit current (I_{sc}). (**b**) The situation is shown for open circuit conditions, also known as "flat band condition". Here, the applied voltage is called the open circuit voltage (V_{oc}). In this case, this voltage corresponds to the difference in the Fermi levels, balancing the built-in field. Since there is no driving force for the charge carriers, the current is zero. (**c**) For V < 0, the device is operated under reverse bias; only a very small injected dark current can flow without illumination. Under illumination, generated charge carriers drift in the strong electric fields to the respective electrodes and the device works as a photodetector. (**d**) Applying a bias larger than V_{oc} (forward bias), the electrodes inject charges efficiently into the semiconductor. If these recombine radiatively, the device works as a LED.

The appropriate *IV* characteristic of an organic solar cell in the dark and under illumination is shown in **Figure 18**. The asymmetric diode behavior results basically from the different injection from the two electrodes into HOMO and LUMO, depending exponentially on the energy barrier.[162] The letters a to d correspond to processes in the MIM model. Comparing solar cell devices of different sizes, the *IV* measurement is normalized to the device area, hence, typically not the current but rather the current density (*J*) is quoted. Under dark conditions, there is almost no current flowing, until the electrodes start to inject at a forward bias larger than V_{oc} (d). Under light, the device generates charges and current flows in the opposite direction to the injected current. Thus, the *IV* curve is shifted to the fourth quadrant of this Cartesian coordinate system. At point (a), the maximum generated photocurrent (J_{sc}) flows under short-circuit conditions. Under open circuit conditions, the generated current at point (b) is zero and the device supplies the maximum usable voltage (V_{oc}). Between (a) and (b), the solar cell generates power (*i.e.* current × voltage). At a certain point (P_{max}), the product of current (J_{max}) and voltage (V_{max}) becomes largest, representing the cell's actual (maximum) power output to an external load (red striped square). The grey striped square corresponds to the product of V_{oc} and J_{sc} that is the theoretical (but never reached) maximum power output of the device. The ratio of the red striped square and the grey striped square is called the fill factor (FF), and is defined as:

$$FF = \frac{V_{max}J_{max}}{V_{OC}J_{SC}} = \frac{P_{max}}{V_{OC}J_{SC}} \tag{8}$$

Ideally, the FF should be 1, but due to field-dependent transport and recombination losses in OPVs it is typically between 0.2–0.7.[163] PCE can be easily calculated from the factors V_{oc}, J_{sc}, and FF,

determined from the *IV* curve. To determine PCE, the power supplied by the cell needs to be compared to the incident light power (P_{in}):

$$PCE = \frac{P_{max}}{P_{in}} = \frac{V_{max}J_{max}}{P_{in}} = \frac{FF \cdot V_{OC}J_{SC}}{P_{in}} \tag{9}$$

In the AM1.5G spectrum, P_{in} of the integrated light spectrum is defined as 100 mW·cm^{-2} (or 1000 W·m^{-2}).[164] The AM1.5G spectrum is often referred to as 1 sun illumination.
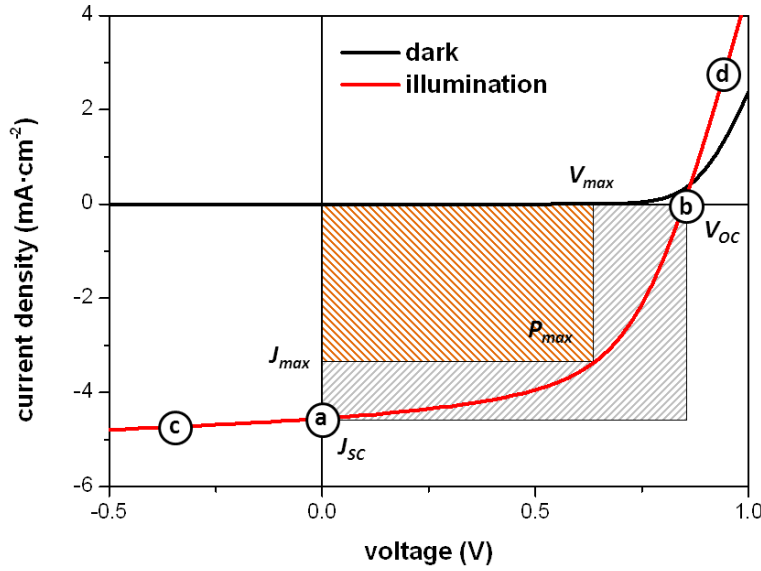
Figure 18: *IV curve of an OPV device. The characteristic intersections with abscissa and ordinate are V_{OC} and J_{SC}, respectively. The grey striped square is the theoretical maximum power, whereas the red striped represents the true maximum power output. The letters a to d correspond to **Figure 17**.*

Another important parameter in solar cell characterization is the EQE, describing the conversion of incident photons of a given wavelength into collected charge carriers. In this measurement, losses by reflection at the surface and transmission through the device are also included.

2.8.3.1 Dependency of device efficiency

Since PCE consists of V_{OC}, J_{SC}, and FF, the efficiency depends on these three factors. Generally, V_{OC} is a sensitive function of energy levels as well as the engineering of the interfaces and the contacts. According to the MIM model, the maximum voltage is predicted as the difference in the W_F of the electrodes, but there is always a loss of about 0.4 V.[162] In experiments, a strong dependence of V_{OC}

on $HOMO_{donor}$[165] and $LUMO_{accetpor}$[166] is also found. The nature of the electrode/semiconductor interface, *e.g.* roughness and the diffusion of electrode material into the semiconductor, causing changes in W_F and also influences V_{OC}.[167, 168] The short-circuit current density J_{SC} represents the amount of charge carriers collected at the electrodes, therefore, all factors affecting the electron generation and the transportation are involved, *e.g.* light absorption in the donor, exciton generation efficiency, exciton diffusion, charge separation efficiencies, and charge carrier mobility in the organic semiconductors.[110] The thickness of the active layer (influencing light harvesting) and the temperature (providing activation energy for hopping) also play an important role.[169] The FF describes the overall energy loss and represents a quality indicator to the device performance. It is composed of various factors, in particular, the extraction efficiencies of the photogenerated charge carriers[170] and the shunt and series resistances of the cell (compare **section 3.6**).

2.9 Bulk heterojunction

Organic semiconductors exhibit moderate charge carrier mobilities of 10^{-7} to 10^{-1} $cm^2 \cdot V^{-1} \cdot s^{-1}$ for holes[171] and 10^{-5} to 10^{-2} $cm^2 \cdot V^{-1} \cdot s^{-1}$ for electrons.[172] In contrast, the hole and electron mobilities in crystalline silicon are 475 and 1500 $cm^2 \cdot V^{-1} \cdot s^{-1}$, respectively. [173] The low charge carrier mobility limits the thickness of the active layer in OPVs, as the distance a charge carrier can be transported without undergoing recombination is limited. Fortunately, organic donor materials have strong absorption coefficients, ensuring sufficient absorption even in thin films.[174] The resulting active layer thickness is restricted to a few hundred nanometers. Another important difference to inorganic materials is the small exciton diffusion length in amorphous and disordered organic semiconductors.[175] In such materials the exciton diffusion length is between 10 and 20 nm.[176] As mentioned before, beyond this range, excitons are incapable of reaching the D/A interface and decay by non-radiative and radiative processes due to their short lifetime. For this reason, the exciton diffusion length also limits the maximum thickness of bilayer devices.[177, 178] Thus, in bilayer devices the charge collection is poor, resulting in very low J_{SC} and PCE. In order to increase the efficiency, the fraction of excitons transported to an interface before relaxation must be increased. This problem was solved by Yu *et al.*,[179] who created an interpenetrating network of donor and acceptor, in which the materials form finely separated phases of tens of nanometers,[180] extending the interfacial area enormously. In device architecture, this structure is often called a bulk heterojunction (BHJ), illustrated in **Figure 19** (**b**).
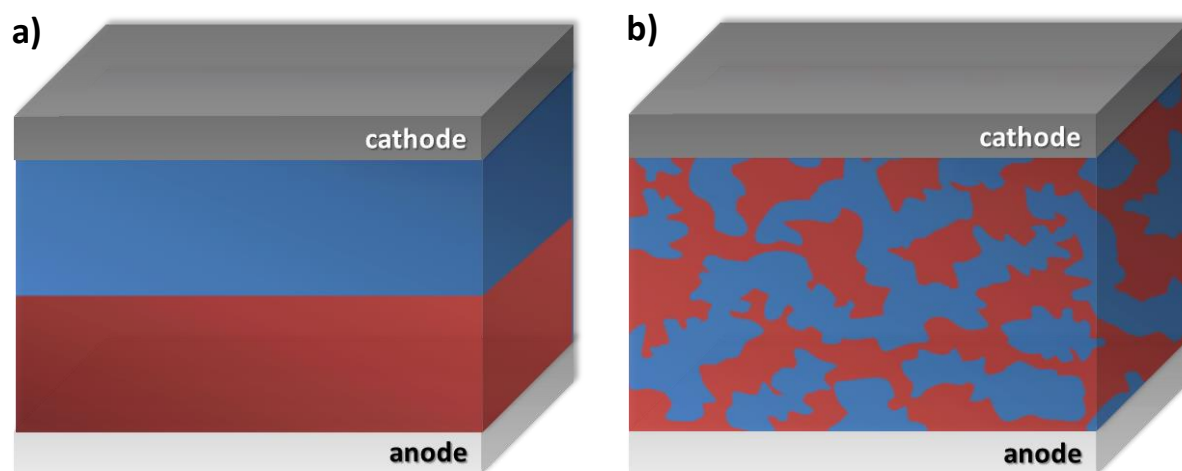
Figure 19: *Comparison of active layer structures in OPVs; (a) bilayer setup and (b) BHJ setup. Red is assigned to donor and blue to acceptor material.*

The concept of a BHJ is to ensure that the D/A interface is within a reach from sites in the domains, where excitons are generated. Hence, due to better exciton collection, BHJ solar cells feature much higher J_{SC} and PCE a bilayer devices. Therefore, today's best all-organic solar devices, using BHJ setup and have reached PCEs > 8%.

Generally, BHJ solar cells are prepared by simple spin coating from solutions, making fabrication quite easy.[7] The description of morphology formation is also based on Flory-Huggins theory. In the case of spin coating, the system is not constricted to a small area as in a droplet, thus, phase separation occurs over the entire bulk. Often, spin coating does not lead to the desired morphology at all, hence, the device must be annealed afterwards (compare **section 4.2.3.1**).[24] Consequently, morphology formation, and thus PCE, depend on a whole set of interconnected parameters such as:[24-34]

- donor/acceptor compound ratio;
- solvent nature associated with the individual solubility of materials;
- interaction of materials with the substrate surface (and air);
- layer thickness;
- drying time;
- annealing conditions.

These circumstances make morphology control in OPVs highly challenging.

An approach to improving BHJ devices is the creation of an ordered heterojunction (OHJ), which is conceptually in between the bilayer and the BHJ device. The aim of this device structure is to combine the good percolation pathways of a bilayer setup and the enlarged D/A interface of a BHJ setup. Furthermore, a pure donor phase at the hole collecting electrode and a pure acceptor phase at the electron collecting electrode are desirable, acting as a diffusion barrier for charge carriers of the "wrong" sign. Obtaining such well-organized nanostructures is challenging and requires highly interdisciplinary research in chemistry, physics, and engineering. Therefore, current devices are at an early stage of development and efficiencies for OHJ devices are lower than 1%.[181]

2.10 P3HT/PCBM solar cells

One of the best performing and well-studied organic solar cell, based on the BHJ concept, uses an active layer consisting of P3HT as donor and PCBM as acceptor.[182] Solar cell devices using these materials have reached efficiencies up to 5%.[24, 183]

Polythiophenes represent an important class of conjugated polymers, because they meet the essential requirements of processability, adequate charge transport properties, and the possibility of structural modifications by incorporation of a wide variety of side-chain functionalities.[184] Due to the poor solubility of unsubstituted polythiophene in organic solvents, a hexyl-chain is added in the 3 position, rendering the otherwise symmetrical monomer asymmetrical. Thus, the 3-hexylthiophene monomers can be coupled with different orientations with respect to the side chain. Polymerization leads to regiorandom (RRa) and regioregular (RR) P3HT, as shown in **Figure 20**. RRa-P3HT has no practical use, owing to its low crystallinity. As a result of the π-π stacking of thiophene rings, RR-P3HT features a high crystallinity, resulting in a good hole mobility up to 0.01 $cm^2 \cdot V^{-1} \cdot s^{-1}$.[185]
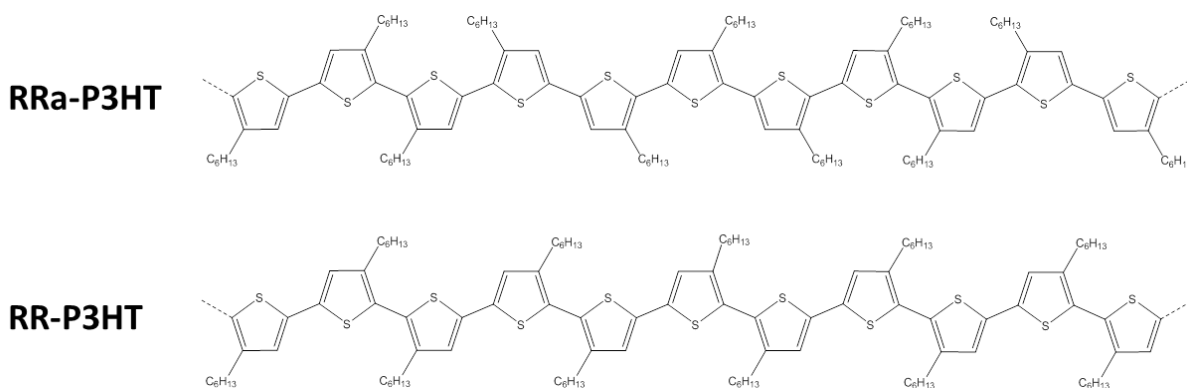
Figure 20: *Sections from regiorandom (top) and regioregular (bottom) P3HT chains.*

The currently best performing small molecule acceptor materials are (Buckminster) fullerenes and their derivatives. The reason for their success is probably the combination of the spherical shape and the favorable electron affinity in combination a with good electron mobility of 10^{-3} cm$^2 \cdot$V$^{-1} \cdot$s^{-1}.[186, 187] Analogously to polythiophene, the C$_{60}$ molecule features a low solubility in organic solvents. In order to remedy this, fullerenes are typically substituted with soluble side chains, as is the case for PCBM, the most commonly used electron acceptor.

Due to the availability of (RR)-P3HT and PCBM as well as their high efficiencies in devices, these materials are well-suitable for fundamental investigations of particle-based solar cells. Hence, the study of Kietzke *et al.* will be expanded by these established semiconducting solar cell materials.

3 Relevant characterization methods

3.1 Transmission electron microscopy

Transmission electron microscopy (TEM) is a special type of microscopy, allowing the direct mapping of objects on a nanometer scale by using electrons. TEM is well suited to investigate particles in micrometer range down to the nanometer level, especially their morphology. The operation principle is similar to a conventional light microscope, however, the sample is irradiated with high-energy electrons (50 to 200 kV). In microscopy, the physical limit of resolution is given by the wavelength of the radiation used. As the (de Broglie) wavelength of electrons is far below of visible light, TEM has a much higher resolution (up to 1 nm). The electron beam is generated by thermal emission from a thermionic cathode, using electromagnetic lenses, the electrons are focused towards the sample. Due to the short mean free path of electrons, interactions between the electrons and the air molecules are prevented by operation in high vacuum.

The contrast formation is effected by the transmission of electrons through the sample. Depending on the density and the atomic number of the atoms in a sample, the electrons are scattered (elastically and inelastically) at different angles. The higher the atomic number or the thicker the sample, the stronger is the diffraction. The transmitted electrons are visualized either on a fluorescent screen or by a CCD camera. Excluding the strongly diffracted electrons by an aperture, matter appears bright or dark.[188] The TEM setup and principle of contrast formation are shown in **Figure 21**.

TEM is not limited to contrast formation, it also provides information on sample composition by using electron spectroscopic imaging (ESI).[189] This technique is based on electron energy loss spectroscopy (EELS). The sample is exposed to a beam of monochromatic electrons. Some of the penetrating electrons will undergo inelastic scattering at the shell of atoms in the sample. Depending on the particular element, the scattered electrons undergo a specific energy loss. The characteristic loss can be matched to a certain element. Thus, the favored elements can be identified. For better visualization, the EELS image is colored and overlaid with the original TEM image. In this way, the specific element can be localized within the particles.
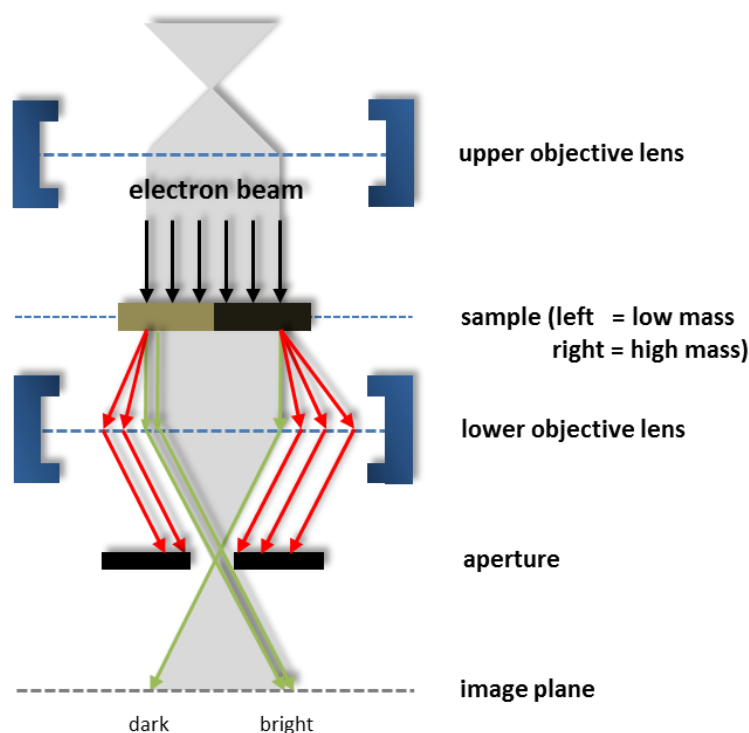
Figure 21: *Schematic illustration of a transmission electron microscope. The arrows represent electrons; black represents the initial electron beam, red the strongly diffracted electrons, and green the less diffracted electrons. Due to strong diffraction, "red electrons" are excluded by the aperture, whereas "green electrons" pass the aperture. In this way, a binary image is created on the image plane.*

3.2 Scanning electron microscopy

Another powerful method to investigate nanoparticles is scanning electron microscopy (SEM), which also uses electrons instead of light. An electron gun produces an electron beam which is focused by magnetic lenses to a small area of the sample. Typically, the energy of the electron beam ranges from a few keV to 50 keV. Usually, for polymers it is operated at low voltages. An image is generated by scanning the sample in a raster pattern. Analogously to TEM, contrast formation is based on the number of electrons reaching the detector. Here, the emitted electrons are of interest. Hence, structure and topography of the particles are detected. When the electron beam strikes the sample, a wide variety of emissions that are all useful for imaging are produced, illustrated in **Figure 22**. The interaction region is described as drop- or pear-shaped. The higher the acceleration voltage, the deeper the electrons are able to penetrate inside the sample.[190] In SEM, a standard topography image arises on the basis of secondary electrons (SE). Due to their small energy of about 4 eV, only electrons generated close to the surface are able to leave the sample. The remaining electrons are absorbed by the sample. As a result, edges or sharp peaks appear brighter because of a higher

emission, whereas relatively flat areas appear dark. This is known as the "edge effect", resulting in a pseudo three dimensional image. Furthermore, backscattered electrons (BE), produced by elastic interactions with the nuclei of the sample atoms, contain information about the chemical composition. The higher the atomic number, the more the electrons are backscattered. In a BE-SEM image, areas comprising more heavy atoms appear brighter.[191]
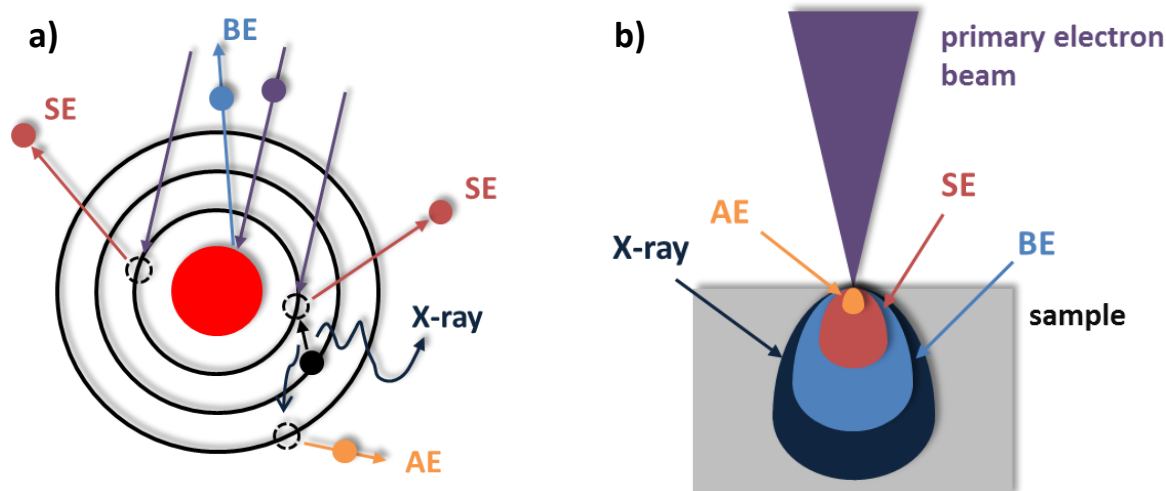
Figure 22: *(a) Interactions between the primary electron beam and a sample atom, leading to the creation of secondary electrons (SE), backscattered electrons (BE), Auger electrons (AE), and X-rays. (b) Penetration depth of SE, BE, AE, and X-rays.*

3.3 Optical spectroscopy

3.3.1 Ultra-violet and visible absorption

UV-Vis spectroscopy is among the earliest techniques to determine organic structures. Organic molecules absorb light in the UV-Vis spectral region, generally, between 200 and 800 nm. This kind of spectroscopy yields information of the chemical structure of the molecules, but it also provides information of the orientation and structural ordering of the molecules. The absorption of light occurs by applying incident light in the region of the electronic transitions, which corresponds to E_g. Absorption of UV-Vis radiation is usually assigned to the movement of electrons from binding σ and π orbitals as well as nonbonding (n) orbitals to the antibonding σ* and π* orbitals, as shown in **Figure 23**.
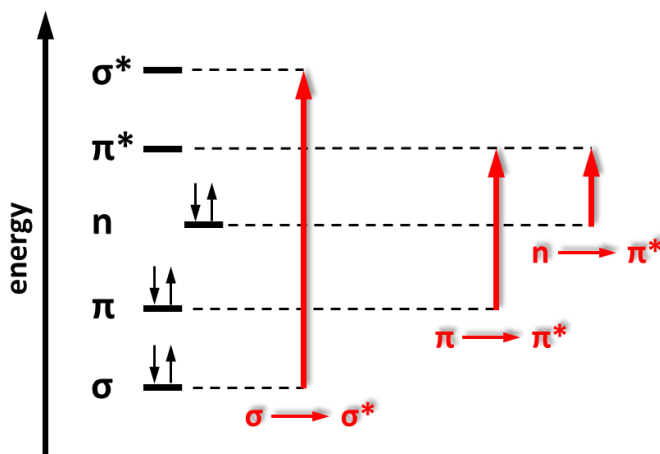
Figure 23: Possible transitions in organic compounds by optical excitation.

The Lambert-Beer law describes the attenuation of light intensity upon passing through a medium as a function of extinction coefficient (ε), concentration (c), and path length (l). The logarithmic ratio between the radiation falling on the material (I_0) and the radiation transmitted through the material (I) is referred to as absorbance (A).[192] Amongst others, the setup of a UV-Vis spectrometer is shown in **Figure 24**.

$$\log\left(\frac{I_0}{I}\right) = \varepsilon c l \tag{10}$$

$$A = \log\left(\frac{I_0}{I}\right) \tag{11}$$
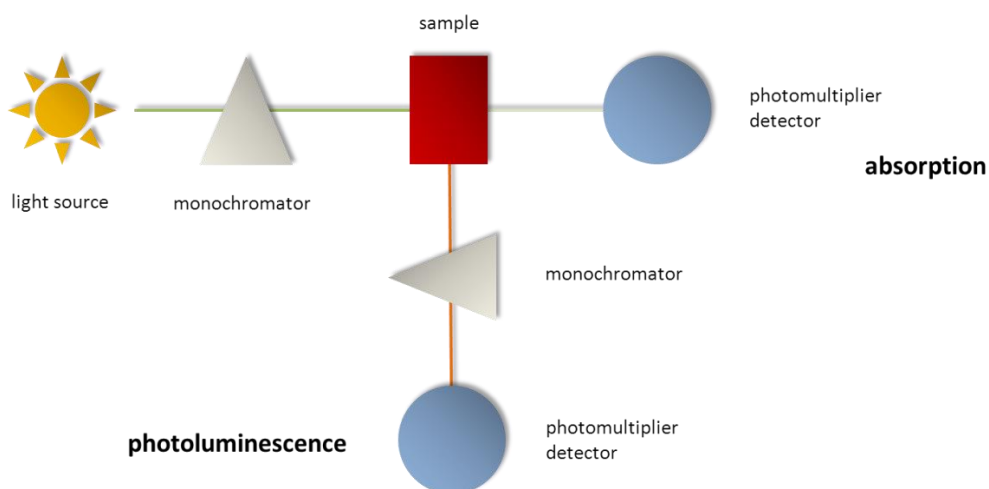
Figure 24: Schematic illustration of a setup of absorption and photoluminescence measurement. Absorption is measured at an angle of 180° and photoluminescence at an angle of 90°.

3.3.2 Photoluminescence

Photoluminescence (PL) is the spontaneous emission of light from a material under optical excitation. The term embraces fluorescence and phosphorescence, these processes differing in terms of the time after irradiation over which the luminescence occurs. The phenomena of PL can be explained on the basis of a Jablonski energy diagram, as shown in **Figure 25 (a)**. A typical Jablonski diagram illustrates the singlet (electronic) ground state S_0, the first excited state S_1, and additional higher excited singlet states. The stacks of horizontal lines represent the quantised vibrational energy states. Positioned to the right of S_1 is the first excited triplet state T_1.

The absorption of light leads to an electron elevation as described in **section 3.3.1**, the transition from S_0 to S_1. Once the electron reaches at a certain vibrational energy level of S_1, due to thermal dissipation it slowly relaxes to the lowest vibrational level. In the case of fluorescence, the electron relaxation from this level occurs radiatively. As a consequence of the thermal dissipation, the emitted light contains less energy than the absorbed light. Therefore, the PL emission is shifted to longer wavelengths (the so-called Stokes shift), as shown in **Figure 25 (b)**. In the ideal case, the PL spectrum is a mirror image of the absorption spectrum.
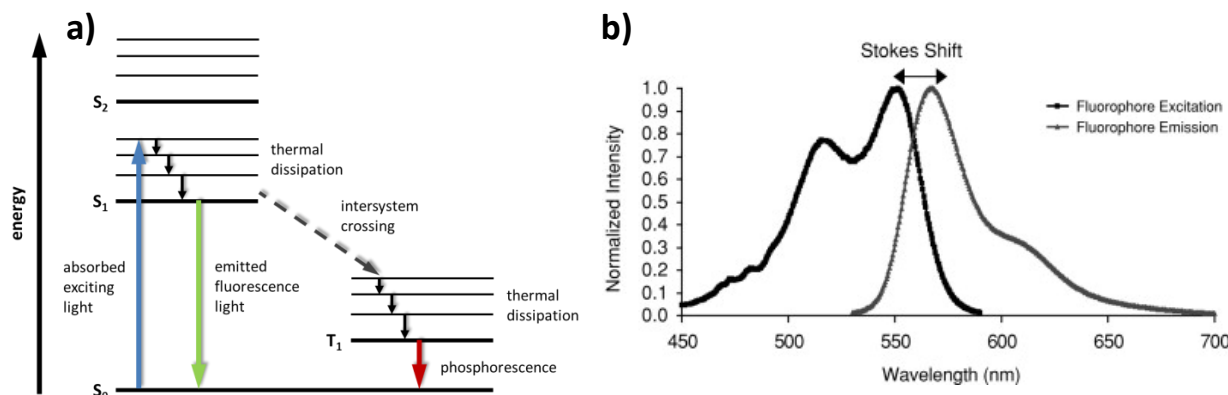
Figure 25: *(a) Jablonski energy diagram. Thicker lines represent the electronic energy levels, thinner lines denote the vibrational energy states; rotational energy states are ignored. (b) Illustration of an absorption spectrum and the corresponding emission spectrum, taken from the work of Wolf.*[193]

Other relaxation pathways are also possible. The excited state energy can be dissipated either non-radiatively as heat, as energy transfer by collisions with other molecules (quenching), or by intersystem crossing to T_1. The latter event is relatively rare, but ultimately results in the emission of a photon through phosphorescence by in relaxation back to S_0. In general, transitions from triplet to singlet states are forbidden, nevertheless, because of spin-orbit coupling it is possible. This leads to

very low rate constants and a time delayed emission.[192, 193] The setup of PL measurement is illustrated in **Figure 24**. In this work, PL spectroscopy or rather the PL intensity is primarily used to estimate the P3HT domain size within the particles.

3.4 X-ray diffraction

X-ray diffraction (XRD) is a common technique used for the identification of crystalline materials. This technique is based on the elastic scattering of X-rays at a lattice. X-rays are generated when a high energy electron beam bombards a solid target. As shown in **Figure 22**, high energy electrons eject inner shell electrons in the atoms, the resulting gaps are filled with electrons from higher levels, and X-rays with a certain energy are emitted. A common target is copper, emitting 8 keV X-rays, corresponding to a wavelength of 0.154 nm. Since X-ray wavelengths are comparable to the size of atoms, they are ideally suited for probing structural arrangements of the samples. In XRD, the X-rays primarily interact with electrons of the sample atoms, some X-rays from the incident beam will be deflected away from the direction where they originally traveled (elastic scattering). Diffracted X-ray waves from different atoms can interfere with one another, either constructively (signal) or destructively (elimination). The resulting interference pattern is the basis of the diffraction analysis, given by Bragg's law:

$$n\lambda = 2d\sin\theta \tag{12}$$

Bragg's law describes the condition for constructive interference on lattice planes with an interplanar distance d, as shown in **Figure 26**. Constructive interference occurs when diffracted X-rays at different planes are in phase. Under a certain scatting angle θ, this applies if the path length of each X-ray beam is equal to an integer multiple (n) of the wavelength (λ). X-rays waves that do not satisfy this condition are eliminated.[194] A diffraction pattern is obtained by measuring the intensity of the scattered waves as a function of the scattering angle. The signals in a diffraction pattern are directly related to the atomic spacing. This allows material identification and provides information about the degree of crystallinity.
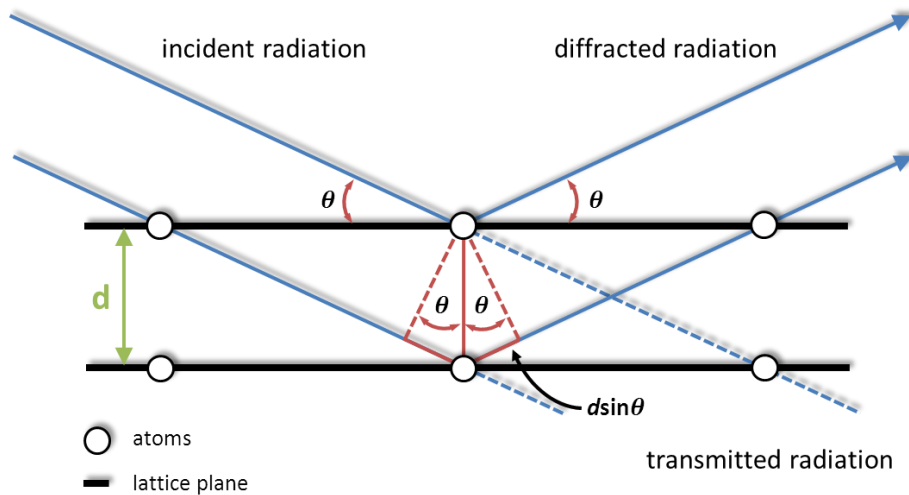
Figure 26: *Diffraction in a crystalline lattice. Two X-ray beams with identical wavelengths and phase are scattered in different planes. The lower beam traverses an extra distance of dsin θ . Constructive interference occurs when this length is equal to an integer multiple (n) of the X-ray wavelength.*

3.5 Contact angle measurement

Wetting with a liquid (usually water) supplies information on the hydrophilicity of a surface. Depending on the interfacial energies, the "shape" of the water phase varies. If a surface is wetted completely, a liquid film is formed. In the case of almost no wetting, the resulting shape is a spherical droplet. The shape of the droplet can be described by the contact angle (θ), given by Young's relation:[195]

$$\cos\theta = \frac{\gamma_{sv} - \gamma_{sl}}{\gamma_{lv}} \tag{13}$$

The letters s, l, and v correspond to solid, liquid, and vapor, respectively.

To analyze the droplet shape by the sessile drop method, a horizontal camera detect θ by fitting a mathematical expression to the shape of the sitting drop. In the course of this, the slope of the drop tangent is calculated, allowing the determination of the contact angle, as shown in **Figure 27**. As mentioned in **section 2.4.2**, interfacial energies relate to interaction forces. In the case of no attractive forces, the contact angle is ideally 180° and the drop forms a perfect sphere. For water on very hydrophobic surfaces, *e.g.* polytetrafluoroethylene, angles of up to 120° can be achieved. In contrast to this, a liquid film is created when the interactions are maximized. It should be noted that

angles below 10° are hardly measurable and difficult to determine. Generally speaking, the value of the contact angle provides a first indication of the polarity of a surface.[196]
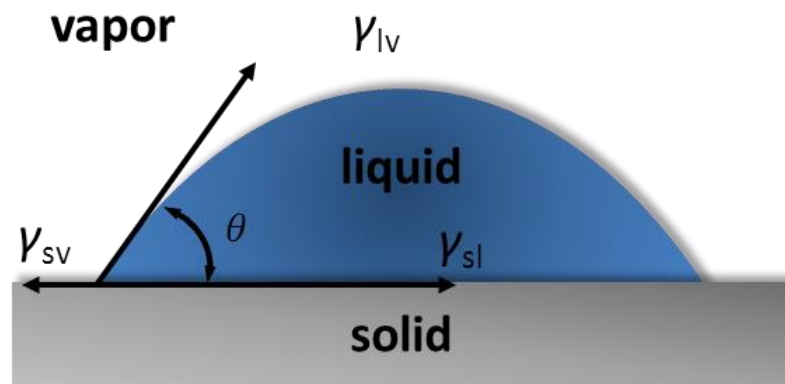
Figure 27: Schematic illustration of a sessile drop contact angle measurement by using water. The contact angle is given by the drop tangent and solid/liquid interface line.

3.6 Current-voltage measurement

The analysis of *IV* curves was already explained in **section 2.8.3**. In this section, further information on *IV* curve generation will be given.

From an electrical point of view, solar cells are equivalent to a current generator in a parallel circuit with an asymmetric and non-linear resistive element, *i.e.* a diode. Real OPVs are imperfect systems and undergo power losses under operation. These losses are electrically equivalent to a series (R_s) and a shunt (R_{sh}) resistor within the cell, as shown in **Figure 28**. For this reason, the determined value of the FF is mainly a result of these resistances.
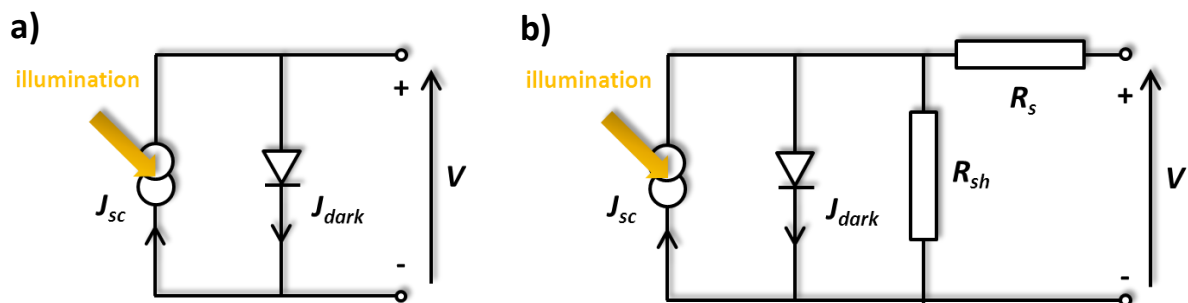
Figure 28: Equivalent circuit diagram of (a) ideal OPV device and (b) real OPV device. The circuit consists of a current source (J_{sc}), a diode, accounting for the nonlinear voltage dependence, and a series and a shunt resistor, representing the energy losses.

The R_s can be considered as a combination of all ohmic resistances, describing the loss of current as a consequence of poor charge carrier mobility in the active layer. The resistance is increased in thicker layers as a result of the longer traveling distance of the charges. The R_{sh} describes the recombination of charge carriers near the D/A interface, but it may also refer to the recombination at the electrodes. For an efficient solar cell devices, R_s needs to be as small and R_{sh} needs to be as large as possible.[197, 198]

4 Results and discussion

In this chapter, the complete development process of P3HT/PCBM PBOPV devices is shown. As mentioned previously, the main focus areas are the investigation of the P3HT/PCBM composite particle morphology, the formation of adequate particle layers, and the fabrication of P3HT/PCBM PBOPVs. A further emphasis will be an improvement of the PBOPVs. Some aspects of the results whose further discussion is either beyond the scope of this investigation or not appropriate at this point, will be covered in **section 7.1**. The experimental details of all investigations are listed in **chapter 5**.

Unless otherwise stated, P3HT/PCBM composite particles are prepared in a mass ratio of 1:1, using toluene as solvent and SDS as surfactant. The evaporation of toluene is conducted at 60 °C. The mass ratio of the other composite particles is also 1:1. The volume ratio of a blend of P3HT and PCBM particles is 1:1 of the pure dispersions. To remove the majority of the surfactant, the dispersions are dialyzed after preparation. The setup of the PBOPVs conforms basically to the BHJ structure, introduced in **section 2.9**. However, a buffer inter layer is additionally used. ITO is used as anode and aluminum is used as cathode.

4.1 P3HT/PCBM particle morphology investigations

As reported in **section 2.9**, the formation of the active layer of SPOPVs made by spin coating is an interplay of several factors. With respect to the morphology, using the miniemulsion concept, a couple of factors can be neglected. On the one hand, the space where phase separation occurs is limited to the particle size. On the other hand, in miniemulsions, the materials are surrounded by water, making the water/material interface to an important parameter in particle preparation (see **section 0**). The eventual particle morphology is of great interest and begs the question of whether P3HT/PCBM composite particles are suitable to build a functioning solar cell.

4.1.1 Material distinction

In general, the P3HT/PCBM composite particle morphology is investigated visually. Due to its transmission character, TEM is the method of choice. Even though SEM cannot detect the inner particle phase, it is also a very helpful technique in particle morphology investigation and a good supplement to TEM. In order to apply these techniques, a clear differentiation of the materials by means of a distinguishable contrast is essential. Thus, a contrast investigation with P3HT and PCBM particles is performed. The characteristics of the particles which are used for material distinction are listed in **Table 1**. The average particle diameter and the polydispersity were determined by dynamic light scattering (DLS).

Table 1: *Average diameter and polydispersity of P3HT and PCBM composite particles.*

material	diameter (nm)	polydispersity
P3HT	142	0.33
PCBM	135	0.29

4.1.1.1 TEM investigations

The pure P3HT and PCBM particles are shown in **Figure 29** (**a**) and (**b**). The PCBM colloids are perfectly shaped and feature a helpful contrast to the background. On the contrary, P3HT particles are slightly irregular in shape, appearing brighter and becoming more diffuse to the edge. Consequently, the particle blend shows a small contrast in shape, but also a small contrast in grey scale, as shown in **Figure 29** (**c**). In literature, it is assumed that grey scale contrast formation is primarily an effect of density differences.[199] The density of pure P3HT and PCBM is 1.1 and 1.5 $g \cdot cm^{-3}$, respectively. Therefore, P3HT appears bright and PCBM dark. In order to increase the contrast, staining by using heavy elements is a common procedure in TEM. The heavy nuclei show stronger electron diffraction, thus, the sample appears darker.[191] A common staining agent in TEM is osmium tetroxide (OsO_4), which reacts with double bonds and aromatic systems. In optoelectronics, the treatment of polythiophene with iodine is a convenient procedure to increase the conductivity by removing electrons from the π system.[200] Since iodine is a heavy element, it should also be a suitable staining agent. Iodination of pure C_{60} has not been observed under ambient conditions.[201] The reaction of OsO_4 with C_{60} is established.[202] In literature, the reaction of OsO_4 with polythiophenes

has not been investigated in detail. However, OsO_4 is a strong oxidant, implying that it may also react with P3HT. The staining experiments are shown in **Figure 29** (**d**) and (**e**). In contrast to the non-stained blend, it seems that there is no contrast anymore, upon the use of iodine. This implies an evidence for the better reaction with P3HT, resulting in darker colloids, making it impossible to distinguish the particles. Therefore, iodine staining is not suited for the morphology investigation in TEM. The use of OsO_4 leads to very easily distinguishable particles. Since the contrast is drastically increased, there is a high response of OsO_4 either to P3HT or PCBM. Regardless of whether OsO_4 reacts with the polythiophene or fullerene derivative, due to the good contrast, it is a perfect staining agent for this system.
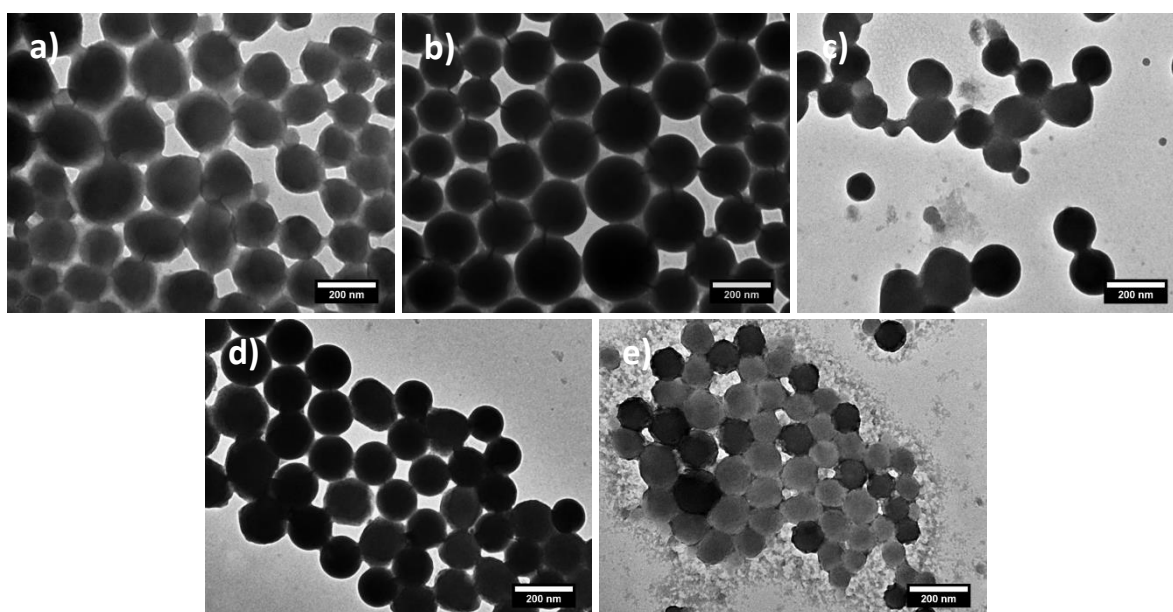
Figure 29: *TEM images of (a) P3HT particles, (b) PCBM particles, (c) blend of P3HT and PCBM particles, (d) blend of P3HT and PCBM particles stained with iodine, and (e) blend of P3HT PCBM particles stained with OsO_4.*

To illuminate the staining reaction of OsO_4, ESI-TEM is applied. As EELS is much more sensitive to light elements, a direct detection of osmium is not achievable.[191] To identify the OsO_4 reaction, the sulfur in P3HT and the high contrast of osmium stained particles can be used for an indirect investigation. Since PCBM does not contain sulfur, the sulfur EELS signal is suitable to distinguish between P3HT and PCBM. The high contrast between OsO_4 stained particles can be utilized to detected the osmium; dark particles denote to the material that has reacted with the staining agent. Hence, the combination of both allows an unambiguous assignment of the reaction. The colloids are stabilized with SDS. The dispersions were dialyzed, thus, only a small amount of SDS remains on the particle surface. For this reason, the sulfur in SDS does not impair the sulfur determination of P3HT.

The ESI-TEM images from the non-stained, iodine stained, and OsO_4 stained particle blends are shown In **Figure 30**. As a proof of principle, **Figure 30** (**a**) and (**b**) shows the non-stained particle blend. It can be seen that only the brighter and deformed particles offer a sulfur signal. The dark and spherical particles show no signal. Hence, this kind of method is very suitable for P3HT/PCBM distinction. On the right bottom of the ESI image, the limit of element verification is demonstrated. Smaller P3HT particles show no signal, indicating that EELS requires a certain concentration of the element under investigation. Despite of the non-existent contrast of iodine stained particles, using EELS, it is possible visualize to the P3HT parts, as shown in **Figure 30** (**c**) and (**d**). The ESI investigation with OsO_4 stained particles are shown in **Figure 30** (**e**) and (**f**). Only the bright particles feature a sulfur signal, thus, PCBM must be the dark species. This demonstrates that OsO_4 reacts specifically with PCBM.
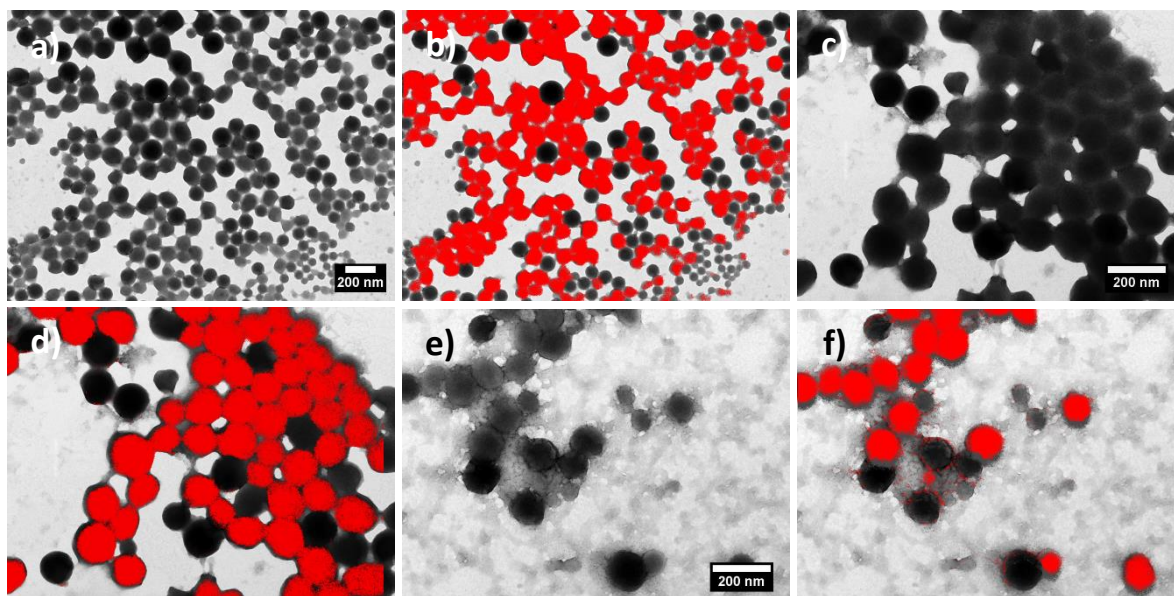
Figure 30: TEM and ESI-TEM images of blends of P3HT and PCBM particles; (a and b) non-stained, (c and d) iodine stained, and (e and f) OsO_4 stained. The sulfur signals are red colored. The ESI-TEM images feature the same scale bar as the corresponding TEM images.

4.1.1.2 SEM investigations

The SEM images of pure P3HT and PCBM particles are shown in **Figure 31** (**a**) and (**b**). Similar to the TEM results, the deformed character of P3HT particles is also observed. In addition, the SEM image shows that the surface of P3HT particles appears bumpy or rather "tennis ball-like". Due to the hairy surface structure of these particles, the density decreases radially to the particle rim. This explains why P3HT particles become brighter and diffuse to their edges in TEM. It is assumed that the hairy architecture is a result of thiophene ring stacking, formed by interchain π-π stacking.[203]

This leads to a lamellar structure of conjugated sheets, favoring a 1D growth (compare **section 4.1.3**). The surface of PCBM particles is flat and reminiscent of "table tennis balls". Some PCBM particles exhibit a dent. This phenomenon is a consequence of phase separation described by the Flory-Huggins theory and is well-known in literature; for further explanation see **section 7.1.2**. Due to the differences in surface structure, both kinds of particles can be distinguished very well, as shown in the particle blend in **Figure 31** (**c**). In contrast to the TEM investigations, there is no enhancement in grey scale contrast formation by using iodine and OsO$_4$, as shown in **Figure 31** (**d**) and (**e**).
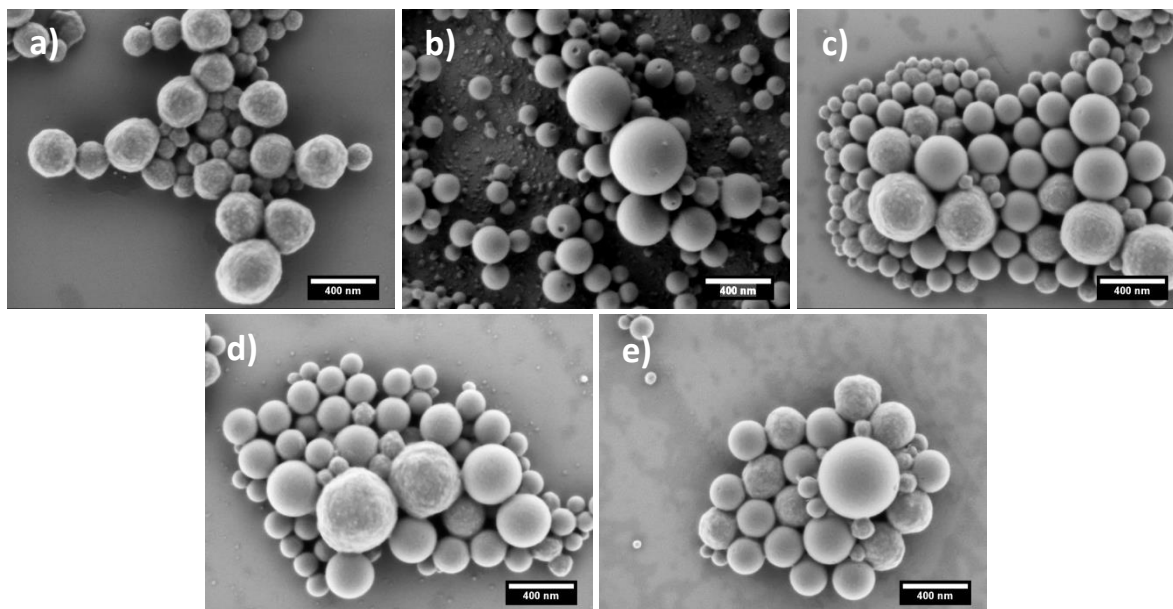

Figure 31: SEM images of (a) P3HT particles, (b) PCBM particles, (c) blend of P3HT and PCBM particles, (d) blend of P3HT and PCBM particles stained with iodine, and (e) blend of P3HT and PCBM particles stained with OsO$_4$.

4.1.2 Composite particle morphology

Due to a better interpretation and assessment of the electron microscopy images of P3HT/PCBM composite particles, a theoretical estimation of potential particle morphologies can be made. As described in **section 2.4.1**, the particle morphology is given by Δ*G*. Each morphology by can be understood as a combination of different $\gamma_{ij}A_{ij}$. The final morphology will be the one offering the smallest Δ*G*, if the system is allowed to getting to thermodynamic equilibrium. The important interactions happen at the material/water interface. Therefore, an estimation of the particle morphology can be confined to the comparison of the interfacial energies between the blend materials and water (γ_{sl}).[204]

With respect to the particle morphology, the well-known and easy determinable comparator system polystyrene (PS)/poly(L-lactide) (PLLA) is used to appraise the interfacial energies of P3HT and PCBM between water. Starting from the comparator system, PS and PLLA will be exchanged stepwise with P3HT and PCBM. By knowing all γ_{sl}, it is possible to draw inferences from the resulting particle morphology of PS/P3HT, PS/PCBM, PLLA/P3HT, and PLLA/PCBM to the morphology of P3HT/PCBM composite particles. The characteristics of the particles which are used in this section are listed in **Table 2**.

Table 2: *Average diameter and polydispersity of particles which are used for interfacial energy determination and P3HT/PCBM composite particle morphology investigations.*

material	Application	diameter (nm)	polydispersity
PS/PLLA	interfacial energy determination	187	0.34
PS/P3HT	interfacial energy determination	129	0.26
PS/PCBM	interfacial energy determination	136	0.30
PLLA/P3HT	interfacial energy determination	143	0.31
PLLA/PCBM	interfacial energy determination	122	0.28
P3HT	morphology investigations	142	0.33
PCBM	morphology investigations	135	0.29
P3HT/PCBM	morphology investigations	134	0.27

4.1.2.1 Interfacial energy determination

According to Young's relation in **section 3.5**, γ_{sl} can be calculated by knowing γ_{sv}, γ_{lv}, and θ. For a variety of liquids the surface tensions (γ_{lv}) are well-known, as shown in **Table 3**. The contact angle can be determined by the sessile drop method. For the identification of the surface energies (γ_{sv}) a method introduced by Owens/Wendt,[205] Rabel,[206] and Kaelble[207] (OWRK) is used. Using the OWRK method, γ_{sv} is extrapolated from the interactions between the used material and liquids of different polarities, as shown in **section 4.1.2.1.1**.

Table 3: *Surface tensions of the liquids used for γ_{sv} determination, according to the OWRK method. The surface tensions are divided into a disperse (γ_{lv}^{D}) and a polar (γ_{lv}^{P}) part. All data are taken from the liquid database of Krüss.*[208]

liquid	γ_{lv}^{D} (mN·m^{-1})	γ_{lv}^{P} (mN·m^{-1})	γ_{lv} (mN·m^{-1})
milliQ water	26.0	46.8	72.8
formamide	28.7	29.5	58.2
1,5-pentanediol	27.6	15.7	43.3

4.1.2.1.1 Determination of γ_{sv}

In the OWRK method, the idea of Fowkes is applied.[87] The interfacial energies can be separated to the involved interactions between the molecules, namely disperse and polar interactions. The combinations of the disperse and the polar contributions form the sum of the interfacial energy.

$$\gamma_i = \gamma_i^{D} + \gamma_i^{P} \tag{14}$$

According to the work of Fowkes, γ_{sl} can also be described as:

$$\gamma_{sl} = \left| \gamma_s - \gamma_l \right| \tag{15}$$

By forming the geometric mean, Owens and Wendt achieved:

$$\gamma_{sl} = \gamma_{sv} + \gamma_{lv} - 2\left(\sqrt{\gamma_{sv}^{D}\gamma_{lv}^{D}} + \sqrt{\gamma_{sv}^{P}\gamma_{lv}^{P}} \right) \tag{16}$$

Kaelble obtained the same equation by forming several combinations of two liquids and calculated the mean values of the resulting values of the surface energy. Rabel rendered it possible to calculate the disperse and polar fractions of the surface energy with the aid of a single linear regression from the contact angle data of various liquids.

Briefly, Rabel combined **Equation 16** with Young's relation (**Equation 13**) and adapted the resulting equation by transposition to the general equation for a straight line (**Equation 17**).

$$y = mx + b \tag{17}$$

The transposed equation is:

$$\underbrace{\frac{(1+\cos\theta)\gamma_{lv}}{2\sqrt{\gamma_{lv}^D}}}_{y} = \underbrace{\sqrt{\gamma_{sv}^P}}_{m}\underbrace{\sqrt{\frac{\gamma_{lv}^P}{\gamma_{lv}^D}}}_{x} + \underbrace{\sqrt{\gamma_{sv}^D}}_{b} \tag{18}$$

Using different liquids, a linear regression through the data points of the respective γ_{lv} and θ in a

y-x plot is applied. The disperse surface energy γ_{sv}^D is obtained from the square of the curve slope *m*;

γ_{sv}^P arises from the square of the ordinate intercept *b*. The sum leads to γ_{sv} :

$$\gamma_{sv}^D + \gamma_{sv}^P = \gamma_{sv} \tag{19}$$

A representative example of such a plot is given in **section 7.1.3**. In order to achieve γ_{sv}, the contact angle of at least two liquids of various polarities must be determined on a substrate. For more precise results, determination with three liquids is carried out in this work. The used liquids, along with their polar and dispersed surface tensions, are presented in **Table 3**. For the determination of the surface energies of PS, PLLA, P3HT, and PCBM, the materials were dissolved in a suitable solvent and spin coated onto silicon. The measured contact angles and the computed values of γ_{sv} by using milliQ water, formamide, and, 1,5-pentanediol are shown in **Table 4**.

Table 4: *Measured contact angles and resulting γ_{sv} of PS, PLLA, P3HT, and PCBM by using milliQ water, formamide, and 1,5-pentanediol. The literature values of the contact angles and the surface energies are denoted in brackets.*

material	contact angle (°)			surface energies (mN·m⁻¹)		
	milliQ water	formamide	1,5-pentanediol	γ_{sv}^P	γ_{sv}^D	γ_{sv}
PS	90.3 (90)[209]	67.3	54.2	0.29	40.21	40.50 (40.7)[210]
PLLA	63.1 (63)[211]	54.8	41.6	4.56	44.03	48.59 (50)[211]
P3HT	103.2 (102.1)[212]	98.5	75.1	0.02	27.89	27.91 (26.9)[213]
PCBM	81.3 (75,5)[212]	70.2	53.7	0.77	37.45	38.22 (37.8)[213]

The contact angles (with water) and the surface energies of PS and PLLA conform to the literature, 90.3°, 40.50 mN·m⁻¹ and 63.1°, 48.59 mN·m⁻¹, respectively. P3HT shows also with a contact angle of

103.2° and a surface energy of 27.91 mN·m^{-1} a good agreement with values given in the literature. In the case of PCBM, the contact angle of 81.3° deviates, however, the resulting surface energy of 38.22 mN·m^{-1} fits well into the overall series. Furthermore, a first estimation of the material polarity based on the contact angles can be performed. Regarding their interactions with water, the descending order of polarity of this material set is: PLLA, PCBM, PS and P3HT.

4.1.2.1.2 Determination of γ_{sl}

If γ_{sv} is known, γ_{sl} can be calculated from Young's relation. The final interfacial energies at material/water interface are listed in **Table 5**. The interfacial energies conform to the polarity estimation made in **section 4.1.2.1.1**. The values lie between 19.96 mN·m^{-1} for PLLA and 44.53 mN·m^{-1} for P3HT. Due to the ester groups of PLLA and PCBM, both molecules are more hydrophilic than PS and P3HT, which contain no polar group within the chemical structure. Based on these ascertained data, a helpful tool in order to estimate the P3HT/PCBM composite particle morphology can be developed, which is demonstrated in the next section.

Table 5: *Interfacial energies of PS, PLLA, P3HT, and PCBM calculated from Young's relation.*

Material	γ_{sl} (mN·m^{-1})
PLLA	19.96
PCBM	27.20
PS	40.88
P3HT	44.53

4.1.2.1.3 Morphological consequences of γ_{sl}

As reported in **section 2.4.1**, a discrepancy in γ_{sl} between the materials leads to different particle morphologies. In order to estimate the P3HT/PCBM morphology, the materials of the PS/PLLA system were exchanged systematically with P3HT and PCBM. On the basis of γ_{sl} it is possible to draw inferences from the resulting particle morphologies about the P3HT/PCBM composite particle morphology. The morphologies of the exchanged particle systems are shown in **Figure 32**.

The PS/PLLA particles exhibit Janus morphology, as shown in **Figure 32** (**a**). This indicates that an interfacial energy difference of around 20 mN·m^{-1} is sufficient for Janus formation. In TEM, PS appears dark and PLLA bright, as PLLA is degenerated in the electron beam.[214] Therefore, the PS/PLLA particles were protected by a layer of carbon. Consequently, the even lower energy difference in PS/PCBM and PLLA/PCBM of approximately 14 and 7 mN·m^{-1}, respectively, also yield Janus particles, as shown in **Figure 32** (**d**) and (**e**).The same applies to the PS/P3HT system, the particles also feature the Janus morphology, as shown in **Figure 32** (**b**). According to **section 4.1.1.2**, the bumpy part corresponds to P3HT and the smooth part to PS. The PLLA/P3HT system show a discrepancy of 25 mN·m^{-1}, thus, the Janus morphology turns into a core-shell structure, as shown in **Figure 32** (**c**). Because of the higher polarity of the polylactide, PLLA forms the shell and P3HT the core. The electron beam destroys and deforms the PLLA shell, allowing a look inside at the P3HT core. Otherwise the determination of a core-shell structure would not be possible in SEM.
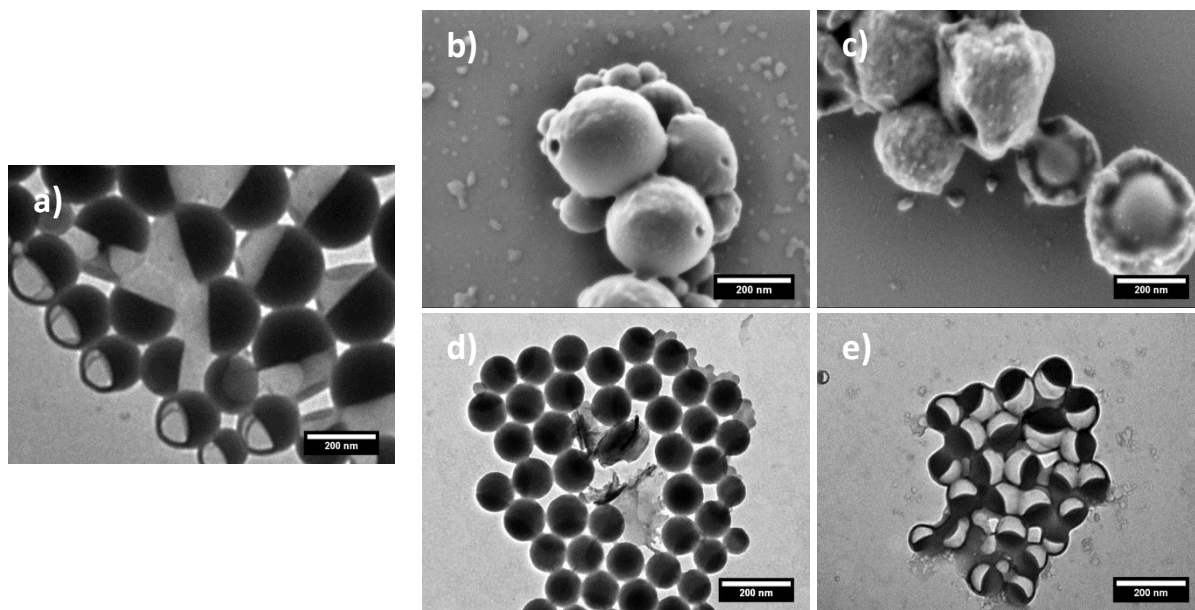
Figure 32: *Electron microscope images of composite particles consisting of (a) PS/PLLA, (b) PS/P3HT, (c) PLLA/P3HT, (d) PS/PCBM, and (e) PLLA/PCBM. Due to the protection against the electron beam, particles consisting of PLLA and observed by TEM are covered with carbon. These particles exhibit a black fringe.*

However, it is assumed that the values of **Table 5** do not reflect the real interfacial energies, the stabilization of the particle with SDS must also be taken into consideration. Since surfactants reduce the interfacial energy, the actual γ_{sl} must be lower than the obtained values. Upon particle preparation, the majority of the applied SDS is located at the solvent/water interface. Upon removing the solvent, the droplets shrink, implying an excess of surfactant inside the water phase.

At the same time, the water also evaporates, causing a further increase of the SDS concentration. Hence, the exact amount of SDS on the particle surface during the morphology formation is practically unknown and cannot be determined. Starting with a SDS concentration in the initial miniemulsion of 1.66 mg·mL^{-1}, depending on the amount of residual water, the system can exhibit a concentration up to 5 mg·mL^{-1} in the final dispersion.

The effect of various SDS concentrations on the contact angle on PS, PLLA, P3HT, and PCBM is shown in **Figure 33** (**a**). By increasing the SDS concentration, the contact angles on all substrates decline, showing an asymptotic behavior. At a concentration of approximately 1.5 mg·mL^{-1}, the contact angles show no significant change. Thus, an exact knowledge of the real SDS amount at the particle surface is not necessary, since the used SDS concentration in particle preparation is beyond this concentration. The recalculated values of γ_{sl} from the new contact angles are illustrated in **Figure 33** (**b**). As expected, the recalculated interfacial energies become much smaller by increasing the amount of SDS. Furthermore, the differences between the interfacial energies also decrease. Applying a SDS concentration of 2.5 mg·mL^{-1}, the final values of the interfacial energies of PS, PLLA, P3HT, and PCBM are 8.47, 7.03, 10.15, and 8.20 mN·m^{-1}, respectively.

These new results offer a different interpretation of the TEM and SEM images shown in **Figure 32**. Now the conditions for Janus in the PS/PLLA, PS/P3HT, PS/PCBM, and PLLA/PCBM systems are approximately 1.4, 1.7, 0.3, and 1.2 mN·m^{-1}, respectively. This conforms to the requirement as shown in the theory: Janus particles are only formed if the interfacial energies of both materials are almost equal. With respect to the core-shell structure of the PLLA/P3HT system, the gap is around 3 mN·m^{-1}. Hence, this approach provides more realistic values which fit into the theory.
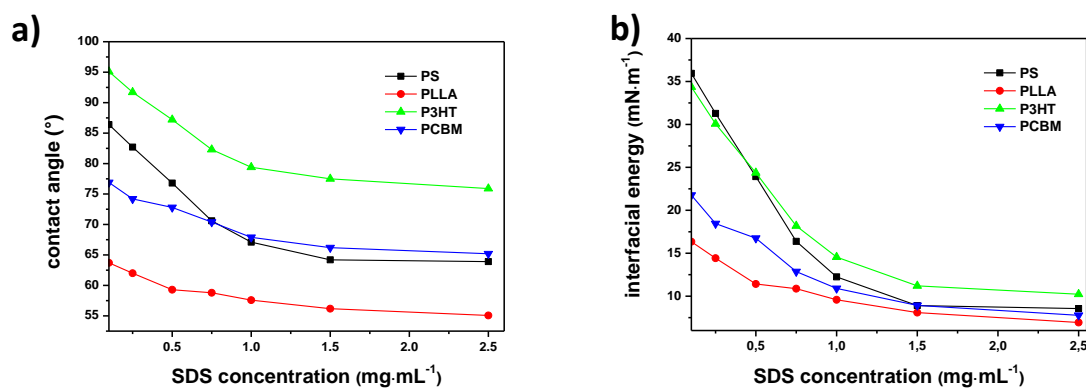
Figure 33: *(a) Contact angles of different SDS solutions on PS, PLLA, P3HT, and PCBM. (b) Corresponding γ_{sl} calculated from the obtained contact angles.*

In P3HT/PCBM particles the difference is around 2 mN·m^{-1}. Therefore, the Janus morphology may be favored in this system. However, a core-shell structure cannot be completely excluded. The resulting electron microscope images and a morphology interpretation of P3HT/PCBM composite particles are given in **section 4.1.2.2**.

4.1.2.2 Electron microscope images interpretation

The TEM images of P3HT/PCBM composite particles are shown In **Figure 34** (**a**) to (**c**). In general, the particles exhibit no evident morphology. In all cases, regardless of whether they are stained or not, the particles appear uniformly dark as pure PCBM particles. Even osmium staining does not lead to a definite morphology. Thus, no explicit morphology can be determined from the TEM images. The SEM images clarify the existence of small "grooves" on the particle surface, as shown in **Figure 34** (**d**) to (**f**). In relation to TEM, the "groove" character is only slightly enhanced by staining with iodine and OsO$_4$. As the "grooves" possibly represent the transition from one phase to the other, it may indicate that P3HT/PCBM composite particles consist of small domains.
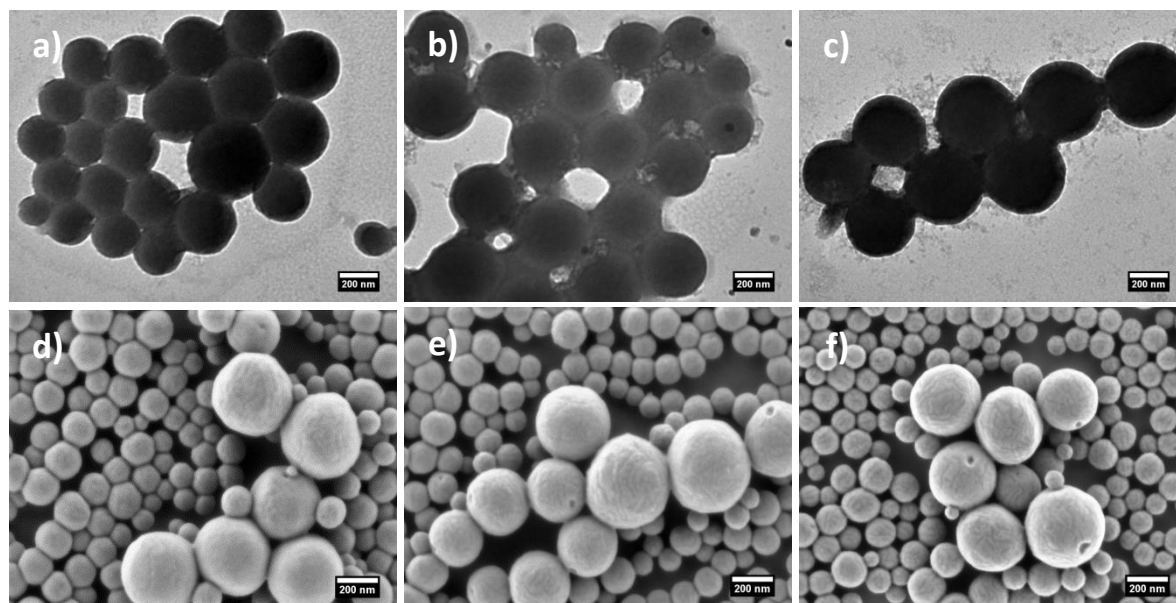
Figure 34: *Electron microscope images of P3HT/PCBM composite particles; (a and d) non-stained, (b and e) iodine stained, and (c and f) OsO$_4$ stained.*

In order to verify the domain structure, sulfur ESI-TEM fails. As shown in **section 4.1.1.1**, EELS require a certain amount or rather area of P3HT. The "grooves" are in range of a few tens of nanometers which is not sufficient to investigate it via EELS. The same applies to the SEM analogue,

dispersive X-ray spectroscopy (EDX). The osmium is only located on the surface, thus, an insufficient amount for elementary analysis is present in the particles. As reported in **section 3.2**, back scattered electrons (BEs) are also element sensitive and can be used to visualize the osmium parts.

Regarding the contrast formation in SEM, by using BEs bright areas indicate regions containing heavy elements, whereas dark parts are an indication for light elements. A BE-SEM image of the osmium stained P3HT/PCBM composite particles is shown in **Figure 35** (**a**). In comparison to iodine and OsO_4 staining, using BEs the "groove" pattern is reinforced. But the more important observation is that the "grooves" appear dark, whereas the parts in between are bright. Since OsO_4 reacts solely with PCBM, the bright areas can be assigned to PCBM and the dark parts to P3HT. This is a clear proof for the domain structure of P3HT/PCBM composite particles. However, due to the fact that PCBM occupies more space on the surface, the particles can be seen as a kind of partial core-shell structure, or partially engulfed phases. This morphology consistent with the interfacial energies determined in **section 0**, as PCBM features a lower γ_{sl}. Moreover, the presence of domains is an indication that the morphology formation in the P3HT/PCBM system is also kinetically controlled. However, the particles which are shown in **Figure 35** (**a**) reflect only the situation on the surface.
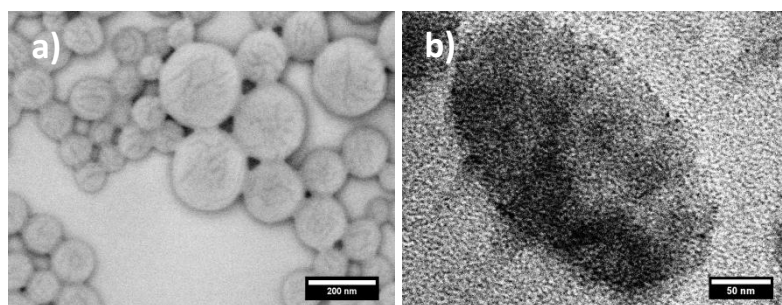
Figure 35: *Electron microscope images of OsO_4 stained P3HT/PCBM composite particles. (a) BE-SEM; bright are assigned to osmium or rather PCBM and dark to P3HT. (b) CS-TEM; bright is assigned to P3HT and dark to PCBM.*

To investigate the morphology within the particles, a look inside the colloids is required. This is conducted by cross section (CS) TEM. For this purpose, the particles were embedded in an epoxy resin. To produce cross sections, the sold resin was cut by a diamond knife into 80 nm thick stripes. To give a better contrast and for an unambiguous material assignment, the particles were stained with OsO_4. A CS-TEM image of a P3HT/PCBM composite particle is shown in **Figure 35** (**b**). The originally partial core-shell structure is no longer present, instead, a further phase separation into almost pure P3HT and PCBM phases has occurred. The new particle morphology resembles to a

Janus particle. The phenomenon of phase separation can be explained by the work of Watts,[215] who discovered a diffusion of PCBM molecules across the P3HT phase under certain conditions, *e.g.* the temperature. Upon the preparation of the cross sections, the resin was hardened at 60 °C. However, the diffusion process happens at temperatures below 60 °C. Hence, with respect to the temperature, the P3HT/PCBM morphology can be regarded as metastable.[216] A detailed description of the diffusion process and the conditions under which phase separation occurs will be given in **section 4.2.3.1**.

This shows that direct visual investigation of the P3HT/PCBM structure inside the particles is not possible. A method which is independent from imaging interpretation, providing another view inside the particles will be introduced the following section.

4.1.2.3 Photoluminescence interpretation

It is possible to take a look inside a P3HT/PCBM particle without changing the existing morphology. This can be done by taking advantage of the limitation of the exciton diffusion length in organic semiconductors, as reported in **section 2.9**. Excitons which are not undergoing a charge separation recombine by radiative processes. The question of whether PL occurs depends on the distance from the place of the exciton's origin to the next D/A interface or rather the domain size of P3HT. If the place of origin is within twice of the exciton diffusion length, a charge transfer to PCBM is expected and PL is quenched.[217] In the case of larger domains, a recombination of the excitons takes place and the resulting PL can be measured. Using this simple concept, on the basis of the amount of PL it can be estimated whether the particle morphology corresponds to a core-shell or a domain structure.

For this investigation, the PL intensity of P3HT/PCBM composite particles is compared to the PL intensity of pure P3HT particles and a blend of P3HT and PCBM particles. In the literature, the exciton diffusion length of P3HT is commonly quoted as being around 8 nm.[218] Assuming that the composite particles have a pure core-shell morphology, the amount of PL compared to pure P3HT particles or the particle blend should be 78% or 39%, respectively. The geometrical considerations are demonstrated in **section 7.1.4**. Despite the presence of PCBM there should be no quenching in the particle blend, as the P3HT and PCBM particles are stabilized with SDS stabilization and not come in contact. The PL spectra of the employed particle systems are shown in **Figure 36**. The absorption spectrum of the P3HT/PCBM system will be discussed in **section 4.1.3**.
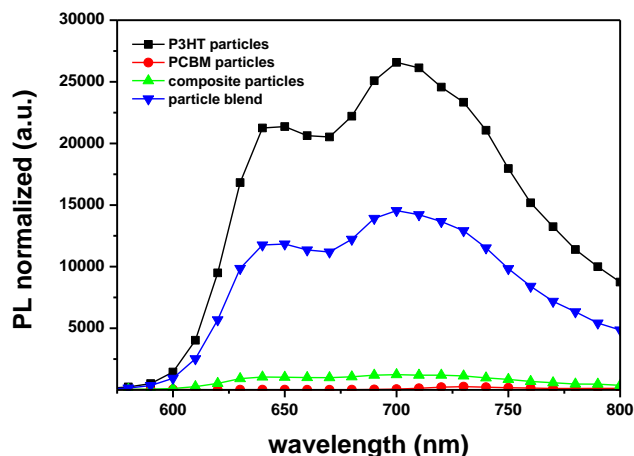
Figure 36: PL spectra of pure P3HT particles, pure PCBM particles, blend of P3HT and PCBM particles, and P3HT/PCBM composite particles. The PL is normalized to the solid content of the dispersions.

The pure P3HT particles feature the highest PL intensity. As the particle blend only consists of 50% of P3HT, the amount of PL is decreased. The integration of the PL spectra shows that the PL intensity of the particle blend is about 54% of the pure P3HT particles. This indicates a linear dependence of the PL regarding the matter content. The PL intensity of the composite particles is around 8% of the particle blend. Thus, the composite particles cannot exhibit a core-shell structure, since the PL intensity is too low. On the basis of the low PL and the SEM investigations shown in **section 4.1.2.2**, it can be concluded that P3HT/PCBM composite particles consist of domains. For the sake of completeness, pure PCBM particles are also demonstrated in **Figure 36**, unsurprisingly they offer no PL. In view of the fact that that 92% of PL is quenched and estimating that the size of the domains is not uniform, the majority of the domains must be within the range of the exciton diffusion length. Therefore, the P3HT domains exhibit a hypothetical estimated average domain size of approximately 16 nm, assuming an exciton diffusion length of 8 nm.

4.1.2.4 Cognitions of particle morphology investigations

To summarize the morphology section, using a combination of electron microscopy, interfacial energy comparisons, and PL investigations it is possible to determine the P3HT/PCBM composite particle morphology. On the surface the composite particles show a "groove" pattern, resulting in a partial core-shell morphology in which PCBM takes up more space than P3HT. The overall particle morphology is characterized by a domain structure with an estimated P3HT domain size of 16 nm.

With respect to the domain structure, the morphology of P3HT/PCBM composite particles conforms to the BHJ concept, representing a good basis for the fabrication of PBOPVs.

4.1.3 Influence of evaporation temperature

According to Winzor and Sundberg,[77] the phase separation and the concomitant morphology formation in secondary dispersion systems is influenced by the evaporation temperature or rather the time taken for fully solvent removal. Consequently, the domain sizes of P3HT and PCBM must be also affected by the evaporation temperature. In order to investigate this assumption, the evaporation temperature is varied from 30 to 90 °C in 20 °C steps. As introduced in **section 2.2**, upon releasing, the solvent is transported from the initial droplet through the aqueous phase to the water/air interface where the evaporation occurs. The evaporation in such a system is determined by the azeotrope of the involved liquids. For water and toluene the azeotrope lies at 84 °C. The weight composition at this point is approximately 20% water and 80% toluene.[219] This implies that even though toluene exhibits a higher boiling point than water, the solvent can be completely removed without any significant loss of water. At 60 °C the complete removal time was about 3 h, reducing the temperature causes a prolongation of the evaporation time. A temperature increase results in a drastically reduced duration, especially when the temperature is above the azeotrope. The resulting evaporation times at 30, 50, 70 and 90 °C are 6 h, 4 h, 100 min, and 30 min, respectively. The exact time point of complete evaporation was identified by a simple smell test. The characteristics of the particles which are used for temperature variation are listed in **Table 6**.

Table 6: Average diameter and polydispersity of the particles which are used for temperature variation investigations.

preparation temperature (°C)	diameter (nm)	polydispersity
30	153	0.27
50	157	0.27
70	164	0.31
90	143	0.30

In order to obtain information about a potential morphology change upon temperature variation, the knowledge of the P3HT/PCBM absorption spectrum is required. The absorption spectra of pristine P3HT, PCBM, and P3HT/PCBM films are shown in **Figure 37** (**a**). PCBM shows the strongest absorption in the UV region, corresponding to the formation of higher excited singlet states.[220] A typical P3HT spectrum features a main peak at 520 nm, a sub peak at 550 nm, and another sub peak at 620 nm. The three peaks are also called vibronic absorption shoulders. The P3HT absorption is well-known to be sensitive to the level of P3HT chain order.[221] The shoulders at 550 nm and 620 nm are results of side chain interdigitation and π-π stacking of the P3HT chains, as shown in **Figure 37** (**b**) and (**c**). The higher the P3HT order the more interdigitation and stacking occurs, the more pronounced are the vibronic shoulders. Generally, the UV-Vis spectrum of the P3HT/PCBM blend is an overlay of the pure components. However, in relation to pure P3HT the absorption maximum of the blend is blue-shifted; in the present case by over 80 nm. Moreover, the spectrum of the blend shows a less structured absorption profile, which can be explained by the presence of PCBM, hindering P3HT chain alignment.[222]
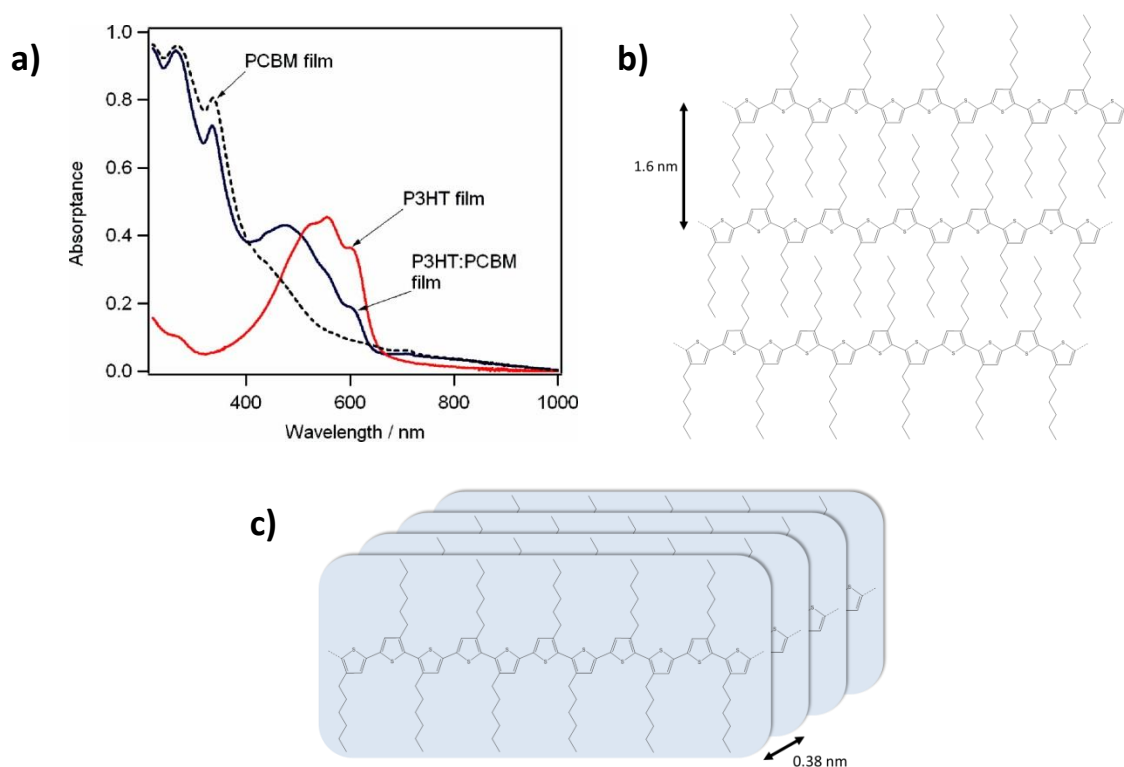
Figure 37: (a) UV-Vis spectra of pristine P3HT, PCBM, and P3HT/PCBM films. The spectra are taken from the work of Cook.[222] (b) Schematic illustration of side chain interactions between the P3HT chains, leading to interdigitation. (c) Schematic illustration of the π-π stacking of the thiophene rings. The interdigitation and stacking distances between the P3HT chains are 1.60 nm and 0.38 nm, respectively.[221]

The UV-Vis spectra of P3HT/PCBM composite particle dispersions prepared at various temperatures are shown in **Figure 38** (**a**). Upon the evaporation of toluene at 90 °C, the absorption spectrum features only rudimentary vibronic shoulders. When the preparation temperature is decreased, the curves are more structured and the shoulders start to become clear. Besides the particle morphology, this shows that a P3HT order is also affected from the evaporation temperature. It can be assumed that at low temperatures or rather slow morphology formation the P3HT chains have more time for self-organization and arrange in a crystal configuration. A similar but much more pronounced behavior is observed in spin coated P3HT/PCBM films made from chlorobenzene (CB). A very slow evaporation of CB is accompanied by a strong increase in absorbance and a significant red-shift.[223] Both observations are an indicative of more ordered structures. The red-shift can be explained by fact that a crystalline system features an enhanced conjugation length which shifts the absorption spectrum to lower energies.[224]
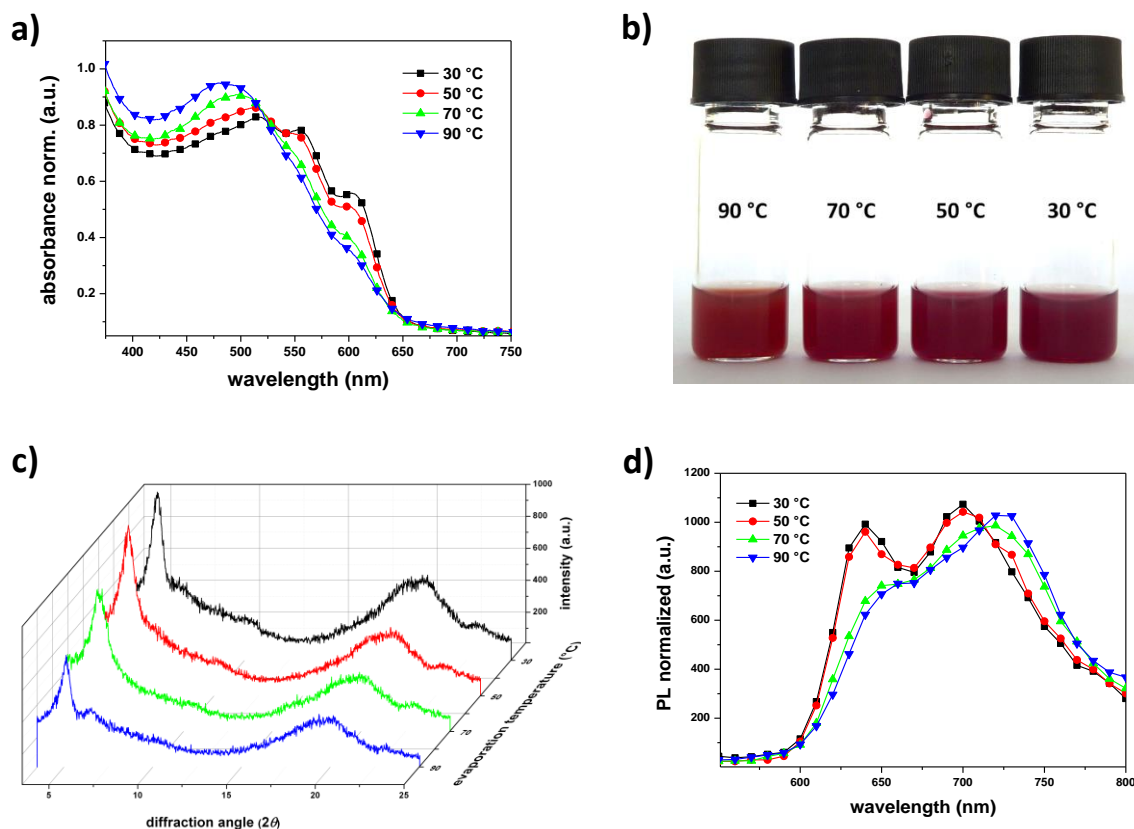
Figure 38: *(a) UV-Vis spectra, (b) dispersion pictures, (c) XRD diffractograms (of the freeze-dried particles), and (d) PL spectra of P3HT/PCBM composite particles prepared at different evaporation temperatures.*

In relation to the spin coated P3HT/PCBM films, an integration of the absorption spectra of the P3HT/PCBM composite particles indicates that there is almost no change in absorbance. Note that spin coating is very fast preparation method. For this reason, the resulting P3HT/PCBM films are nearly amorphous; reducing the evaporation velocity results in significant differences in the UV-Vis spectra. The preparation time of the composite particle is many times longer than for the spin coated films, even at 90 °C. Therefore, the differences in the absorption spectra are less marked. However, a small red-shift of approximately 35 nm of the particles prepared 90 °C to the particles prepared 30 °C is observed. This effect is also shown in **Figure 38** (**b**). The dispersions turning slightly from a more tangerine like color into a red color upon decreasing the evaporation temperature.

The crystallinity of P3HT can be validated by using XRD. Based on the chain arrangements as shown in **Figure 37**, the XRD diffractogram of the freeze-dried P3HT/PCBM composite particles should display two reflections: one small signal at $2\theta = 5°$, assigned to the π-π sacking and one wide signal located at $2\theta = 23°$ assigned to the interdigitation. The diffractograms in **Figure 38** (**c**) show both reflections, which are amplified by reducing the evaporation temperature. This is the final evidence for the assumption that lower solvent evaporation temperatures leads to a higher P3HT order. In principle, PCBM also exhibits a few reflections, but in the mixture with P3HT these are weak pronounced and masked by the P3HT signals. As discussed in **section 2.10**, besides the change in UV-Vis spectra, an increase in P3HT order also causes an increase in the hole mobility. In crystalline systems, the charge carrier mobility is no longer restricted to hopping from one disordered state to the next.[203]

As the degree and velocity of the phase separation is affected by the evaporation temperature, regarding the domain structure of the P3HT/PCBM composite particles, larger domains are expected at lower evaporation temperatures. This effect should be reflected in the PL spectra of the corresponding dispersions. As demonstrated in **Figure 38** (**d**), at first sight, there is almost no difference in the amount of PL. This shows that there is no meaningful change in the P3HT domain size upon the variation of the evaporation temperature. Certainly, here, the differences in the P3HT domain sizes are not quite pronounced as it was the case in **section 4.1.2.3.** Hence, the introduced quenching concept cannot be applied to this approach and another way of investigation needs to be found.

In the course of this work it became apparent that ethanol and hexane are almost selective solvents for PCBM. The treatment of a P3HT and PCBM particle blend with ethanol and hexane is

shown in **Figure 39**. Applying ethanol, the polythiophene is not dissolved. The P3HT particles remain unaffected on the substrate. As opposed to this, the PCBM particles are completely dissolved from the particle blend. Using hexane, PCBM is also completely removed. However, it seems that P3HT is marginal attacked by the hexane. Small P3HT particles are removed and the remaining larger P3HT particles are slightly merged. Nevertheless, this kind of dissolving offers a convenient visually clarification method for a domain size investigation in P3HT/PCBM composite particles.
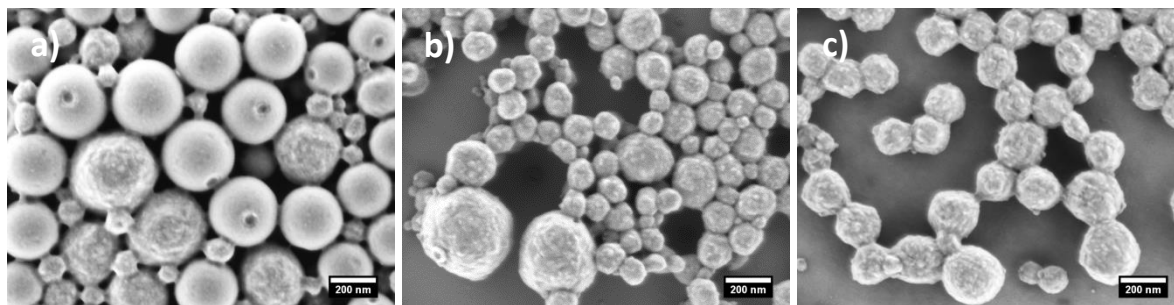
Figure 39: *(a) Blend of P3HT and PCBM particles. (b) Corresponding particle blend treated with ethanol. (c) Corresponding particle blend treated with hexane.*

The ethanol and hexane treatment of P3HT/PCBM composite particles prepared at different temperatures is shown in **Figure 40**. The untreated particles exhibit a change in surface structuring from low to high evaporation temperatures, *i.e.* the patterning becomes finer, as shown in the **left column**. Actually, this fact by itself suggests a change in domain size. Dissolving of PCBM by ethanol and hexane provides the ultimately confirmation. The ethanol and hexane treated particles reveal that the resulting P3HT domain size strongly depends on the evaporation temperature, as shown in the **middle** and the **right column**. By dissolving with ethanol, the average domain size shrinks from 63 to 11 nm by increasing the temperature from 30 to 90 °C, respectively. In the case of hexane, the domains are smaller (54 to 15 nm) and are not quite as pronounced as for the ethanol treatment. The reason probably lies in the slight solubility of P3HT in hexane. The distinctions in the domain sizes clearly demonstrate an influence of the evaporation temperature on the particle morphology. Hence, the overall trend conforms to the assumption that larger domains are expected at lower evaporation temperatures. Further, this experiment also gives a good visual confirmation of the domain character of P3HT/PCBM composite particles.
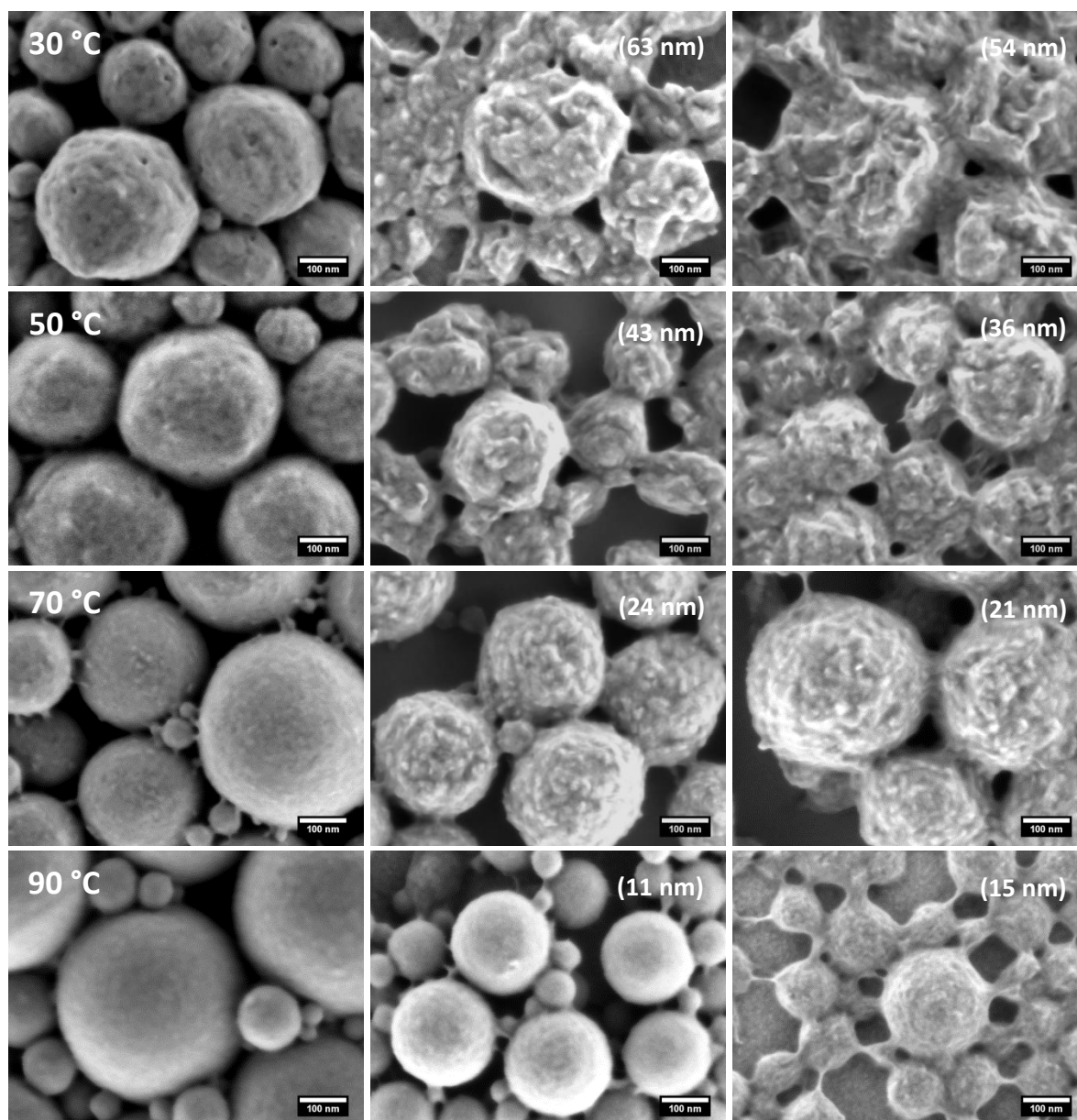
Figure 40: *SEM images of P3HT/PCBM composite particles prepared at different temperatures. (Left column) pristine, (middle column) ethanol treated, and (right column) hexane treated composite particles. The average P3HT domain sizes are denoted in brackets.*

In **section 4.1.2.3** an average P3HT domain size of 16 nm for particles prepared at 60 °C was estimated. In terms of the present the case, the domain size of particles prepared at 60 °C would be larger, namely approximately 36 nm (compare **section 4.3.3**). The estimated value of 16 nm was evaluated on the basis of an assumed exciton diffusion length and a rough comparison of the PL intensities. Hence, it is believed that the domain sizes which are determined optically by SEM reflect the effective particle structure much better. Generally, this kind of analysis also may contain errors,

since the behavior of the domains by dissolving only one component out of the particles is not precisely known.

Considering the BHJ concept, on the basis of the small P3HT domains, especially the particles prepared at higher temperatures should be well suited for solar cell applications. Nevertheless, the crystallinity associated with the charge carrier mobility is also of crucial importance for efficient OPVs. These two factors are also linked to the preparation temperature, however, they are less pronounced at high preparation temperatures. The performance of the introduced P3HT/PCBM composite particles in solar cells will be examined in **section 4.3.3**.

4.2 Particle layer formation and reprocessing

A basic prerequisite for the active layer in PBOPVs is a fully-closed particle film. In devices that do not feature such a layer there is the danger of a short circuit, since ITO and the counter electrode may come into contact. In order to achieve such films, the coating methods Langmuir trough deposition, drop casting, and spin coating will be applied and introduced in this section. Furthermore, essential reprocessing steps, *i.e.* annealing and surfactant elution of the obtained particles layers, will be also shown. The characteristics of the P3HT/PCBM composite particle dispersions which are used in this section are listed in **Table 7**.

Table 7: *Characteristics of the dispersions which are used of particle layer formation and particle layer annealing.*

application	diameter (nm)	polydispersity	solid content (wt.-%)	surfactant
Langmuir trough deposition	163	0.24	1.60	SDS
drop casting	156	0.36	1.60	CTAC
drop casting	154	0.32	1.60	SDS
spin coating	93	0.28	1.25 – 5.0	SDS
annealing	89	0.32	3.33	SDS

To compare different coating methods, a standard substrate is required. A suitable substrate is silicon due to two facts. Firstly, particle films on silicon wafers can be easily investigated by SEM without any further preparation step. Secondly, as will be later described in **section 4.3.1**, the behavior of the P3HT/PCBM composite particle dispersions on plasma activated silicon wafers and plasma activated buffer layers is almost equal.

4.2.1 General coating information

From a conceptual point of view, the particle coating techniques can be divided into two main categories: direct assembly on a substrate and liquid interface-mediated processes. In general, the assembly of the particles and the associated quality of the resulting film is based on the

polydispersity of the colloids and the interplay of three forces: Van der Waals forces, capillary forces, and electrostatic forces. Van der Waals forces are attractive, short distance, dispersed, and specific interaction forces between molecules. But they also act among small colloids.[225, 226] Capillary forces are attractive and long range forces, occurring by the positioning of two or more particles at a liquid interface. The origin of capillary forces is a deformation of the liquid interface around the colloids, caused by the finite contact angle of the particles. On the one hand, at the liquid/air interface, this deformation leads to a Laplace pressure resulting in an attraction of the colloids, minimizing the interface bending. On the other hand, the presence of a very thin liquid film on colloids at a solid surface leads to attractive immersion forces, given when the thickness of liquid film is smaller than the particle diameter.[227] Due to ionic stabilization by SDS, there are also electrostatic repulsive forces between the particles, preventing coalescence or precipitation. The balance of these forces is crucial for the formation of high quality particle layers.

4.2.2 Particle layer preparation methods

4.2.2.1 Langmuir trough deposition

A special feature of colloids is their ability to attach at interfaces, forming an energy well that effectively traps the colloids at a fixed position between the phases.[228] Therefore, a convenient method to produce colloidal layers is to utilize the assembly of particles at the water/air interface. The most common technique using the liquid interface is the Langmuir trough deposition.[229] The setup of a Langmuir trough is shown in **section 7.1.5**.

In literature, perfect and highly ordered dense packed 2D colloid arrays have been achieved, by using Langmuir trough deposition.[230] It should be noted that the reported particles were larger, monodisperse, and feature more negatively charged by covalently bonded carboxylic groups than the present P3HT/PCBM composite particles. All factors influence the particle arrangement to a great extent. Larger colloids exhibit better arrangement at the water/air interface. Generally, monomodal particles are more favorable for hexagonal packing. Due to the higher charge, there is an increase in electrostatic repulsion, allowing a higher colloid mobility. Thus, the particles can find their minimum free energy position. In other words, electrostatic repulsion provides the required mobility for an ordered particle formation before an aggregation takes place.[231] The P3HT/PCBM composite particles are stabilized with SDS. In principle, a negatively charged surface is present. But

based on the dynamics of the SDS molecules, it can be assumed that most of the surfactant is in or on the water phase upon contact with the water/air interface. For this reason, it is believed that the colloids are practically non-charged.

The addition of colloids from an aqueous dispersion to a water/air interface is condemned to failure, since the particles will be incorporated in the water phase of the trough. However, a particle spreading at the interface is desirable. Therefore, the polarity and density of the dispersion needs to be changed. This is attained by the addition of a small amount of butanol to the dispersion. The particles are transferred to the water/air interface via a glass slide. Generally, the addition of organic solvents to an aqueous dispersion has negative effects on the colloid stability, causing slow coagulation. Since the dispersion is transferred by a glass slide, this does not affect the quality of the particle layer, as the coagulated particles remain on the glass slide. Upon spreading at water/air interface, patches of particles films in a range from millimeters to centimeters are formed and remain afloat at the interface. The patches are compressed by barriers to a homogeneous film (see **section 4.2.2.1.1**).

When a homogeneous colloid film is formed, it needs to be transferred to a substrate. Several transfer methods have been proposed, displayed in **Figure 41**. Prominent techniques are the Langmuir-Blodgett[232] and the Langmuir-Schaefer[233] transfer. With respect to OPVs, the particles have to be transferred to a (hydrophobic) buffer layer. However, due to poor interactions with the substrate (compare **section 4.3.1**), none of the procedures can be applied. Therefore, the particles need to be transferred by another process, which is performed by simply lowering the water level on an immersed substrate, as shown in **Figure 41** (**c**).

a)   **b)**   **c)**
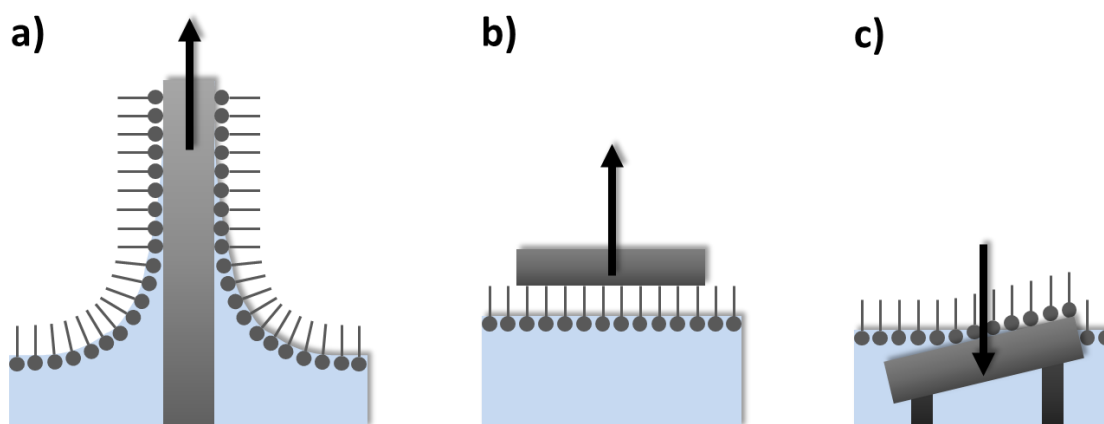
Figure 41: Transfer of a molecular monolayer to a solid substrate. a) Langmuir-Blodgett, b) Langmuir-Schaefer, and c) surface lowering transfer.

4.2.2.1.1 Raft dragging

In order to achieve a homogeneous film, the floating patches are dragged by barriers after the dispersion transfer to the water/air interface is completed. The process of dragging can be displayed by a surface pressure (Π) isotherm, providing information on surface tension increment caused by a surface area decrement (see **section 7.1.5**). Three different dragged particle films and their corresponding locations in a Π isotherm are demonstrated in **Figure 42**. A particle film without compression is shown **Figure 42** (**b**), corresponding to position 1 in the isotherm. Due to the dominant attractive van der Waals and capillary forces, the particles aggregate in a disordered monolayer upon contact at the water/air interface, resulting in a non-closed particle layer. In the course of compression, the barriers come closer resulting in an increased Π. In **Figure 42** (**b**) the patches are combined to uniform film, which corresponds to position 2 in the isotherm. However, in comparison to the non-dragged film, a better particle packing as a consequence of the higher surface pressure is absent. The reason for this must be the already mentioned immobility of the particles, caused by the missing surface charge. Continued squeezing of the barriers produces first a flattening and then a further increase of Π, which corresponds to position 3 in the isotherm. This behavior can be explained by the collapsed and piled up particle film, as shown in **Figure 42** (**d**). A direct comparison between the particles films from position 1 and 3 in the isotherm is shown **Figure 42** (**e**) and (**f**).
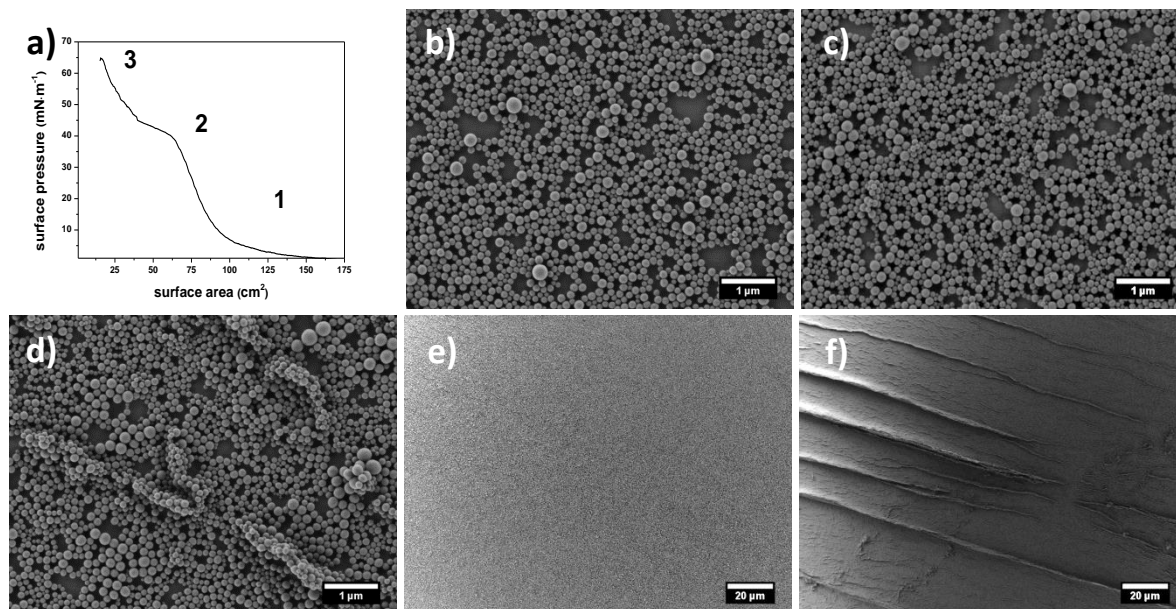
Figure 42: *a) Surface pressure isotherm of particle films upon patches compression. (b, c, and d) Corresponding SEM images of particle films achieved at the positions 1 (b), 2 (c), and 3 (d) of the isotherm. (e and f) Overview of a non-dragged particle film (position 1 (e)) and a dragged particle film (position 3 (f)). The dispersion were transferred to the trough with a constant flow of 1.53 mL·h^{-1}.*

This attempt shows that SDS stabilized P3HT/PCBM composite particles remains in the arrangement in which they are applied to the water/air interface. A subsequent compression of the colloids by the barriers is not possible. Therefore, the assembly of particles needs to be tuned directly during the transfer to the water/air interface.

4.2.2.1.2 Variation of dispersion flow

Since the colloids are trapped by the addition to the water/air interface, a promising approach to achieve 2D colloid arrays is the variation of the flow rate. The flow is controlled by a syringe pump. The results of applying flow rates of 3.05, 2.29, 1.59, and 0.74 mL·h^{-1} is shown in **Figure 43**. In order to attain a uniform film, the rafts are compressed until the piling starts, meaning a flattening of the isotherm. Note that the particle flow is subject to upper and lower limits, variations are only possible within a certain range. At 3.05 mL·h^{-1} the particle packing density is low. The reduction of the flow rate leads to closer packed colloids. However, the compression stagnated at a rate of 1.59 mL·h^{-1}. Below this flow rate no further increase in the particle packing occurs. This shows that lower velocities are needed for a good assembly, implying that the particles require a long transfer time to the interface. As a minimum flow is needed to overcome transition from glass slide to water/air interface, close-packed particle films cannot be generated by this method. In order to obtain acceptable particle arrays, the mobility of colloids must be substantially increased.
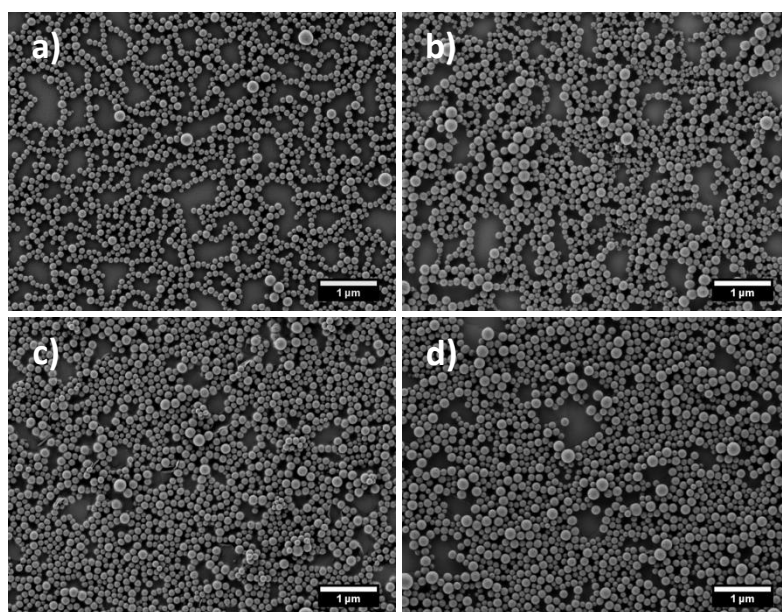
Figure 43: Influence of various dispersion flows to the particle packing; (a) 3.05, (b) 2.29, (c) 1.59, and (d) 0.74 mL·h^{-1}.

4.2.2.1.3 "Piston oil" effect

Surfactants like SDS also exert a noticeable influence on the particle packing. The surfactant molecules accumulate at the air/water interface and constitute a soft barrier, facilitating the packing of the colloids. On a molecular scale, colloids crossing over to the water/air interface and push against the surfactant layer, this in turn slows down the particles and pushes them together. Thus, the formation of 2D colloid arrays is favored. Dunsmuir[234] described this special feature as the "piston oil" effect. It is considered very probable that beside the water/air interface, SDS also attaches at the particle surface, increasing the surface charge and thus the repulsion forces.[231] Therefore, the addition of SDS reduces the incoming flow velocity and increases the particle mobility at the water/air interface. Particles layers prepared with increasing SDS concentrations are shown in **Figure 44**. If no SDS is used for the layer formation, a film similar to that shown in **Figure 43** (**b**) is generated. The increase of the SDS concentration improves the colloid assembly. The higher the SDS concentration, the better is the particle packing. Using concentrations of 700 mg·L^{-1} and 875 mg·L^{-1} yield close-packed monolayers, as shown in **Figure 44** (**e**) and (**f**). However, this technique has an upper limit. At concentrations over 700 mg·L^{-1} there is almost no increase in the particle packing. Additionally, it was found that the use of concentrations higher than 875 mg·L^{-1} resulted in a redispersion of the colloids from the water/air interface into the bulk of the water phase. Further, small monolayer patches which are floated at the air/water interface redispersed with time.
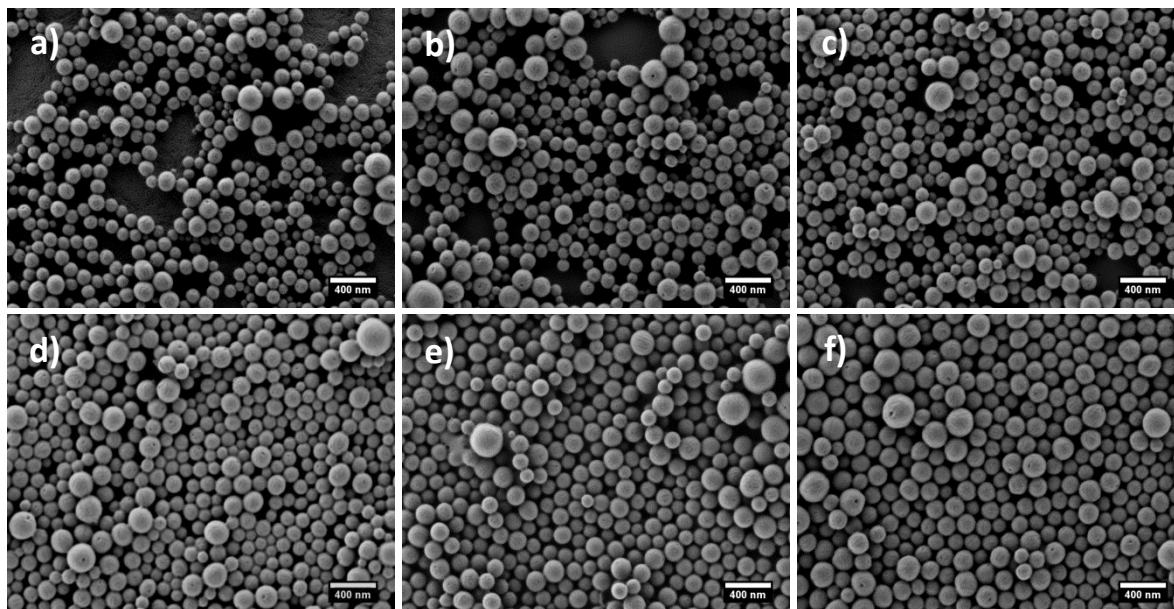
Figure 44: *Demonstration of the "piston oil" effect. SEM images of particle films prepared with various SDS concentrations in the water phase; (a) no SDS, (b) 175, (c) 350, (d) 525, (e) 700, and (f) 875 mg·L^{-1}. The films were prepared with a constant flow rate of 2.29 mL·h^{-1}.*

4.2.2.2 Drop casting

Horizontal dispersion evaporation is assumed to be the easiest method to create colloidal layers. In the simplest case, a drop of a colloidal dispersion is placed on a substrate and evaporated; the result is a particle layer. In comparison to Langmuir trough deposition, the particles are not located at a water/air interface. Therefore, the electrostatic repulsive forces can be neglected. The self-assembly process is mainly driven by attractive van der Waals forces and capillary (immersion) forces, given by the water level and the diameter of the particles. For the horizontal evaporation technique, a two stage mechanism is proposed, illustrated in **Figure 45**. Firstly, nuclei are formed, governed by attractive capillary forces appearing between particles which are partly immersed in the liquid layer. Due to water evaporation from the already ordered colloids a particle flux is caused, resulting in crystal-like growth.[235] As mentioned in **section 4.2.1**, immersion forces occur only if the water depth is smaller than the particle diameter. Hence, a condition for drop casting is a complete wetting or rather a very low contact angle.
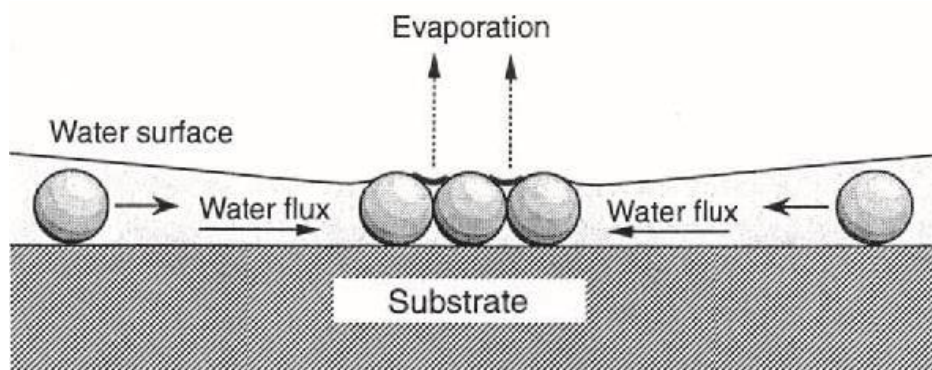
Figure 45: *Process of 2D colloid array formation on a substrate. The illustration is taken from the work of Denkov.[235]*

In case of poor wetting, the dispersion forms a droplet instead of a thin film. In this instance, the array formation starts usually somewhere at the periphery of the droplet. As a result of the directional motion of the particles from the droplet center towards the rim, multi-layers of particles accumulate at the drop periphery. Simultaneously, the droplet center is depleted of particles.[236] Coined from the typical appearance of a coffee stain this phenomenon is known as the "coffee-ring effect", reported by Deegan *et al.*[237]

The flaw of poor wetting of a dispersion can be remedied in two ways. Firstly, polar groups can be inserted on the substrate, facilitating wettability. This can be achieved by plasma treatment, leading to the creation of polar groups.[238] Secondly, an adequate surfactant can be chosen to enable the

attachment of the dispersion on the substrate. The results of both measures are shown in **Table 8**. In this attempt, the wettability of milliQ water, a SDS and CTAC solution, and P3HT/PCBM composite particles dispersions stabilized with SDS and CTAC on several argon plasma activated silicon wafers is investigated. The SDS and CTAC solutions feature the same amount of surfactant as the corresponding P3HT/PCBM dispersions. Without activation, the contact angle of water on silicon is 40.5°. However, a short plasma treatment of 5 s improves the wettability to a complete spreading. The wettability of the SDS solution and the SDS stabilized particles is also enhanced by plasma treatment. However, complete wetting is not obtained. After plasma treatment of 60 s, the achieved contact angles are around 19.4 and 20.3°, respectively. In contrast, the use of the CTAC solution and CTAC stabilized particles results in a complete wetting, in case of the dispersion even without plasma activation.

Table 8: Wettability of milliQ water, SDS solution, CTAC solution, and P3HT/PCBM composite particle dispersion stabilized with SDS and CTAC on several argon plasma activated silicon wafers.

activation time (s)	milliQ water (°)	milliQ + SDS (°)	milliQ + CTAC (°)	SDS dispersion (°)	CTAC dispersion (°)
not activated	40.5	39.9	complete wetting	27.2	complete wetting
5	complete wetting	31.8	"	25.1	"
30	"	21.5	"	21.9	"
60	"	19.4	"	20.3	"

In principle, the contact angle of SDS stabilized P3HT/PCBM composite particles is quite low. Regarding drop casting, the contact angle is still too high and leads to the above described "coffee-ring", as shown in **Figure 46** (**a**). Note that the SEM image shows the inner circle of the stain. Consequently, P3HT/PCBM composite particles stabilized with SDS are not appropriate for particle film formation by using drop casting. In contrast, by applying CTAC stabilized composite particles a homogenous close-packed colloid layer is formed, as shown in **Figure 46** (**b**). However, the presented colloid film is not a monolayer. It is multi-layer film having a thickness in the order of 1.5 µm up to 1.8 µm. A CS-SEM image of the respective film is shown **Figure 46** (**c**).
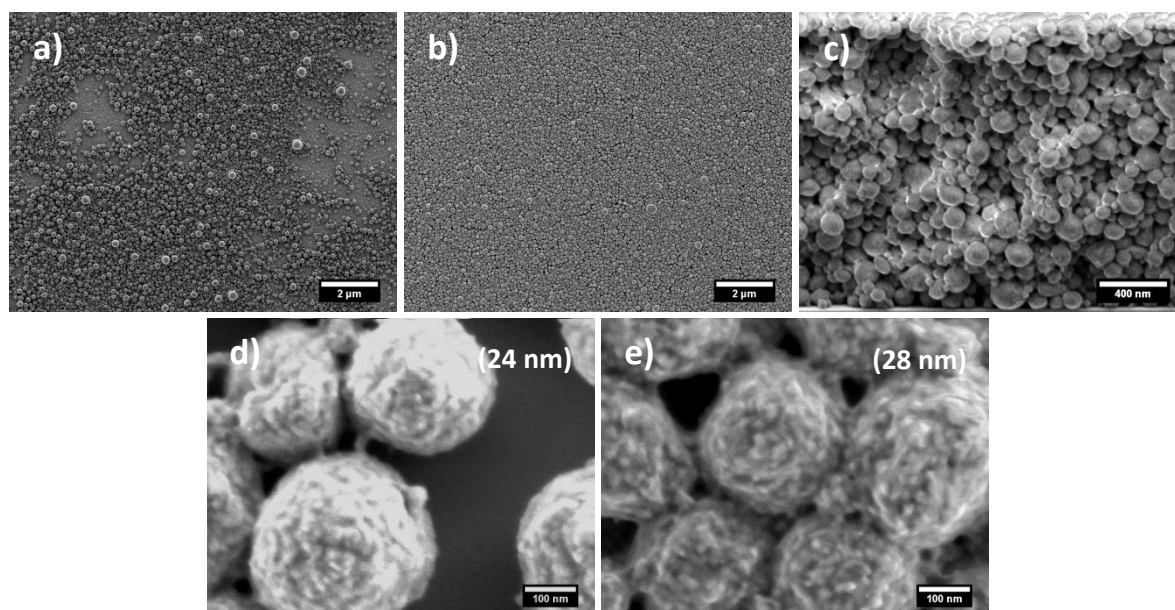
Figure 46: *(a) Drop cast film of SDS stabilized P3HT/PCBM composite particles. The image section shows the inner circle of the stain. (b) Drop cast film of CTAC stabilized P3HT/PCBM composite particles. (c) CS-SEM of the corresponding CTAC stabilized particle film. (d) Particle morphology of CTAC stabilized P3HT/PCBM particles visualized by ethanol treatment. (e) Particle morphology of CTAC stabilized P3HT/PCBM particles visualized by hexane treatment. The average P3HT domain sizes are denoted in brackets.*

The particle diameter and the size distribution of P3HT/PCBM composite particles stabilized with CTAC are in the same range as the SDS stabilized composite particles. The morphology of ethanol and hexane treated CTAC stabilized composite particles prepared at 70 °C is shown in **Figure 46** (**d**) and (**e**). Similar to the SDS stabilized particles as shown in **section 4.1.3**, CTAC stabilized particles also show a similar domain structure. The size of P3HT domains are in same range. This means that a change of the surfactant has no influence on the inner particle morphology.

In spite of the large film thickness, considering the ease and fast processing, this way of coating is a powerful technique for the formation close-packed particle films, even with polydisperse colloids.

4.2.2.3 Spin coating

Similar to drop casting, spin coating is also a fast and simple method for colloidal assembly. Due to the rotation, associated with a spreading of the dispersion, the resultant macroscopic film is more homogeneous. However, strong lateral forces occurring during the coating process and hamper the colloidal crystallization. In literature, this problem was solved by increasing the viscosity, *i.e.* using high solid contents and the addition of a monomer.[239] The monomer provides mechanical stability

by photopolymerization. Furthermore, high-boiling organic solvents were applied in order to decrease the vapor pressure. Besides, the rotation speed was reduced.[240]

All these measures prolong the evaporation time and allow the particles to assemble, even by shearing. However, transferring to P3HT/PCBM composite particle dispersions, some of the introduced measures cannot be applied. Using a monomer is not possible, as the resulting polymer would disrupt the charge carrier mobility in the active layer. As described in **section 4.2.2.1**, the addition of organic solvents causes particle coagulation. For this reasons, the particle film has to be prepared from the pure dispersion. Regarding the above introduced measures, in case of P3HT/PCBM dispersions, only the solid contents can be increased. As certain minimal rotation speed is required, the speed is set at 1000 rpm. Note that the acceleration is very low (20 rpm·min^{-1}). In this way, the colloids receive sufficient time for assembly. Analog to drop casting, spin coating requires also a good wetting. Otherwise the dispersion forms a droplet and is launched from the substrate by lateral forces. However, the wettability of the SDS stabilized P3HT/PCBM composite particle dispersion is sufficient as the rotation force spreads the dispersion uniformly over entire the substrate. The influence of the solid content on the particle assembly and film quality is demonstrated in **Figure 47**.
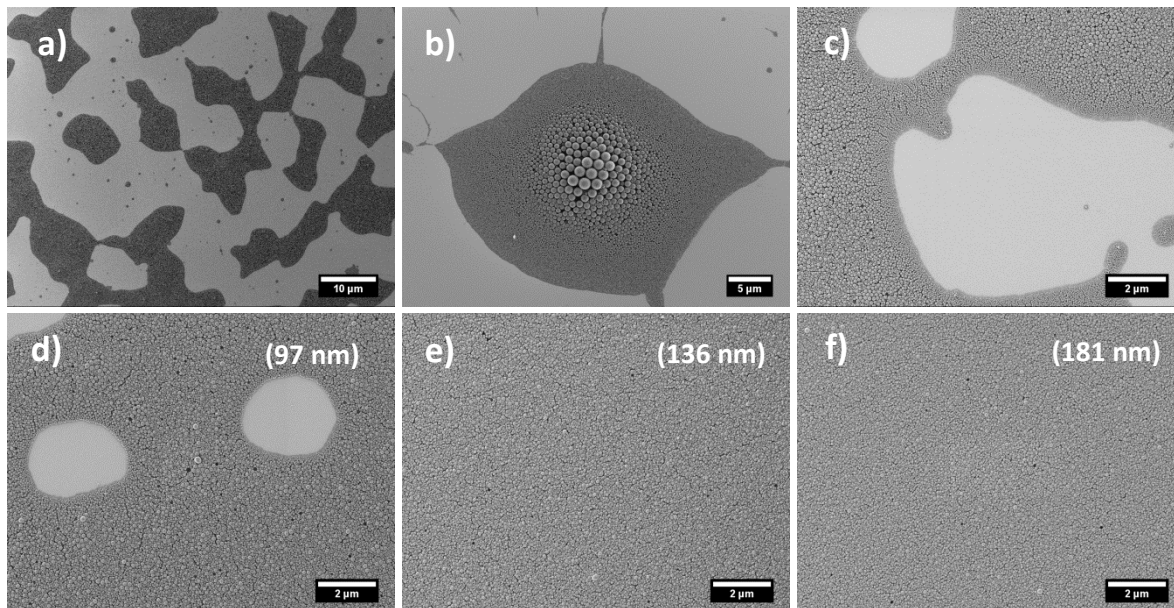
Figure 47: *Quality of spin coated particle layers with rising solid contents; (a and b) 0.5, (c) 1.25, (d) 2.5, (e) 3.75, and (f) 5 wt.-%. The film thicknesses are denoted in brackets.*

Using a solid content of 0.5 wt.-%, the colloids form individual incoherent agglomerates, as shown in **Figure 47** (**a**). Within these agglomerates the colloids are sorted according to their size. Larger particles are located in the center, whereas smaller ones are located at the outer rim, as shown in **Figure 47** (**b**). A solid content of 1.25 wt.-% lead to connected agglomerates, however, there are still uncovered parts on the substrate. A further increase entails that the uncovered parts become smaller. Using 3.75 wt.-%, a homogeneous close-packed particle layer is formed. Note that there is no change in the layer structure by applying 5 wt.-%, only the layer thickness is increased. As the average particle size is 93 nm, the close-packed films in **Figure 47** (**e**) and (**f**) must be constructed of more than one particle layer, compare **Figure 53** in **section 4.2.3.1**.

Additional testing implied that a coherent close-packed colloid film is already formed at a solid content of 3.33 wt.-%. The thickness of the resulting film is approximately 120 nm. In the further course of this work, spin coated particle films will be prepared with this solid content.

4.2.3 Particle layer reprocessing

The introduced three coating methods are all suitable for close-packed colloid array formation. However, the generated particle films cannot be directly brought into operation, all films need to be reprocessed in different manners. The contact between the particles within the colloid films is low. Thus, an application as solar cell requires a thermal annealing procedure, causing a coalescence of the particles. Further, in order to prevent charge traps inside the active layer, the surfactant must be removed from the particle film. Additionally, regarding the low charge carrier mobility in organic semiconductors, particle films made by drop casting are significantly too thick to be applied in solar cells. Therefore, the layer thickness must be decreased. In this section the essential reprocessing steps are shown. In addition, a rough estimation of the reprocessed films concerning their application in PBOPVs will be given.

4.2.3.1 Particle layer annealing

The morphology of the active layer of P3HT/PCBM SPOPVs is often not well-developed and cannot be applied directly into a solar cell device. Therefore, an essential step in the device fabrication, in order to achieve high efficiencies, is the annealing of the active layer. The main

reasons for an improvement upon annealing are the formation of an interpenetrating network and the crystallization of the semiconductors.[24] The effect of annealing of P3HT/PCBM films spin coated from CB is demonstrated In **Figure 48**. After coating, P3HT and PCBM are highly mixed and thus the domains are very small. Upon heating, the P3HT and PCBM phases separate and the domains grow. The longer the thermal treatment, the better is the demixing and interpenetration. It should be noted that the domain size is not the only criterion for the solar cell efficiency. For a successful charge transport to the electrodes, a percolation of the respective domains is also of crucial importance. A detailed explanation for the observations occurring during the annealing process is given below.
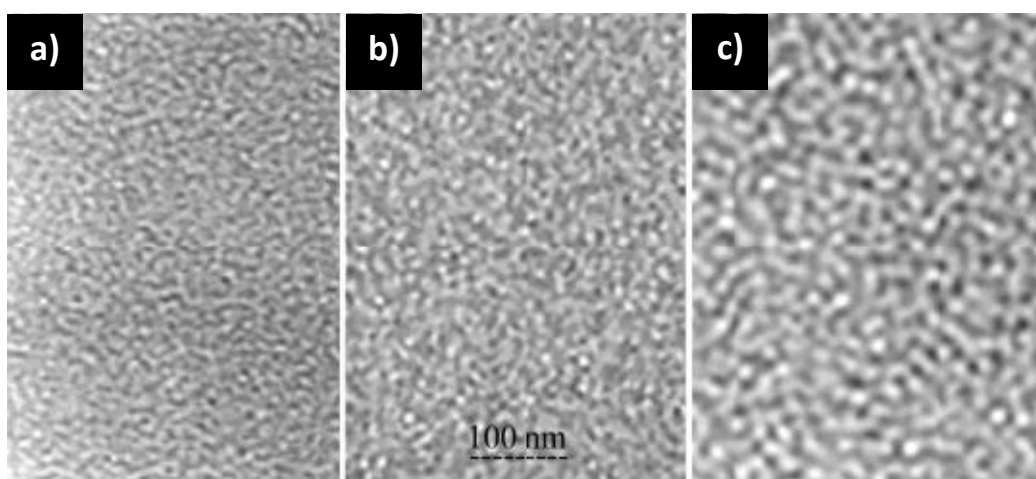
Figure 48: TEM images of thin spin coated P3HT/PCBM films prepared from CB. (a) Before thermal annealing, (b) after thermal annealing at 150 °C for 30 min, and (c) after thermal annealing at 150 °C for 2 h. The images are taken from the work of Ma.[24]

Depending on P3HT crystallinity[241] and volume fraction,[242] P3HT and PCBM are partially miscible. At a volume fraction of amorphous P3HT > 0.42 the P3HT/PCBM blend becomes miscible, meaning that both phases form a homogeneous system. This fact can be explained by the characteristics of the PCBM molecule. Due to the small size and spherical shape of the PCBM molecules, they are able to diffuse through the amorphous regions of P3HT. Note that solution-processed spin coated P3HT/PCBM films consist mainly of amorphous phases. The typical P3HT/PCBM blend of a mass ratio of 1:1 exhibits more than 42 vol.-% of P3HT (see **section 7.1.4**). Thus, in case of solution-processed P3HT/PCBM films the volume fraction of amorphous P3HT is beyond the binodal line and the both phases are miscible. Hence, pristine spin coated P3HT/PCBM films are homogeneous, as shown in **Figure 48** (**a**). The thermal metastability of the P3HT/PCBM morphology is also caused by the incorporation of PCBM in P3HT. The glass transition temperature of P3HT is 12.1 °C and of PCBM it is

131.2 °C.[243] The T_g of a 1:1 mixture lies between 50 and 60 °C, caused by inclusion of PCBM within the amorphous phases of P3HT. Therefore, the morphology starts to change at temperatures higher than 50 °C. In the course of annealing process, the P3HT chains start to reorganize and crystallize.[244] As a consequence of the crystallization, $\varphi_{P3HT-amorphous}$ decreases. At $\varphi_{P3HT-amorphous}$ < 0.42, P3HT and PCBM are immiscible, they start to phase separate and domains are formed, as shown in **Figure 48** (**b**) and (**c**).

The partially miscibility of the P3HT/PCBM system casts a different light on the composite particle preparation shown in **section 4.1.3**. The fact that particles prepared at lower temperatures feature larger domains can be also explained by the miscibility of P3HT and PCBM. At slower evaporation rates, the order of the P3HT chains is higher. This diminishes $\varphi_{P3HT-amorphous}$ and leads to a phase separation, resulting in larger domains. Due to faster evaporation, particles prepared at 90 °C have much higher amounts of amorphous P3HT. Consequently, P3HT and PCBM are partially miscible, the phase separation is less pronounced, and the domains are smaller.

As known form **section 4.1.3**, P3HT/PCBM composite particles already feature a proper domain size and certain crystallinity, however, a annealing procedure is still necessary. Besides phase separation and material order improvement, another effect of the annealing is the melting of the particles. In PBOPVs, this effect is exploited in order to optimize the particle layer.[36] A drawback of using particles is the low contact between the colloids, but also between the colloids and the buffer layer as well as the counter electrode. A large contact area promotes charge transport to the electrodes. By the example of spin coated PS particles, the low contact between the particles and the substrate is demonstrated in **Figure 49**.
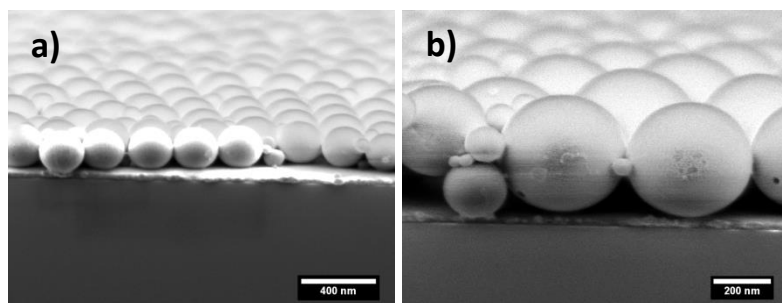
Figure 49: *Illustration of the low contact between particles and substrate, by the example of PS particles spin coated on the hole conductor poly(thiophene-3-[2[(2-methoxyethoxy)ethoxy]-2,5-diyl) (Plexcore).*

Besides the increase of the contact, the particle melting will also close small gaps and fissures inside the particle layer, preventing a contact between the anode and the cathode. Otherwise this would lead to a short circuit.

In this section, the general behavior of P3HT/PCBM composite particles upon thermal treatment is investigated. Regarding PBOPVs, a detailed discussion of the annealing process and the effects on device efficiency will be given in **section 4.3.2**. The annealing process is conducted on a hot plate under nitrogen atmosphere. The spin coated P3HT/PCBM composite particle films were treated at various temperatures from 65 to 155 °C. The substrates were preheated for 12.5 min at the desired temperature. The resulting films are shown in **Figure 50**. As the T_g of the P3HT/PCBM blend is between 50 and 60 °C, the particles starts to soften at 65 °C. The elevation of the temperature induces an improved contact among the colloids, accompanied by the fact that the gaps between the particles are almost vanished. At 95 °C the colloid film is fully melted, however, small domains in the range of 100 to 200 nm emerge. As a consequence of continuous P3HT crystallization and the amount of amorphous P3HT decrease. The P3HT/PCBM blend is the unstable area within the binodal line, and thus phase a separation occurs. For this reason it is assumed that these structures are separated PCBM phases.[241, 245] Annealing at higher temperature causes that the PCBM phases become larger and form agglomerates.[246, 247] The higher the annealing temperature, the larger are the PCBM agglomerates. Above 110 °C, only the structure of the agglomerates changes but not their size.
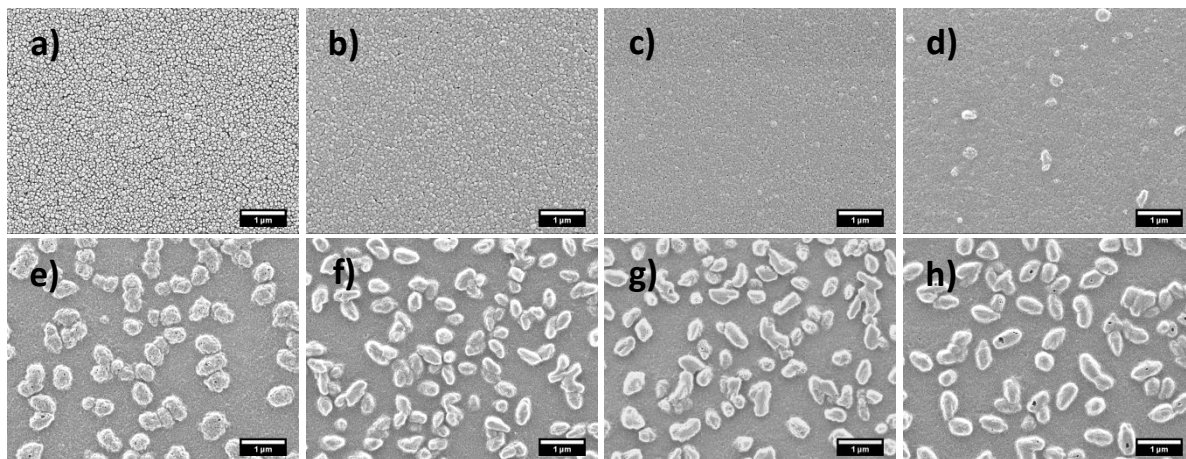
Figure 50: *Effect of annealing at various temperatures on P3HT/PCBM composite particle films. (a) Pristine, (b) 65, (c) 80, (d) 95, (e) 110, (f) 125, (g) 140, and (h) 155 °C. The annealing time is each 12.5 min. The composite particles were spin coated on silicon.*

Due to the phase separation, excitons generated in P3HT are no longer quenched by PCBM and PL arises.[248] Thus, the evolution of phase separation during the annealing process can be followed by confocal laser scanning microscopy (CLSM).[246, 249] CLSM is an optical microscopy technique using PL instead of/or in addition to reflection and absorption.[250] Its main advantage, regarding conventional PL spectroscopy, is that apart from information about the total PL amount also spatial information about the PL location is obtained. The CLSM images of the respective annealed films are shown in **Figure 51**.
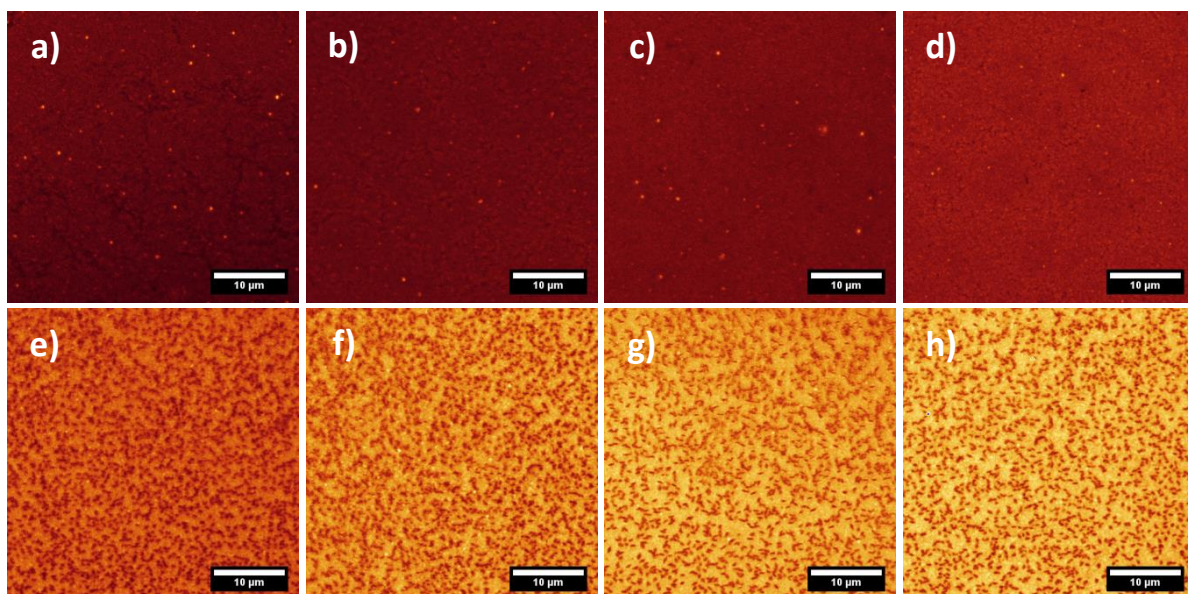
Figure 51: *Investigation of the annealing process regarding the phase separation by using CLSM. (a) Pristine, (b) 65, (c) 80, (d) 95, (e) 110, (f) 125, (g) 140, and (h) 155 °C. The P3HT/PCBM composite particles were spin coated on very thin glass slides.*

Note that bright/yellow is assigned to regions showing PL, whereas dark/red indicates no PL. In agreement with **section 4.1.2.3**, the pristine composite particle film exhibit marginally any PL. Additionally, small fissures inside the pristine layer are readily identifiable. Note that the bright spots are particles with either unbalanced P3HT/PCBM fractions or large P3HT domains, generating PL. Due to a resolution of approximately 200 nm the spots appear much larger in CLSM. Overall, from the pristine particle film to the film annealed at 80 °C, the CLSM images become brighter, indicating a small degree of phase separation. With respect the domain size, only a slight enlargement occurs. Furthermore, it can be seen that the fissures close. At 95 °C, the SEM investigations show the onset of PCBM agglomerate formation. In the CLSM no agglomerates can be identified, but compared to 80 °C, the PL is significantly increased. At 110 °C a distinct phase separation is observed. Small dark regions arise and the areas in between become bright. This is the explicit evidence that the

agglomerates consist of PCBM, as they show no PL. Due to the advanced degree of phase separation at higher temperatures, the amount of PL of P3HT increases and the number of PCBM agglomerates decreases. The latter one was not observed in SEM.

As demonstrated via SEM and CLSM investigations, in the course of annealing, small PCBM domains form large agglomerates. The formation of the agglomerates occurs by a diffusion of PCBM though P3HT. As shown in **Figure 52** (**b**), the positions of the originally small PCBM phases around a large agglomerate can be still clearly observed.

Time-resolved photoluminescence (TRPL) spectroscopy is a powerful tool for studying charge transfer processes in BHJs (see **section 7.1.6**).[251] Note that the lifetime of an exciton is an average value, thus, the exciton decay can be expressed in time as an exponential drop of the PL intensities. Similar to the PL investigation shown in section **4.1.2.3**, the dynamics of excitons also provides information regarding the film morphology. On the basis of the excitons decays, conclusions about the P3HT domain sizes can be made. In the further course of the thesis, this method is used for P3HT domain size estimation. For this reason the method will be introduced on a known example. During excitation ($t = 0$) excitons are generated, they start to recombine and PL is detected. With time the PL decreases. Due to diffusion, some excitons reach the D/A interface where a charge transfer happens. This reduces the PL additionally, leading to a faster decay. For this reason, small domains entail a fast decay and large domains a slow decay. The TRPL dynamics of the respective annealed particle films are shown in **Figure 52** (**a**).
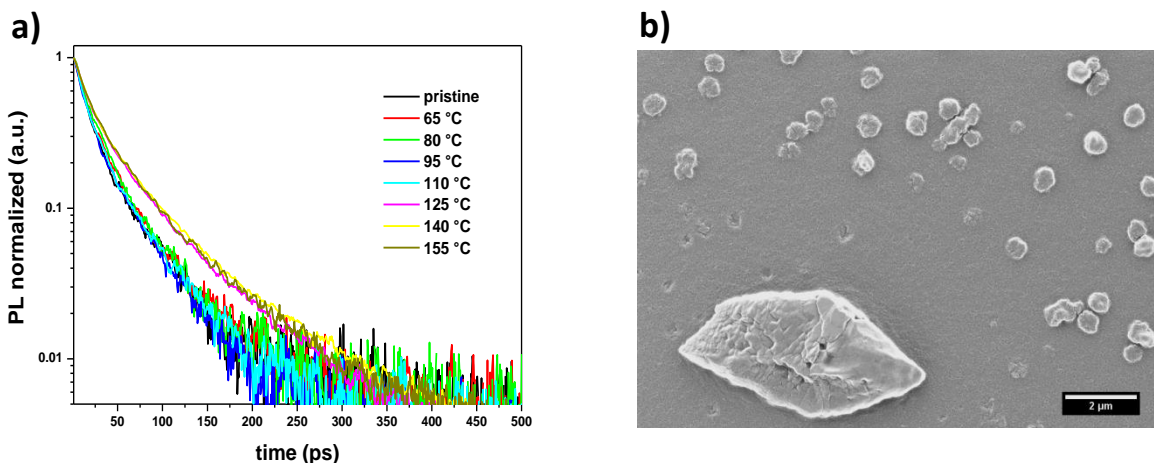
Figure 52: *(a) TRPL dynamics of P3HT/PCM composite particle films annealed at various temperatures. (b) Demonstration of the diffusion of small PCBM crystals to large an agglomerate. The dents around the large agglomerate reveal the initial positions of the small PCBM crystals.*

The PL of the pristine film and the films annealed up to 110 °C show almost the same decay. At 125 °C the slope becomes shallow, indicating larger domains. The decay of particle films annealed at 125, 140, and 155 °C is on the same level. Taken as a whole, except the film annealed at 110 °C, the TRPL results agree with the CLSM images. Thus, TRPL spectroscopy is a good method to investigate the P3HT domain size of annealed particle films.

The effect of particle melting upon annealing and the consequences of the reorganization of the film structure are shown in **Figure 53**. As mentioned in **section 4.2.2.3**, the spin coated particle layer must be built of more than one layer. **Figure 53** (**a**) demonstrates that the film is constructed of two interdependent particle layers. The pristine particle film has a thickness of 116 nm, however, there is a lot of free space between the particles. The melting process causes a collapse of the colloids and the space between the particles is eliminated. As a result of this compression, the film shrinks and loses more than 50% of its height, giving a thickness of around 50 nm at 95 °C. Annealing at higher temperatures leads to a complete phase separation, as shown in **Figure 53** (**b**). P3HT remains as a thin film, covering the whole substrate. PCBM piles up and forms large structures. PCBM agglomerates of more than 1 µm in height have been found by annealing at 155 °C. Due to the towering of PCBM, the surface roughness increases with the temperature. Besides a reduced exciton quenching, the phase separation has consequences for the light absorption (see **Figure 54**).
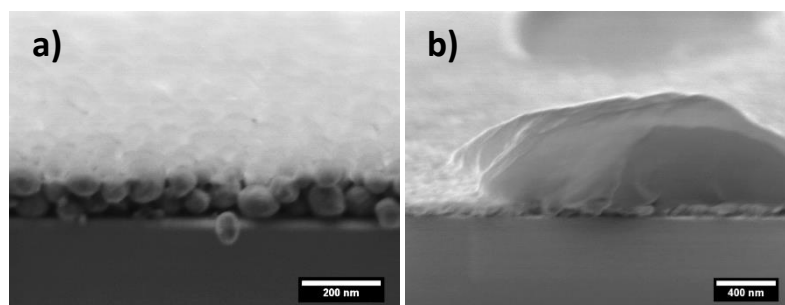
Figure 53: Change in particle film structure upon annealing; (a) structure of a pristine particle layer and (b) film structure after annealing at 155 °C for 12.5 min.

As mentioned, the crystallinity of P3HT and PCBM increases during the annealing process. The increase in the P3HT order is shown in **Figure 54 (a)**. The P3HT order rises steadily with the annealing temperature. At 125 °C there is strong an increases of the crystallinity, but this increase saturates at higher annealing temperatures. According to SEM, CLSM, and TRPL spectroscopy, the strong increase of the crystallinity is associated with an advanced phase separation. In relation to **section 4.1.3**, only the reflection of the chain interdigitation at $2\theta = 5°$ can be identified, but in this

case, the signals are less pronounced. The low signal can be explained by the simple fact that particle films on a substrate contain less material than a freeze-dried solid particle powder. In addition, the orientation of the P3HT domains on the wafer also plays a role (see **section 4.4.3**). The absence of the signal at $2\theta = 23°$ can be explained by the reorganization of P3HT upon crystallization, as illustrated in **Figure 54** (**b**). Regarding a substrate, P3HT can self-organize in two orientations. Either the π–π stacking direction is perpendicular (face-on) or parallel to the substrate (edge-on). The associated alkyl-stacking direction is then parallel (face-on) or perpendicular to the substrate (edge-on).[252] Since only the signal at $2\theta = 5°$ is visible, this is an indicative of an edge-on configuration.[248] Note that due to the low material amount, it is also possible that the signal of $2\theta = 23°$ is not visible in the noise.
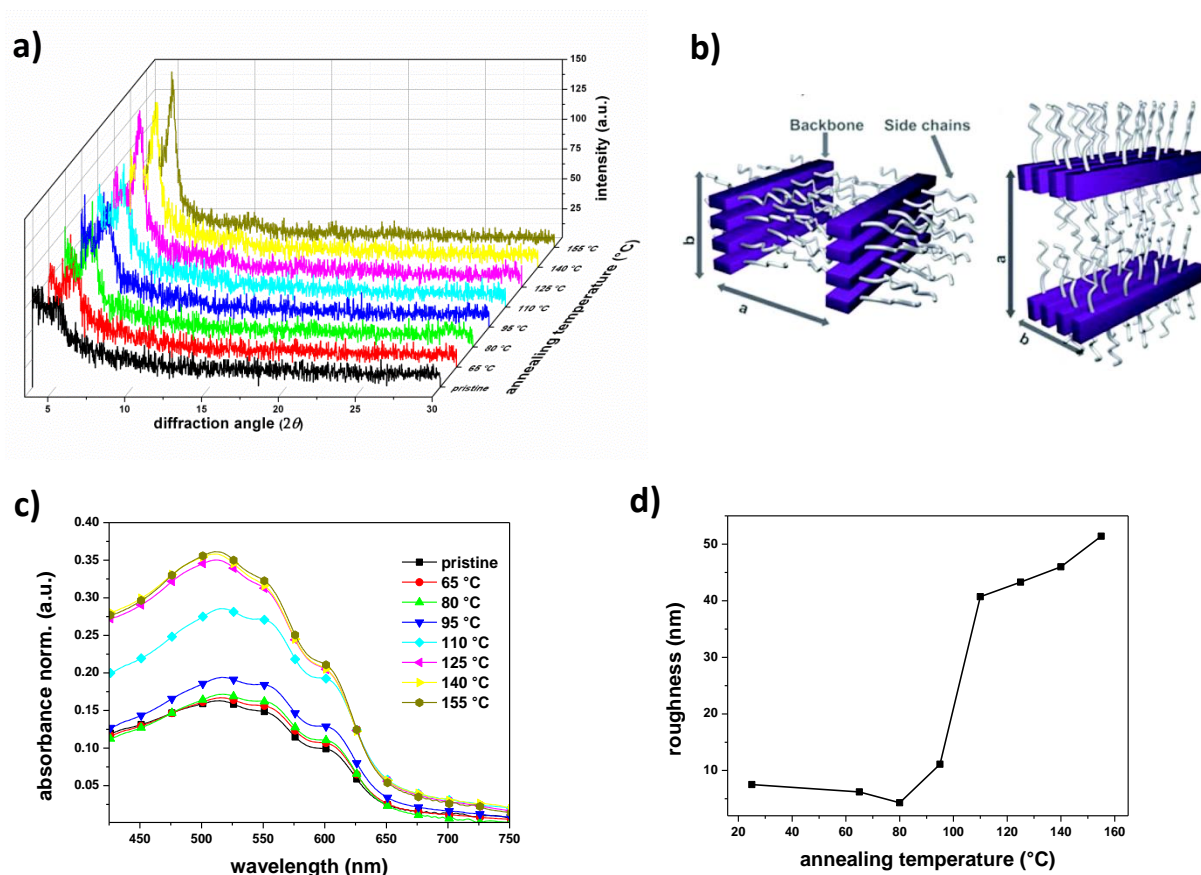
Figure 54: (a) XRD diffractogram of P3HT/PCBM composite particle films annealed at different temperatures. (b) Arrangement of crystalline P3HT on surfaces. (Left side) edge-on and (right side) face-on configuration; a and b are assign to interdigitation and stacking, respectively. The image is taken from the work of Collins.[245] (c) UV-Vis spectra of the corresponding annealed P3HT/PCBM composite particle films. (d) Surface roughness of the corresponding annealed P3HT/PCBM composite particle films, determined by atomic force microscopy (AFM). The pristine particle film is figured as 25 °C.

The UV-Vis spectra of the annealed films are shown in **Figure 54** (**c**). By increasing the annealing temperature the films show a large increase in absorption. Astonishingly, the emergence of the characteristic vibronic shoulders of ordered P3HT is not observed. Hence, a major part of the increased absorption is probably caused by light scattering at the film surface. The absence of the shoulders may be explained by the fact that the composite particles already exhibit a certain crystallinity, thus, an additional increase would be small and not observable. As already shown, the formation of PCBM agglomerates is accompanied by a change in surface structure. This has an effect on the surface roughness, as demonstrated in **Figure 54** (**d**). As a result of the melting, first, the particles coalesce and the surface becomes smoother until a minimal roughness at an annealing temperature of 80 °C is obtained. Applying higher temperatures, the appearance of PCBM agglomerates is accompanied by an intense increase in surface roughness. Note that light scattering at rougher surfaces is higher, as a consequence, less light passes through the sample and a higher absorbance is recorded. Comparing **Figure 54** (**c**) and (**d**), it is obvious that the absorption increases in the same manner as the surface roughness. This is a clear proof that the increase of the absorption is caused by the surface roughness.

4.2.3.2 Surfactant elution and layer thickness reduction

4.2.3.2.1 Langmuir trough made particle films

Using the "piston oil" effect, acceptable particle layers were obtained at higher SDS concentrations. Due to the high amount of surfactant at water/air interface, parts of the SDS are integrated inside the film by compression of the patches. The surfactant removal was conducted by dropping a few milliliters of ethanol on the particle layer. Afterwards the wafer was blown dry with nitrogen. Since this is a very short process, a dissolving of PCBM as described in **section 4.1.3** will not occur, as revealed in **Figure 55** (**a**) and (**b**). The surface structure of non-washed and ethanol-washed P3HT/PCBM composite particles does not differ significantly. However, the surfactant is completely removed from the particles, as demonstrated in **section 7.1.7**. As a result of the high SDS concentration, removing the surfactant leaves behind uncovered parts inside the particle layer, as shown in **Figure 55** (**c**).
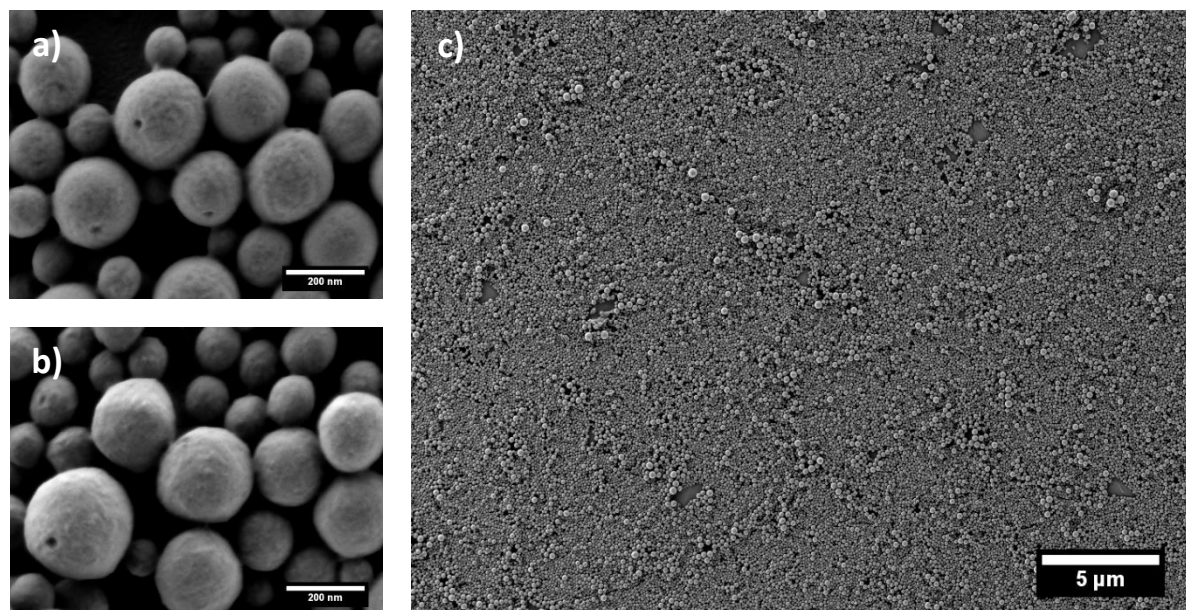
Figure 55: Effect of ethanol-washing on P3HT/PCBM composite particle films. (a) Non-washed and (b) ethanol-washed film. (c) Overview image of an ethanol-washed film, the elution of SDS leaves voids inside the particle layer. The particle films was made with an SDS concentration of 875 mg·L^{-1}.

The "piston oil" technique requires a huge amount of surfactant, therefore, the accompanying effect of the arising voids is unavoidable. As long as the particles are not larger, monodisperse, and feature covalently bound charges on the surface, better films cannot be obtained via Langmuir trough deposition. In view of short circuits, the washed particle films will probably not be suitable for a solar cell application. Nevertheless, in comparison to direct coating methods, the major benefit of Langmuir trough made particles films is that this method is independent from substrate properties. Problems concerning the wettability can be neglected.

4.2.3.2.2   Drop cast particle films

In contrast to Langmuir trough made particle films, using drop casting a micrometer thick multi-layer is formed. Due to the low charge carrier mobility in organic semiconductors, the layer must be reduced at least to approximately 500 nm.[22] To achieve this goal, two different approaches can be applied. The first one is the utilization of lower solid contents. Theoretically, lower amounts of particles should yield thinner films. However, it turns out that homogeneous drop cast particle layer requires a certain solid content, as specified in **section 7.1.8**. The second approach is to remove parts from an existing film. This means that more than 1 µm must be eliminated, optimally, without damaging of the remaining subjacent layer. As demonstrated in **section 4.2.3.1**, annealing causes a

diminution of the colloid layer by particle coalescence. In order to investigate the melting effect on micrometer-sized particle multi-layers, the drop cast films were annealed at 65, 80, and 95 °C. The corresponding CS-SEM images and the resulting film thicknesses are shown in **Figure 56**. The thermal treatment of the drop cast films effect that the average film thickness shrinks from initial 1750 nm to 1250 nm at 95 °C. It should be noted that CS-SEM requires a high voltage electron beam in which the materials decompose. Thus, the visual effect of melting of the particles during the annealing process can be only observed in a certain context, as described **section 7.1.9**.
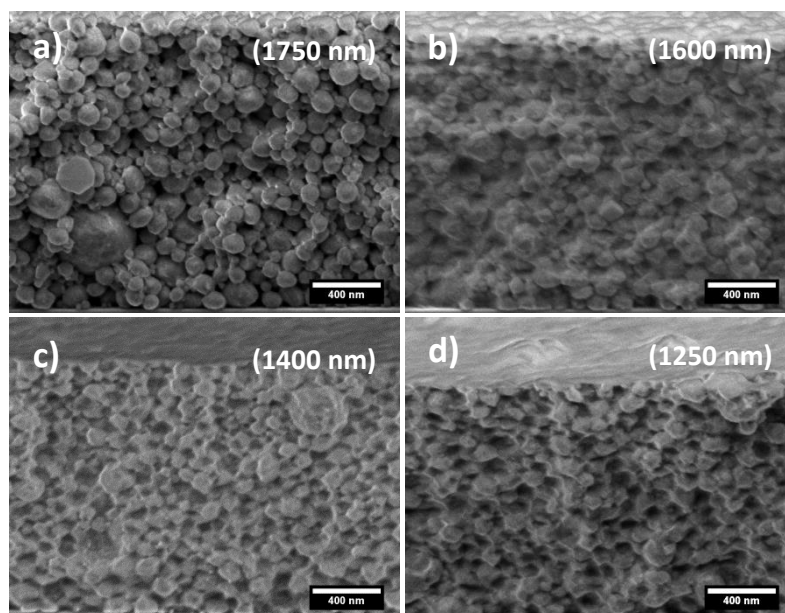
Figure 56: Annealing of drop cast P3HT/PCBM composite particle films; (a) pristine, (b) 65, (c) 80, and (d) 95 °C. The films are annealed for 12.5 min. The film thicknesses are denoted in brackets.

Another convenient way of decreasing the layer thickness is reported by Wang *et al.*,[253] removing protrudent PCBM agglomerates from an annealed P3HT/PCBM layer by using plasma. However, in case of Wang only a few nanometers were eliminated. Given by the fact that it was possible to remove only specific part from the colloid layer, this seems to be a practical method.

First of all, the behavior of P3HT and PCBM on plasma needs to be investigated. The treatment of pure P3HT and pure PCBM particles with argon plasma is shown in **Figure 57**. Upon argon plasma treatment, PCBM is ablated partly, whereas the structure of the P3HT particles is only slightly affected. Thus, PCBM is more sensitive to argon plasma. Besides the ablation, it is obvious that this kind of treatment has also an influence to the functionally of the semiconducting materials and thus an influence to the final performance of OPVs. These ramifications will be discussed in **section 4.3.7**.
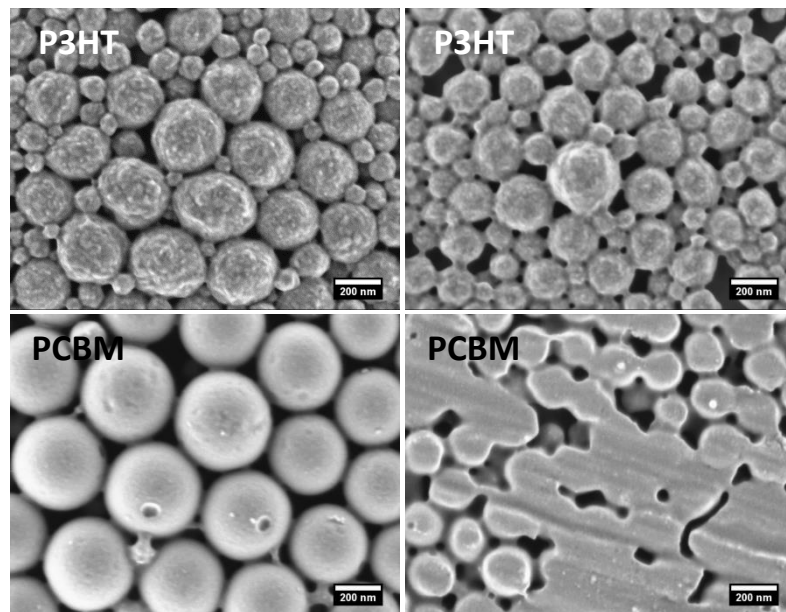
Figure 57: (Left column) untreated P3HT and PCBM particles and (right column) corresponding argon plasma treated particles. The particles were exposed to argon plasma for 20 s at 100 W and a pressure of 20 mbar.

The impact of different exposure times of argon plasma to the thickness of drop cast colloid films is shown in Figure 58 (**a**) to (**d**). The films were treated with argon plasma for 2.5, 5, 7.5, and 10 min. As expected, the plasma reduces the layer thickness. A pristine film with a thickness of around 1700 nm is lowered to approximately 650 nm after plasma treatment of 10 min. The material ablation is greatest in the first 2.5 min (400 nm), then the etching rate is lowered to 150 nm in the last 2.5 min. Arising from the CS-SEM images, is seems that only the film surface is affected, the subjacent layer is not influenced by the plasma and seems entirely intact. However, due to the described beam damage in CS-SEM, this observation cannot be clearly determined. The change in surface structure of the drop cast films during the plasma treatment is shown in Figure 58 (**e**) to (**i**). It can be deduced that smaller P3HT/PCBM composite particles degrade faster, as revealed by the fissures within the surface in Figure 58 (**e**). Due to the fact that PCBM is more sensitive to plasma, the remaining composite particles feature a clear P3HT domain structure, as shown in Figure 58 (**f**). In case of argon plasma, the domain structure is significantly better pronounced than using ethanol or hexane. By extending the exposure time, the colloids melt and the fissures close. After 10 min, an almost uniform layer is formed, as shown in Figure 58 (**i**). Since PCBM is more degraded, it is believed that the surface mainly consists of etched P3HT.

This attempt shows that plasma treatment can be used for a selective P3HT/PCBM film ablation. However, local differences in the degree of the plasma power may arise. This means that there are spots of a higher etching effect, leading to ablations far below the average film level.
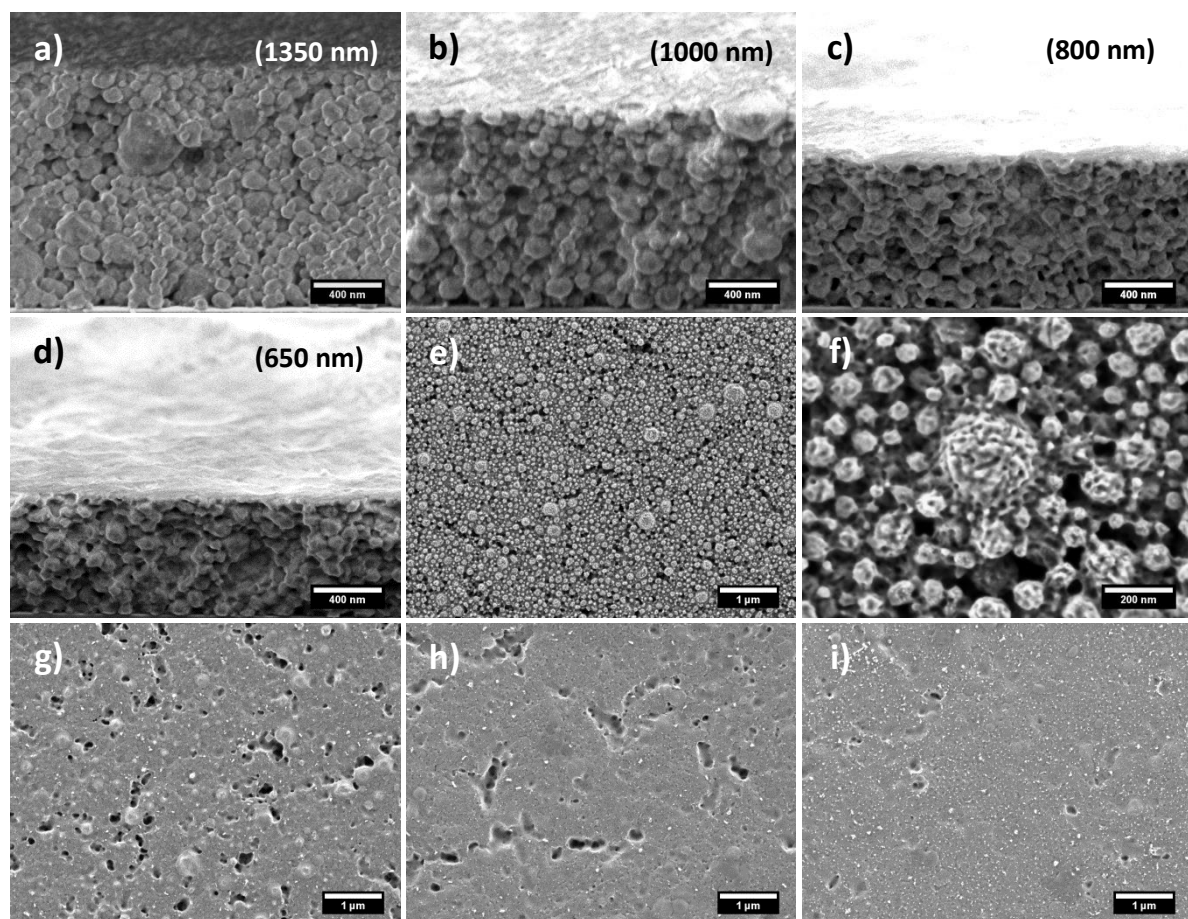
Figure 58: Effect of argon plasma treatment to drop cast P3HT/PCBM composite particle layers regarding film thickness and surface structure; (a, e and f) 2.5, (b and g) 5, (c and h) 7.5, and (d and i) 10 min. The films were exposed to argon plasma at 300 W and a pressure of 20 mbar. The film thicknesses are denoted in brackets.

To summarize, annealing and plasma treatment are suitable methods to decrease the film thickness. Indeed, plasma etching is more effective than thermal treatment, but entails more challenges. To achieve a better contact between the particles, an annealing step is required in any case. Thus, a combination of both methods should be the best way to obtain the desired film thickness of 500 nm. In order to ensure an effective ablation, firstly, the drop cast films are plasma treated, removing a large part of the colloid layers. Due to the described small local differences in the etching efficiency, the films are only exposed for 7.5 min to the argon plasma. Secondly, the fine tuning of the layer thickness is performed by annealing at temperatures from 80 to 155 °C.

The resulting films thicknesses and morphologies are shown in **Figure 59**. After plasma treatment and annealing at 80 °C, the layer thickness is lowered to 823 nm. Applying higher temperatures resulting in thicknesses of 614 nm at 110 °C and ultimately of 511 nm at 155 °C. Regarding the beam damage, the morphology of the layers annealed at 80 and 95 °C cannot be exactly determined. However, at 110 °C the film structure changes. According to **Figure 50** in **section 4.2.3.1**, this indicates the emergence of PCBM agglomerates. Analogous to the annealing experiment in **section 4.2.3.1**, in the further course of the annealing, large PCBM agglomerates can be observed. However, opposed to **section 4.2.3.1**, the PCBM agglomerates do not protrude from the surface. This can be explained by either the depletion of PCBM at the surface or the formation of an impenetrable P3HT layer.

It is assumed, films that exhibit a strong phase separation are not suitable for organic solar cells. Therefore, for a potential application in PBOPVs only the substrates annealed at 95 or 110 °C can be used. However, the thicknesses of these films are above the set limit of 500 nm.
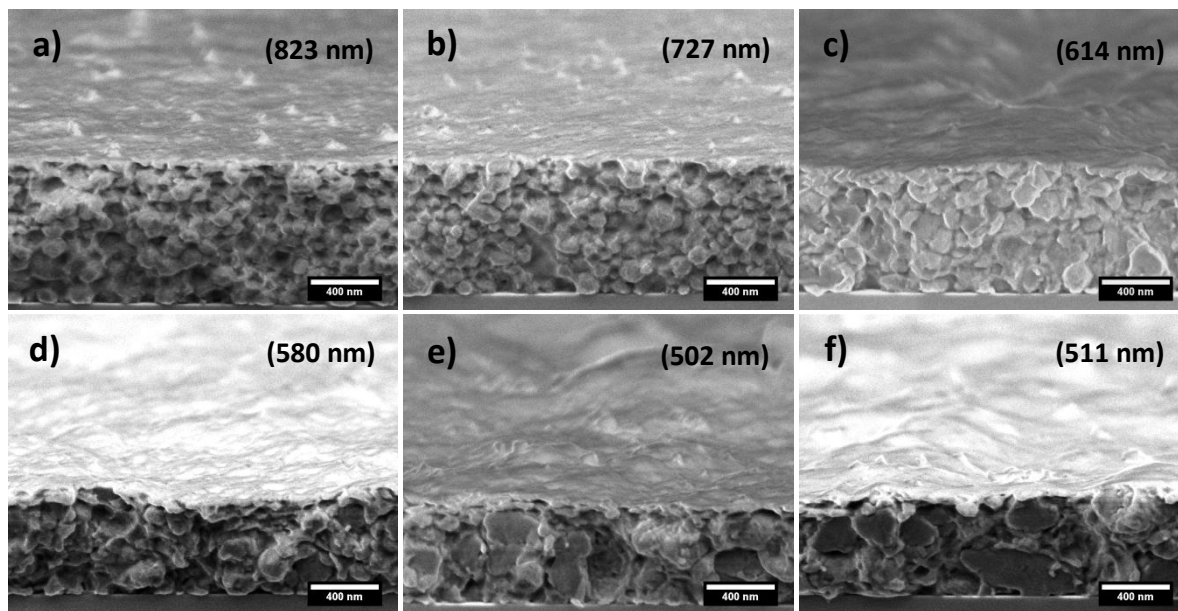
Figure 59: *CS-SEM images of plasma treated drop cast P3HT/PCBM composite particle films. Afterwards the films were annealed at (a) 80, (b) 95, (c) 110, (d) 125, (e) 140, and (f) 155 °C for 12.5 min. The films were exposed to argon plasma for 7.5 min at 300 W and a pressure of 20 mbar. The film thicknesses are denoted in brackets.*

Besides the layer thickness lowering, the other important reprocessing step of drop cast films is the removal of CTAC out of the particle layer. For this purpose, ethanol washing as introduced in **section 4.2.3.2.1** is also applied. As the surface of a plasma treated and annealed P3HT/PCBM

particle film is sealed by melted P3HT, the washing process is conducted before film ablation. Since drop cast particle layers are much thicker than films made by Langmuir trough deposition, it is a debatable point whether ethanol penetrates the entire colloid film.

Due to the large film thickness or rather the high amount of surfactant, CTAC can be detected by XRD. Prerequisite for reflections in XRD are crystalline domains. As known from **section 4.2.3.1**, in a P3HT/PCBM blend, this can be achieved by annealing at 110 °C or higher temperatures. CTAC is a small molecule and should be able to diffuse through the P3HT phase, forming crystalline structures. To ensure an adequate CTAC crystallization, the annealing procedure was conducted at 155 °C for 20 min. A diffractogram of pure CTAC and CTAC annealed within a P3HT/PCBM matrix is shown in **Figure 60** (**a**) The XRD investigation of a pristine and ethanol-washed drop cast film is shown in **Figure 60** (**b**). The major signals of CTAC are located at 2θ = 19°, 22.4° and 24.7°. In the pristine drop cast film, the mentioned three peaks and two other signals at 2θ = 14.5° and 15.7° can be identified. The origin of the latter signals is not exactly clear, since they are no reflections of CTAC, P3HT, PCBM, or even the annealed blend. However, in the ethanol-washed film the two unknown signals vanish, meaning these signals are likely impurities. The more important fact is that the CTAC signal at 2θ = 22.4° is nearly disappeared. This indicates that ethanol also removes the surfactant from a micrometer-sized drop cast particle film. A closer look to the signal at 2θ = 5° in **Figure 60** (**b**) reveals that the absence of the CTAC leads to a much better P3HT assembly upon annealing. This is consistent with the results of **section 7.1.13**; the existence of a surfactant within a P3HT/PCBM blend decreases the glass transition temperature.
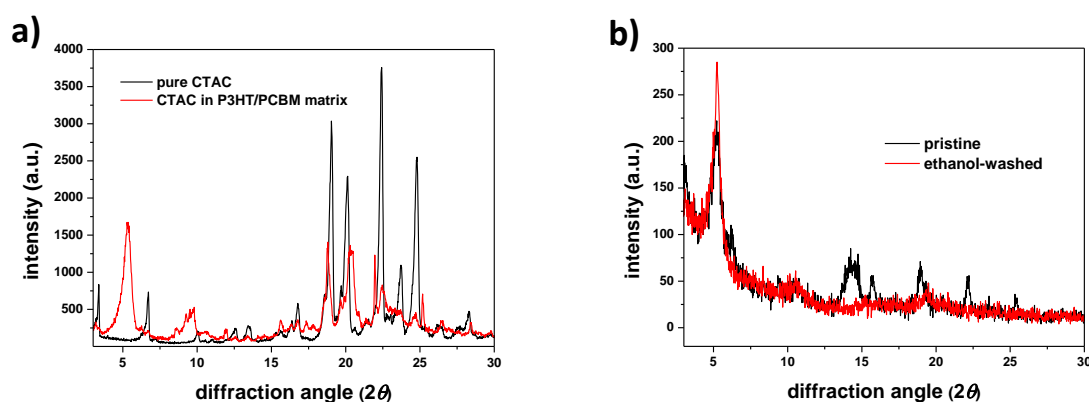
Figure 60: *(a) XRD diffractograms of CTAC and CTAC annealed in a P3HT/PCBM matrix. (b) XRD diffractograms of an annealed pristine and ethanol-washed drop cast P3HT/PCBM composite particle film. The annealing is conducted at 155 °C for 20 min.*

Regarding the quality of drop cast films, actually, the arising colloid films are more a kind of multi-layer-patches arrangements in the range of millimeters to centimeters. A homogeneous drying of the drop cast films is impeded by sudden jumps of the receding water evaporation front,[236] which leads to large micrometer-sized rifts, as shown in **Figure 61** (**a**). Nevertheless, the rifts should not impair the solar cell performance to a great extent, as the active area of one cell within a device is approximately 0.14 cm^2, compare **Figure 86** in **section 6.1.7**. The main problems are the smaller cracks within a patch, as shown in **Figure 61** (**b**). The cracks are probably caused by frictions in the particle layer during the drying process. Often these imperfections are too large and cannot be closed by annealing, as shown in **Figure 61** (**c**).
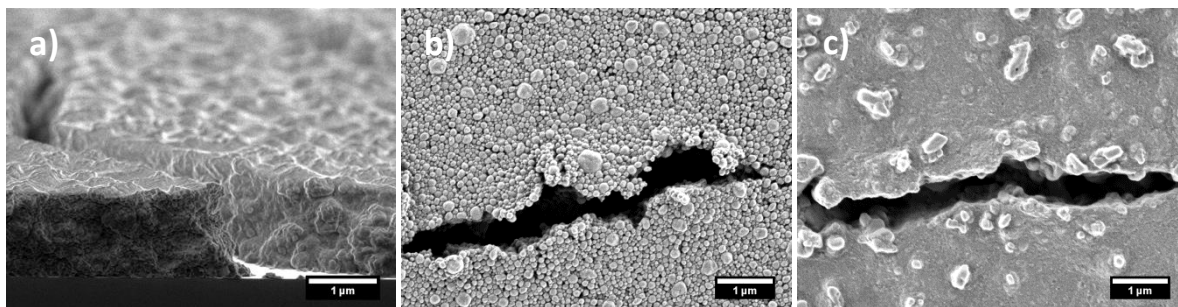
Figure 61: *(a) CS-SEM image of a mircometer-sized rift after annealing, (b) SEM image of a small crack before annealing, and (c) corresponding crack after annealing. The annealing is conducted at 125 °C for 12.5 min.*

Generally, the combination of plasma treatment and annealing leads to acceptable film thicknesses. However, in the view of the plasma etched P3HT on the film surface and the cracks in the particle layer, a reasonable application of drop cast particle films in OPVs is questionable, if not impossible. Nevertheless, this way of producing particle films is fast and simple, resulting in a very good colloid assembly, even with multimodal particles.

4.2.3.2.3 Spin coated particle films

Except of the SDS elution, spin coated colloid films required no further reprocessing step. On the basis of a non-washed and a washed particle film, the outcome of the ethanol elution process is shown in **Figure 62**. The SEM images show that short ethanol treatment has no influence on the quality of the particle film. The particle structure and the particle packing of the non-washed and the ethanol-washed layer are equal.
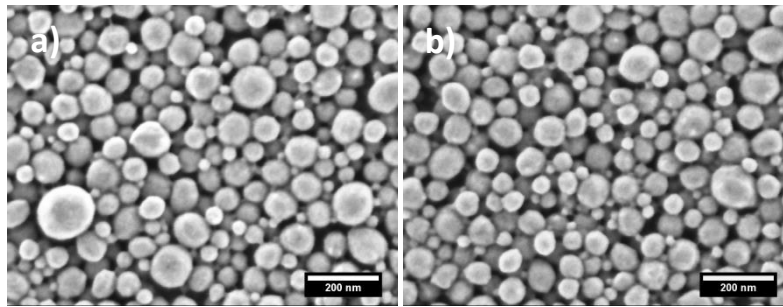
Figure 62: Effect of ethanol washing on a spin coated P3HT/PCBM composite particle layer. (a) Non-washed and (b) washed particle layer.

With respect to OPVs, spin coating seems to be the best and most promising method to achieve an active particle layer, as the coating procedure and the subsequent reprocessing step are fast, simple, and uncomplicated. In addition to that, the spin coated particle layers exhibit no voids, rifts, or cracks inside the film.

4.3 Fabrication of particle-based organic photovoltaics

Concerning film quality, particle packing, and reprocessing effort, spin coating is the best preparation technique for large-area, uniform, and close-packed colloid arrays. For this reason, spin coated P3HT/PCBM composite particle layers were used for the determination of the right PBOPVs fabrication conditions, regarding buffer layer, annealing temperature, and particle preparation temperature. The whole fabrication procedure of PBOPVs is illustrated in **Figure 63**. In comparison to SPOPVs, some preparation steps differ or are conducted elsewhere. The individual fabrication steps are described in detail in the followings sections.
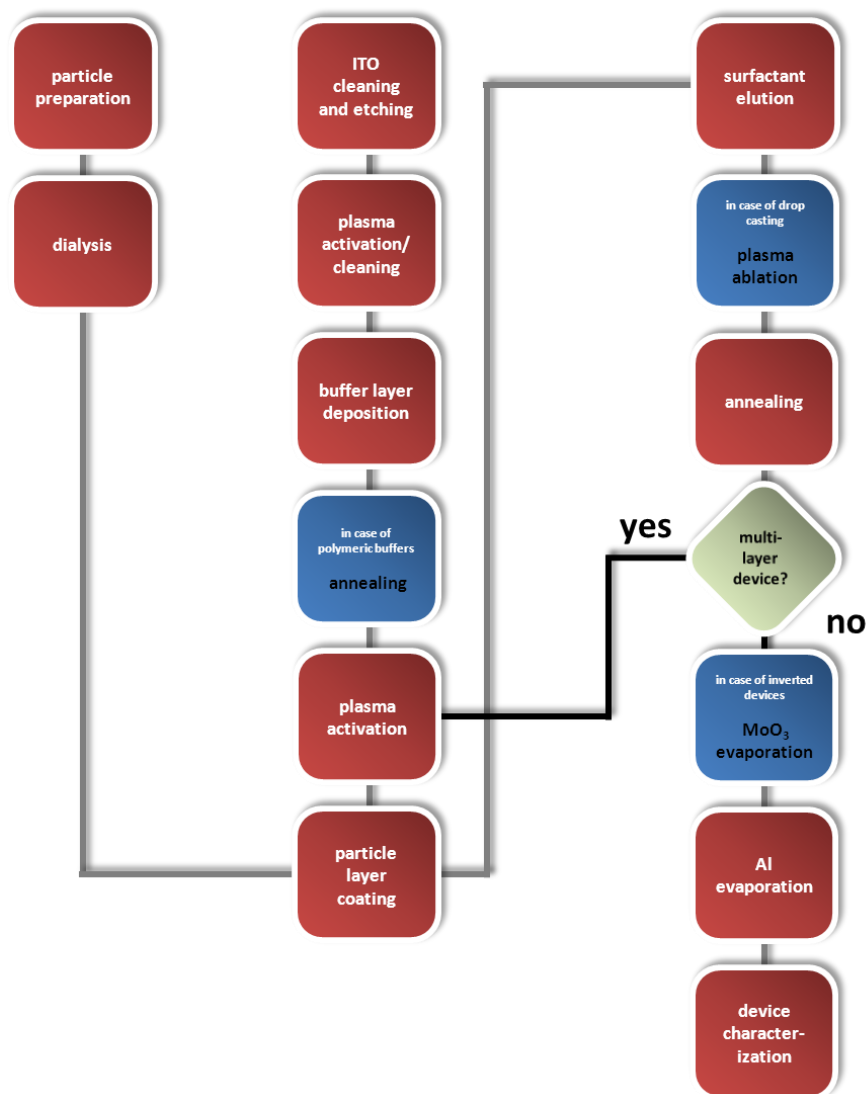
Figure 63: *Schematic overview of major processes occurring in PBOPV fabrication. Red boxes represent essential steps. The steps in the blue boxes are carried out only if certain requirements are met. The green box is assigned to the question: how to proceed in case of a multi-layer device. Referring to ITO etching and Al evaporation, a more descriptive illustration will be given in **section 6.1.7**.*

In general, the solar cell fabrication starts with ITO-coated glass wafers. The thickness of the buffer layers is in the range of 25 to 35 nm. Unless otherwise stated, the active particle layer is made by spin coating. In case of inverted solar cells, a 20 nm molybdenum oxide (MoO_3) layer is inserted by thermal evaporation between the active layer and the counter electrode. The counter electrode is a 100 nm thick aluminum layer, deposited by thermal evaporation. Unless otherwise stated, the P3HT/PCBM composite particles are prepared at 60 °C, stabilized with SDS, and feature a solid content of 3.33 wt.-%. The average particle diameter is 97 nm and the polydispersity is 0.29.

On the one hand, the aim of this section is to find the fabrication conditions for a functional PBOPV device and to study in which way the conditions influences the solar cells. On the other hand, factors for a potential improvement of the fabricated devices will be studied.

4.3.1 Determination of an adequate buffer layer

As described in **section 2.8.1**, PEDOT:PSS is used as a buffer layer in SPOPVs. This hole conducting buffer material is fully water soluble. In the case of SPOPVs, this is not an issue. However, by using aqueous dispersions, PEDOT:PSS partly dissolves during the spin coating process. For this reason, a more hydrophobic buffer material such as Plexcore is required. Analogous to PEDOT:PSS, Plexcore is also a hole conducting polythiophene based semiconductor. The chemical structure of Plexcore is given **section 7.1.1**. The protonated sulfonate groups of the Plexcore molecule result in a lower polarity, causing marginal water solubility and hence high water resistance. The water treatment of several potential buffer materials is examined in **section 7.1.10**. With respect to the hydrophobicity, P3HT itself might also be a suitable buffer material. Generally, other potential buffer materials are metal oxides, *e.g.* MnO_3 and zinc oxide (ZnO).[254, 255] However, analogous to PEDOT:PSS, MoO_3 is also partly removed by water during the spin coating process. Further, ZnO is an electron conductor and thus a hole blocking material. Using this material inverts the charge collection; holes move to Al and electrons towards ITO. If aluminum is used as the counter electrode, this kind of setup requires a hole conductor between the active layer and Al. Due to the feasibility of thermal evaporation, MoO_3 is often used.[256] The resulting new device setup is called an inverted solar cell; for further information see **section 7.1.12**. As introduced in **section 4.2.2**, the quality of particle films made by direct coating methods strongly depends on the wettability. Thus, owing to the good plasma resistance, ITO (without a buffer) should be also suitable for a good particle arrangement.

The question which buffer material is adequate for PBOPVs is mainly related to the quality of the resulting colloid film. Note that under this consideration, energetic aspects of the buffers layers are neglected. The buffer materials PEDOT:PSS, Plexcore, P3HT (dissolved in CB), and ZnO (dispersed in butanol) were applied by spin coating, whereas MoO_3 was vapor deposited. To obtain good film properties, the polymeric buffer materials require an additional annealing step after coating, which was performed at 150 °C for 15 min under nitrogen atmosphere. In order to achieve good wetting, the non-polar buffer materials, ZnO, and ITO must be plasma activated. Similarly to previous sections, this was done by argon plasma. Note that the polymeric buffer materials may be affected by the plasma. Due to the partial water solubility, PEDOT:PSS and MoO_3 were not activated.

The contact angles of milliQ water on pristine and plasma activated buffer substrates are listed in **Table 9**. The substrates were exposed to argon plasma for 20 s. In contrast to the plasma ablation shown in **section 4.2.3.2.2**, the plasma activation was accomplished at mild conditions (100 Watt and 20 mbar). Except P3HT, all buffer materials exhibit a complete wetting. Since P3HT is a very hydrophobic polymer, the plasma exposure only yields a contact angle of 60.4°. It was found that the activation effect occurs mostly in the first few seconds of the plasma treatment (see **section 7.1.11**). Hence, a further exposure to the plasma only damage P3HT. However, the contact angle can be decreased by using a dispersion, as shown in **section 4.2.2.2**. Thus, a P3HT/PCBM composite particle dispersion yield a contact angle of 28.6°.

Table 9: Contact angles of milliQ water on different buffer materials before and after plasma treatment of 20 s. The contact angle of a P3HT/PCBM composite particle dispersion on P3HT is denoted in brackets.

buffer layer	contact angle	
	pristine (°)	plasma activated (°)
Plexcore	51.5	complete wetting
P3HT	102.7	60.4 (28.6)
ZnO	68.2	complete wetting
ITO	43.8	complete wetting

The spin coating of P3HT/PCBM composite particles on the introduced buffer layers is shown in **Figure 64**. In view of the good water solubility, it is not surprising that poor particle films are obtained on PEDOT:PSS and MoO_3, as shown in **Figure 64** (**a**) and (**b**). The outcome on ITO is

considerably better, as shown in **Figure 64** (**c**). However, this particle layer is not perfectly closed. Generally, the colloid packing on the P3HT buffer is excellent, but some defect spots are present. In comparison to **Figure 47** (**c**) and (**d**) in **section 4.2.2.3**, this is probably not an effect of low solid content. Rather, it can be assumed that this is a consequence of the poor wetting. The best results are obtained with Plexcore and ZnO, as shown in **Figure 64** (**e**) and (**f**). These films are similar to the particle films spin coated on activated silicon, as shown in **Figure 47** (**e**) and (**f**). Besides the differences in particle packing, there are also significant differences in the layer thicknesses. The smallest thickness is obtained on ITO (98 nm). The thicknesses of the P3HT and Plexcore films are almost equal with 127 and 132 nm, respectively. The thickest layer is achieved by coating on ZnO, featuring a thickness of 176 nm.
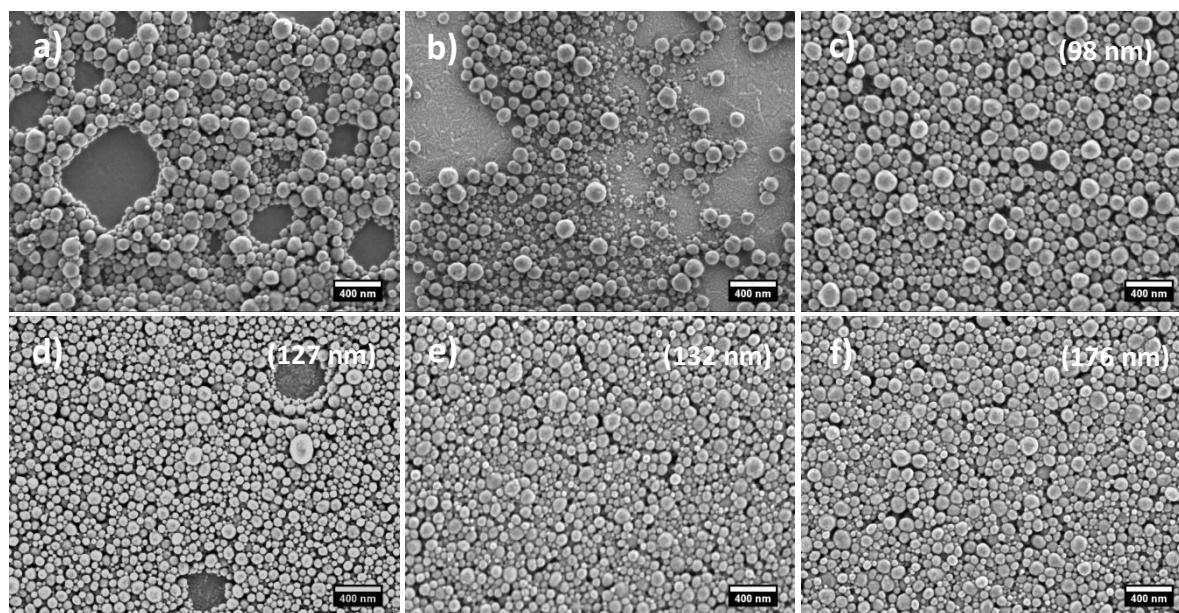
Figure 64: *Quality of spin coated P3HT/PCBM composite particle films on various buffer layers; (a) PEDOT:PSS, (b) MoO₃, (c) no buffer layer (pure ITO), (d) P3HT, (e) Plexcore, and (f) ZnO. The layer thicknesses are denoted in brackets.*

Despite the lack in quality of some particle layers, all films are used for solar cell fabrication. The spin coated particle films were annealed at 110 °C for 12.5 min. The reason for using this temperature is given in **section 4.3.2**. Due to the poor and non-closed particle layers, the PEDOT:PSS and MoO$_3$ devices exhibit a short circuit. The cells show large areas without any particles. In some parts, the buffer layer is completely dissolved. Hence, ITO and Al are shorted, making the device faulty. The scanning electron microscopy images of the annealed particle layers of ITO, P3HT, Plexcore, and ZnO are shown in **Figure 65** (**a**) to (**e**). Additionally, the resulting *IV* curves of these

solar cells are depicted in **Figure 65** (**f**). The corresponding characteristics of the functioning PBOPVs are shown in **Figure 66** (**a**).

The pristine colloid film on ITO exhibits small gaps between the particles. As **Figure 65** (**a**) and (**b**) reveal, annealing does not close these gaps completely. Similar to the PEDOT:PSS and MoO$_3$ devices, ITO is also directly connected to Al, causing a short circuit. The CS-SEM image in **Figure 65** (**c**) illustrates a defect spot in the P3HT device. It can be clearly seen that there is a P3HT buffer layer inside the spot. Thus, a short circuit is prevented. However, as consequence of the high number of imperfections, the *IV* curve only intersects the fourth quadrant of the Cartesian coordinate system for a short range, resulting in a very low PCE. The holes within the active layer may lead to general problems in charge transport, which are reflected in the linear behavior of the *IV* curve and the low FF. The annealed particle layers of the Plexcore and ZnO devices are closed and uniform, as shown in **Figure 65** (**d**) and (**e**). It is no wonder that the devices, exhibiting the best initial particle film quality, have the highest PCE. The Plexcore cell has an efficiency of 0.29% and the ZnO device a PCE of 0.53%. The two *IV* curves are solar cell-like, showing the typical diode characteristic. In contrast to the currently best P3HT/PCBM SPOPVs with a efficiency of 5%,[24, 183] the prepared POPBVs have a relatively small PCE. Nevertheless, they are functional OPVs. A deeper inspection of the *IV* curves and a detailed comparison with SPOPVs will be given in **section 4.3.8.3**.
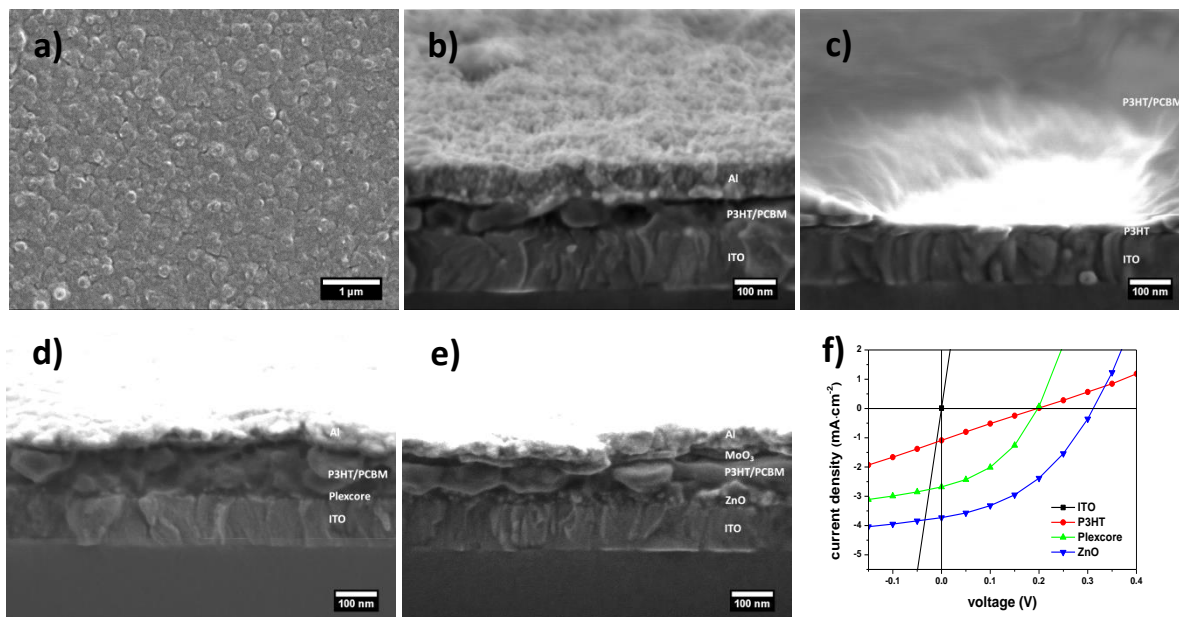
Figure 65: SEM and CS-SEM images of PBOPVs made of different buffer layers; (a and b) no buffer layer (pure ITO), (c) P3HT, (d) Plexcore, and (e) ZnO. Regarding the thickness of the individual layers, due to different charging by the electron beam, the materials may be deformed in the CS-SEM image. (f) IV curves of the corresponding PBOPV devices.

Except the FF, the inverted structure generally offers significantly better characteristics. There may be morphological, energetic, and structural reasons for this difference. It is assumed that the phase separation of P3HT/PCBM particles is the same on all buffer layers. According to **Figure 53** in **section 4.2.3.1**, at advanced phase separation, the PCBM crystals align on top and P3HT at the bottom of the substrate. As shown in **Figure 51** in **section 4.2.3.1**, there is a small phase separation of P3HT and PCBM upon annealing before the PCBM agglomerates are formed. Thus, it may be possible that this separation occurs on a small-scale even at lower temperatures. However, in inverted devices the electrons move towards ITO and the holes to aluminum, making the opposed phase separated structure favorable. Since ZnO devices have a better PCE, this scenario cannot explain the discrepancy in the solar cell characteristics. As mentioned in **section 2.8.3**, at larger forward biases, the electrodes start to inject charges into the device, which can be observed under dark conditions. The dark current is referred to as a reverse bias leakage current. In efficient devices, the photogenerated current needs to overcome the dark current. In inverted devices the charge transport is reversed, hence, the energetic aspects change (see **section 7.1.12**). In comparison with the common setup, inverted devices have increased energetic gaps for holes (from $HOMO_{P3HT}$ to the corresponding electrode) and electrons (from $LUMO_{PCBM}$ to the counter electrode). This may constitute a higher barrier for the injection or rather an attenuation of the leakage current, shifting the dark current to larger forward biases. Finally, this leads to a higher net photocurrent. The dark current of the ZnO device is shifted to a higher bias, as shown in **Figure 66** (**b**). This confirms the theory of the attenuation of the leakage current inside inverted devices. However, the effect is minor. Hence, it is questionable whether this is the main reason for the higher J_{SC} of the ZnO device. Another factor, also influencing the photocurrent, is the thickness of the active layer. As mentioned above, spin coating on ZnO leads to a thicker film. After annealing the melted particle layer of the ZnO device is still thicker than film of the Plexcore device. The thickness of the active layer in the ZnO device is 83 nm, whereas in the conventional Plexcore cell it is 63 nm. A thicker active layer harvests more light, leading to more excitons, resulting in a higher J_{SC}. As will be shown in **section 4.3.8.3,** the differences in V_{OC} of can be also explained by the amount of J_{SC}.

Even though the inverted OPVs exhibit a higher efficiency, further solar cell testing will be performed with Plexcore devices. These devices also offer an acceptable PCE, but are much easier to prepare.

a)

substrate	V_{OC} (V)	J_{SC} (mA·cm^{-1})	FF	PCE (%)
P3HT	0.19	1.09	0.17	0.06
Plexcore	0.20	2.68	0.39	0.29
ZnO	0.31	3.77	0.43	0.53

b)
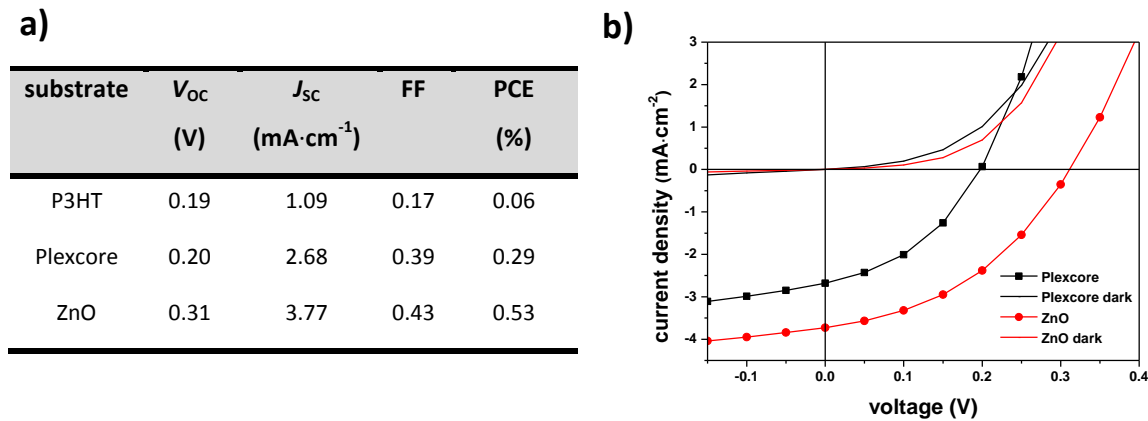
Figure 66: (a) Solar cell characteristics of PBOPVs coated on P3HT, Plexcore, and ZnO. (b) Comparison of the IV curves of the Plexcore and the ZnO device under dark and illuminated conditions.

4.3.2 Determination of an adequate annealing temperature

In order to eliminate the low contact between the particles in the pristine colloid layer, annealing is required. As shown in **section 4.2.3.1**, during the thermal treatment the domain size and the crystallinity of the films change drastically; both increase at elevated temperatures. Efficient PBOPVs require a certain degree of melting for ameliorate the contact, a low phase separation for minimal exciton losses, and an adequate crystallinity for good charge carrier mobility. From the data in **section 4.2.3.1** it is obvious that the optimal annealing temperature is in between 80 and 110 °C. At these temperatures the colloids are melted, giving acceptable phase separation and P3HT ordering. The subsequent solar cell characteristics and *IV* cures of Plexcore devices, annealed between 65 and 155 °C, are shown in **Figure 67**.

The best solar cell efficiency was found at an annealing temperature of 110 °C, here, the PCE is around 0.35%. The characteristics of the 110 °C device are in the same range as for the Plexcore device shown in the previous section. Annealing at 95 °C leads to an efficiency of 0.14%. Due to the low contact and the insufficient material order, the devices annealed at lower temperatures show very low PCEs. Annealing until 110 °C, the more the particles are melted, the higher is the PCE. At temperatures higher than 110 °C, the phase separation increases and PCBM agglomerates are formed. This causes an exciton loss, which leads also to poor efficiencies. Note that the large V_{OC} values of the poor devices are a result of the flat *IV* curves and can be neglected. Since the best annealing conditions are achieved at 110 °C, further investigations will be carried out by using this annealing temperature.

a)

temperature (°C)	V_{OC} (V)	J_{SC} (mA·cm^{-2})	FF	PCE (%)
pristine	0.38	-	0.18	-
65	0.26	0.11	0.19	0.006
80	0.34	0.15	0.17	0.014
95	**0.27**	**1.41**	**0.35**	**0.143**
110	**0.27**	**2.83**	**0.41**	**0.347**
125	0.26	0.25	0.15	0.020
140	0.30	0.07	0.20	0.004
155	0.43	0.09	0.17	0.008

b)
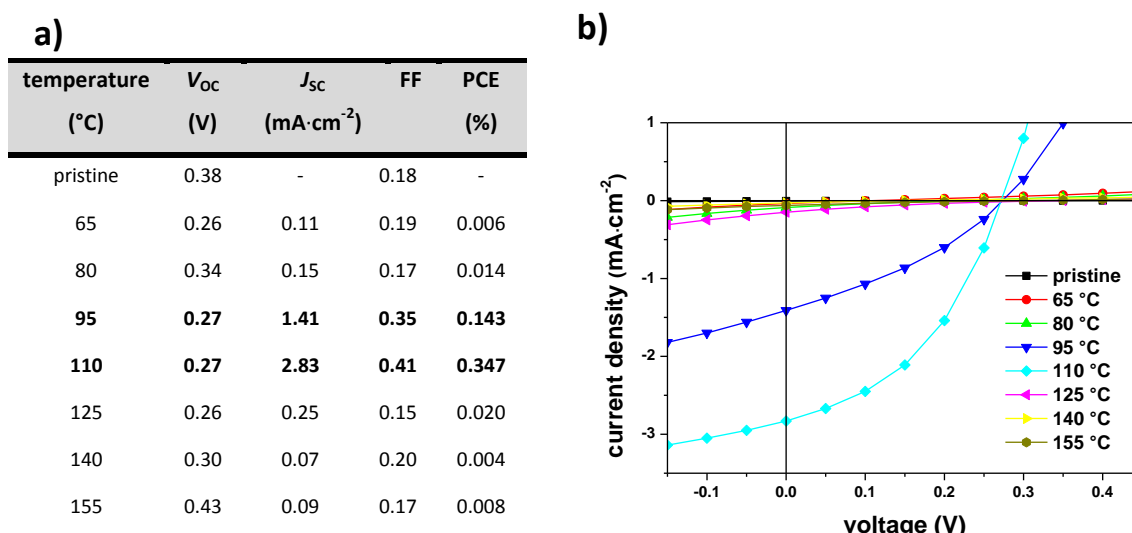
Figure 67: *(a) Solar cell characteristics of Plexcore devices annealed at various temperatures. The bold values label the most efficient OPVs. Dashes in the pristine device are assigned to values that are far below the specified range. (b) IV cures of the corresponding devices.*

As known from the SEM and the CLSM images in **section 4.2.3.1**, at an annealing temperature of 110 °C the active layer features large PCBM aggregates, indicating a massive loss of excitons. In addition, the high surface roughness causes a loss of light absorption by scattering. However, according to the TRPL results, strong PL occurs not until 125 °C. Below this temperature, the PL is almost on the same level. In spite of the latter, it is astonishing that the best PCE is acquired at an annealing temperature of 110 °C. In fact, 95 °C would be much more plausible.

A simple explanation for this mismatch is the discrepancy in the annealing parameters of the used standard system (silicon) and the solar cell system. In **section 4.2.3.1** the colloids were coated on silicon wafers. In case of OPVs, the particles were coated, irrespective of the thin buffer layer, on an ITO glass wafer. Since annealing was conducted on a hot plate, it depends on the thermal conductivity of the substrates. Besides, the substrate thickness must also be considered. The silicon wafers have a thermal conductivity of approximately 150 W·m^{-1}·K^{-1} and thickness of 0.7 mm. Conductivity and thickness of ITO substrates is around 1 W·m^{-1}·K^{-1} and 1.1 mm, respectively.[257] Thus, it can be suspected that the degree of melting at a fixed temperature differs strongly between silicon and ITO. In order to test this assumption, the temperatures during the annealing process on both substrates were verified. The temperatures are listed in **Table 10**. As expected, the temperatures on Si are higher compared to those on ITO. At lower set temperatures, the real temperatures on both wafers nearly coincide. From 95 °C onwards, the difference in surface

temperature becomes larger. Above 125 °C, the disparity is around 10 °C. In general the temperature on the plate is approximately 10 °C above the set temperature. Due to the excellent thermal conductivity coefficient in combination with the thin substrate, the temperatures of the silicon wafer and the hot plate are almost equal.

Table 10: *Discrepancies in surface temperatures of hot plate, silicon wafer, and ITO glass substrate at various set temperatures during the annealing process.*

set temperature (°C)	temperature on hot plate (°C)	temperature on Si (°C)	temperature on ITO glass (°C)
65	68	67	66
80	88	85	82
95	104	101	96
110	121	118	111
125	136	133	126
140	150	149	140
155	167	164	154

Moreover, it should be noted that the glass substrates, used for CLSM investigations, are much thinner than the ITO glass wafers (< 0.2 mm). This balances the poor thermal conductivity and makes the surface temperatures similar to those of the silicon wafers. Thus, there is no mismatch between SEM and CLSM images shown in **section 4.2.3.1**.

Due to the discrepancy in the surface temperature, the results of **section 4.2.3.1** are not consistent with solar cells efficiencies. Note that the general trend during the annealing process is the same. It appears that as a result of the lower thermal conductivity and larger thickness, the degree of melting on ITO glass substrates fall behind the degree of melting on silicon wafers. This explains why the highest efficiency is obtained at 110 °C. The SEM images of P3HT/PCBM composite particles annealed on ITO/Plexcore substrates are shown in **Figure 68**. The observed trend resembles the annealing experiments performed on silicon. However, the particles melt to a lesser extent. Here, also at 95 °C the first PCBM agglomerates are formed. The crucial difference is that the number and size of the PCBM agglomerates are smaller and does not increase significantly up to 110 °C. Hence, the cells have adequate PCEs at these two annealing temperatures. Applying higher

temperatures leads to a PCBM crystal growth. In general, the pure PCBM phases have a totally different appearance. Instead of many small crystals, only a few and large agglomerates are formed.
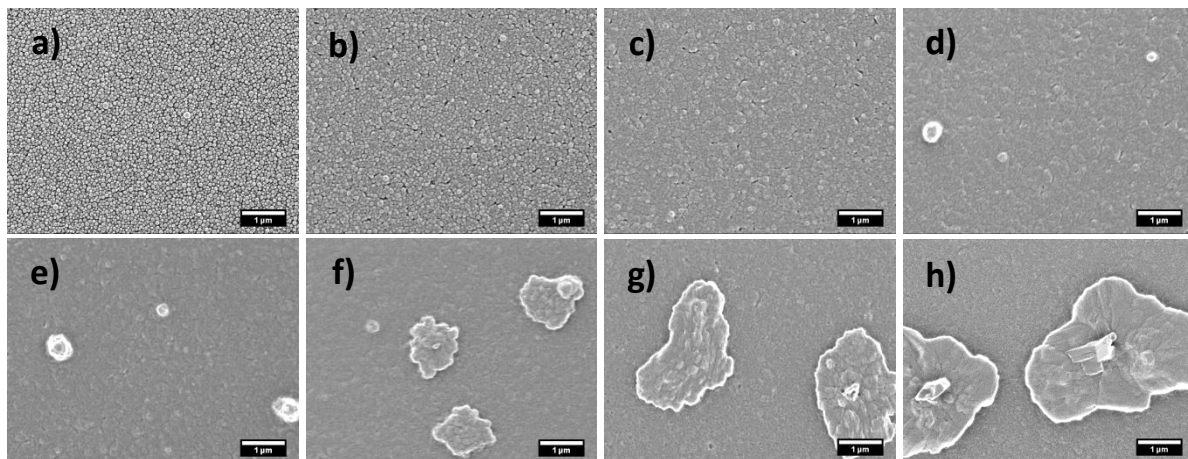
Figure 68: *Effect of annealing to P3HT/PCBM composite particles spin coated on ITO/Plexcore substrates; (a) Pristine (b) 65, (c) 80, (d) 95, (e) 110, (f) 125, (g) 140, and (h) 155 °C.*

4.3.3 Influence of particle preparation temperature

In particle preparation the variation of the evaporation temperature causes a change in domain size and crystallinity. In **section 4.3.2** it was argued that the solar cells efficiency depends on these two parameters. The particles shown in **section 4.1.3** already offer different levels of phase separation and material order. The question arises, how these particles react during the annealing process and how the PCE is influenced. For this investigation particles prepared at 30, 60 and, 90 °C were used. The characteristics of these particles are listed in **Table 11**.

Table 11: *Average diameter and polydispersity of P3HT/PCBM composite particles prepared at 30, 60, and 90 °C.*

evaporation temperature (°C)	Diameter (nm)	polydispersity
30	159	0.32
60	144	0.32
90	148	0.30

The morphology of the particles prepared at 30 and 90 °C has been already determined in **section 4.1.3**. Their structure is again illustrated in **Figure 69**. The morphology of particles prepared at 60 °C

(after ethanol treatment) is also illustrated. The average P3HT domain size of the particles prepared at 60 °C is 36 nm. Thus, P3HT domains are in between the dimensions of particles prepared at 50 °C (43 nm) and 70 °C (24 nm). The estimated material order must also be between the crystallinity of the particles prepared at 50 and 70 °C.
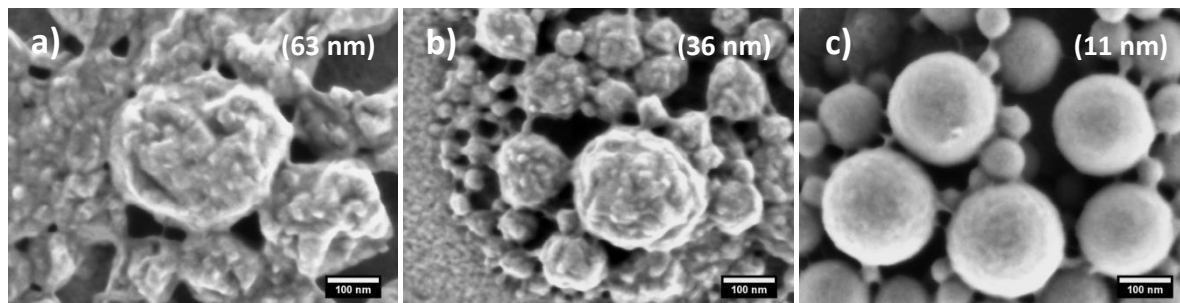
Figure 69: *Morphology of ethanol treated P3HT/PCBM composite particles prepared at (a) 30, (b) 60, and (c) 90 °C. The average P3HT domain sizes are denoted in brackets.*

In all cases, spin coating of the composite particles on ITO/Plexcore substrates leads to close-packed colloid arrays, as shown in **Figure 70**.
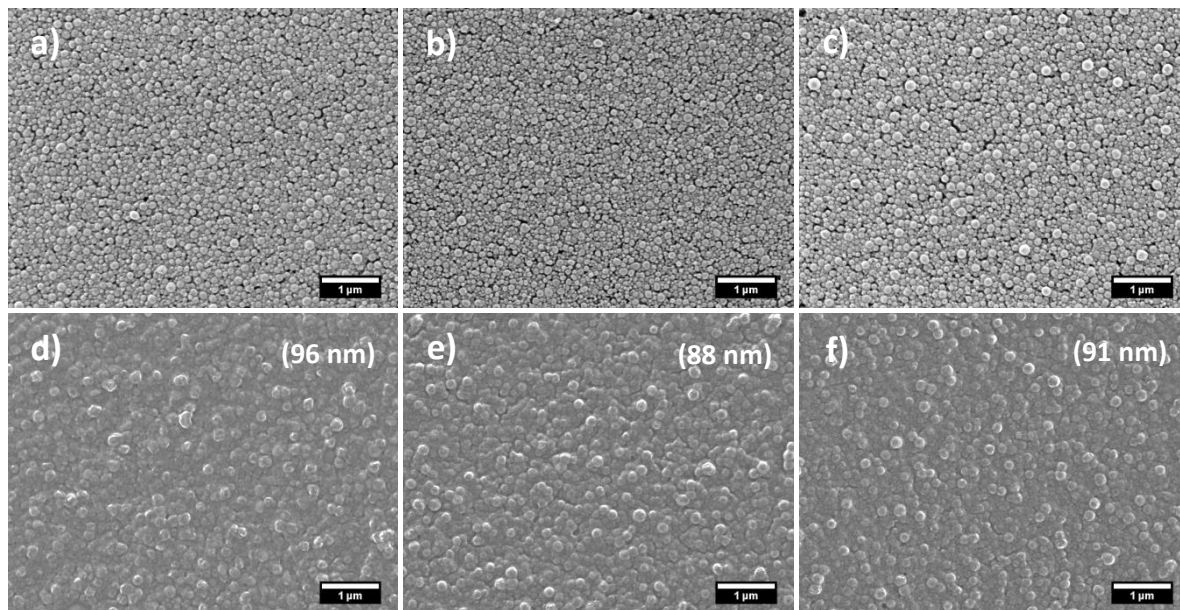
Figure 70: *P3HT/PCBM composite particle films on ITO/Plexcore substrates. (Upper row) spin coated particle layers and (lower row) eventual annealed particle films. The particles are prepared at (a and d) 30, (b and e) 60, and (c and f) 90 °C. The film thicknesses are denoted in brackets. The annealing is conducted at 110 °C for 12.5 nm.*

The effect of thermal treatment is also similar in all cases. After annealing, the particles are in close contact and almost no gaps remains. In comparison to the Plexcore device shown in **section**

4.3.1, due to the larger initial particle diameters, the final annealed film thicknesses are thicker. With approximately 90 nm, the thicknesses are in range of the inverted ZnO device.

The solar cell performances of the present devices are shown **Figure 71**. The best efficiency is 0.52%, achieved at a particle preparation temperature of 60 °C. This PCE is much higher than the efficiency of the introduced Plexcore devices. In these devices the particles were also prepared at 60 °C. Hence, the only parameter that was changed was the particle size and consequently the film thickness. Therefore, the reason for the increased efficiency must lie in the thicker active layer, leading to better light harvesting. The other two kinds of PBOPVs show significantly lower PCEs of 0.15% and 0.24% for devices prepared at 30 °C and 90 °C, respectively. Particle size, layer thickness, annealing effect, and quality of the melted films are similar. Consequently, the differences in the device performance arise from the morphology and crystallinity, set by the particle preparation conditions.

a)

temperature	V_{OC}	J_{SC}	FF	PCE
(°C)	(V)	(mA·cm⁻²)		(%)
30	0.20	1.71	0.34	0.15
60	0.27	3.56	0.41	0.52
90	0.26	2.36	0.31	0.24

b)
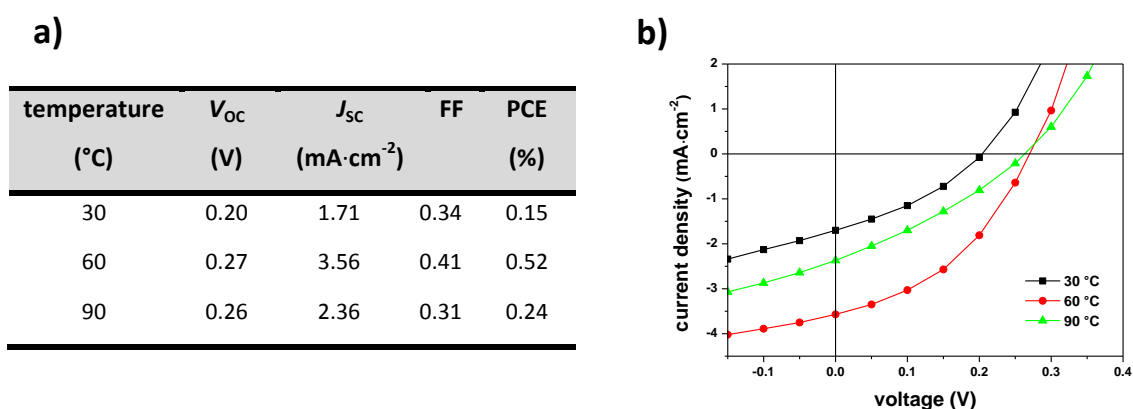
Figure 71: (a) Characteristics and (b) IV curves of PBOPVs made of P3HT/PCBM composite particles prepared at various temperatures.

As reported in **section 4.2.3.1**, the increase of the P3HT domain sizes in the course of particle melting is relatively small until PCBM agglomerates are formed. In the following consideration, it is assumed that the relative increase of the domain sizes is similar in all cases. The same applies to the material order, a constant crystallinity increment is assumed in all cases. The domain size and the material order are inversely proportional to the evaporation temperature. Based on these preconditions, the device prepared at 30 °C should feature large domains and a high material order, whereas the 90 °C device should exhibit small domains and a low crystallinity. The properties of the 60 °C device are expected in between. This assumption is confirmed by **Figure 72**, showing XRD diffractograms, TRPL dynamics, and CLSM images of the devices. The device prepared at 30 °C shows

minimal PL, but also minimal crystallinity. The device prepared at 90 °C features exactly the opposite and the device prepared at 60 °C is in between. To recall, good solar cells require small domains and a high material order. OPVs consisting of particles made at 30 °C and 90 °C provide only one characteristic. Thus, it is not surprising that the best conditions are obtained with particles prepared at 60 °C, which offer a compromise between domain size and crystallinity.
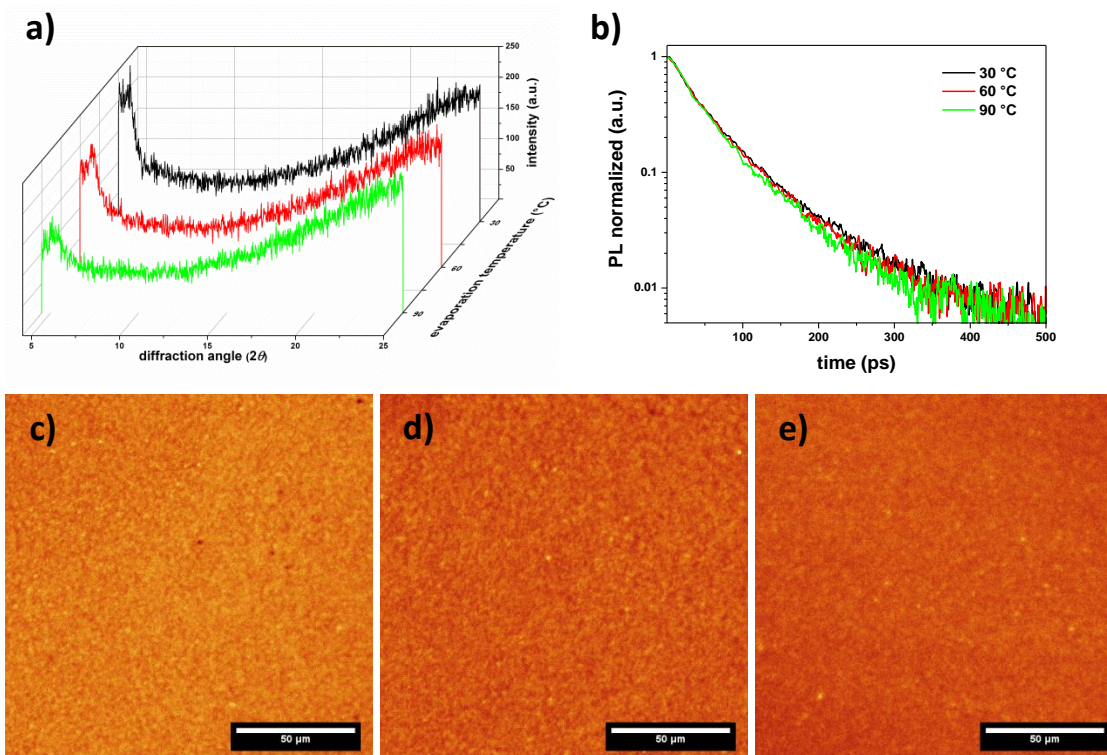
Figure 72: *(a) XRD diffractogram and (b) TRPL dynamics of PBOPVs made of composite particles prepared at various temperatures. (c to e) Corresponding CLSM images of the particle layers prepared at (c) 30, (d) 60, and (e) 90 °C.*

Regarding the XRD diffractogram shown in **Figure 72** (**a**), the amorphous halo at higher diffraction angles is not a consequence of supersized π-π stacking. In this case, the films were measured on ITO glass wafers. The halo is caused by the glass, having a wide signal between 2θ = 15 and 40°.

4.3.4 Determination of an adequate annealing time

In literature, device annealing of SPOPVs is conducted before the counter electrode is evaporated. As ascertained in **section 4.2.3.1**, the particle layer shrinks during the annealing process. Hence, this procedure may not be applied for PBOPVs. The CS-SEM images of devices annealed before and after

aluminum evaporation are shown in **Figure 73** (**a**) and (**b**). In principle, the pre-annealed device represents the previously introduced Plexcore PBOPVs. The pre-annealed device exhibits a smooth and even aluminum electrode, since Al is evaporated on melted particles. Owing to the shrinkage of the active layer in the post-annealed device, the aluminum layer also undergoes a subsidence process. In the course of this process, the layer is deformed. Parts of Al pile up, resulting in an undulating electrode. This affects the contact between the active layer and the electrode. The device characteristics and *IV* curves are given in **Figure 73** (**c**) and (**d**). The characteristics of the pre-annealed device are similar to the devices presented in the previous sections. Also the *IV* curve shows the typical trend. This demonstrates a good reproducibility of the entire PBOPV fabrication process. The PCE of the post-annealed device is with 0.03% very low. This is attributed to poor charge transport and extraction due to the reduced contact between active layer and the bumpy aluminum electrode. The phenomena of poor interfaces will be revisited in another context in **section 4.3.8.3**.

substrate	V_{OC}	J_{SC}	FF	PCE
	(V)	(mA·cm^{-1})		(%)
pre-annealed	0.23	2.61	0.38	0.31
post-annealed	0.26	0.35	0.21	0.03
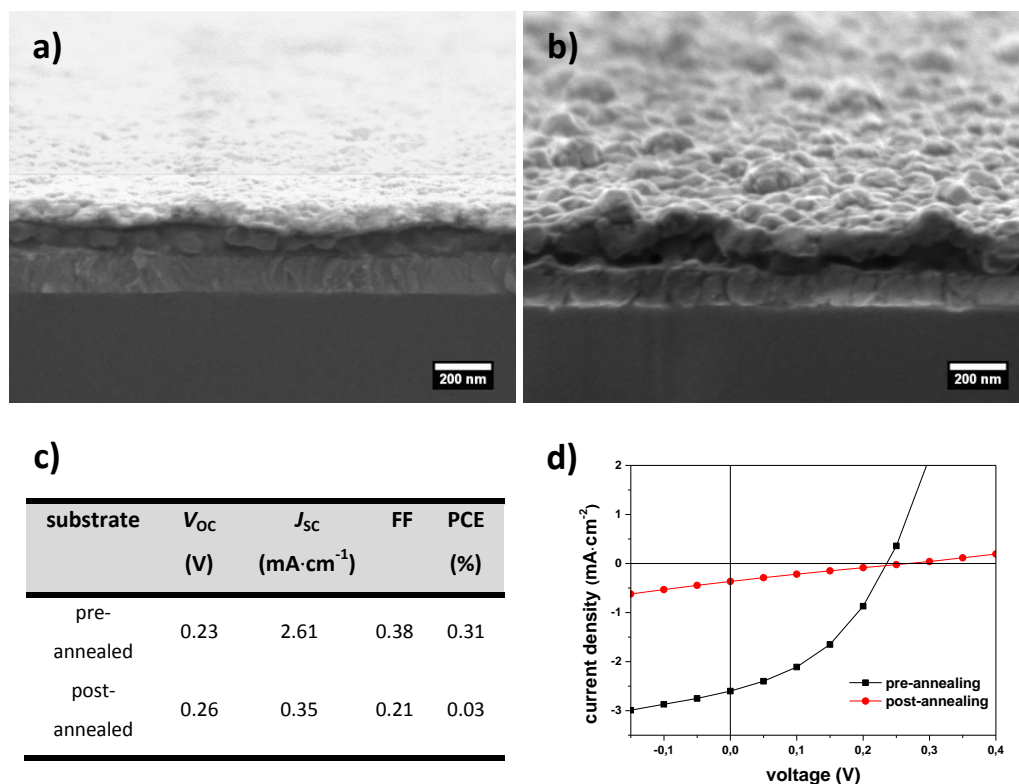
Figure 73: CS-SEM images of PBOPVs; the annealing process is conducted (a) before and (b) after the aluminium evaporation. The annealing process is conductued at 110 °C for 12.5 min. (c) Characteristics and (d) IV curves of the corresponding PBOPVs.

4.3.5 Necessity for surfactant elution

In spite of dialysis, there is still a residual amount of surfactant inside the dispersion. Moreover, a complete removal is undesired, as a certain amount of surfactant is needed to prevent coalescence and to maintain the dispersion character. This implies that in coated colloid layers there is still some surfactant present. As reported in **section 4.2.3.2.1**, ethanol washing is an effective procedure to remove the surfactant from the colloid arrays. The elution process is applied before annealing, at this fabrication step the particle film is porous and the surfactant is completely washed out. In **section 4.2.3.2.2** it has been shown that residual surfactant disrupts the crystallinity of P3HT during the annealing process. This has also a great influence on the P3HT/PCBM film morphology. A SEM image of an annealed non-washed P3HT/PCBM composite particle film is shown in **Figure 74** (**a**). The annealing was conducted at 110 °C. Opposed to **Figure 68** (**e**) in **section 4.3.2**, the existence of SDS leads to the formation of a large number of PCBM agglomerates. The surfactant reduces the T_g of a P3HT/PCBM blend from 52 to 33 °C, as clarified by differential scanning calorimetry (DSC) measurements shown in **section 7.1.13**. Thus, the phase separation of a non-washed device is much more elevated compared to a washed device annealed at the same temperature. Moreover, SDS is an ionic surfactant. Considering the charged head group and the counterion, it is highly probable that SDS acts as a trap for the photogenerated charges. The high exciton loss caused by the film morphology and the charge recombination inside the active layer diminishes the overall device quality and FF, as illustrated by the flat run of *IV* curve in **Figure 74** (**b**). The non-washed device features only 0.04% PCE and a FF of 0.2. This shows that surfactant elution is an essential procedure in PBOPV fabrication. To allow a comparison with an eluted PBOPV device, the device annealed at 110 °C from **section 4.3.2** acts as a reference in the *IV* illustration.
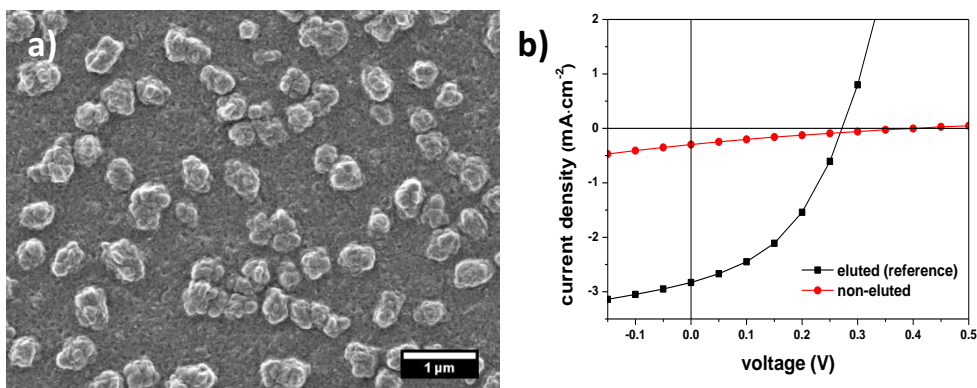
Figure 74: *(a) Non-washed P3HT/PCBM composite particle layer on ITO/Plexcore, annealed at 110 °C for 12.5 min. (b) Corresponding IV curve including reference.*

4.3.6 Devices made by Langmuir trough deposition and drop casting

As indicated in **section 4.2.3.2.1** and **4.2.3.2.2**, particle films made by Langmuir trough deposition and drop casting do not offer ideal properties for an application in a solar cell. For the sake of completeness, devices made by these two coating methods are briefly discussed in this section. Basically, the main deficiency of the trough made films is the voids in the particle packing caused by incorporated SDS. The shortcomings of the drop cast films are probably the damage of the semiconductors caused by plasma etching as well as the rifts and cracks inside the particle layer. The voids and holes in the active layer that cannot be closed by annealing are potential hotspots for short circuits. Thus, in addition to the common device structure by using Plexcore, the inverted setup is also applied to the Langmuir trough made and drop cast films. Due to the two buffer layers, the inverted structure may prevent short circuits. In the case of drop casting, the inverted structure is more favorable, as plasma ablation leaves a P3HT layer on the surface, conforming a hole conductor next to the Al electrode. Using Langmuir trough deposition, the coating process is independent of the substrate characteristics, therefore, Plexcore and ZnO substrates can be used without any restrictions. On the contrary, drop casting is strongly influenced by the substrate characteristics. The assembly of P3HT/PCBM particles on a Plexcore layer does not lead to a satisfactory result. For this reason, the pure ITO substrate without any buffer layer is used instead of Plexcore. Drop casting of P3HT/PCBM composite particles on plasma activated ITO and ZnO substrates yields close-packed particle films like on silicon, as demonstrated in **section 7.1.14**. The thicknesses of the particle multi-layers are in also in range of the silicon films. Consequently, reprocessing as introduced in **section 4.2.3.2.2** can be applied. The *IV* curves of the two Langmuir trough made devices and two drop cast devices are shown in **Figure 75**. In virtue of a better classification, the device from **section 4.3.2** acts again as a reference.

In short, the general performance of the devices made by Langmuir trough deposition is slightly better than the drop cast solar devices. In comparison to spin coated PBOPVs the efficiencies are low. As a consequence of the voids within the layer, the function of the Plexcore cell made by Langmuir trough deposition is massively lowered. Indeed, the voids do not lead to a short circuit but the efficiency is nominal. Due to the additional buffer layer in the inverted setup, the performance of the Langmuir trough made ZnO device is better, showing a FF and PCE of 0.21 and 0.08%, respectively. Regarding drop cast devices, cracks and rifts in the particle films are the reasons why the common device on pure ITO has a short circuit. Taking advantage of the two buffer layers, the inverted ZnO cells show no short circuit anymore. However, the PCE is low (0.02%). Theoretically, a

film thickness of approximately 650 nm should have a high light harvesting, accompanied by a large J_{SC}. Practically, almost no photocurrent is collected at the electrodes. This may have several reasons. An important aspect is the plasma etched P3HT remnant at the top of the active layer. As will be shown in the next section, the performance of P3HT suffers strongly under the plasma treatment. Thus, it cannot be assumed that the near-surface P3HT is an adequate hole conductor anymore. As shown in the P3HT device in **section 4.3.1**, imperfections in the active layer lead to general problems in the charge transport. Additionally, as a result of the large layer film thickness, a decreased charge carrier mobility must be taken into account. Further, due to the longer travel distance of the photogenerated charges across the active layer there is also an increased recombination.
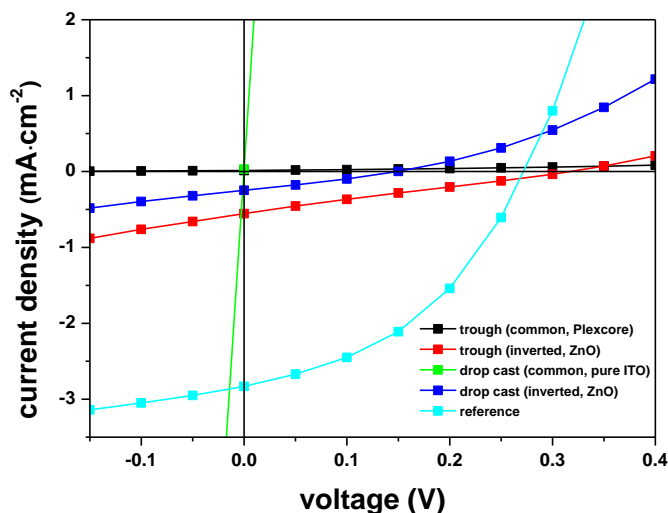
Figure 75: *IV curve of common and inverted PBOPVs fabricated by Langmuir trough deposition and drop casting.*

4.3.7 Multi-layer devices

The big potential of aqueous dispersions is the orthogonality to hydrophobic layers, giving the chance to build multi-layer structures. A multi-layer solar cell device offers various advantages, *e.g.* due to more layers, the device would benefit from a higher light absorption. Further, with respect to a better charge collection, there is also the possibility to apply particles of various P3HT/PCBM ratios to produce a kind of gradient solar cell, ensuring high concentrations of P3HT next to ITO and high amounts of PCBM at the aluminum interface.

Theoretically, dispersions are the ideal way to prepare a layer on a present film without dissolving the subjacent layer. Practically, as reported in **section 4.3.1**, the hydrophobicity does not allow a

direct application of the dispersion. Therefore, the underlying film needs also to be treated with argon plasma. **Figure 76** shows the effect of plasma activation on a P3HT/PCBM composite particle film at various exposure times (5 to 20 s).
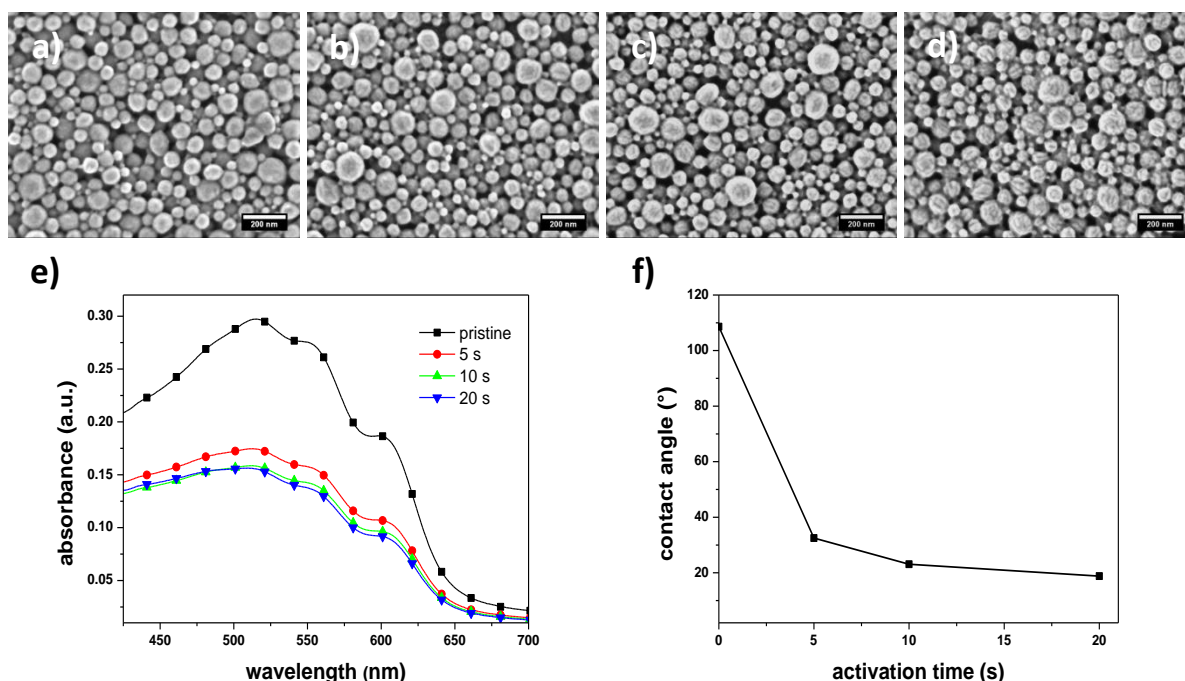
Figure 76: SEM images of P3HT/PCBM composite particle layers after argon plasma treatment of several times; (a) pristine, (b) 5, (c) 10, and (d) 20 s. (e) Corresponding absorbance spectra and (f) obtained contact angles with milliQ water.

According to the SEM images shown in **Figure 76** (**a**) to (**d**), in the first 5 s of the treatment, the particles are not much affected by the plasma. However, the absorption spectra in **Figure 76** (**e**) reveal that in this period over 50% of the absorption is lost, indicating a strong destruction of the chemical structure of P3HT. Upon further treatment, the effect on the absorbance is marginal, however, the particles are ablated significantly. Given these observations, it can be assumed that the charge transport across P3HT is also affected, since conductivity requires an intact chain structure. As reported in **section 4.2.3.2.2**, PCBM is degraded more in a plasma stream. Therefore, the typical domain structure of the P3HT domains appears in the course of the activation. As shown in **Figure 76** (**f**), after plasma treatment of 20 s, the contact angle with milliQ water is below 20°, which is sufficient for spin coating. In contrast to the plasma activation of the P3HT buffer layer shown in **section 4.3.1**, the activation of P3HT/PCBM composite particle films results in much lower contact angles. This may be attributed to the porous colloid structure, exhibiting a higher roughness than the planar P3HT buffer film.

Preparing a multi-layer device, the overlying layers are also applied by spin coating, followed by ethanol washing and plasma activation. It should be noted that using spin coating, every imperfection of the underlying particle layer is transferred to the next layer and is reinforced. In this way, the overall quality of annealed multi-layer particle films diminishes by increasing the number of layers, as shown in **Figure 77** (**a**) to (**d**). The situation regarding the quality on the macroscopic level is demonstrated in **section 7.1.15**. Based on the worse layer quality, the increase in film thickness of the multi-layer devices is non-linear. After the third layer, the increase in thickness is no more than half of the initial state. This fact, in combination with the P3HT degradation causes that the increment of the absorbance in multi-layer devices increasingly decline, until it almost stagnates at the third layer, as shown in **Figure 77** (**e**).
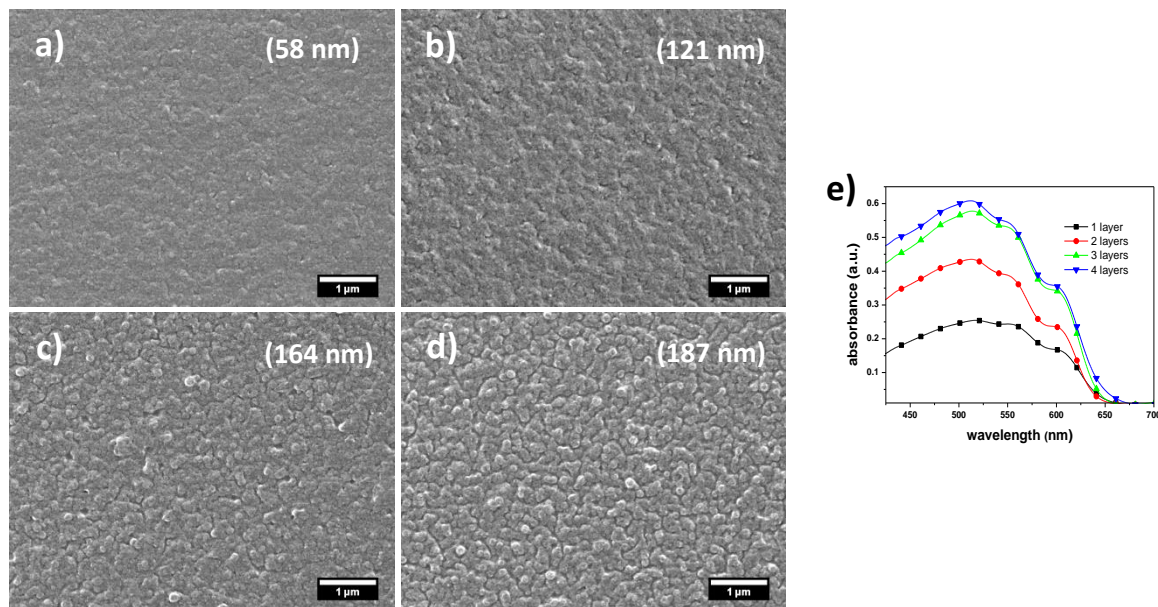
Figure 77: *SEM images of spin coated and annealed P3HT/PCBM PBOPVs of various layers; (a) one layer, (b) two layer, (c) three layers, and (d) four layers. The film thicknesses are denoted in brackets. (e) Corresponding UV-Vis spectra.*

As a consequence of the better light harvesting of the bilayer device, an explicitly higher PCE than for the monolayer device is expected. The characteristics and *IV* curves in **Figure 78** show that the efficiency of a bilayer device is marginally larger, giving 0.31% instead of 0.29% for the monolayer device. This indicates that the first layer of bilayer device has been destroyed by the plasma, contributing only an insignificantly part to the device performance. Note that PCBM, which has been etched away, is no longer available for the charge separation, this also diminishes the efficiency of the device. Fabricating a three layer device yields, not surprisingly, a very low efficiency (0.05%). The two subjacent particle layers undergo a plasma treatment process, which leads to a poor

conductivity. This can be clearly seen in the diminished FF and the *IV* curve characteristics. Coating with fourth layers leads to a further deterioration of the device performance.

a)

number of layers	V_{OC} (V)	J_{SC} (mA·cm^{-2})	FF	PCE (%)
1	0.22	2.46	0.36	0.29
2	0.29	2.71	0.30	0.31
3	0.28	0.53	0.21	0.05
4	0.32	0.19	0.23	0.01

b)
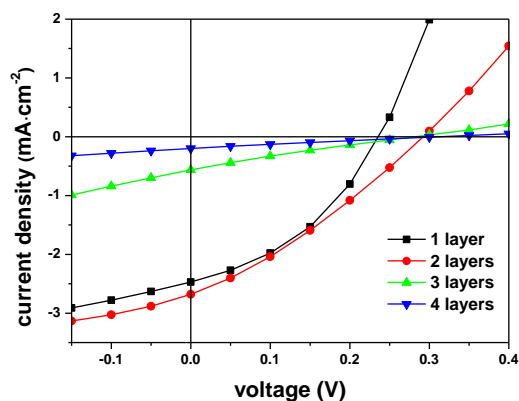
Figure 78: (a) Characteristics and (b) IV curves of multi-layered PBOPV devices.

In theory, multi-layered OPVs are a subject of high interest. With respect to the attained PCE, due to the plasma activation, they bring no improvement to PBOPVs. In practice, other ways to improve the wetting of aqueous dispersions that does not destroy the particle structure are required.

4.3.8 Comparison of fabricated devices with other OPVs

For a better performance assessment, the fabricated PBOPVs are compared with other particle-based devices (see **section 1.3**) and a SPOPV device. In particular, the two best cells, the inverted ZnO device shown in **section 4.3.1** and the device made of composite particles prepared at 60 °C from **section 4.3.3**, are used for this comparison. In the course of this, strengths but also weaknesses of the fabricated devices will be disclosed, in order to obtain information for a potential cell improvement which will be discussed in **section 4.4**.

4.3.8.1 Comparison to Kietzke´s device

As mentioned, Kietzke *et al.* built the first PBOPV device using PFB (D) and F8BT (A).[35] The chemical structures of these semiconductors are given in **section 2.7**. This work was also a foundation for a subsequent improved of the device efficiency, featuring an EQE of 4%,[36] as

demonstrated in **Figure 79** (**a**). At this time it was the highest value reported for the employed material combination.

In this context it should be noted that the phase separation of a PFB/F8BT system leads to micrometer-sized phases, featuring difference in height between the phases, as shown in **Figure 79** (**c**). The domain size and the height difference between the donor and the acceptor are poor preconditions for solar cells. Thus, the limitation of the phase separation by capturing the materials in 100 nm particles was a real innovation and an advancement in PFB/F8BT OPVs. Virtually, no information about the final active layer quality is given, making a direct comparison impossible. However, the E_g of PFB is 2.9 eV, in comparison to P3HT (1.9 eV),[258] less incident radiation of the sunlight is harvested. Amongst others, this may be the main reason why the fabricated Plexcore device exhibits a much higher EQE of 35%, as illustrated in **Figure 79** (**b**). Based on the larger EQE, the whole solar cell characteristics of the Plexcore device must also be much higher.
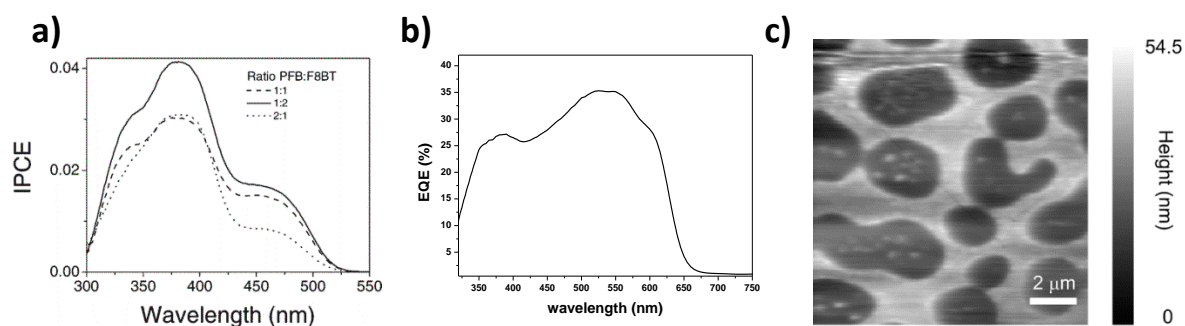
Figure 79: *(a) EQE of a PFB/F8BT PBOPV device taken from the work of Kietzke.[36] In this work, EQE is denoted as IPCE (incident photon-to-converted-electron efficiency). (b) EQE of the P3HT/PCBM PBOPV device from* **section 4.3.3**, *consisting of particles prepared at 60 °C. (c) AFM image, showing the phase separation in a spin coated PFB/F8BT system. The lower level phase has been identified as PFB and the higher level phase as F8BT. This image is taken from the work of McNeill.[259]*

4.3.8.2 Comparison to Andersen´s devices

The main focus of Andersen *et al.* is an environmentally friendly, large scale, and commercially usable fabrication of OPVs.[22] The eco-friendly aspect is achieved by using an aqueous dispersion and the commercially viable approach is realized by coating on a plastic foil using roll-to-roll techniques. The composite particles were also made of PCBM as acceptor, but low band gap polymers as donors. The chemical structures of the low band gap polymers are given in **section 7.1.16**. With respect to a further large scale application, the area of these cells is much larger (4 cm^2). In sum, a general comparison is flawed, however, apart from the PFB/F8BT cells shown in the previous section, these are the only particle-based devices known in literature. The general device structure of Andersen´s

cells is: ITO-ZnO-(polymer/PCBM)-PEDOT:PSS-Ag, meaning an inverted setup. This shows that the authors also recognized that coating of aqueous dispersions on PEDOT:PSS is impractical. Except the electrodes, all layers were applied by roll-to-roll coating.

Three different donors P1, P2, and P3 were used. In **Figure 80** the UV-Vis spectra, the *IV* cures, and the device characteristics, including particle diameter and the annealed film thickness are shown. The general trend in this figure can be described as follows: the "better" the used low band gap polymer and the larger the film thickness, the higher is the PCE. In this case, "better" refers to the absorption of light.

polymer	V_{OC}	J_{SC}	FF	PCE	particle diameter	film thickness
	(V)	(mA·cm^{-2})		(%)	(nm)	(nm)
P1	0.24	1.10	27.5	0.07	-	126
P2	0.47	3.99	29.3	0.55	69	500
P3	0.54	0.92	30.8	0.15	120	612
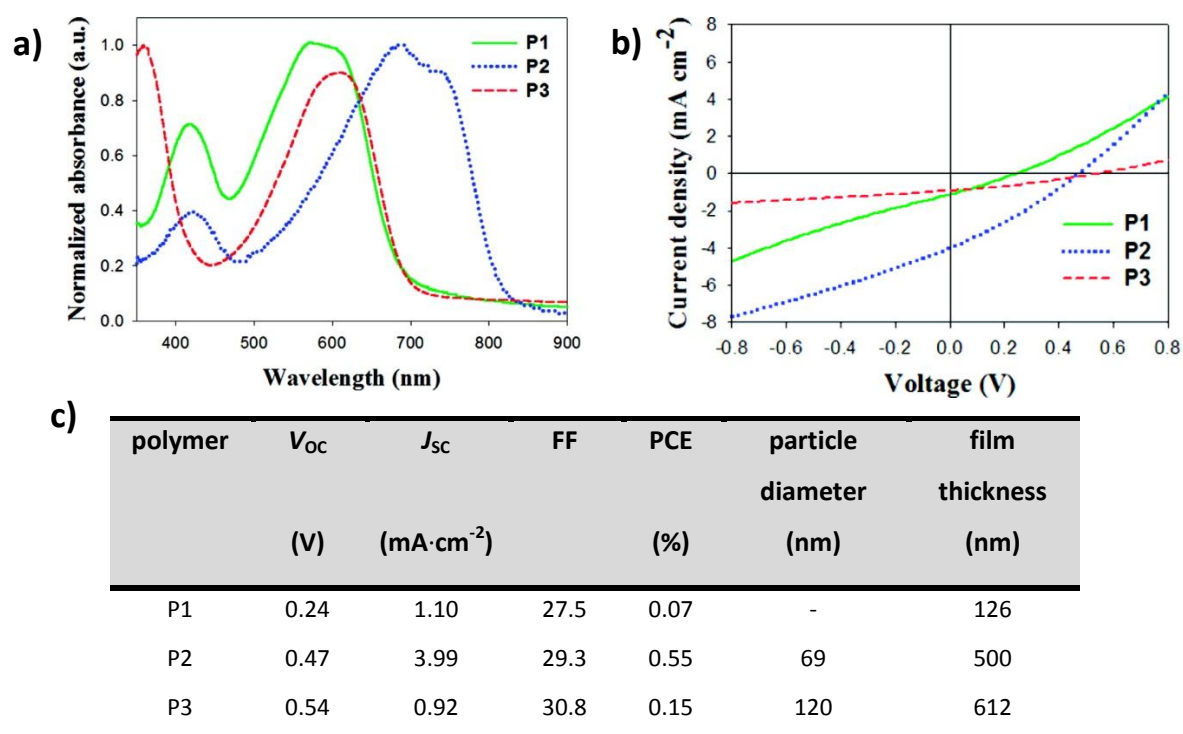
Figure 80: *Data of PBOPVs fabricated by roll-to-roll technique, taken from work of Andersen.[22] (a) UV-Vis spectra, (b) IV cures, and (c) device characteristics include particle sizes and annealed film thickness.*

The UV-Vis spectra in **Figure 80** (**a**) imply the descending order P2 > P1 > P3. Thus, the best PCE in this study is reached by using P2 (0.55%). This value is similar to the ZnO device shown in **section 4.3.1**. However, the film thickness of the roll-to-roll coated device is much higher and the FF lower. In relation to common SPOPVs, the authors also admit that the achieved efficiency is low. They mainly attributed the poor device performance to complications during the drying process, leading to a porous film and microscopic shunts. In principal, the same effect was also observed upon drying in drop casted films, as shown in **section 4.2.3.2.2**. However, in comparison to the drop cast films,

Andersen *et al*. obtained moderate efficiencies. This is probably a result of using a better donors and a consequence of the fact that the active layer was not affected by plasma ablation. Note that the roll-to-roll coating method is a continuous process, thus, ITO and the active layer cannot be pretreated in order to achieve a better wetting. To solve the wetting problem, a nonionic fluorosurfactant is added to the ZnO dispersion and the PEDOT:PSS solution. The particle dispersion was dialyzed, but the device was not washed. Therefore, surfactant and fluorosurfactant are still inside the cells, decreasing the efficiency.

To summarize, the preparation of a functional PBOPV device of 4 cm^2 is remarkable, but in comparison to the film quality of the spin coated P3HT/PCBM PBOPVs, roll-to-roll devices are inferior. With respect to the employed low band gap polymers and thicknesses of the active layers of Andersen´s cells, actually, a much higher efficiency should be attained. Furthermore, it is obvious that using P3HT instead of the low band gap polymer, these cells would exhibit much lower PCEs.

4.3.8.3 Comparison to a SPOPV device

In recent reports, reproducible PCEs for P3HT/PCBM SPOPVs of 3% have been established.[37] In order to find the reasons for the low efficiency of PBOPVs, the 60 °C device from **section 4.3.3** is compared with a typically P3HT/PCBM solution-processed cell made from CB. The SPOPV device is taken from the work of Mauer.[260] Characteristics and *IV* curve of this cell are illustrated in **Figure 81** (**a**). The CB device shows the typical features of a 3% P3HT/PCBM solar cell: V_{OC}, J_{SC}, and FF are around 0.6 V, 7 mA·cm^{-2}, and 0.6, respectively. The thickness of the annealed active layer is approximately 100 nm. As the *IV* curve is mainly determined by V_{OC} and J_{SC}, a comparison of both devices can be simplified considering only the aspects affecting voltage and current.

J_{SC} expresses the amount of charge carriers (per area) collected by the electrodes. Except the buffer layers, both kinds of cells were made by the same materials and exhibits the same thickness. Thus, the light harvesting should be similar. The UV-Vis spectra of the annealed devices are shown in **Figure 81** (**b**). The SPOPV device has a slightly higher absorption at lower wavelengths, with respect to charge generation, this is not a substantial effect. Consequently, the P3HT domain size and the charge transport in the active layer must be responsible for the disparity. Applying TRPL dynamics, **Figure 81** (**c**) shows a faster decay in the solution-processed cell, indicating smaller P3HT domains. This causes a higher yield of charges. The difference is on the same scale as for the devices prepared at 30 and 90 °C shown in **section 4.3.3**. The charge collection at the electrodes requires a barrier-

free charge transport through the active layer. As known from previous sections, this is influenced by the quality of the spin coated layer and the annealing. In **Figure 81** (**d**) and (**e**) the annealed active layers of both devices are shown. The quality of the layers vary widely, the solution-processed film is more uniform than the particle-based film. Despite of annealing, a residual particle structure can still be observed in **Figure 81** (**d**). Indeed, the particles are coalesced, but the fact that a particle structure is still present may engender charge traps due to the poor interaction between the particle fragments. This impedes the charge collection.
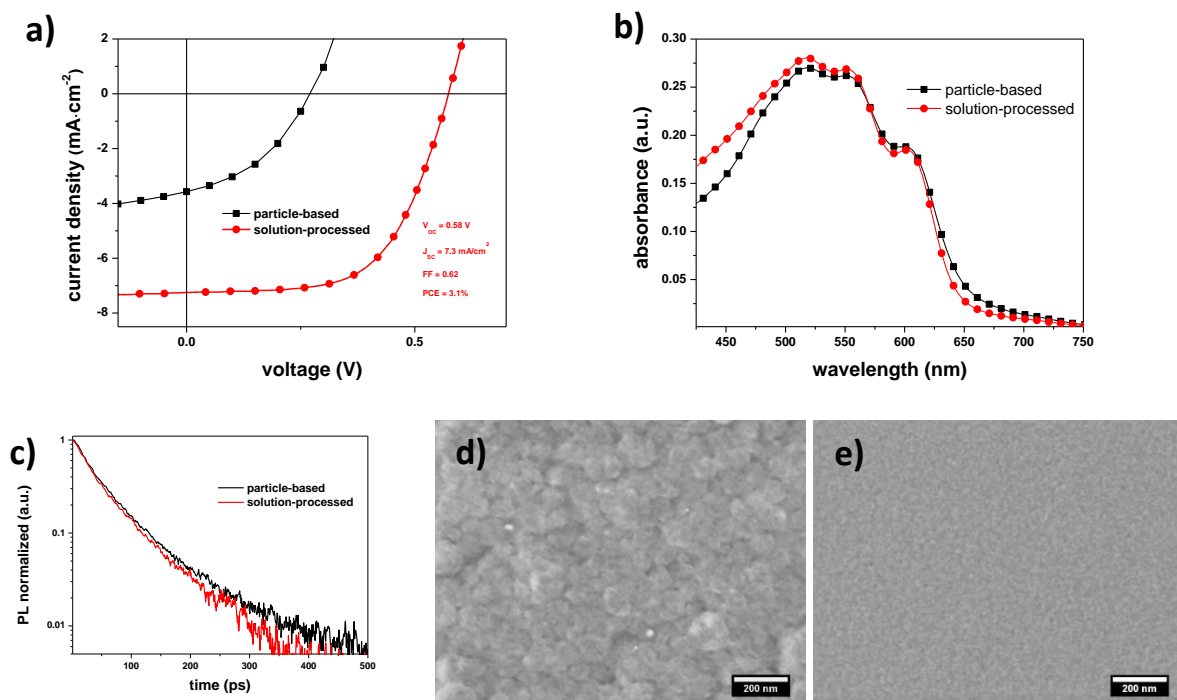
Figure 81: *Comparison of a PBOPV device from* **section 4.3.3** *to a SPOPV device of Mauer;[260] (a) IV curves, (b) UV-Vis spectra, and (c) TRPL dynamics of the devices. (d and e) Corresponding SEM images of the annealed active layers; (d) PBOPV device and (e) SPOPV device.*

The low V_{OC} of PBOPVs may have two reasons. The first reason arises from the diode characteristic. As reported in **section 2.8.3**, under illumination, the photocurrent overcomes the dark current and the *IV* curve is shifted down. It is obvious that a higher photocurrent results in a higher offset of the curve. In **Figure 82** the dark current of the PBOPV device is shifted down to the level of the photocurrent of the SPOPV device. The shift enhances V_{OC} from 0.27 V to approximately 0.42 V. This is only a theoretical consideration, since dark and photocurrent may differ. However, it demonstrates the dependency of V_{OC} on J_{SC}, meaning a low J_{SC} results in a low V_{OC}.
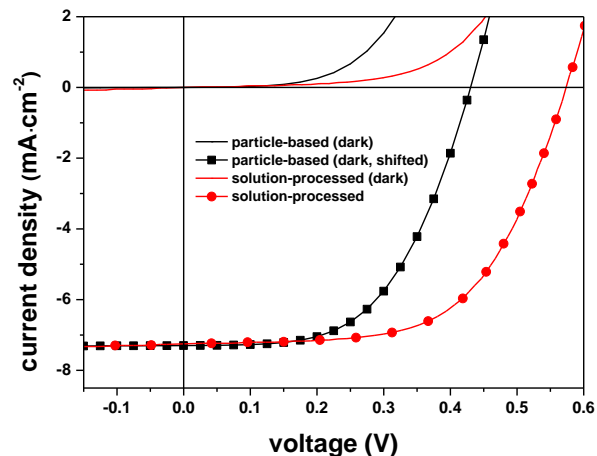
Figure 82: *IV cures of PBOPV and SPOPV devices regarding the dark current.*

The second reason is caused by the interfaces. As mentioned in in **section 2.8.3**, V_{OC} is strongly influenced by the interface within the active layer and interfaces between the active layer and the contacts. Poor interfaces lead to a kind of barrier, decreasing V_{OC}. According to **section 4.3.1,** the barrier can be identified in the behavior of the dark current. As shown in **Figure 82**, the dark current of the PBOPV device is lower, indicating a barrier. The barrier may have different origins. One possible reason is the poor interaction between the particle fragments inside the active layer. Another reason could be the plasma activation of Plexcore. The degradation of the chemical structure causes an electrical barrier. A further reason that will be discussed in another context in **section 4.4.3** is the alignment of the semiconductors at the material/metal interface. This plays an important role in optoelectronic devices.[261]

In summary, the low J_{SC} and the barrier diminish the efficiency of PBOPVs. To eradicate the flaws in P3HT domain size and active layer performance, the preparation of smaller particles (< 25 nm) is suggested. Due to the lower particle diameter, the phase separation is restricted and the P3HT domain size should be in the range of the exciton diffusion length. Additionally, smaller colloids benefit from better colloid packing, resulting in a better layer quality. In the next section, the preparation of "small" P3HT/PCBM composite particles and their performance in OPV devices is shown.

4.4 Advanced particle-based organic photovoltaics

4.4.1 "Small" particle preparation

In order to prepare P3HT/PCBM composite particles in the range of smaller than 25 nm, several approaches are possible. Obviously, an increase of the toluene amount and a decrease of the weight portion of the semiconductors might be an easy way of implementation. However, as mentioned in **section 4.2.2.3**, a certain solid content is required to obtain an adequate spin coated film. Hence, this option is not available. While keeping the amount of semiconductors constant, another approach is a simultaneous increase of the amount of solvent and surfactant plus a longer ultrasonication time and a higher ultrasonication intensity. However, the subtracting effects to the final particle size of these parameters, especially the amount of SDS, are limited.[51] Thus, the desired particle size can only be attained by pursuing a new strategy.

The microemulsion concept introduced in **section 2.1.3** supplies the answer to solve this issue. The contribution of a cosurfactant minimizes the interfacial energy between water and organic phase. In this way, the droplet size is reduced to a few tens of nanometers. However, in **section 7.1.17** it is demonstrated by the example of PS that the solvent evaporation technique cannot be applied to microemulsions. A precondition for the formation of microemulsions is a dispersed phase consisting of small dynamic molecules, thus, applying polymers is condemned to failure. Using PS, instead of a homogenous microemulsion, heterogeneous semi-microemulsion systems (Winsor phases)[262] are formed.

However, the idea of reducing the interfacial energy can be transferred to the miniemulsion approach. Instead of a cosurfactant, a solvent which is soluble in water and toluene, acting as an agent between the phases, is used. Apart from this, the agent should be also a good solvent for P3HT and PCBM. Especially the latter is not easy to achieve. Finally, tetrahydrofuran (THF) was chosen, which lowers the interfacial energy between water and toluene from 36 to 7 mN·m^{-1}; measured by the rotating drop method. Using THF in combination with increased quantities of toluene and SDS as well as rough ultrasonication conditions, 24 nm narrow sized P3HT/PCBM composite particles were prepared (at 30 °C). The particle size was measured with angle dependence DLS, as illustrated in **Figure 83** (**a**).

4.4.2 "Small" composite particle morphology

According to γ_{sl} of P3HT and PCBM, determined in **section 4.1.2.1.2**, a core-shell structure can be expected. In consideration of the high amount of SDS, a Janus morphology should also be possible. Analogous to **section 4.1.2.3**, the PL of the "small" composite particles is compared to the PL of the 140 nm particles prepared at 90 °C, shown in **section 4.1.3**. The particles prepared at 90 °C exhibit the smallest P3HT domains size which was achieved in this thesis so far. **Figure 83** (**b**) shows that the PL intensity of the "small" particle is much lower than the PL intensity of the 140 mm particles. In terms of the very low signal intensity, an assignment of the PL either to the core-shell or the Janus morphology is not possible. Thus, the particle morphology needs to be investigated via electron microcopy. It should be noted that to obtain a better morphology detection, a treatment with ethanol or hexane is not possible. As will be described in the next section, due to the high amount of surfactant, even a short treatment dissolves large particle portions from the wafer. The SEM images are demonstrated in **Figure 83** (**c**) and (**d**). Neither the non-stained nor the OsO_4 stained composite particles show an evident morphology, the both kinds of particles appear uniform. However, the structure of the non-stained and the stained particles show significant differences. The non-stained particles are more degraded, whereas the shape of the stained particles is clearly more pronounced. This is an indication that OsO_4 staining prevents electron beam damage.
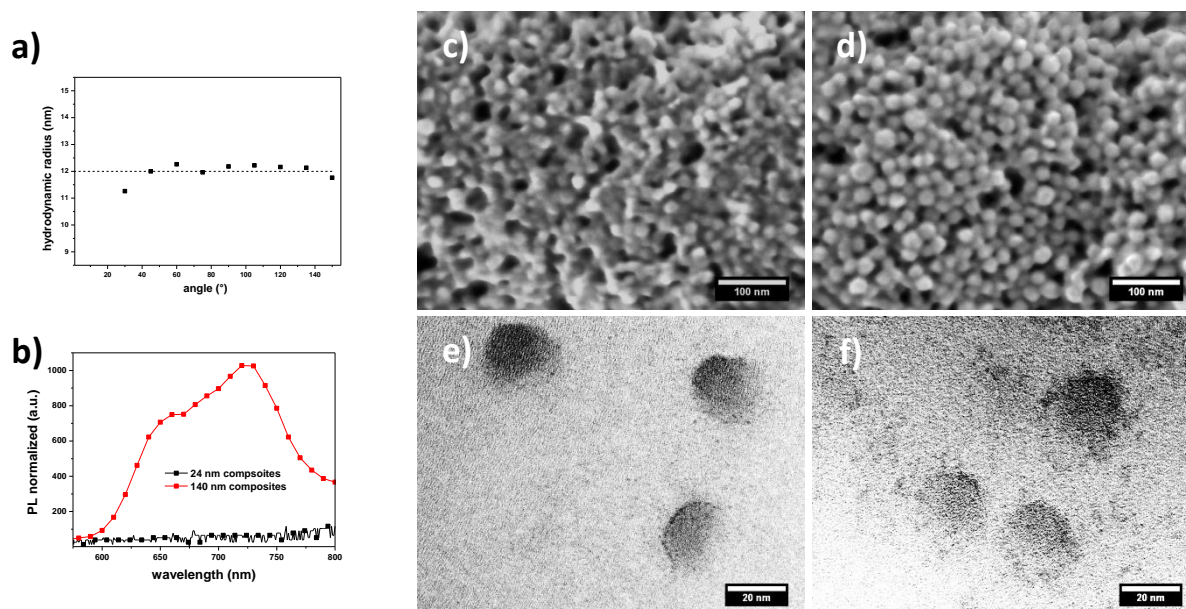
Figure 83: *(a) Angle dependent DLS. The data show the hydrodynamic particle radius. (b) PL spectra of 24 nm P3HT/PCBM particles compared to 140 nm P3HT/PCBM particles shown in **section 4.1.3**. (c) Non-stained and (d) OsO_4 stained SEM images of 24 nm P3HT/PCBM particles. (e) Non-stained and (f) OsO_4 stained TEM images of the 24 nm P3HT/PCBM particles.*

TEM images are depicted in **Figure 83** (**e**) and (**f**). Here, also non-stained and OsO$_4$ stained particles are investigated. Due to the small size of the particles, the contrast to the background is worse. Nevertheless, it seems that the particles exhibit a Janus morphology in both cases. In order to prevent charge traps and to ensure good percolation pathways, the Janus structure fits more into the concept of organic solar cells. In case of a core-shell structure, the P3HT phase or rather the photogenerated holes would be isolated in the core.

4.4.3 Fabrication of "small" particle-based organic photovoltaics

In case of the "small" particles, close-packed colloid layers were also obtained by spin coating. In order to obtain an adequate film, the velocity was lowered to 750 rpm, yielding a final layer thickness of around 200 nm. However, despite of dialysis, large parts of the surface are covered with an SDS film, as shown in **Figure 84** (**a**). Nevertheless, the particle film shows a good packing. Theoretically, the SDS can be removed by ethanol treatment. In contrast to previous films, in this case, ethanol treatment leads to a removal of particles from the layer. The quality of the layer deteriorates and the film contains holes, as shown in **Figure 84** (**b**). The thickness of the eluted film is reduced by more than half to 89 nm.
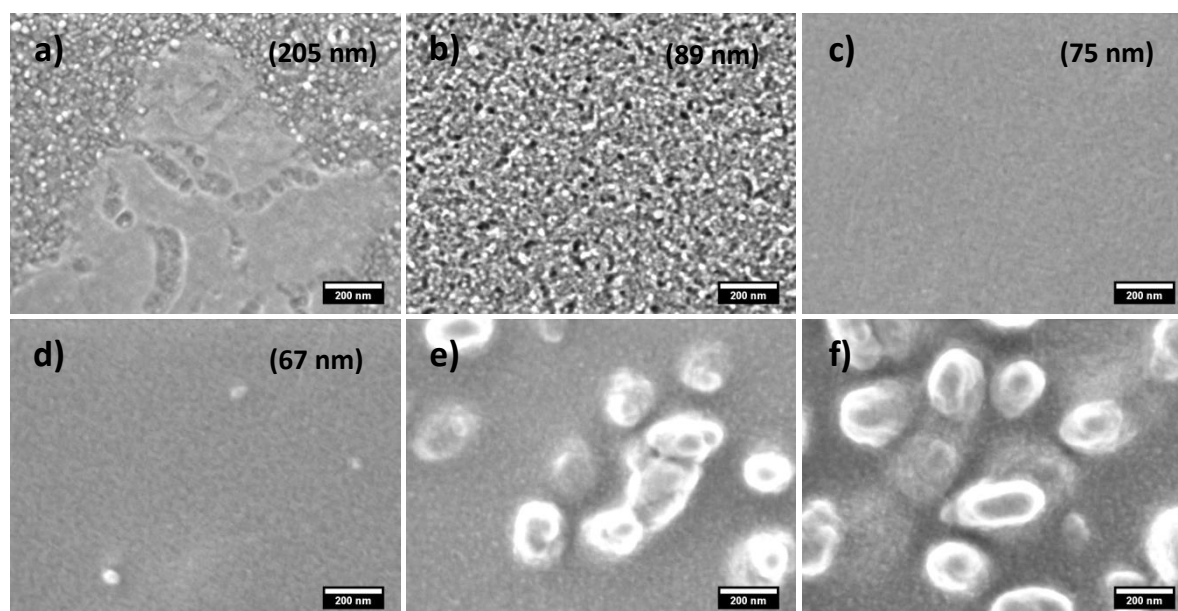
Figure 84: (a) Spin coated "small" P3HT/PCBM particle film on Plexcore. (b) Corresponding film after short ethanol washing. (c to f) Corresponding ethanol-washed films after annealing at (c) 80, (d) 95, (e) 110, and (f) 125 °C for 12.5 min. The film thicknesses are denoted in brackets.

The structure of the particle layers after annealing at 80, 95, 110 and 125 °C are shown in **Figure 84** (**c**) to (**f**). Despite of the holes, a visually homogeneous film is formed at 80 °C. In contrast to **Figure 81** in **section 4.3.8.3**, the present film shows no particle fragments, conforming to the structure of an active layer in a SPOPV device. In the further course of the annealing process, the already described phase separation happens. At 95 °C, only few and small PCBM agglomerates are formed. Applying higher temperatures yield structures similar to the films presented in **section 4.2.3.1**. However, here, the PCBM clusters are smaller in size. Since the particles are coated on Plexcore/ITO glass substrates, it is remarkable that the film annealed at 110 °C shows PCBM agglomerates. The reason for this observation must be the existence of residual SDS in the particle film, lowering the T_g (compare **4.3.5**).

To examine the solar cell performance, the devices annealed at 95 and 110 °C are used for this investigation. The characteristics and *IV* curves are shown in **Figure 85** (**a**) and (**b**). The devices fall far below the expectations, a PCE of only 0.03% for the 95 °C device and 0.16% for the 110 °C device are achieved. This result shows two interesting facts. Firstly, in spite of a good film formation and P3HT domain size of the initial particles, the 95 °C device does not reach the PCE of SPOPVs. Secondly, despite of PCBM agglomerates, the 110 °C devices offers a higher efficiency than the device annealed at 95 °C.

The first fact can be explained as follows: as the TRPL dynamics in **Figure 85** (**c**) reveal, the 95 °C device shows smaller domain sizes than the SPOPV device from **section 4.3.8.3**. Based on the domain size, the 95 °C device should be the better solar cell. However, the surfactant in the active layer lowers the device performance, acting as a charge trap (compare **section 4.3.5**). Furthermore, the XRD diffractograms in **Figure 85** (**d**) show that the crystallinity of the PBOPVs is very low compared to the SPOPV device. The lack of crystallinity can be explained by the work of Kurokawa *et al.*[263] As discussed in **section 4.1.3**, particles prepared at 30 °C should offer an increased material order. Kurokawa reported that the order of polythiophenes chains within nanoparticles depends on the particle size. In this study, large particles showed a lamellar polythiophene structure of high order, whereas small particles had an amorphous coil-like structure. Especially in the case of 24 nm particles, this might be also a factor which causes low material order. Further, a fact that has been widely neglected in this thesis so far is that particles are free rotatable. With respect to the Janus morphology, this means that the colloids align in various orientations on the substrate. This reduces the total material order within the active layer. Moreover, due to this statistically orientation, there is no good interaction between the domains of different particles. This reduces the charge carrier

mobility and changes the energy level of the materials, which causes an electrical barrier.[261] All these enumerated factors diminishing the efficiency of "small" PBOPVs.

a)

annealing temperature (°C)	V_{OC} (V)	J_{SC} (mA·cm^{-2})	FF	PCE (%)
95	0.11	0.06	29.6	0.03
110	0.39	0.08	34.3	0.16

b)

c)

d)
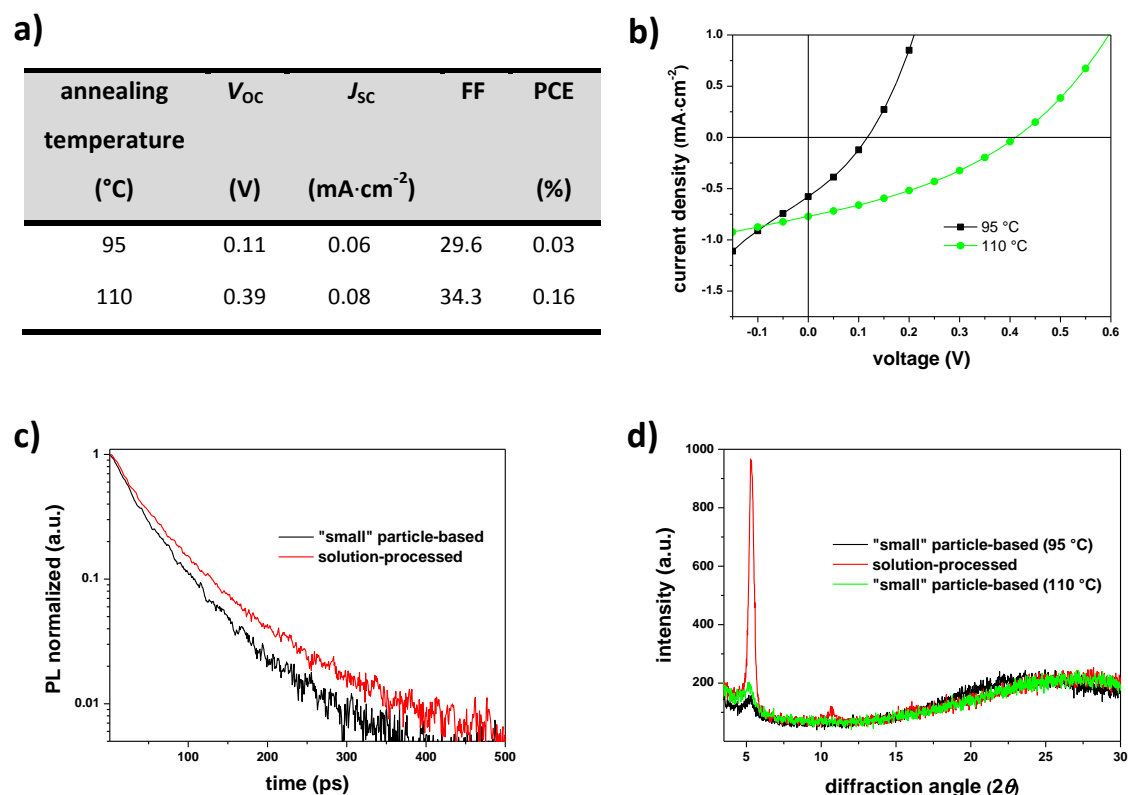
*Figure 85: (a) Characteristics and (b) IV cures of "small" PBOPVs annealed at 95 and 110 °C. (c) TRPL dynamics of the "small" PBOPV device annealed at 95 °C and the SPOPV device from **section 4.3.8.3**. (d) XRD diffractogram of "small" PBOPVs and the SPOPV device from **section 4.3.8.3**.*

The reason why the 110 °C device has a higher PCE than the device annealed at 95 °C can be explained by the material order. In the beginning of the annealing process, due to the statistical orientation of the P3HT domains, the overall crystallinity is low. During the thermal treatment, the particles melt and the domains or rather the P3HT chains change their orientation. By the appearance of the PCBM agglomerates the P3HT is completely melted and reorganizes in more ordered structures. This explains the increase of crystallinity with the appearance of the PCBM clusters, as found in **section 4.2.3.1**. On this account, the device annealed 110 °C device offers higher efficiency, even though evidently larger P3HT domains exist.

Note that this argumentation cannot be transferred to the PBOPVs shown in **section 4.3.2**, since the PCBM agglomerates are larger and further apart. Thus, the exciton quenching is much more pronounced and becomes the critical factor.

4.4.4 Cognitions of using "small" composite particles in OPVs

In spite of the decreased particle size which associated with a domain size reduction and a visual improvement of the annealed active layer quality, the devices underperform. They are even poorer than the initially built PBOPVs. This is attributed to a residual amount of SDS inside the active particle layer, a decreased crystallinity of the composite particles, and decreased interactions between the particles due to statistically orientation. However, these downsides must be taken into account by the use of "small" P3HT/PCBM composite particles. Hence, reducing the particle size is not the right approach to improve the performance of PBOPVs; another way needs to be found.

5 Summary

In this thesis, a basic study of the whole fabrication process of poly(3-hexylthiophene-2,5-diyl) (P3HT)/[6,6]-phenyl-C61-butyric acid methyl ester (PCBM) particle-based organic photovoltaics has been described. The composite particle structure was analyzed in detail, dependences and control mechanisms of the morphology were found. Issues in colloid layer formation were identified and eliminated, resulting in a method to obtain suitable colloid arrays. Further, requirements for particle-based photovoltaics have been identified and optimized. The maximal efficiency reached was 0.53%. In comparison to solution-processed organic photovoltaics, this efficiency is rather low and was ascribed to missing percolation pathways and a non-optimum particle layer morphology. The attempt to remedy the flaws by applying smaller P3HT/PCBM composite particles was not successful.

With this work, the possibility of a reproducible fabrication of functioning particle-based organic photovoltaics was demonstrated. Due to the examinations in morphology, film formation, and their correlation, this thesis also provides fundamental insights which will contribute to push further developments in particle-based devices forward. In the following, the achieved results of the focus areas will be shown briefly.

P3HT/PCBM composite particle morphology investigations

Nanometer-sized P3HT/PCBM composite particles were prepared by using the solvent evaporation technique. A combination of electron microscopy, interfacial energy comparisons, and photoluminescence investigations allowed an unambiguous morphology attribution. The composite particle morphology was a partial core-shell structure characterized by domains, in which PBCM takes up more space on the particle surface than P3HT. The size of the P3HT domains was modified by varying the particle evaporation temperature. By selectively dissolving PCBM out of the particles, it was possible to demonstrate visually that lower evaporation temperatures led to larger domain sizes. The average P3HT domain size could be varied from 11 to 63 nm by decreasing the evaporation temperature from 90 to 30 °C, respectively. Further, it was shown that the crystallinity of P3HT was also associated to the evaporation temperature.

Particle layer formation and reprocessing

Three different colloid coating methods were tested: deposition by Langmuir trough, drop casting, and spin coating. Generally, all coating methods led to closed-packed colloid layers, however, there were significant differences in the layer quality. It was demonstrated that Langmuir trough made and drop cast particles films were not suitable for particle-based photovoltaics, as the layers revealed holes and rifts. Besides, the drop casted layers were too thick. By applying argon plasma ablation, a passable thickness could be achieved, but a destruction of the semiconducting materials must be taken into account. Spin coating offered the only possibility to produce acceptable colloid layers. The quality of the layers was strongly influenced by the solid content of the used dispersions. The higher the solid content, the thicker was the particle layer. The transformation of the spin coated colloid layers into homogeneous films was accomplished by thermal annealing. Upon melting, a shrinkage of more than 50% of the layer thickness was found. Additionally, a phase separation of P3HT and PCBM occurred, accompanied by a favorable increase in crystallinity but also a negative increase of photoluminescence and surface roughness.

Fabrication of particle-based organic photovoltaics

Spin coating on common buffer layers resulted in considerable differences in particle layer qualities. The best results have been achieved on Plexcore and ZnO, featuring 0.29% and 0.53% efficiency, respectively. Owing to good particle melting, low phase separation, and sufficient crystallinity, the optimal annealing temperature was found to be 110 °C. It was demonstrated that the device efficiency was dependent on the particle preparation temperature. As a consequence of maximal crystallinity in combination with minimal P3HT domain size, the best device performance was achieved with particles prepared at 60 °C. Two main differences compared to solution-processed devices became apparent. Firstly, due to the film shrinkage, the aluminum electrode should be evaporated after the annealing process. Secondly, in order to remove the surfactant, the particle layers should be washed with ethanol. Theoretically, multi-layer devices should exhibit a higher efficiency, compared to a monolayer device. Using spin coating, particle-based multi-layer photovoltaics failed to produce the desired effect, since the plasma activation destructed the backbone of P3HT. Further, every imperfection of the subjacent layer was transferred to the next layer and reinforced. Generally, the cause of the poor performance of particle-based devices was

identified as the large P3HT domains and the non-uniform morphology of the annealed particle layer. For this reason, the use of particles smaller than 25 nm should be a promising approach to remedy these weaknesses.

Advanced of particle-based organic photovoltaics

By applying the microemulsion concept, it was shown that the use of tetrahydrofuran lowered the interfacial energy between the aqueous and the organic phase. This led to the preparation of 24 nm particles which showed a Janus morphology. Here, close-packed colloid arrays could be also achieved by using spin coating. It was found that the annealed particle-based films exhibited the same features as annealed solution-processed films. However, the eventual device efficiency was only 0.16%. With respect to the smaller particle size and the Janus morphology, it was shown that the general interactions between the domains of the individual particles were decreased. This had significant negative effects on the overall crystallinity and the charge transport inside the active layer. Thus, an improvement of particle-based photovoltaics could not realized by using smaller composite particles.

6 Experimental section

The procedures of the investigations in **chapter 4** are introduced in this section. This experimental section is divided into a preparation part, giving information of particle preparation, film formation, and solar cell fabrication, and a methodology part that exemplifies the characterization used. Deviating terms and further information were given directly in the corresponding sections of **chapter 4**.

6.1 General preparation procedures

6.1.1 Particle preparation

The nanoparticles were prepared by secondary dispersion technique. Concerning single and composite particles, the general course of particle preparation is always the same. Using only one component leads to pure particles, whereas the use of two materials results in composite particles of a specific morphology. Unless otherwise stated, the general preparation follows the standard recipe for P3HT/PCBM composites shown in **section 6.1.1.1**.

6.1.1.1 P3HT/PCBM composite particle preparation

The recipe for P3HT/PCBM composite particles, applied for spin coated solar cells, was carried out as follows: 100 mg of the semiconducting material (50 mg P3HT and 50 mg PCBM) was dissolved in 2 g toluene at 70 °C for 3 h. Subsequently, the hot organic solution was added to an aqueous solution of 10 mg SDS in 6 g milliQ water and stirred for 10 min at 60 °C. The pre-emulsion was transformed into a miniemulsion by ultrasonication (Branson W450 Digital) under water cooling, for 90 s with a ½" tip at 60% amplitude. Afterwards, the miniemulsion was stirred on a hot plate at 60 °C, evaporating the solvent. The use of semiconducting materials requires a preparation under light exclusion. The removal of excess SDS was accomplished by dialysis tubing (Roth, Visking tubing, MWCO 14.000 $g \cdot mol^{-1}$) against milliQ water. Achieving a total mass of 3 g, milliQ water was added to the dialyzed dispersion, resulting in a solid content of 3.33 wt.-%.

6.1.1.2 Particles for morphology investigation

In total, 20 mg of each material was used. The composite particles were prepared with a mass ratio of 1:1. The materials were dissolved in 1.5 g toluene and added to a solution of 3 mg SDS in 5 g milliQ water. Ultrasonication was accomplished under water cooling for 60 s with a ¼" tip at 70% amplitude. A blend of P3HT and PCBM particles was made by mixing in the pure dispersions in volume ratio of 1:1.

6.1.1.3 P3HT/PCBM composite particles for Langmuir trough deposition and drop casting

25 mg P3HT and 25 mg PCBM were dissolved in 1.5 g toluene. The organic solution was added to a solution of 3.5 mg SDS (Langmuir trough deposition) or 4 mg CTAC (drop casting) in 3.5 g milliQ water. The obtained dispersions were not dialyzed. The resultant dispersions were set with milliQ water to a solid content of 1.6 wt.-%.

6.1.1.4 P3HT/PCBM composite particles for spin coating investigation

P3HT/PCBM composite particles of various solid contents were prepared by dilution of a 5 wt.-% dispersion with milliQ water. The weighed portions, leading to 0.5 g dispersions of the desired solid contents, are shown in **Table 12**. The 5 wt.-% dispersion was prepared by using 75 mg P3HT and 75 mg PCBM.

Table 12: Conditions for the preparation of dispersions of various solid contents by dilution with milliQ water.

desired solid content (wt.-%)	5 wt.-% dispersion (g)	milliQ water (g)
5.00	0.500	0.000
3.75	0.375	0.125
2.50	0.250	0.250
1.25	0.125	0.375
0.50	0.050	0.450

6.1.1.5 Variation of evaporation temperature for OPV performance investigation

25 mg P3HT and 25 mg PCBM were dissolved in 1 g toluene and added to a solution of 5 mg SDS in 3 g milliQ water. The preparation temperatures of the composite particles were varied according to **section 4.1.3**.

6.1.1.6 "Small" P3HT/PCBM composite particles

The organic phase consisted of 4 g toluene and 1.5 g THF. The aqueous phase contained 500 mg SDS in 6 g milliQ water. Ultrasonication was performed under ice cooling for 6 min with a ½" tip, applying 20 s pulse and 10 s pause, at 90% amplitude.

6.1.2 Particle staining

Iodine and OsO_4 treatment were performed by vapor staining. TEM grids or SEM silicon wafers were placed in a petri dish. A small grain of iodine or 100 µL 4% OsO_4 solution were added, subsequently, the dish was covered. In case of iodine, the samples were treated 25 min, for osmium staining, the substrates stayed 35 min in the atmosphere.

6.1.3 Buffer layer and polymer film formation

Films of the buffers and materials used for surface energy determination were conducted by spin coating, except MoO_3 (see **section 6.1.7.3**). The polymers were dissolved in CB, chloroform ($CHCl_3$), or toluene, each forming a 0.016 wt.-% solution. The substrates were activated by argon plasma, the conditions are given in **section 6.1.7.2**. The solutions were applied to the wafers via syringe filters. For organic solutions, a polytetrafluoroethylene filter (pore size 0.2 µm); for water and polar solutions, regenerated cellulose filters (pore size 0.45 µm) were used. In general, spin coating was carried out in two stages. In the first stage, the solution was spread at relatively low rotation. The second stage consisted of higher velocity in order to evaporate the solvent. After coating, the polymeric films were annealed on a hot plate at 130 °C for 15 min under nitrogen atmosphere. The coating conditions are listed in **Table 13**. The ZnO particle dispersion was prepared according to work of Pacholski.[264] Terms and conditions of ZnO spin coating can be taken from the corresponding literature.[265]

Table 13: Spin coating conditions for film formation of the buffer materials and materials used for surface energy determination.

material	solvent	1. stage			2. stage		
		speed (rpm)	acceleration (rpm·min^{-1})	time (s)	speed (rpm)	acceleration (rpm·min^{-1})	time (s)
PS	toluene	2000	500	15	5000	5000	30
PLLA	CHCl$_3$	1500	100	30	3000	3000	15
P3HT	CB	2500	500	15	5000	500	30
PCBM	CB	2500	500	15	5000	500	30
PEDOT:PSS	-	2500	2500	10	5000	5000	30
Plexcore	-	2500	500	30	5000	500	150

6.1.4 Ethanol and hexane treatment

According to **section 6.1.5.3**, the P3HT/PCBM composite particle dispersions were spin coated on plasma activated silicon wafers (1 cm x 1 cm). Subsequently, the substrates were treated either in 20 mL ethanol or hexane for 20 or 40 min, respectively. Afterwards, the substrates were blown dry with nitrogen.

6.1.5 Particle layer formation

6.1.5.1 Langmuir trough deposition

A substrate was positioned tilted in the center of a water filled trough. Depending on whether "piston oil" effect was used, a certain amount of SDS was added to water phase. In order to change hydrophobicity of the dispersion, 75 µL butanol was added to 525 µL of an aqueous dispersion. According to work of Weekes,[266] the dispersion was applied to the water/air interface via a glass slide tilted with an angle of approximately 45°. In order to ensure a constant dispersion flow, a syringe pump was used. To obtain a macroscopic uniform film, the particle patches were compressed by barriers under constant compression (20 mm·s^{-1}). Finally, the water was removed

from the trough by a pump. The resulting particle film was dried under ambient conditions and light exclusion.

6.1.5.2 Drop casting

25 µL of the dispersion was applied to a plasma activated substrate via a microliter pipette. The plasma activation is described in **section 6.1.7.2**. For a uniform distribution, the dispersion was carefully spread with the tip of pipette. Afterwards, the film was dried under ambient conditions and light exclusion.

6.1.5.3 Spin coating

The dispersion was applied to a plasma activated substrate (see **section 6.1.7.2**) via a regenerated cellulose syringe filter (0.45 µm).The coating was conducted in two stages. 1. Stage: 1000 rpm and 20 rpm·min^{-1} for 60 s; 2. stage: 2000 rpm and 500 rpm·min^{-1} for 30 s. For small composite particles, the films were made as follows: 1. stage: 750 rpm and 20 rpm·min^{-1} for 90 s; 2. stage: 2000 rpm and 500 rpm·min^{-1} for 15 s.

6.1.6 Particle film reprocessing

Annealing of the particle films was conducted under nitrogen atmosphere on a hot plate at a certain temperature for 12.5 min, see **section 4.2.3.1**. SDS was removed by ethanol washing. For this, 4 mL ethanol was applied drop-wise to the films. Then, the substrates were blown dry with nitrogen. Ablation of the drop cast films was performed by argon plasma. The particles layers were treated at 300 W for a certain time to the plasma (compare **section 6.1.7.2**).

6.1.7 Particle-based photovoltaic fabrication

Unless otherwise stated, ITO is the anode and aluminum is the cathode. The device set-up conforms to the structure mentioned in **section 2.8.1**, additionally, a buffer is used between ITO and the active layer. Potential buffers are PEDOT:PSS, P3HT, Plexcore, and MoO$_3$ for common devices

and as well as ZnO for inverted solar cells. The active layer consists of P3HT/PCBM composite particles. A scheme of the general device preparation is given in **Figure 86**. The standard recipe for PBOPVs cells is listed below. The standard recipe for inverted solar cells is shown in **section 6.1.7.4**.

The initial point of the fabrication of an OPV device was a pre-manufactured ITO glass wafer. The substrate was patterned by wet etching, followed by cleaning (see **section 6.1.7.1**). The buffer materials were coated and annealed according to **section 6.1.3**. Depending on the coating method, the particle layer formation was conducted accordingly to **section 6.1.5.1**, **6.1.5.2**, or **6.1.5.3**. Then, the particle layer was washed and annealed according to **section 6.1.6**. The best PCE was achieved at an annealing temperature of 110 °C. In case of multi-layer devices, the activation, the coating, and the washing steps were repeated several times. Subsequently, aluminum patterned in six "fingers" was evaporated according to **section 6.1.7.3**.

The active areas of an OPV device are considered to be the area sandwiched between ITO and the Al "fingers", therefore, six separate solar cells are created on one substrate. To close the circuit upon measuring, parts of active layer, covering ITO, must be removed by using a cotton bud and toluene. Note that except for the annealing process and thermal evaporation, the entire fabrication procedure was conducted under ambient conditions.
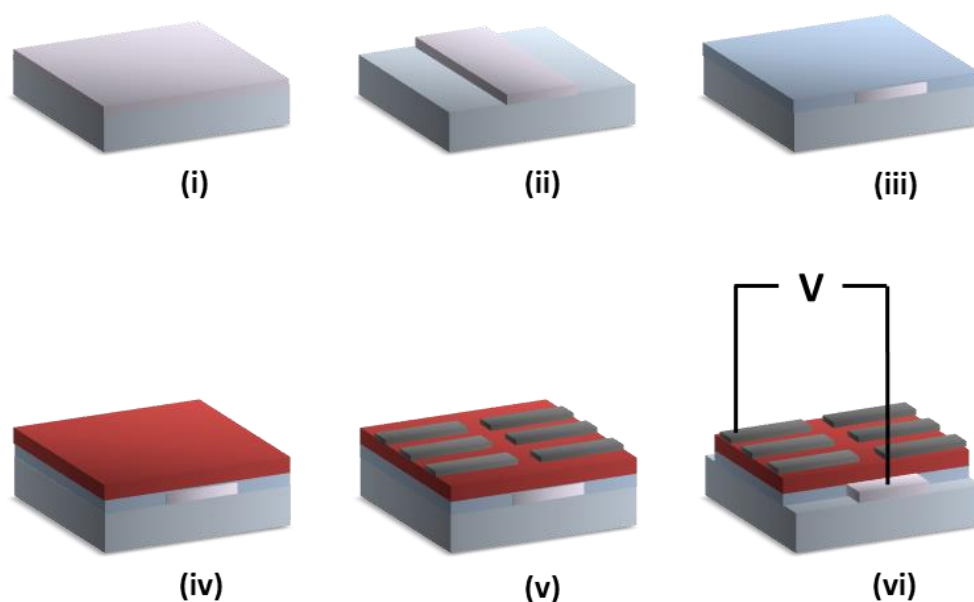

Figure 86: *Scheme of a PBOPV device fabrication; (i) pre-manufactured ITO glass substrate, (ii) ITO patterning by wet etching, (iii) buffer deposition, (iv) active (particle) layer coating and annealing, (v) evaporation of six aluminum electrodes, and (vi) removing parts of hole conductor and active layer in order perform IV measurement.*

6.1.7.1 ITO glass wafer etching and cleaning

The ITO glass substrates were patterned by wet etching of half concentrated hydrochloric acid and zinc powder. The desired ITO area of 2.88 cm^2 was covered with Kapton tape. After etching, the ITO glass substrate was cleaned in diluted Hellmanex solution by treatment in an ultrasonic bath for 10 min, followed by multiple purification steps with milliQ water and ethanol. Preventing the contamination with dust, the ITO glass substrates were stored in ethanol until they were used for photovoltaic fabrication.

6.1.7.2 Argon plasma cleaning and activation

The argon plasma was generated by TePla 200-G. For cleaning and activation, plasma at 0.2 mbar was used. The plasma treatment of ITO and silicon substrates was conducted at 250 W for 10 min. For MoO_3 and ZnO, plasma at 200 W for 3 min was applied. In case of organic substrates, *i.e.* composite particles, P3HT, and Plexcore, plasma at 100 W for 20 s was used.

6.1.7.3 Thermal evaporation of aluminum and MoO_3

All evaporations were carried out in a Univex 300. The pressure in the evaporation chamber was below $2 \cdot 10^{-5}$ mbar before starting the vapor deposition process. Pattering of the Al "fingers" was obtained by using a shadow mask. The aluminum electrodes were evaporated with a rate of 0.5 nm·s^{-1} until a thickness of 100 nm was reached. MoO_3 (25 nm) was deposited with a rate of 0.02 nm·s^{-1}.

6.1.7.4 Inverted particle-based solar cell fabrication

In general, the fabrication of inverted solar cells is similar to common PBOPVs. Unless otherwise stated, the preparation follows the standard recipe described in **section 6.1.7**. Due to the reversed current direction, instead of a hole conductor, the electron conductor ZnO was used as buffer material (compare **section 6.1.3**). As the setup requires a hole conductor between the active layer and aluminum, MoO_3 was deposited on the washed and annealed active particle layer (compare **section 6.1.7.3**).

6.2 General characterization methods

6.2.1 Particle size determination

Generally, the particle diameters were measured by DLS at a fixed scattering angle of 90°, using a Nicomp 380 particle sizer. "Small" P3HT/PCBM composite particles were measured with angle dependent DLS, performed by Christine Rosenauer, using ALV-5000.

6.2.2 Transmission electron microscopy

TEM investigations were accomplished on a Zeiss 902 and Zeiss 912. The particles were observed on carbon layered copper grids (mesh 300). Transferring of the dispersion to the grid was done by dropping 5 µL of a 0.003 wt.-% dispersion on the grid. Water was removed by evaporation, leaving statistically distributed particles. Due to better contrast, composite particles containing PLLA were coated with a thin carbon layer. Carbon deposition was performed with a Balzers BAE 250. ESI-TEM was conducted by Katrin Kirchhoff on a Tecnai F20. The CS-TEM particle preparation process was done by Christoph Sieber. In accordance with the work of Dass,[267] the particles were embedded into epoxy resin. The resin was hardened for 3 days at 60 °C. Afterwards, the resin was cut by a diamond knife in approximately 50 to 100 nm thick slices.

6.2.3 Scanning electron microscopy

SEM images were obtained on a Zeiss LEO 1530. The colloidal dispersions (5 µL of a 0.006 wt.-%) were dropped on silicon wafer. After drying, the coated substrates were washed with a few drops of ethanol and blown dry with nitrogen. In case of solar cells, the devices were short-circuited with a copper wire. BE-SEM was conducted by Gunnar Glasser on a Hitachi SU8000.

6.2.4 Contact angle measurement and surface energy determination

Contact angle measurements were conducted on a Krüss DSA10. The liquids (1.5 µL) were applied to the substrates via a micropipette. Surface energy determination was calculated by the "Drop Shape Analysis" program, using OWRK method.

6.2.5 X-ray diffraction

X-ray diffraction measurements of freeze-dried composite particles and particle films on silicon and glass wafers were performed on a Phillips PW1820 diffractometer, equipped with a copper anode, generating X-rays of 0.154 nm. Scans were taken in a range from 2θ = 2° to 30° with step size of 0.02°.

6.2.6 Optical spectroscopy

UV-Vis measurements of spin coated particle layers were conducted on glass wafers by using a Perkin Elmer Lambda 25 UV-Vis spectrometer. TRPL spectroscopy of particle films on glass or ITO glass substrates was measured by Valentin Kamm and Dominik Gehrig. UV-Vis spectra and PL emission spectra of colloidal dispersions were acquired on a Tecan M1000 plate reader. The PL emission spectra were acquired with excitation wavelength of 510 nm. The spectra of the dispersions were normalized to the solid content.

6.2.7 Confocal laser scanning microscopy

For CLSM investigations, the particles were spin coated on optical glass cover slides (0.17 mm). The CLSM images were taken by Anke Kaltbeitzel on a Leica TCP-SP5.

6.2.8 Film thickness determination

Film thicknesses were determined by scratching the coated layer with a thin needle. A KLA Tencor P-16+ step profiler measured the difference in levels and supplied the film thickness.

6.2.9 Temperature determination on substrates

10 min after setting the temperature on a hot plate, a thermocouple (PT100) was laid flat on a substrate. The final temperature was determined by a Keithley multimeter.

6.2.10 Solar cell investigation

The PBOPV devices were measured under 1.5AMG conditions (100 mW·cm^{-2}) under nitrogen atmosphere. Ensuring 1.5AMG condition, the solar simulator was calibrated with a standard Si-cell (ISE Freiburg) to 1 sun. A Keithley multimeter supplied voltages from -1 to 1 V and measured the (photo)current under dark and illuminated conditions. It was measured in steps of 0.025 V with a delay time of 0.4 s between the steps. This procedure was performed for all six pixels of one device. The size of one pixel is approximately 0.14 cm^{-2}. For better a contact, silver paste was applied to aluminum and ITO. The calculation of V_{OC}, J_{SC}, FF, and PCE from the obtained *IV* data was accomplished by the LabVIEW program "pixel-sweep_2", programmed by Ian Howard.

6.3 Materials

All materials were commercially available and used without further purification.

Poly(3-hexylthiophene-2,5-diyl) (P3HT), [6,6]-phenyl-C61-butyric acid methyl ester (PCBM), poly(thiophene-3-[2-(2-methoxyethoxy)ethoxy]-2,5-diyl) (Plexcore), molybdenum(vi) oxide (MoO$_3$), poly(L-lactide) (PLLA), and toluene were purchased from Sigma-Aldrich. Specifications: P3HT (>99.9%, RR >95%, M_n = 15.000 - 45.000 g·mol^{-1}), PCBM (>99%), Plexcore (2% in 1,2-propanediol/iso-propanol/water, 3:2:1), MoO$_3$ (99.9%), PLLA (M_w = 67.000 g·mol^{-1}), and toluene (99.95%). Sodium dodecyl sulfate (SDS) and cetyltrimethylammonium chloride (CTAC) were purchased from Alfa Aesar. Specifications: SDS (>99%) and CTAC (95+%). Poly(3,4-ethylenedioxythiophene)-poly(styrene sulfonate) (PEDOT:PSS) was obtained from Heraeus. Brand: Clevios P. Polystyrene (PS) was synthesized by anionic polymerization by Thomas Wagner. Specifications: M_w = 50.000 g·mol^{-1}, PDI = 1.04. Aluminum (Al) was purchased from Umicore - Thin Film Products. Specification: >99.8%. Indium tin oxide (ITO) substrates were manufactured by Bte Bedampfungstechnik. Specifications: 100 nm ITO layer evaporated on 1.1 mm thick float glass, 2.4 cm x 2.4 cm, resistance = 20 Ω·sq^{-1}.

Silicon wafers were purchased from CrysTec Kristalltechnologie. Specifications: One-sided polished, 0.7 mm thick. Water of ultra-high purity (milliQ grade, 18.2 M$\Omega\cdot$cm^{-1}) was obtained from a MilliQ Gradient water purification system from Millipore.

7 Appendix

7.1 Additional result information

In this chapter, further and general information are given, complementing the corresponding sections in **chapter 4**. The appertaining sections are denoted in brackets.

7.1.1 Chemical structure of polythiophene-based hole conductors (2.8.1 and 4.3.1)

Figure 87 shown the chemical structure of PEDOT:PSS and Plexcore.
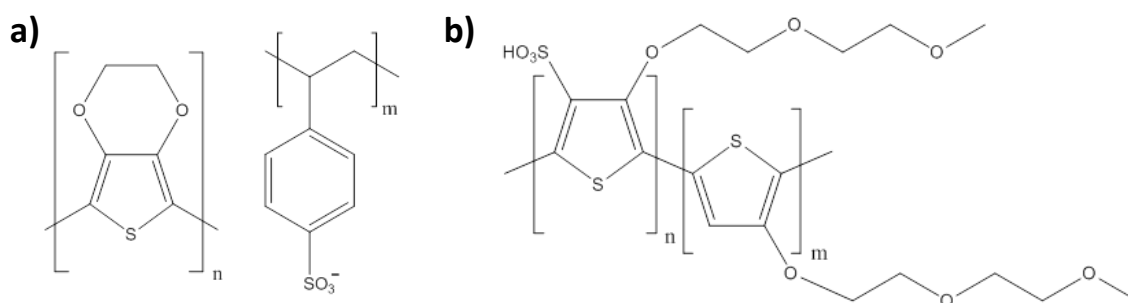
Figure 87: Chemical structure of (a) PEDOT:PSS and (b) Plexcore.

7.1.2 Dent formation in particles (4.1.1.2)

Okubo *et al.*[71] studied dent formation of PS/PMMA composite particles made by solvent evaporation technique in detail. The whole mechanism is shown in **Figure 88**. They found that a dent is a result of differences in phase separation of PS and PMMA during solvent releasing. Depending on the polymer ratio and the used solvent, it is possible to obtain dents inside particles. Generally, a dent formation requires a superior solubility of one component. After phase separation, according to the Flory-Huggins theory, a two-phased system of a PS/toluene and a PMMA/toluene phase is formed. In the PS/PMMA/toluene system, PS has a higher solubility. Due to the polarity of PMMA, the system arranges in an ex-centered PS-core/PMMA-shell structure. The PMMA shell hardens prior to the PS core, as the PMMA shell contains less toluene. After PMMA hardening, the PS core shrinks due to further evaporation and leads to a cave-in at the surface.
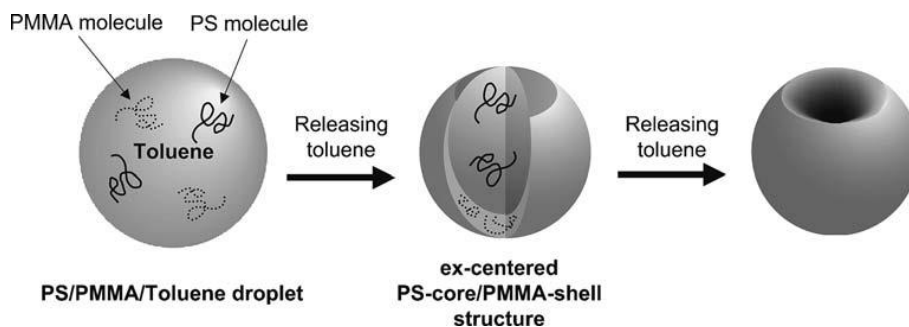
Figure 88: *Illustration of dent formation mechanism in PS/PMMA/toluene system during toluene evaporation. The image is taken from the work of Okubo.*[71]

This knowledge can be directly transferred to pure (PCBM) particles. As described in **section 2.3.2**, the phase separation in such a system leads to a sol and a gel phase. As the sol phase consists of considerably more toluene, the shrinkage upon evaporation is much more pronounced, resulting in a dent on particle surface.

7.1.3 Owens-Wendt-Rabel-Kaelble plot (4.1.2.1.1)

Figure 89 shows an OWRK plot of PMMA. The surface energy is identified by applying water, ethylene glycol, and dimethyl sulfoxide. In order to achieve γ_{sv}, the program "Drop Shape Analysis" plots γ_{lv} and the measured contact angles of the liquids according to **Equation 18**. Subsequently, a regression line is fitted to the three data points. Based on this regression, the program determines γ_{sv}^{D} and γ_{sv}^{P}, the sum results in γ_{sv}.
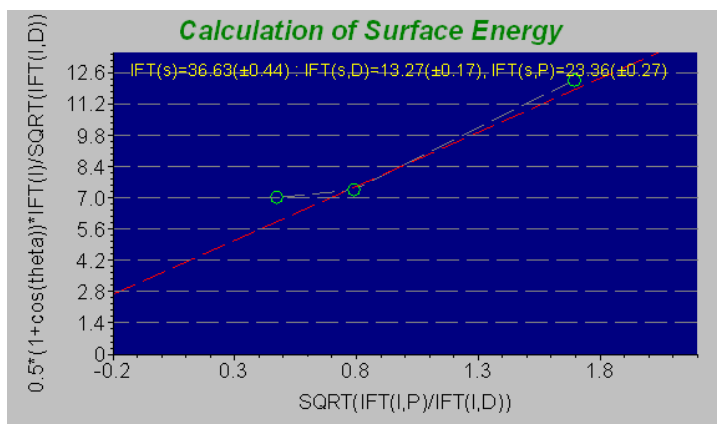

Figure 89: *Screenshot of an OWRK plot in "Drop Shape Analysis" program. The plot shows the data points, the regression line, and the resulting γ_{sv} of PMMA. The surface energy is determined by water, ethylene glycol and, dimethyl sulfoxide.*

7.1.4 Calculation of photoluminescence emitting part in core-shell particles (4.1.2.3)

The density of P3HT and PCBM is 1.1 and 1.5 g·cm^{-1}, respectively. Hence, the volume fraction of the components in composite particles of 1:1 mass ratio is φ_{P3HT} = 0.58 and φ_{PCBM} = 0.42. Applying the volume (*V*) equation of a sphere, the diameter of the P3HT phase within a core-shell particle can be determined.

$$V = \frac{4}{3}\pi r^3 \tag{20}$$

In a 140 nm P3HT/PCBM core-shell particle, the diameter of a P3HT core is approximately 125 nm, consequently, the thickness of a PCBM shell is approximately 7 nm. Due to the exciton diffusion length, in range of 8 nm to the PCBM interface all excitons are quenched, reducing thereby the diameter of the emitting part to 109 nm. In comparison to pure P3HT particles of 140 nm that undergo no quenching, the core-shell particles emit only 78% of PL.

If the PL amount of the composite particles is in range of 78% to pure P3HT particles or 39% to the blend of P3HT and PCBM particles, the composites features a core-shell structure. The calculated diameter of the emitting P3HT phase within a P3HT/PCBM core-shell particle is visualized in **Figure 90**.
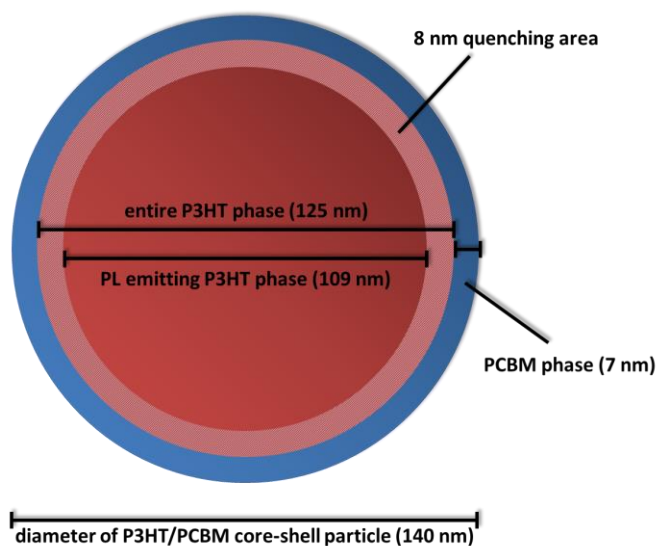

Figure 90: Illustration of the structure of a P3HT/PCBM core-shell particle with respect to PL emission. Due to exciton quenching, the effective PL emitting part of P3HT is reduced from originally 125 to 109 nm.

7.1.5 Langmuir trough (section 4.2.2.1)

The setup of a common Langmuir trough is shown in **Figure 91**. Linchpin of this system is a Teflon trough. Molecules or particles applied to water/air interface start to interact. These interacting forces result in a two-dimensional analog to the Laplace pressure called surface pressure *Π*, describing the depression of surface tension in relation to the value of a pristine interface. The surface pressure is recorded by the Wilhelmy plate method. Forces, resulting from compression by pushing the barriers together, are measured by a thin paper plate, partially immersed into the water phase. The plate is connected to a sensitive balance that records the changes in surface tension at the water/air interphase.
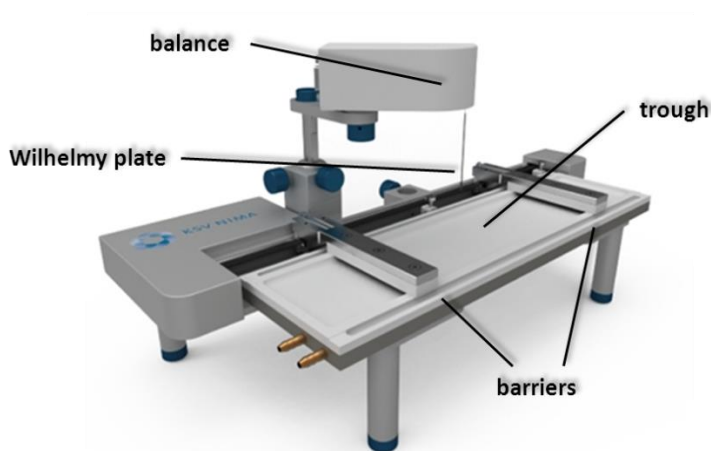
Figure 91: *Photograph of a Langmuir trough. The image is taken from KSV-NIMA product catalogue.*[268]

7.1.6 Time-resolved photoluminescence spectroscopy (4.2.3.1)

TRPL spectroscopy represents an extension of common PL spectroscopy. Here, the PL emission is monitored as a function of time after excitation by a light. Information about the time dependence is attained by using a streak system, depicted in **Figure 92**. A sample is excited with a short laser pulse. Emitted photons are focused onto a spectrograph, where light is diffracted and spectrally resolved. In the streak system, a photocathode converts photons into electrons. The electrons experience a perpendicular time-resolved electric field. Depending upon the time at which the photons arrive at the cathode, electrons are deflected to a certain extent, thus, sorting electrons by their time of creation. The resulting electrons are detected by a CCD camera.
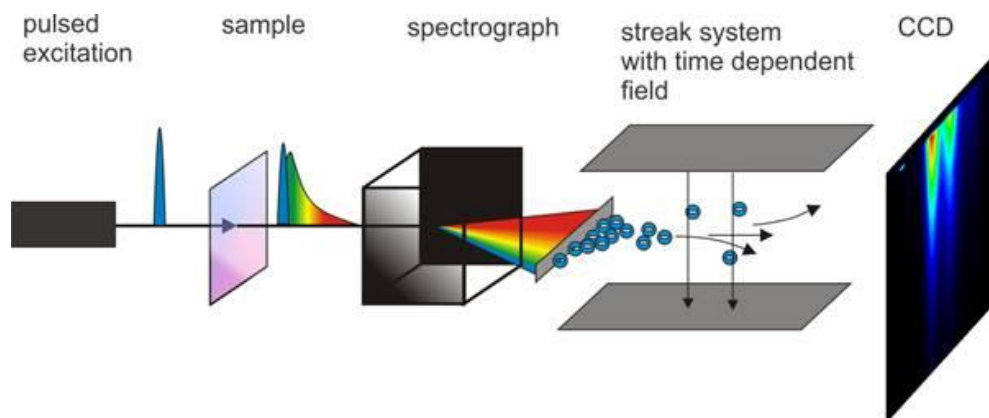
Figure 92: *Schematic illustration of a streak system setup.*

A typical CCD image produced by the streak camera is shown in **Figure 93**. The in-plane coordinates represent the spectral (*x*-axis, blue) and temporal (*y*-axis, red) information. The intensity of the PL is recorded along the out-of-plane coordinate (*z*-axis), here, denoted by colors. A typical PL spectrum is shown at the top. The TRPL decay dynamics is depicted at the right side, showing the decay of excitons with respect to the time.
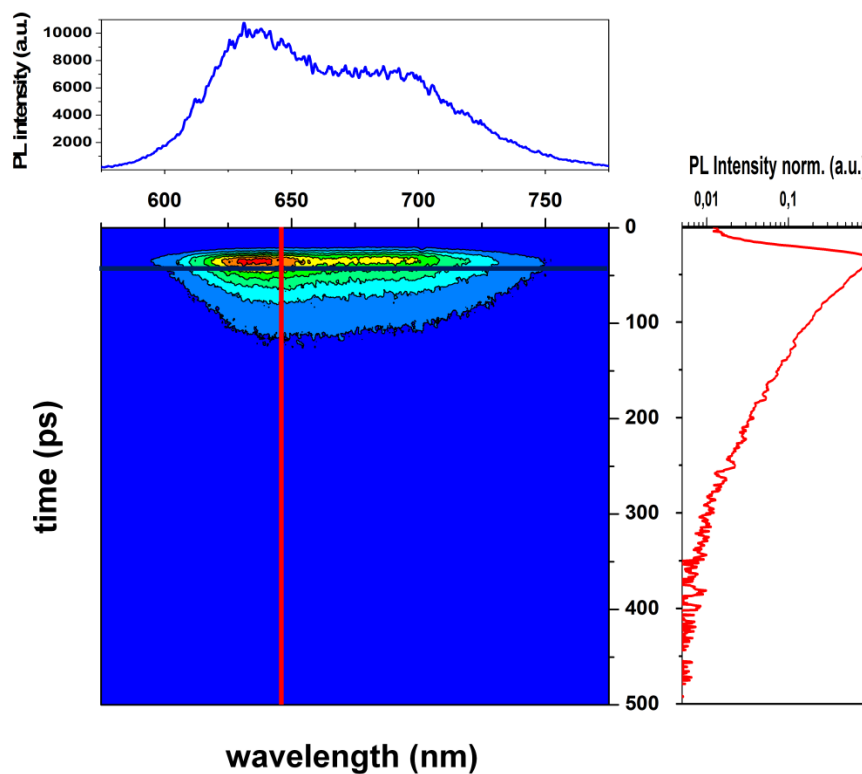
Figure 93: *Streak camera image, with a typical PL spectrum (above, blue) and TRPL dynamics (right side, red). The blue and red lines in the streak image displays the areas from which the data of PL and TRPL are taken.*

7.1.7 Determination of surfactant (4.2.3.2.1)

In order to determine the effectivity of ethanol washing, two 2 cm^2 particle films (on silicon) are used. One of which is washed with ethanol and the other left as prepared. The samples are placed in CHCl$_3$, after dissolving and solvent evaporation, the residue is collected by dissolving in a defined amount of milliQ water. The surfactant in the water phase is detected by measuring the surface tension, using the Du Noüy ring method.

MilliQ water has a surface tension of 72.91 mN·m^{-1}. The surface tension of the washed particle layer is 72.51 mNm^{-1}, whereas the non-washed particle film exhibits a surface tension of 67.27 mN·m^{-1}. This demonstrates that ethanol washing is a good method to remove almost all surfactant out of a colloid layer.

7.1.8 Decreasing of film thickness by reducing solid content (4.2.3.2.2)

Dispersions of lower solid content are prepared as follows: starting from a system with a solid content of 1.6 wt.-%, the dispersion is diluted with a CTAC solution of the same concentration in ratios of 1:2, 1:4, and 1:8.

Upon applying these dispersions to argon plasma activated silicon wafers, the spreading behavior of all dispersions is analogous to that of the undiluted dispersion, as all dispersions feature the same amount of surfactant. Upon particle layer formation, the water evaporation starts on the edge of the silicon wafer. The water frontline then moves to the center of the wafer, leaving behind a fine particle multi-layer. Macroscopic reflection microscope images of the particle layers are shown in **Figure 94**. As mentioned in **section 4.2.2.2**, the use of a dispersion of 1.6 wt.-% leads to a macroscopically homogeneous film. In spite of the good spreading behavior, reducing the solid content leads to a process similar to the "coffee-ring effect". In the beginning of particle film formation, a micrometer multi-layer film, similar to that produced from the undiluted dispersion, is formed. However, at a certain point the layer formation stops and a thin, undefined, and non-closed particle layer remains in the wafer center. This effect is more pronounced when dispersions of lower solid content are used. This indicates that this type of coating requires a certain minimum solid content. Above this content regular assembly of colloids occurs. However, below this content there are not enough particles available for a further ordering and the layer formation stops. This can be

clearly seen in **Figure 94** (**b**) to (**d**), where the bright zone in the middle of the wafer increasingly migrates to the periphery, as the solid content is decreased.
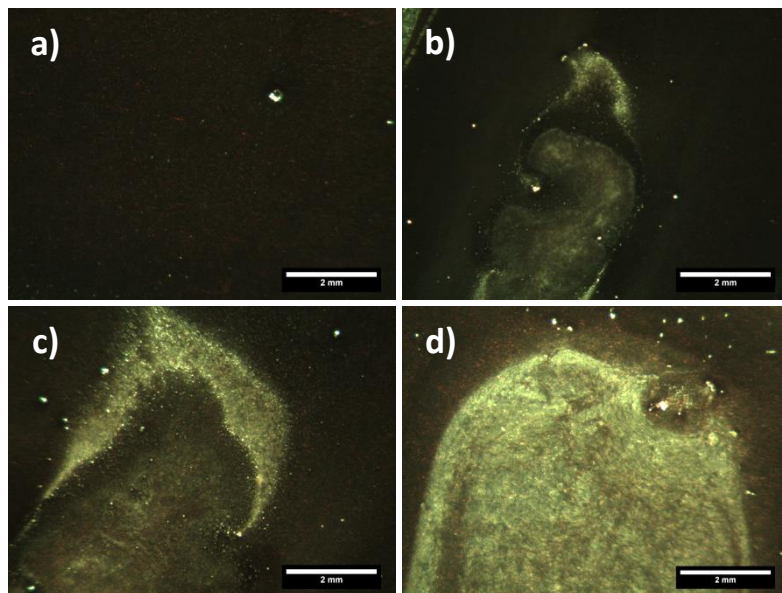
Figure 94: Reflection microscope images of drop cast P3HT/PCBM composite particle films on silicon wafers, made from different solid contents; (a) 1.6, (b) 0.8, (c) 0.4, and (d) 0.2 wt.-%. The dark regions are assigned to thick particle multi-layers, bright areas to depleted particle layers or to the pure silicon substrate.

7.1.9 Beam damage in CS-SEM (section 4.2.3.2.2)

As mentioned in **section 0** and **4.4.2**, the electron beam employed in SEM can degrade the samples. In general, all polymers are affected to a greater or lesser extent by the electron beam.[191] As opposed to conventional SEM, in CS-SEM, only very small areas are observed. In order to achieve acceptable images, a higher electron acceleration is required. For this reason, in CS-SEM the materials are more strongly influenced by beam damage, as shown in **Figure 95** by the example of plasma treated (5 min) and annealed (95 °C) drop cast particle layers. With a short exposure time (< 1 s) almost no beam defects occur, whereas at longer times (> 5 s), the electron beam destroys and removes parts of the melted layer. Hence, the melted colloid film may appear as a structured pristine particle layer. Note that this effect is weaker at higher particle melting, or when PCBM agglomerates are present.
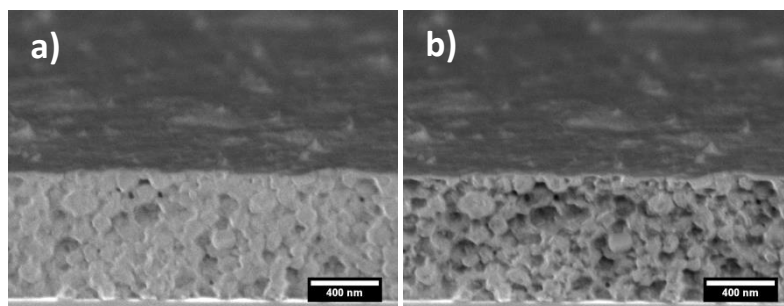
Figure 95: CS-SEM images of plasma treated and annealed drop cast P3HT/PCBM composite particle layers at different beam exposure times; (a) < 1 s and (b) > 5 s.

7.1.10   Influence of water on buffer materials (4.3.1)

The behavior of PEDOT:PSS, MoO$_3$, and Plexcore films upon spin coating is investigated optically by SEM. For this purpose, the film quality and thicknesses before and after spin coating are measured. The spin coating procedure is performed with MilliQ water. Note that the Plexcore film was argon plasma activated before spin coating. The SEM images of the buffers films are shown in **Figure 96**. The PEDOT:PSS layer dissolves during the spin coating process, as shown in (**a**) and (**b**). The initial film thickness is 36 nm, which is reduced by the coating procedure to only 5 nm. Moreover, parts of the PEDOT:PSS film have been completely removed. The same applies to the MoO$_3$ layer, as shown in (**c**) and (**d**). Here, the majority of the film is removed by water. Note that MoO$_3$ is vapor deposited, following the structure of ITO, which is not homogeneous.
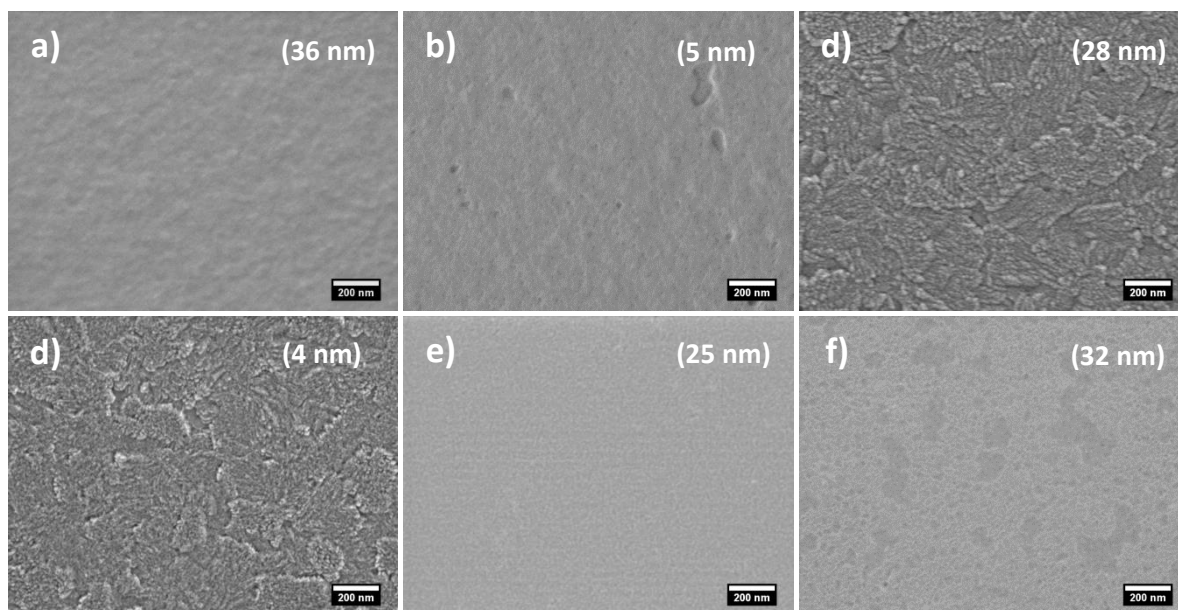
Figure 96: Influence of milliQ water to hole transporting buffer layers upon spin coating; (a and b) PEDOT:PSS, (c and d) MoO$_3$, and (e and f) Plexcore. The average film thicknesses are denoted in brackets.

In contrast, the Plexcore film is not dissolved, but it seems that it swells, as shown in **Figure 96** (**e**) and (**f**). In the course of spin coating, the Plexcore film thickness increases by 7 nm, accompanied by changes in the surface structure. Due to the low water solubility of Plexcore, it is believed that the increase in thickness is a result of a small amount of swelling.

7.1.11 Effect of plasma activation on Plexcore (4.3.1)

The effect of plasma activation on a Plexcore film with respect to the contact angle is shown in **Figure 97**. The activation shows the strongest effect at the beginning of the plasma treatment, lowering the contact angle from 60.8 to 17.2°. Between 5 and 15 s, the effect becomes gradually weaker. After 15 s there is almost no change of the contact angle. This indicates that plasma treatment for longer than 20 s brings no further improvement for the wetting.
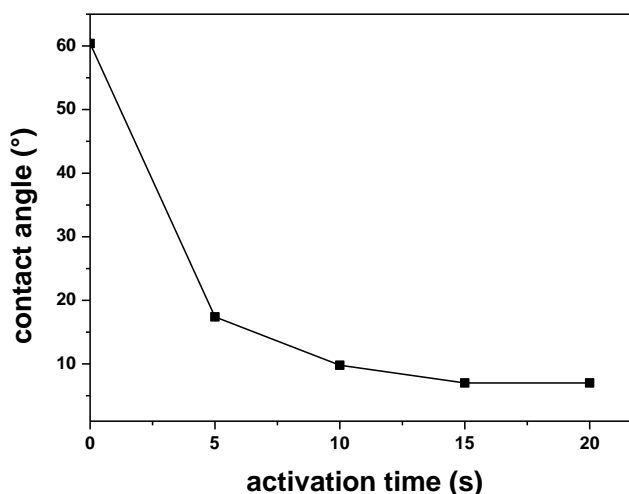
Figure 97: *Effect of argon plasma activation on Plexcore, regarding the contact angle with milliQ water.*

7.1.12 Inverted organic photovoltaics (4.3.1)

The inverted solar cell structure has been introduced in order to allow high-work function metals to be used as electrodes. In conventional solar cell structures, facile oxidation of low-work-function metals, *e.g.* aluminum, causes an inherent instability.[254] The fabrication of a device, featuring an inverted geometry removes the need for an air-sensitive low-work-function electrode, as the electrode is used to collect holes. Typically, silver is used as the counter metal electrode in inverted

OPVs. However, the reversed charge direction requires the use of electron conducting buffer between ITO and the active layer; often ZnO is used as new buffer material.

Aluminum can still be used as counter electrode, but the electrons have to be blocked on their route towards the electrode. As shown in **Figure 98 (a)**, the conduction band of MoO_3 is much higher than the $LUMO_{P3HT}$, blocking electrons, but allowing holes to pass.[255] For this reason and on the account of its ease of deposition, MoO_3 is inserted as an electron blocking layer between the active layer and Al. The resulting device geometry is shown in **Figure 98 (b)**.
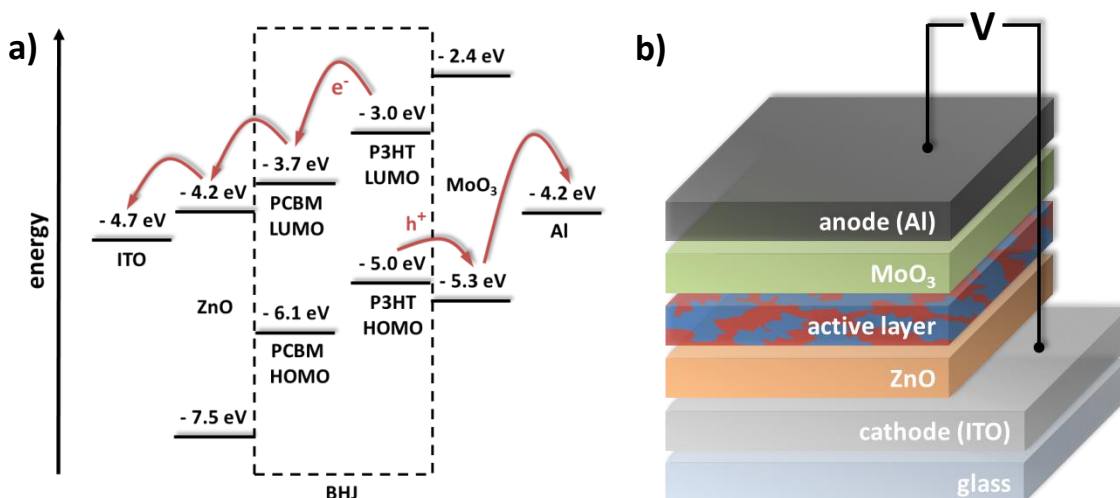
Figure 98: *(a) Energy diagram of an inverted P3HT/PCBM OPV device, containing ZnO, MoO₃, and aluminum. The red arrows show the direction of the charge transport. (b) Schematic setup of an inverted BHJ solar cell. In this case, ITO acts as cathode and aluminum as anode.*

7.1.13   Differential scanning calorimetry (4.3.5)

In **Figure 99** a DSC thermogram of a P3HT/PCBM blend and freeze-dried P3HT/PCBM composite particles is shown; the mass ratio is each 1:1. The glass transition temperature of the P3HT/PCBM blend is 52 °C, preparing composite particles causes a shift to 33 °C. Although the dispersion is dialyzed, there is still some residual SDS inside the system that cannot be removed without destabilizing the dispersion. Thus, the surfactant is embedded between the particles and affects melting/crystallization upon temperature variation, resulting in a lower T_g.
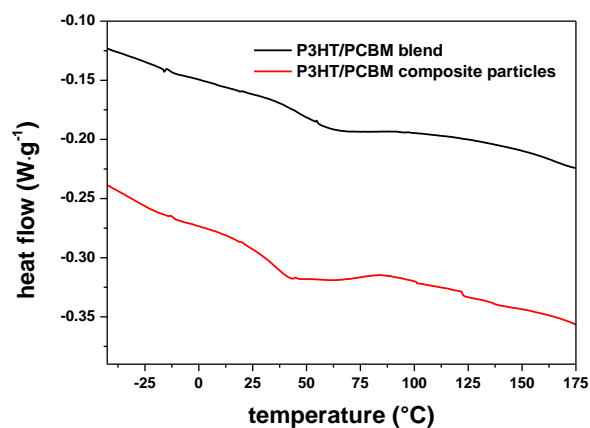
Figure 99: *DSC thermogram of a P3HT/PCBM blend and freeze-dried P3HT/PCBM composite particles. The P3HT:PCBM mass ratio is each 1:1.*

7.1.14   Drop casting on ITO and ZnO substrates (4.3.6)

By using plasma activated ITO and ZnO substrates instead of silicon substrates, drop casting of CTAC stabilized P3HT/PCBM composite particles also leads to close-packed multiple particle layers, as shown in **Figure 100**. The resulting layer thicknesses are in the range of the films coated on silicon substrates.
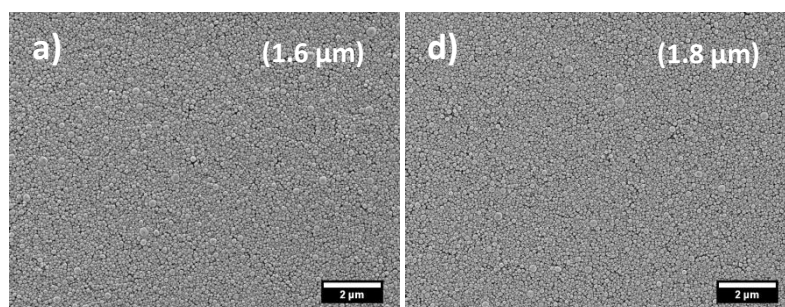
Figure 100: *Drop casted P3HT/PCBM composite particle films on activated (a) ITO and (b) ZnO substrate. The average film thicknesses are denoted in brackets.*

7.1.15   Spin coated multi-layer particle films (4.3.7)

The preparation of multi-particle films made by spin coating is very sensitive to the substrate. This means that imperfections of the subjacent layer are carried to the next layer. As the reflection microscope images in **Figure 101** clarify, this effect is not limited to the microscopic film structure. The macroscopic film quality is also decreased upon increasing the number of layers.
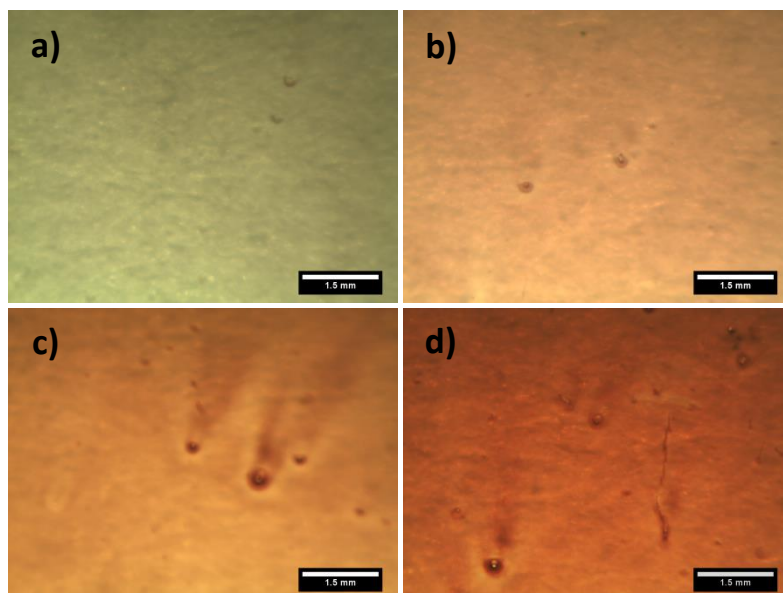
Figure 101: *Reflection microscope images of PBOPVs consisting of (a) monolayer, (b) bilayer, (c) three layers, and (d) four layers. The discrepancy in color is a result of differences in the film thicknesses, leading to different light reflections.*

7.1.16 Chemical structure of low band gap polymers (4.3.8.2)

Figure 102 shows the chemical structures of poly[4,8-bis(2-ethylhexyloxy)benzo(1,2-b:4,5-b')dithiophene-alt-5,6-bis(octyloxy)-4,7-di(thiophene-2-yl)(2,1,3-benzothiadiazole)-5,5'-diyl] (**P1**), poly[(4,4'-bis(2-ethylhexyl)dithieno[3,2-b:2',3'-d]silole)-2,6-diyl-alt-(2,1,3-benzothiadiazole)-4,7-diyl] (**P2**), and poly[2,3-bis-(3-octyloxyphenyl)quinoxaline-5,8-diyl-alt-thiophene-2,5-diyl] (**P3**).
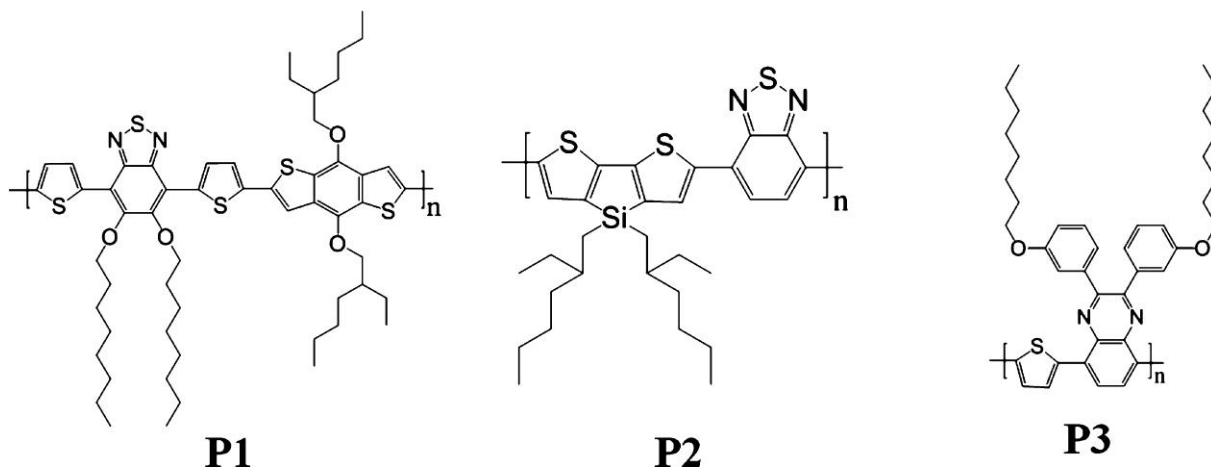
Figure 102: *Chemical structure of P1, P2, and P3, taken from the work of Andersen.*[22]

7.1.17 Winsor phases of PS microemulsions (4.4.1)

For the preparation of "small" particles, the microemulsion technique with PS (100 mg), containing 5% P3HT (organic phase staining) is used. The polymers are dissolved in toluene, the resulting solution is handled as a pure toluene phase. According to the ternary toluene/water/SDS-butanol phase diagram in **Figure 103** (**a**),[269] the conditions for a microemulsion were also used for the particle preparation.

The estimated total amount of the microemulsion is 10 g. However, butanol lowers the solubility of PS and P3HT in toluene. Regarding the solubility, a minimum of 2 g toluene is required. With respect to dialysis, the maximum amount of the surfactant phase is 4 g. Therefore, the section of the phase diagram, corresponding to a microemulsion, is highly restricted (red area). Three different compositions (A, B, and C) were tested, the weight portions for these are listed in **Figure 103** (**b**).

sample	water	toluene	$^1/_3$ SDS + $^2/_3$ butanol
	(g)	(g)	(g)
A	4	3	3
B	5	2	3
C	3	3	4
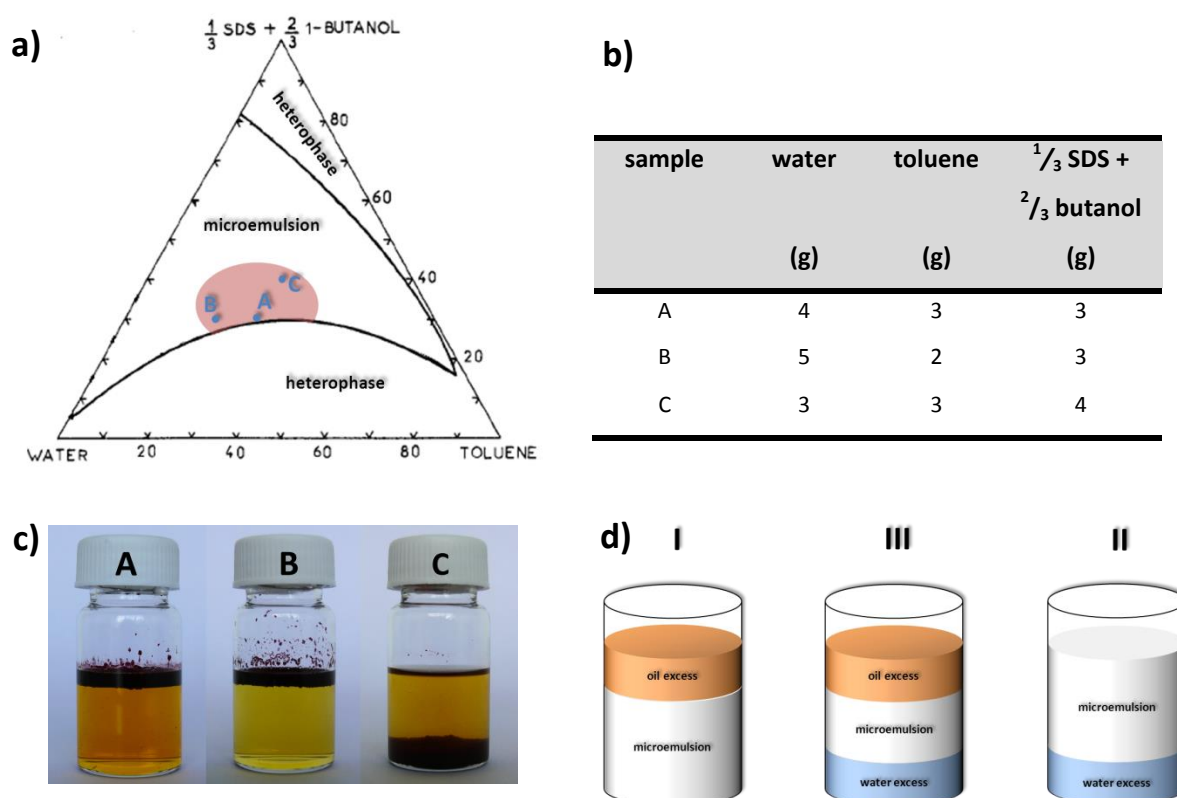
Figure 103: (a) Ternary phase diagram of a water/toluene/SDS-butanol system, taken from the work of Minero.[269] (b) Weight fractions of the compositions A, B, and C. (c) Pictures of the corresponding emulsions. (d) Characterization of the Winsor phases. Winsor I indicate a water microemulsion phase coexisting, with a surfactant-poor oil phase. Winsor II is an oil microemulsion phase, coexisting with a surfactant-poor water phase. Winsor III represents a microemulsion middle phase in combination with water and oil surfactant-poor phases. It should be noted that a pure microemulsion is also called Winsor IV.[262]

The pictures of the resulting emulsions are shown in **Figure 103** (**c**). Apparently, the compositions A, B, and C do not lead to microemulsions. Winsor studied the behavior of microemulsions and classified the observations,[262] resulting in the so called Winsor phases, shown in **Figure 103** (**d**). With regard to these phases, the emulsions A, B, and C correspond to Winsor I. The emulsion C appears to resemble Windsor III, since the polymers are precipitated and a small amount of the organic phase remains as the upper phase. As indicated by the P3HT staining, only a minor amount of P3HT and thus PS are dispersed in the microemulsion part. The majority remains trapped in the toluene phase. It might appear that a microemulsion may be obtained by using considerably more SDS and butanol. However, in C, a higher amount of the surfactants are used, nevertheless, resulting in emulsified toluene and phase separated polymers.

The probable reason for the failure of this method is the fact that microemulsions are spontaneously formed systems. The phases need a high degree of diffusivity to form a homogeneous heterophase system. Since polymers diffuse very slowly, they remain in the toluene phase and do not form a microemulsion. Consequently, microemulsions cannot be used for particle preparation via the solvent evaporation technique.

7.2 Abbreviations

A   electron acceptor

AE   Auger electrons

AFM   atomic force microscopy

Al   aluminum

BE   backscattered electrons

BHJ   bulk heterojunction

CB   chlorobenzene

CHCl$_3$ chloroform

CLSM   confocal laser scanning microscopy

CMC   critical micelle concentration

CN-MEH-PPV	poly-[2-methoxy-5-(2'-ethylhexyloxy)-1,4-(1-cyanovinylene)phenylene]
CS	cross section
CTAC	cetyltrimethylammonium chloride
D	electron donor
DLS	dynamic light scattering
DSC	differential scanning calorimetry
EDX	dispersive X-ray spectroscopy
EELS	electron energy loss spectroscopy
EQE	external quantum efficiency
ESI	electron spectroscopic imaging
F8TB	poly(9,9'-dioctylfluorene-co-benzothiadiazole)
HOMO	highest occupied molecule orbital
IPCE	incident photon-to-converted-electron efficiency
ITO	indium tin oxide
JP	Janus particle
LEDs	light-emitting diodes
LUMO	lowest unoccupied molecular orbital
MDMO-PPV	poly[2-methoxy-5-(3',7'-dimethyloctyloxy)]-1,4-phenylenevinylene
milliQ	ultrapure water generated by a purification system from Millipore
MIM	metal-insulator-metal
MnO_3	molybdenum(vi) oxide
NREL	National Renewable Energy Laboratory
OHJ	ordered heterojunction
OPV	organic photovoltaic
OsO_4	osmium tetroxide

OWRK	Owens-Wend-Rabel-Kaelble
P1	poly[4,8-bis(2-ethylhexyloxy)benzo(1,2-b:4,5-b')dithiophene-alt-5,6-bis(octyloxy)-4,7-di(thiophene-2-yl)(2,1,3-benzothiadiazole)-5,5'-diyl]
P2	poly[(4,4'-bis(2-ethylhexyl)dithieno[3,2-b:2',3'-d]silole)-2,6-diyl-alt-(2,1,3-benzothiadiazole)-4,7-diyl]
P3	poly[2,3-bis-(3-octyloxyphenyl)quinoxaline-5,8-diyl-alt-thiophene-2,5-diyl]
P3HT	poly(3-hexylthiophene-2,5-diyl)
PBOPV	particle-based organic photovoltaic
PCBM	[6,6]-phenyl-C61-butyric acid methyl ester
PCE	power conversion efficiency
PEDOT:PSS	poly(3,4-ethylenedioxythiophene)-poly(styrenesulfonate)
PFB	poly(9,9'-dioctylfluorene-co-bis-N,N'-(4-butylphenyl)-bis-N,N'-phenyl-1,4-phenylenediamine
PL	photoluminescence
Plexcore	poly(thiophene-3-[2[(2-methoxyethoxy)ethoxy]-2,5-diyl)
PLLA	poly(L-lactid)
PMMA	poly(methyl methacrylate)
PS	polystyrene
PV	photovoltaic
RR	regioregular
RRa	regiorandom
SDS	sodium dodecyl sulfate
SE	secondary electrons
SEM	scanning electron microscopy
SPOPV	solution-processed organic photovoltaic
TEM	transmission electron microscopy

THF   tetrahydrofuran

TRPL   time resolved photoluminescence

UV   ultraviolet

Vis   visible

XRD   X-ray diffraction

ZnO   zinc oxide

7.3 Symbols

γ interfacial energy/surface energy/surface tension

γ^D dispersed part of interfacial energy/surface energy/surface tension

γ^P polar part of interfacial energy/surface energy/surface tension

δ   solubility parameter

ε extinction coefficient

θ diffraction angle/contact angle

λ   wavelength

Π   surface pressure

φ volume ratio

χ   Flory-Huggins parameter

A interfacial area/absorbance

c concentration

d interplanar distance

E_g energy gap

FF   fill factor

ΔG Gibbs free energy

ΔG_{mix}	Gibbs free energy of mixing
ΔH_{mix}	enthalpy of mixing
I	current/intensity of transmitted light
I_0	intensity of incident light
J	current density
J_{SC}	short circuit density
J_{max}	current density at maximum power
l	path length
n	number of moles/integer multiple
P_{in}	incident light power
P_{La}	Laplace pressure
P_{max}	maximum power
r	radius
R	gas constant
R_s	series resistor
R_{sh}	shunt resistor
S	spreading coefficient
S_0	electronic ground state
S_1	first excited electronic state
ΔS_{mix}	entropy of mixing
T	temperature
T_1	first excited electronic triplet state
T_c	critical temperature
T_g	glass transitions temperature
V	voltage/volume

V_{max}	voltage at maximum power
V_{OC}	open circuit voltage
V_R	reference volume
W_F	work function
wt.-%	solid content

8 Acknowledgments

The acknowledgements are only available in the printed version.

9 References

[1]   U.S. Energy Information Administration, *International Energy Outlook* **2011**.

[2]   C. Brabec, V. Dyakonov, U. Scherf, *Organic Photovoltaics: Materials, Device Physics and Manufacturing Technologies*, Wiley-VCH, Weinheim, **2008**.

[3]   N. Nakicenovic, N.A. Grubler, A. McDonald, *Global Energy Perspectives*, Cambridge University Press, Cambridge, **1998**.

[4]   D.M. Chapin, C.S. Fuller, G.L. Pearson, *J. Appl. Phys.* **1954**, 25, 676.

[5]   E.A. Alsema, *Prog. Photovolt. Res. Appl.* **2000**, 8, 17.

[6]   S.S. Sun, N.S. Sariciftci, *Organic Photovoltaics: Mechanisms, Materials and Devices*, CRC Press, Boca Raton, **2005**.

[7]   F.C. Krebs, *Sol. Energ. Mat. Sol. Cells* **2009**, 93, 465.

[8]   G. Hadziioannou, P.F. van Hutten, *Semiconducting Polymers: Chemistry, Physics and Engineering*, Wiley-VCH, Weinheim, **1999**.

[9]   C. Winder, N.S. Sariciftci, *J. Mater. Chem.* **2004**, 14, 1077.

[10]   P.W.M. Blom, M.C.J.M. Vissenberg, *Mater. Sci. Eng., R* **2000**, 27, 5.

[11]   A. Facchetti, *Mater. Today* **2007**, 10, 28.

[12]   A.Kraft, A.C. Grimsdale, A.B.Holmes, *Angew. Chem. Int. Ed*. **1998**, 37, 402.

[13]   K.M. Coakley, M.D. McGehee, *Chem. Mater.* **2004**, 16, 4533.

[14]   G. Lagaly, O. Schulz, R. Zimehl, *Dispersionen und Emulsionen*, Steinkopf, Darmstadt, **1997**.

[15]   H.S. Nalwa, *Handbook of Nanostructured Materials and Nanotechnology - Volume 5*, Academic Press, San Diego, **2000**.

[16]   M. Antonietti, K. Tauer, *Macromol. Chem. Phys.* **2003**, 204, 207.

[17]   P.B. O'Donnell, J.W. McGinity, *Adv. Drug Delivery Rev.* **1997**, 28, 25.

[18]   K. Landfester, *Macromol. Rapid Comm.* **2001**, 22, 896.

[19]   M. Jørgensen, K. Norrman, F.C. Krebs Sol. *Energy Mater. Sol. Cells* **2008**, 92, 686.

[20]   T.T. Larsen-Olsen, T.R. Andersen, B. Andreasen, A.P.L. Böttiger, E. Bundgaard, K. Norrman, J.W. Andreasen, M. Jørgensen, F.C. Krebs, *Energy Mater. Sol. Cells* **2012**, 97, 43.

[21]   F.C. Krebs, *Stability and Degradation of Organic and Polymer Solar Cells*, Wiley, Hoboken, **2012**.

[22]   T.R. Andersen, T.T. Larsen-Olsen, B. Andreasen, A.P.L. Böttiger, J.E. Carlé, M. Helgesen, E. Bundgaard, K. Norrman, J.W. Andreasen, M. Jørgensen, F.C. Krebs, *ASC nano* **2011**, 5, 4188.

[23]   K. Landfester, R. Montenegro, U. Scherf, R. Günther, U. Asawapirom, S. Patil, D. Neher, T. Kietzke, *Adv. Mater* **2002**, 9, 14.

[24]   W. Ma, C. Yang, X. Gong, K. Lee, A.J. Heeger, *Adv. Funct. Matter* **2005**, 15, 1617.

[25]   H. Hoppe, M. Niggemann, C. Winder, J. Kraut, R. Hiesgen, A. Hinsch, D. Meissner, N.S. Sariciftci, *Adv. Funct. Mater.* **2004**, 14, 1005.

[26]   R.A.L. Jones, L.J. Norton, E.J. Kramer, F.S Bates, P. Wiltzius, *Phys. Rev. Lett.* **1991**, 66, 1326.

[27]   M. Böltau, S. Walheim, J. Mlynek, G. Krausch, U. Steiner, *Nature* **1998**, 391, 877.

[28]   G. Krausch, *Mater. Sci. Eng., R* **1995**, 14, 1.

[29]   S. Walheim, M. Böltau, J. Mlynek, G. Krausch, U. Steiner, *Macromolecules* **1997**, 30, 4995.

[30]   P. Müller-Buschbaum, J.S. Gutmann, M. Stamm, *Macromolecules* **2000**, 33, 4886.

[31]   J.J.M. Halls, A.C. Arias, J.D. MacKenzie, W. Wu, M. Inbasekaran, P. Woo, R.H. Friend, *Adv. Mater.* **2000**, 12, 498.

References

[32] S.E. Shaheen, C.J. Brabec, N.S. Sariciftci, F. Padinger, T. Fromherz, J.C. Hummelen, *Appl. Phys. Lett.* **2000**, 78, 841.

[33] F.C. Chen, C.J. Ko, J.L. Wu, W.C. Chen, *Energy Mater. Sol. Cells* **2010**, 94, 2426.

[34] J.H. Park, J.S. Kim, J.H. Lee, W.H. Lee, K. Cho, *J. Phys. Chem. C* **2009**, 113, 17579.

[35] T. Kietzke, D. Neher, K. Landfester, R. Montenegro, U. Scherf, *Nat. Mater.* **2003**, 2, 408.

[36] T. Kietzke, D. Neher, M. Kumke, R. Montenegro, K. Landfester, U. Scherf, *Macromolecules* **2004**, 37, 4882.

[37] M.T. Dang, L. Hirsch, G. Wantz, *Adv. Mater.* **2011**, 23, 3597.

[38] E.D. Sudol, M.S. El-Aasser, *Emulsion Polymers and Emulsion Polymerization*, Wiley, Chichester, **1997**.

[39] H.D. Dörfler, *Grenzflachen und kolloid-disperse Systeme*, Springer, Berlin, **2002**.

[40] W.Z. Ostwald, *Phys. Chem.* **1901**, 37, 385.

[41] W.I. Higuchi, J. Misra, *J. Pharm. Sci.* **1962**, 51, 459.

[42] J.A. Webster, M.E. Cates, *Langmuir* **1998**, 14, 2086.

[43] P. Kumar, K.L. Mittal, *Handbook of Microemulsions: Science and Technology*, Dekker, New York, **1999**.

[44] M.J. Lawrence, G.D. Rees, *Adv. Drug Delivery Rev.* **2000**, 45, 89.

[45] Y.J. Chou, M.S. El-Aasser, J.W. Vanderhoff, *J. Dispersion Sci. Technol.* **1980**, 1, 129.

[46] S. Shaw, *Introduction to Colloid and Surface Chemistry*, Butterworth & Co, London, **1986**.

[47] B. Abismail, J.P. Canselier, A.M. Wilhelm, *Ultrason. Sonochem.* **1999**, 6, 75.

[48] P. Walstra, *Chem. Eng. Sci.* **1993**, 48, 333.

[49] H. Karbstein, H. Schubert, *Chem. Eng. Process.* **1995**, 34, 211.

[50] W. Lauterborn, C.D. Ohl, *Ultrason. Sonochem.* **1997**, 4, 65.

[51] K. Landfester, N. Bechthold, F. Tiarks, M. Antonietti, *Macromolecules* **1999**, 32, 5228.

[52] K. Landfester, *Angew. Chem. Int. Ed.* **2009**, 48, 4488.

[53] R.D. McCullough, R.D. Lowe, *J. Chem. Soc., Chem. Commun*. **1992**, 1, 70.

[54] T.A. Chen, X. Wu, R. D. Rieke, *J. Am. Chem. Soc.* **1995**,117, 233.

[55] F. Caruso (Ed), *Colloids and Colloids Assemblies*, Wiley-VCH, Weinheim, **2004**.

[56] I.D. Rosca, F. Watari, M. Uo, *J. Controlled Release* **2004**, 99, 271.

[57] M. Urban, A. Musyanovych,.K. Landfester, *Macromol. Chem. Phys.* **2009**, 210, 961.

[58] L.A. Utracki, *Polymer Alloys and Blends: Thermodynamics and Rheologie*, Hanser, München, **1989**.

[59] P.L. Flory, *J. Chem. Phys.* **1941**, 9, 660.

[60] M.L. Huggins, *J. Chem. Phys.* **1941**, 9, 440.

[61] P.C. Hiemenz, *Polymer Chemistry*, Dekker, New York, **1984**.

[62] J.H. Hildebrand, R.L. Scott, *The Solubility of Nonelectrolytes*, Van Nostrand-Reinhold, Princeton, **1950**.

[63] J.H. Hildebrand, R.L. Scott, *Regular Solutions*, Prentice-Hall, Englewood Cliffs, **1962**.

[64] J. Colombani, J. Bert, *J. Non-Equilib. Thermodyn.* **2004**, 29, 389.

[65] E.P. Favvas, A.C. Mitropoulos, *Journal of Engineering Science and Technology Review* **2008**, 1, 25.

[66] R.L. Scott, *J. Chem. Phys* **1949**, 17, 279.

[67] H. Tompa, *Trans. Frarady Soc.* **1949**, 45, 1142.

[68] S. Krause, *Pure Appl. Chem.* **1986**, 58, 1553.

[69] L.M. Robeson, *Polymer Blends: A Comprehensive Review*, Hanser, München, **2007**.

[70] G.M. Bristow, *J. Appl. Polym. Sci*. **1959**, 11, 120.

[71] M. Okubo, N. Saito, T. Fujibayashi, *Colloid Polym. Sci.* **2005**, 283, 691.

[72]   S. Torza, S.G Mason, *J. Colloid Interface Sci*. **1970**, 33, 67.

[73]   D. Bonn, J. Eggers, J. Indekeu, J. Meunier, E. Rolley, *Rev. Mod. Phys.* **2009**, 81, 739.

[74]   J. Berg, D.C. Sundberg, B. Kronberg, *Polym. Mater. Sci. Eng.* **1986**, 54, 367.

[75]   C.L. Winzor, D.C. Sundberg, *Polymers* **1987**, 33, 3797.

[76]   D.C. Sundberg, A.P. Casassa, J. Pantazopoulos, M.R. Muscato, B. Kronberg, J. Berg, *J. Appl. Polym. Sci.* **1990**, 41, 1425.

[77]   C.L. Winzor, D.C. Sundberg, *Polymers* **1992**, 33, 4269.

[78]   Y. Chen, V. Dimonie, M.S. El-Aasser, *J. Appl. Polym. Sci*. **1992**, 46, 691.

[79]   E.J. Sundberg, D.C. Sundberg, *J. Appl. Polym. Sci.* **1993**, 47, 1277.

[80]   A. Walther, A.H.E. Müller, *Soft Matter* **2008**, 4, 663.

[81]   L.J. Gonzalez-Ortiz, J.M. Asua, *Macromolecules* **1995**, 28, 3135.

[82]   V. Herrera, Z. Palmillas, R. Pirri, Y. Reyes, J.R. Leiza, J.M. Asua, *Macromolecules* **2010**, 43, 1356.

[83]   V.L. Dimonie, E.S. Daniels, L. Shaffer, M.S. El-Aasser, *Control of Particle Morphology in Emulsion Polymerization and Emulsion Polymers*, Wiley, New York, **1997**.

[84]   S. Lee, A. Rudin, *J. Polym. Sci., Part A: Polym. Chem.* **1992**, 30, 2211.

[85]   K. Matyjaszewski, Y. Gnanou, L. Leibler, *Macromolecular Engineering: Precise Synthesis, Materials Properties and Applications*, Wiley-VCH, Weinheim, **2007**.

[86]   M.R. Muscanto, D.C. Sundberg, *J. Polym. Sci., Part B: Polym. Phys.* **1991**, 29, 1021.

[87]   M.F. Fowkes, *Ind. Eng. Chem.* **1964**, 56, 40.

[88]   S. Muroi, H. Hashimoto, K. Hosoi, *J. Polym. Sci., Part A: Polym. Chem.* **1984**, 22, 1365.

[89]   Y.C. Chen, V. Dimonie, M.S. El-Aasser, *J. Appl. Polym. Sci.* **1992**, 45, 487.

[90]   N. Saito, Y. Kagari, M. Okubo, *Langmuir* **2006**, 22, 9397.

[91]   J. Berg, D.C. Sundberg, B.J. Kronberg, *J. Microencapsul.* **1989**, 6, 327.

[92]   M. Okubo, K. Kanaida, T. Matsumoto, *Colloid. Polym. Sci.* **1987**, 265, 876.

[93]   M. Okubo, Y. Katsuta, T. Matsumoto, *J. Polym. Sci., Part C: Polym. Lett.* **1982**, 20, 45.

[94]   D.I. Lee, T. Ishikawa, *J. Polym. Sci., Part A: Polym. Chem.* **1983**, 21, 147.

[95]   C. Casagrande, M. Veyssie, *C. R. Acad. Sci.* **1988**, 306, 1423.

[96]   P.D. de Gennes, *Angew. Chem.* **1992**, 104, 856.

[97]   B.P. Binks, *Curr. Opin. Colloid Interface Sci.* **2002**, 7, 21.

[98]   A. Walther, M. Hoffmann, A.H.E. Müller, *Angew. Chem.* **2008**, 120, 723.

[99]   Q. Xu, X. Kang, R.A. Bogomolni, S. Chen, *Langmuir* **2010**, 26, 14923.

[100]   M. Paulus, P. Degen, T. Brenner, S. Tiemeyer, B. Struth, M. Tolan, H. Rehage, *Langmuir* **2010**, 26, 15945

[101]   B.P. Binks, P.D.I. Fletcher, *Langmuir* **2001**, 17, 4708.

[102]   S. Gangwal, O.J. Cayre, M.Z. Bazant, O.D. Velev, *Phys. Rev. Lett.* **2008**, 100, 058302.

[103]   J.R. Howse, R.A.L. Jones, A.J. Ryan, T. Gough, R. Vafabakhsh, R. Golestanian, *Phys. Rev. Lett.* **2007**, 99, 048102.

[104]   E. Becquerel, *C. R. Acad. Sci.* **1839**, 9, 561.

[105]   W.G. Adams, R.E. Day, *Proc. R. Soc.* **1877**, A25, 113.

[106]   C.E. Fritts, *Am. J. Sci.* **1883**, 26, 465.

[107]   J.H. Zhao, A.H. Wang, M.A. Green, F. Ferrazza, *Appl. Phys. Lett.* **1998**, 73, 1991.

[108]   M.A. Green, K. Emery, Y. Hishikawa, W. Warta, *Prog. Photovolt: Res. Appl*. **2011**; 19, 84.

[109]   C.W. Tang, Appl. Phys. Lett. **1986**, 48, 183.

[110]   H. Spanggaard, F.C. Krebs, *Sol. Energ. Mat. Sol. Cells* **2004**, 83, 125.

[111]   M. Grätzel, *Nature* **2001**, 414, 338.

References

[112]   http://www.heliatek.com/wp-content/uploads/2013/01/130116_PR_Heliatek_achieves_record_cell_effiency_for_OPV.pdf

[113]   http://www.nrel.gov/ncpv/images/efficiency_chart.jpg

[114]   W. Shockley, H.J. Queisser, *J. Appl. Phys.* **1961**, 32, 510.

[115]   A. De Vos, *J. Phys. D: Appl. Phys.* **1980**, 13, 839.

[116]   B. Kippelen, J.L. Bredas, *Energy Environ. Sci.* **2009**, 2, 251.

[117]   L. Schmidt-Mende, U. Bach, R. Humphry-Baker, T. Horiuchi, H. Miura, S. Ito, S. Uchida, M. Grätzel, *Adv. Mater.* **2005**, 17, 813.

[118]   B. O'Regan, M. Grätzel, *Nature* **1991**, 353, 737.

[119]   W.J.E. Beek, M.M. Wienk, R.A.J. Janssen, *Adv. Mater.* **2004**, 16, 1009.

[120]   W.U. Huynh, J.J. Dittmer, A.P. Alivisatos, *Science* **2002**, 295, 2425.

[121]   D.C. Olson, S.E. Shaheen, R.T. Collins, D.S. Ginley, *J. Phys. Chem. C* **2007**, 111, 16670.

[122]   A.C. Arango, L.R. Johnson, V.N. Bliznyuk, Z. Schlesinger, S.A. Carter, H.H. Hoerhold, *Adv. Mater.* **2000**, 12, 1689.

[123]   K.M. Coakley, Y.X. Liu, M.D. McGehee, K.L. Frindell, G.D. Stucky, *Adv. Funct. Mater.* **2003**, 13, 301.

[124]   P. Peumans, S. Uchida, S.R. Forrest, *Nature* **2003**, 425, 158.

[125]   C.R. McNeill, A. Abrusci, J. Zaumseil, R. Wilson, M.J. McKiernan, J.H. Burroughes, J.J.M. Halls, N.C. Greenham, R.H. Friend, *Appl. Phys. Lett.* **2007**, 90, 193506.

[126]   C.R. McNeill, N.C. Greenham, *Adv. Mater.* **2009**, 21, 3840.

[127]   T. Kietzke, H.H. Horhold, D. Neher, *Chem. Mater.* **2005**, 17, 6532.

[128]   S.M. Lindner, S. Hüttner, A. Chiche, M. Thelakkat, G Krausch, *Angew. Chem. Int. Ed.* **2006**, 45, 3364.

[129]   A.B. Tamayo, B. Walker, T.Q. Nguyen, *J. Phys. Chem. C* **2008**, 112, 11545.

[130]   B. Walker, B. Tamayo, X.D. Dang, P. Zalar, J.H. Seo, A. Garcia, M. Tantiwiwat, T.Q. Nguyen, *Adv. Funct. Mater.* **2009**, 19, 3063.

[131]   http://rredc.nrel.gov/solar/spectra/am1.5/

[132]   H. Shirakawa, E.J. Louis, A.G. MacDiarmid, C.K. Chiang, A.J. Heeger, *J. Chem. Soc. Chem. Commun.* **1977**, 16, 578.

[133]   R.E. Peierls, *Quantum theory of solids*, Clarendon, Oxford, **1955**.

[134]   G. Barbarella, M. Melucci, G. Gotgui, *Adv. Mater.* **2005**, 17, 1581.

[135]   J.L. Reddinger, J.R. Reynolds, *Adv. Polym. Sci.* **1999**, 145, 57.

[136]   A. Heeger, *Rev. Mod. Phys.* **2001**, 73, 681.

[137]   D.L. Wise, G.E. Wink, D.J. Trantolo, T.M. Cooper, J.D. Gresser, *Electrical and optical polymer systems*, Dekker, New York, **1998**.

[138]   H.G. Wagemann, H. Eschrich, *Photovoltaik: Solarstrahlung und Halbleitereigenschaften, Solarzellenkonzepte und Aufgaben*, Vieweg+Teubner, Wiesbaden, **2007**.

[139]   A. Dhanabalan, J.K.J. van Duren, P.A. van Hal, J.L.J. van Dogen, R.A.J. Janssen, *Adv. Funct. Mater.* **2001**, 11, 255.

[140]   H. Neugebauer, C.J. Brabec, N.S. Sariciftci, R. Kiebooms, F. Wudl, S. Luzzati, *J. Chem. Phys.* **1999**, 110, 12108.

[141]   Y.M. Chang, W.F. Su, L. Wang, *Sol. Energ. Mat. Sol. Cells* **2008**, 92, 761.

[142]   H. Hoppe, N.S. Sariciftci, *J. Mater. Res.* **2004**, 19, 1924.

[143]   C. Jonda, A.B.R. Mayer, U. Stolz, A. Elschner, A. Karbach, *J. Mater. Sci.* **2000**, 35, 5645.

[144]   A. Elschner, F. Bruder, H.W. Heuer, F. Jonas, A. Karbach, S. Kirchmeyer, S. Thurm, *Synthetic Met* **2000**, 111, 139.

[145]   S.A. Carter, M. Angelopoulos, S. Karg, P.J. Brock, J.C. Scott, *Appl. Phys. Lett.* **1997**, 70, 2067.

[146] G.A. Chamberlain, P.J. Cooney, S. Dennison, *Nature* **1981**, 289, 45.

[147] A.K. Ghosh, T. Feng, *J. Appl. Phys.* **1978**, 49, 5982.

[148] Y. Park, V. Choong, Y. Gao, B.R. Hsieh, C.W. Tang, *Appl. Phys. Lett.* **1996**, 68, 2699*.*

[149] H.B. Michaelson, *J. Appl. Phys.* **1997**, 48, 4729.

[150] C. Deibel, V. Dyakonov, *Rep. Prog. Phys.* **2010**, 73, 096401.

[151] B.A. Gregg, M.C. Hanna, *J. Appl. Phys.* **2003**, 93, 3605.

[152] L.W. Barbour, R.D. Pensack, M. Hegadorn, S. Arzhantsev, J.B. Asbury, *J. Phys. Chem. C* **2008**, 112, 39266.

[153] E. Collini, G.D. Scholes, *Science* **2009**, 323, 369.

[154] C. Deibel, T. Strobel, V. Dyakonov, *Adv. Mater.* **2010**, 22, 4097.

[155] T.R. Clarke, J.R. Durrant, *Chem. Rev.* **2010**, 110, 6736.

[156] L. Onsager, *Phys. Rev.* **1938**, 54, 554.

[157] C.L. Braun, *J. Chem. Phys* **1984**, 80, 4157.

[158] H. Bässler, *Phys. Status Solidi B* **1993**, 175, 15.

[159] Y. Olivier, V. Lemaur, J.L. Brédas, J. Cornil*, J. Phys. Chem. A* **2006**, 110, 6356.

[160] L.J.A. Koster, E.C.P. Smits, V.D. Mihailetchi, P.W.M. Blom, *Phys. Rev* B **2005**, 72, 08205.

[161] S.M. Sze, *Physics of Semiconductor Devices*, John Wiley & Sons, New York, **1981**.

[162] I.D. Parker, *J. Appl. Phys.* **1994**, 75, 1656.

[163] T. Kietzke, *Advances in OptoElectronics* **Volume 2007**, Article ID 40285.

[164] J. Rostalski, D. Meissner, *Sol. Energy Mater. Sol. Cells* **2000**, 61,87.

[165] H. Kim, S.H. Jin, H. Suh, K. Lee*, Proc. SPIE* **2004**, 5215, 111.

[166] C.J. Brabec, A. Cravino, D. Meissner, N.S. Sariciftci, M.T. Rispens, L. Sanchez, J.C. Hummelen, T. Fromherz, *Thin Solid Films* **2002**, 403,368.

[167] J.J. van Duren, J. Loos, F. Morissey, C.M. Leewis, K.P. Kivits, L.J. Vanzendoorn, M.T. Rispens, J.C. Hummelen, R.A.J. Janssen, Adv. Funct. Mater. **2002**, 12, 665.

[168] C.W. Bulle-Lieuwma, W.J.H. van Genip, J.K.J. van Duren, P. Jankheim, R. Janssen, J.W. Niemantsverdiet, *Appl. Surf. Sci.* **2003**, 203, 547.

[169] M. Pope, C.E. Swenberg, *Electronic Processes in Organic Crystals and Polymers*, Oxford University Press, Oxford, **1999**.

[170] R. Mauer, I.A. Howard, F. Laquai, *J. Phys. Chem. Lett.* **2010**, 1, 3500.

[171] R.J. Kline, M.D. McGehee, E.N. Kadnikova, J.S. Liu, J.M.J. Frechet, *Adv Mater.* **2003**, 15, 1519.

[172] L.L. Chua, J. Zaumseil, J.F. Chang, E.C.W. Ou, P.K.H. Ho, H. Sirringhaus, R.H. Friend, *Nature* **2005**, 434, 194.

[173] S.M. Sze, *VLSI Technology*, McGraw-Hill, New York, **1988**.

[174] H. Hoppe, N.S. Sariciftci, D. Meissner, *Mol. Cryst. Liq.* Cryst. *Sci. Technol., Sect. A.* **2002**, 385, 113.

[175] J.J.M. Halls, K. Pichler, R.H. Friend, S.C. Moratti, A.B. Holmes, *Appl.Phys. Lett.* **1996**, 68, 3120.

[176] J.M. Nunzi,. *C. R. Physique* **2002**, 3, 523.

[177] A. Mozer, N.S. Sariciftci, *C. R. Chimie* **2006**, 9, 568.

[178] P. Peumans, A. Yakimov, S.R. Forrest, *J. Appl. Phys.* **2003**, 93, 3693.

[179] G. Yu, J. Gao, J.C. Hummelen, F. Wudl, A.J. Heeger, *Science* **1995**, 270, 1789.

[180] L.H. Sperling, *Adv. Chem. Ser.* **1994**, 239, 3.

[181] S.S. Williams, M.J. Hampton, V. Gowrishankar, I.K. Ding, J.L. Templeton, E.T. Samulski, J.M. DeSimone, M.D. McGehee, *Chem. Mater.* **2008**, 20*,* 5229.

[182] F.C. Krebs. *Polymeric Solar Cells: Materials, Design and Manufacture*, DEStech, Lancaster, **2010**.

[183] M. Reyes-Reyes, K. Kim, D.L. Carroll, *Appl. Phys. Lett.* **2005**, 087506.

[184] T.A. Skotheim, *Handbook of Conducting Polymers*, Dekker, New York, **1997**.

[185] Z. Bao, A. Dodabalapur, A. Lovinger, *Appl. Phys. Lett.* **1996**, 69, 4108.

[186] H. Imahori, *Bull. Chem. Soc. Japan* **2007**, 80, 621.

[187] V.D. Mihailetchi, J.K.J. van Duren, P.W.M. Blom, J.C. Hummelen, R.A.J. Janssen, J.M. Kroon, M.T. Rispens, W.J.H. Verhees, M.M. Wienk, *Adv. Funct. Mater.* **2003**, 13, 43.

[188] S.L. Flegler, J.W. Heckman, K.L. Klomparens, *Elektronenmikroskopie*, Spektrum, Heidelberg, **1995**.

[189] L. Reimer, *Energy-Filtering Transmission Electron Microscopy*, Springer, Berlin, **1995**.

[190] J.I. Goldstein, D.E. Newbury, P. Echlin, D.C. Joy, C.E. Fiori, E. Lifshin, *Scanning Electron Microscopy and X-ray Microanalysis*, Plenum Press, New York, **1981**.

[191] L.C. Sawyer, D. Grubb, G.F. Meyers, *Polymer Microscopy*, Springer, Berlin, **2008**.

[192] P.W. Atkins, *Physikalische Chemie*, Wiley-VCH, Weinheim, **2001**.

[193] D.E. Wolf, *Methods Cell Biol*. **2003**, 72, 157.

[194] J. Als-Nielsen, D. McMorrow, *Elements of Modern X-ray Physics*, John Wiley & Sons, New York, **2001**.

[195] A. Ulman, *An Introduction to Ultrathin Organic Films: From Langmuir-Blodgett to Self-Assembly*, Academic Press, London, **1991**.

[196] D.Y. Kwok, A.W. Neumann, *Adv. Colloid Interface Sci.* **1999**, 81, 167.

[197] A. Jain, A. Kapoor, *Sol. Energy Mater. Sol. Cells* **2005**, 86, 197.

[198] A. Cheknane, H.S. Hilal, F. Djeffal, B. Benyoucef, J.P. Charles, *Microelectron. J*. **2008**, 39, 1173.

[199] S.S. van Bavel, M. Bärenklau, G. de With, H. Hoppe, J. Loos, *Adv. Funct. Mater.* **2010**, 20, 1458.

[200] M.T. Loponen, T. Taka, J. Laakso, K. Vakiparta, K. Suuronen, P. Valkeinen, J.E. Osterholm, *Synthetic Metals* **1991**, 41, 479.

[201] A. Hirsch, M. Bettreich, *Fullerenes*, Wiley-VCH,.Weinheim, **2005**.

[202] J.M. Hawkins, S. Loren, A. Meyer, T.A. Lewis, F.J. Hollander, *Science* **1991**, 252, 312.

[203] H. Sirringhaus, P.J. Brown, R.H. Friend, M.M. Nielsen, K. Bechgaard, B.M.W. Langeveld-Voss, A.J.H. Spiering, R.A.J. Janssen, E.W. Meijer, P. Herwig, D.M. De Leeuw, *Nature* **1999**, 401, 685.

[204] K. Motoyoshi, A. Tajima, T. Higuchi, H. Yabu, M. Shimomura, *Soft Matter* **2010**, 6, 1253.

[205] D.K. Owens, R.C. Wendt, *J. Appl. Polym. Sci.* **1969**, 13, 1741.

[206] W. Rabel, *Farbe Lack* **1971**, 77, 997.

[207] D.H. Kälble, *J. Adhesion* **1970**, 2, 66.

[208] Fa. Krüss, *Drop Shape Analysis DSA1 v 1.92*, **2009**.

[209] L.H. Wang, R.S Porter, *J. Appl. Polym. Sci*. **1983**, 28, 1439.

[210] S. Wu, *J. Phys. Chem*. **1970**, 74, 632.

[211] G.H. Koo, J. Jang, *Fibers Polym.* **2008**, 9, 674.

[212] B. Xue, B. Vaughan, C.H. Poh, K.B. Burke, L. Thomsen, A. Stapleton, X. Zhou, G.W. Bryant, W. Belcher, P.C. Dastoor, *J. Phys. Chem. C* **2010**, 114, 15797.

[213] D.S. Germack, C.K. Chan, B.H. Hamadani, L.J. Richter, D.A. Fischer, D.J. Gundlach, D.M. DeLongchamp, *Appl. Phys. Lett.* **2009**, 94, 233303.

[214] J.S Loo, C.P. Ooi, F.Y. Boey, *Biomaterials* **2005**, 26, 1359.

[215] B. Watts, W.J. Belcher, L. Thomsen, H. Ade, P.C. Dastoor, *Macromolecules* **2009**, 42, 8392.

[216] N.D. Treat, M.A. Brady, G. Smith, M.F. Toney, E.J. Kramer, C.J. Hawker, M.L. Chabinyc, *Adv. Energy Mater.* **2011**, 1, 82.

[217] A.J. Ferguson, N. Kopidakis, S.E. Shaheen, G. Rumbles, *J. Phys. Chem. C* **2008**, 112, 9865.

[218] P.E. Shaw, A. Rusecka, I.D.W. Samuel, *Adv. Mater.* **2008**, 20, 3516.

[219] R.C. Weast (Ed), *CRC Handbook of Chemistry and Physics*, CRC Press, Boca Raton, **1982**.

[220] S. Cook, H. Ohkita, Y. Kim, J.J. Benson-Smith, D.D.C. Bradley, J.R. Durrant, *Chem. Phys. Lett.* **2007**, 445, 276.

[221] T.A. Chen, X. Wu, R.D. Rieke, *J. Am. Chem. Soc* **1995**, 117, 233.

[222] S. Cook, R. Katoh, A. Furube, *J. Phys. Chem. C* **2009**, 113, 2547.

[223] G.Li, V. Shrotriya, .J. Huang, Y. Yao, T. Moriarty, K. Emery, Y. Yang, *Nat. Mater.* **2005**, 4, 864.

[224] M. Sunderberg, O. Inganas, S. Stafstrom, G. Gustafsson,B. Sjogren, *Solid State Commun.* **1989**, 71, 435.

[225] H.J. Butt, K. Graf, M. Kappl, *Physics and Chemistry of Interfaces*, Wiley-VCH, Weinheim, **2006**.

[226] E.M. Lifshitz, *Soviet Phys. JETP* **1956**, 2, 73.

[227] E. Sheppard, N. Tcheurekdjian, *J. Colloid Interface Sci.* **1968**, 28, 481.

[228] P. Pieranski, *Phys. Rev. Lett.* **1980**, 45, 569.

[229] M. Bardosova, M.E. Pemble, I.M. Povey, R.H. Tredgold, *Adv. Mater*. **2010**, 22, 3104.

[230] E. Sirotkin, J.D. Apweiler, F.Y. Ogrin, *Langmuir* **2010**, 26, 10677.

[231] M. Retsch, Z. Zhou, S. Rivera, M. Kappl, X.S. Zhao, U. Jonas, Q. Li, *Macromol. Chem. Phys.* **2009**, 210, 230.

[232] K.B. Blodgett, *J. Am. Chem. Soc.* **1934**, 56, 495.

[233] I. Langmuir, V.J. Schaefer, D.M. Wrinch, *Science* **1937**, 85, 76.

[234] Eur 0270212 A1 (**1987**) invs., H. Dunsmuir, H.W. Deckman, J. A. McHenry.

[235] N.D. Denkov, O.D. Velev, P.A. Kralchevsky, I.B. Ivanov, H. Yoshimura, K. Nagayama, *Nature* **1993**, 361, 26.

[236] N. Denkov, O. Velev, P. Kralchevski, I. Ivanov, H. Yoshimura, K. Nagayama, *Langmuir* **1992**, 8, 3183.

[237] R.D. Deegan, O. Bakajin, T.F. Dupont, G. Huber, S.R. Nagel, T.A. Witten, *Nature* **1997**, 389, 827.

[238] B.K. Tay, D. Sheeja, S.P. Lau, J.X. Guo, *Diamond Relat. Mater.* **2003**, 12, 2072.

[239] P. Jiang, M.J. McFarland, *J. Am. Chem. Soc.* **2004**, 126, 13778.

[240] A. Mihi, M. Ocana, H. Miguez, *Adv. Mater.* **2006**, 18, 2244.

[241] C.H. Woo, B.C. Thompson, B.J. Kim, M.F. Toney, J.M.J. Fréchet, *J. Am. Chem. Soc.* **2008**, 130, 16324.

[242] D.R. Kozub, K. Vakhshouri, L.M. Orme, C. Wang, A. Hexemer, E.D. Gomez, *Macromolecules* **2011**, 44, 5722.

[243] J. Zhao, A. Swinnen, G. van Assche, J. Manca, D. Vanderzande, B. van Mele, *J. Phys. Chem. B* **2009**, 113, 1587.

[244] Y. Zhao, G. X. Yuan, P. Roche, M. Leclerc, *Polymer* **1995**, 36, 2211.

[245] B.A. Collins, J.R. Tumbleston, H. Ade, *J. Phys. Chem.Lett*. **2011**, 2, 3135.

[246] A. Swinnen, I. Haeldermans, M. van de Ven, J. D'Haen, G. Vanhoyland, S. Aresu, M. D'Olieslaeger, J. Manca, *Adv. Funct. Mater.* **2006**, 16, 760.

[247] X.N. Yang, J. Loos, S.C. Veenstra, W.J.H. Verhees, M.M. Wienk, J.M. Kroon, M.A.J. Michels, R.A.J. Janssen, *Nano Lett*. **2005**, 5, 579.

[248] U. Zhokhavets, T. Erb, H. Hoppe, G. Gobsch, N.S. Sariciftci, *Thin Solid Films* **2006**, 496, 679.

[249] F.C. Chen, C.J. Ko, J.L. Wu, W.C. Chen, *Sol. Energy Mater. Sol. Cells* **2010**, 94, 2426.

[250] J.B. Pawley (Ed), *Handbook of Biological Confocal Microscopy*, Springer, Berlin, **2006**

[251] N.S. Sariciftci, L. Smilowitz, A.J. Heeger, F. Wudl, *Synth. Met.* **1993**, 59, 333.

[252]   T. Agostinelli, S. Lilliu, J.G. Labram, M. Campoy-Quiles, M. Hampton, E. Pires, J. Rawle, O. Bikondoa, D.D.C. Bradley, T.D. Anthopoulos, J. Nelson, J.E. MacDonald, *Adv. Funct. Mater.* **2011**, 21, 1701.

[253]   I.J. Wang, S.C. Shiu, M.Y. Lin, J.S. Huang, Y.H. Lin, C.F. Lin, *Sol. Energy Mater. Sol. Cells* 94 **2010**, 94, 1681.

[254]   M.S. White, D.C. Olson, S.E. Shaheen, N. Kopidakis, D.S. Ginley, *Appl. Phys. Lett.* **2006**, 89, 143517.

[255]   B. Zhang, D.H. Lee, H. Chae, C. Park, S.M. Cho, *Korean J. Chem. Eng.* **2010**, 27, 999.

[256]   V. Shrotriya, G. Li, Y. Yao, C.W. Chu, Y. Yang, *Appl. Phys. Lett.* **2006**, 88, 073508.

[257]   F. Geotti-Bianchini, J. Lohrengel, *Glastechnische Berichte* **1993**, 66, 25.

[258]   V.Shrotriya, J. Ouyang, R.J. Tseng, G. Li, Y. Yang, *Chem. Phys. Lett.* **2005**, 411, 138.

[259]   C.R. McNeill, H. Frohne, J.L. Holdsworth, P.C. Dastoor, *Nano Lett.* **2004**, 4, 219.

[260]   Ralf Mauer, *Dissertation: Charge Generation, Transport and Recombination in Organic Solar Cells*, Johannes Gutenberg Universität Mainz, **2012**.

[261]   N. Koch, A. Vollmer, S. Duhm, Y. Sakamoto, T. Suzuki, *Adv. Mater.* **2007**, 19, 112.

[262]   P.A. Winsor, *Trans. Faraday Soc.* **1948**, 44, 376.

[263]   N. Kurokawa, H. Yoshikawa, N. Hirota, K. Hyodo, H. Masuhara, *Chem.Phys. Chem.* **2004**, 5, 1609.

[264]   C. Pacholski, A. Kornowski, H. Weller, *Angew. Chem. Int. Ed.* **2002**, 41, 1188.

[265]   D. Lee, W.K. Bae, I. Park, D.Y. Yoon, S. Lee, C. Lee, *Sol. Energy Mater. Sol. Cells* **2011**, 95, 365.

[266]   S.M. Weekes, F.Y. Ogrin, W.A. Murray, P.S. Keatley, *Langmuir* **2007**, 23, 1057.

[267]   Martin Dass, *Dissertation: Elektronenmikroskopische Studien über polymere Nanopartikel und ihr Potential für biomedizinische Anwendungen*, Universität Ulm, **2010**.

[268]   http://www.ksvnima.com/langmuir-and-langmuir-blodgett-troughs

[269]   C. Minero, E. Pramauro, E. Pelizzetti, *Langmuir* **1988**, 4, 101.